OPTIMIZATION OF DIFFUSION-ENCODING GRADIENT SCHEME FOR DIFFUSION-WEIGHTED MAGNETIC RESONANCE IMAGING OF NERVE FIBERS

By

Shantanu Majumdar

A DISSERTATION

Submitted to
Michigan State University
in partial fulfillment of the requirements
for the degree of

DOCTOR OF PHILOSOPHY

Electrical Engineering

2011

ABSTRACT

OPTIMIZATION OF DIFFUSION-ENCODING GRADIENT SCHEME FOR DIFFUSION-WEIGHTED MAGNETIC RESONANCE IMAGING OF NERVE FIBERS

By

Shantanu Majumdar

Diffusion-Weighted Magnetic Resonance Imaging (DWMRI or DWI) is a specialized imaging technique that can be used to quantify diffusivity of water molecules in biological tissues. Nerve fibers in nervous tissues consist of axon bundles which are highly directional microscopic tube-like structures with semi-permeable boundaries. Water molecules within fibers exhibit diffusion anisotropy due to preferential movement of the molecules along the direction of the fiber. The diffusion anisotropy can be measured by collecting data using a series of diffusion-encoding gradients (diffusion-encoding gradient scheme) in the DWI experiment and solving the inverse problem that characterizes the diffusion anisotropy process. The direction of highest diffusivity gives the direction of the nerve fibers. Hence, DWI provides a completely non-invasive technique to image nerve fibers and study nerve connectivity in the brain, the spinal cord or the peripheral nervous system.

In model-based DWI methods (such as diffusion tensor imaging, DTI), the diffusion process is characterized by a parametric relation between the measured DWI signal and the diffusion model parameters (diffusivity, fiber orientation) as well as the experimental parameters (gradient strengths and directions in the scheme). The model parameters are estimated by solving the inverse problem corresponding to the diffusion process under a given experimental setting. The estimated model parameters are further used to compute secondary diffusion-related quantities (such as mean diffusivity and fractional anisotropy which are potential biomarkers of the health of the nerve fibers) or to reconstruct fiber tracts connecting different locations in the imaged structure (fiber tractography). It is important that the diffusion model parameters are precisely estimated since these directly affect any secondary processing step. The precision of the estimated model parameters

depends on the selection of the experimental parameters and thus can be improved by optimal selection of these parameters.

In this work, a framework to optimize the diffusion-encoding gradient scheme is developed for model-based DWI methods. The framework reduces the estimation uncertainty of diffusion model parameters (thus improves precision) by optimally selecting the diffusion-encoding gradients to minimize an analytical lower bound of the estimation uncertainty (known as the Cramer-Rao lower bound, CRLB). Focus has been on special structures, such as the spinal cord, where the axon bundles are oriented in specific direction known a priori. This availability of a priori information of the fiber orientation has been exploited and embedded into the optimization framework to reduce uncertainty of parameter estimation. The framework uses subject-specific information on diffusion parameters and also allows for a safety margin beyond the expected performance range of diffusion parameters, thereby making it more relevant and less biased. The framework has been validated via Monte Carlo simulations as well as by conducting DTI experiments on human subjects. Also results from fiber tractography show improvement in the quality of tracked nerve fibers upon using the optimized gradient scheme. Thus, the use of the optimization framework can improve the quality of DWI diagnostics by improving precision of the imaging technique and encourage comparison of patient groups.

Copyright by

Shantanu Majumdar

2011

ACKNOWLEDGMENTS

I would like to convey my deepest gratitude to my advisors, Dr. Satish Udpa, Dr. L. Guy Raguin and Dr. David C. Zhu for showing me the right direction in pursuing this doctoral research. Their valued advice has always helped me in understanding the details of this research. Above all, their professional and moral support gave me the strength to reach this final stage of my doctoral research. I would also like to thank Dr. Lalita Udpa and Dr. Jane Turner for their valuable inputs. My thanks to the faculty and staff at the Department of Electrical and Computer Engineering, Michigan State University for providing their help.

I am thankful to the Department of Radiology, Michigan State University, for letting me use the 3T GE Signa HDx research MRI scanner. Special thanks to Dr. Jim Potchen, Tom Cooper, Dr. Kevin Berger from the Department of Radiology. My thanks to all the volunteers who participated in the human study.

I would also like to thank my colleagues from the Nondestructive Evaluation Laboratory, Michigan State University for providing me with helpful advice from time to time. Finally, I thank my mother, my father and my sister for their unrelenting support in helping me go through this journey.

TABLE OF CONTENTS

LI	ST (OF TABLES	ix
LI	ST (OF FIGURES	xi
LI	ST (OF SELECTED ABBREVIATIONS x	viii
LI	ST (OF SELECTED SYMBOLS	xix
1	Intr 1.1 1.2 1.3 1.4 1.5	Neuronal connectivity Diffusion-weighted imaging	1 1 3 6 8 10
2	A re 2.1 2.2 2.3	eview of current techniques in neuroimaging Neuronal connectivity: DWI and other competing technologies Applications of DWI	12 12 14 17
3	3.1 3.2 3.3 3.4	Sic principles of nuclear magnetic resonance imaging Nuclear magnetic resonance and signal generation MR Imaging	20 26 27 27 29 29 30 32
4	4.1 4.2 4.3 4.4 4.5 4.6	Self-diffusion of water in nervous tissue Pulsed gradient spin echo sequence for diffusion quantification Propagator formalism Parametric DWI 4.4.1 DTI formulation 4.4.2 ADTI formulation 4.4.3 QUAQ formulation Non-parametric DWI Experimental DTI protocol used in this work 4.6.1 Pulse sequence	34 34 37 40 42 46 48 50 51

		4.6.2	Experimental settings
	4.7	Fiber	assignment by continuous tracking
5	Opt	imizat	ion of gradient scheme in diffusion-weighted imaging 58
	5.1		al concepts in parameter estimation and optimization 59
		5.1.1	Cramer-Rao Lower Bound
		5.1.2	Sensitivity matrix
		5.1.3	Noise models
		5.1.4	Choice of estimators for different noise models
		5.1.5	Relation with FA, MD and α 64
	5.2	CRLB	for different noise models
		5.2.1	Rician noise case
		5.2.2	Gaussian noise case at high SNR
		5.2.3	Interpretation of CRLB
		5.2.4	Sensitivity matrix computation
	5.3	Partit	ioning CRLB matrix for optimized estimation of selected parameters 84
		5.3.1	Diffusivities
		5.3.2	Angular parameters
	5.4	Gradie	ent scheme optimization framework
		5.4.1	Reformulation of the gradient scheme
		5.4.2	Algorithm
		5.4.3	Optimization Efficiency
		5.4.4	b-factor optimization
		5.4.5	Additional constraints on FA and MD in gradient scheme optimiza-
			tion
	5.5	Comp	arison of optimized gradient schemes and their predicted performances 96
		5.5.1	Distribution of gradient directions
		5.5.2	Performance curves
6	Eva	luatio	of estimation performance by simulations 102
	6.1		characterization
		6.1.1	Method
		6.1.2	Results
		6.1.3	Discussion
	6.2	Perfor	mance of Estimators
		6.2.1	Rician noise
		6.2.2	Gaussian noise
	6.3	Valida	tion of performance curves
	6.4	Simula	ation for effect of b-factor, N and Λ in ADTI model
		6.4.1	Performance indices
		6.4.2	Simulation parameters
		6.4.3	Effect of <i>b</i> -factor
		6.4.4	Effect of number of diffusion gradient directions (N) 116
		6.4.5	Effect of Cone angle (Λ)

		6.4.6	Selection of b-factor, N and Λ	120
	6.5	Comp	arison of performance indices for optimized gradient schemes	121
		6.5.1	ADTI model	122
		6.5.2	DTI model	123
7	Spir		d axisymmetric diffusion tensor imaging	125
	7.1	A valie	dation study for gradient scheme optimization	125
		7.1.1	Experimental Protocol	126
		7.1.2	Statistical Analysis	130
		7.1.3	Results for optimization using cone of fibers obtained from a priori	
			information	131
		7.1.4	Results for optimization without a priori knowledge of cone of fiber	rs133
	7.2	Fiber	tracking analysis	135
		7.2.1	Method	137
		7.2.2	Fiber tracking results	138
	7.3	A part	titioned CRLB based optimization of b-factor and diffusion gradient	
		scheme	e	142
		7.3.1	Method	143
		7.3.2	Results	144
	7.4		sion	146
		7.4.1	Justification for the use of axisymmetric diffusion model for cervical	
			spinal cord	146
		7.4.2	Optimized distribution of gradient directions	148
		7.4.3	Clinical relevance	150
		7.4.4	Fiber tracking in cervical spinal cord	152
		7.4.5	Partitioned CRLB-based b-factor and gradient scheme optimization	
		7.4.6	Justification for the use of prior information	155
8	Con	clusio	ns	157
	8.1	Summ	ary	157
		8.1.1	Gradient scheme optimization	158
		8.1.2	Simulation experiments	159
		8.1.3	Spinal cord ADTI experiments	161
	8.2	Contri	butions	163
	8.3	Future	e Work	164
\mathbf{A}	PPE	NDIC	ES	168
	A	Flowel	harts and instructions for the overall optimization procedure	168
	В	Gradie	ent tables for the spinal cord imaging study	180
ВІ	BLI	OGRA	PHY	188

LIST OF TABLES

6.1	Simulation results for the least-squares (LS) estimator performance assuming Rician noise model	109
6.2	Simulation results for the least-squares with bias correction (LSC) estimator performance assuming Rician noise model	110
6.3	Simulation results for the maximum likelihood (ML) estimator performance assuming Rician noise model	110
6.4	Simulation results for the least-squares (LS) estimator performance assuming Gaussian noise model	111
6.5	Simulation results for the ADTI optimized gradient scheme for Rician noise model	122
6.6	Simulation results for the DTI optimized gradient scheme for the Rician noise model	123
7.1	Average diffusivities and cone angles from preliminary DTI experiment data of five subjects	127
7.2	Performance comparison of the optimized scheme (OPT30) and MF30 from subject data	133
7.3	eSNR comparison of the optimized scheme (OPT30) and MF30 from DTI subject data	133
7.4	Comparison of standard deviations (SD) of angular parameters at ROI voxels from subject data using optimized gradient scheme (OPT30) and MF30	134
7.5	Comparison of standard deviations (SD) of diffusivities at ROI voxels from subject data using optimized gradient scheme (OPT30) and MF30	134
7.6	Comparison of standard deviations (SD) of FA at ROI voxels from subject data using optimized gradient scheme (OPT30) and MF30	134
7.7	Comparison of mean values of diffusivities and angular deviation at ROI voxels from subject data using optimized gradient scheme (OPT30) and MF30	135
7.8	Comparison of standard deviations (SD) of estimated ADTI model parameters and FA at the ROI voxels for subject 1 with gradients optimized for a completely uncertain fiber orientation (OPT30-90) and MF30	137

7.9	Comparison of fiber tracking results for OPT30 and MF30 protocols using simulated fibers	140
7.10	Comparison of fiber tracking results for OPT30 and MF30 protocol for the total number of reconstructed fibers (TF) through the ROI using 5 ADTI subject data	141
7.11	Comparison of fiber tracking results for OPT30 and MF30 protocol for the average fibers per voxel (AF) using 5 ADTI subject data	141
7.12	Comparison of fiber tracking results for OPT30 and MF30 protocol for the average length (in mm) of fibers (AL) tracked using 5 ADTI subject data	141
7.13	Comparison of ADTI parameter standard deviations (RMS) in the ROI voxels for data based on MF30 and OPT30 gradient schemes and one healthy subject	145
7.14	Comparison of ADTI parameter mean values in the ROI voxels for data based on MF30 and OPT30 gradient schemes and one healthy subject	146
B.1	DTI Gradient Table for Subject 1	181
B.2	DTI Gradient Table for Subject 2	182
В.3	DTI Gradient Table for Subject 3	183
B.4	DTI Gradient Table for Subject 4	184
B.5	DTI Gradient Table for Subject 5	185
B.6	DTI Gradient Table for Subject 1 with $\Lambda = 90^{\circ}$	186

LIST OF FIGURES

1.1	(a) T_2 -weighted image, (b) fractional anisotropy (FA) map and (c) mean diffusivity (MD) map. The data for these images are acquired using a DTI protocol (with MF30 gradient scheme and $b = 1000 \text{ s mm}^{-2}$) and the images are processed using FSL software package (Analysis Group, FMRIB, Oxford, UK)	4
1.2	Fiber tracking through Corpus Callosum (a) Axial view, (b) Coronal view. The fibers shown are 3D reconstructed streamline fibers projected onto the 2D image views. The color coding indicates the fiber orientation on the RGB scale, namely, red is right(R)-left(L), blue is superior(S)-inferior(I) and green is anterior(A)-posterior(P) orientations respectively. Note that the axial and coronal views are not on the same scale. The data for these images are acquired using a DTI protocol (with MF30 gradient scheme and $b=1000~{\rm smm^{-2}}$) and fiber tracking is performed using MedINRIA software package (Asclepios Research Project, INRIA Sophia Antipolis, France). For interpretation of the references to color in this and all other figures, the reader is referred to the electronic version of this dissertation.	£3
1.3	DTI results on a healthy adult human in the cervical spinal cord/brainstem region. (a) Fiber orientations estimated by DTI superimposed over a T_2 -weighted image, (b) distribution of the angle between the fiber orientations and the mean fiber orientation	8
3.1	(a) Alignment of spins with B_0 (most are parallel, while some can be antiparallel to B_0 . M is the net magnetization vector. (b) Separation of spin energy into low and high levels when subjected to B_0	21
3.2	(a) M when RF pulse, B_1 , is applied as seen in the laboratory reference frame (b) M nutated by flip angle θ as seen in the rotating reference frame. (c) M during relaxation after RF pulse is turned off as seen in the laboratory reference frame. $M_{\rm Z}$ and $M_{\rm XY}$ are the longitudinal and transverse magnetizations respectively	24
3.3	(a) T_1 recovery of longitudinal magnetization and (b) T_2 decay of transverse magnetization. M_0 is the equilibrium magnetization	25
3.4	Schematic showing slice (Δz) selection in z-direction using G_z field in (a) and the sinc-modulated B_1 RF signal in frequency (b) and time (c) domains respectively	28
3.5	Schematic showing k-space imaging using 2D Fourier transform method.	29

3.6	(a) Schematic showing absence of spatial encoding when no gradient field is used. (b) Schematic showing encoding of a fixed length $(2L)$ in x-direction using gradient field, G_x
3.7	Gradient echo pulse sequence diagram showing the timings of the slice selection, phase-encoding and frequency-encoding gradients
3.8	Spin-echo pulse sequence diagram showing the timings of the slice selection, phase-encoding and frequency-encoding gradients
4.1	Brownian motion of water molecules in (a) a healthy axon fiber and (b) an axon fiber with a rupture
4.2	Schematic of the PGSE sequence showing only the timing of the diffusion-encoding gradient and the RF pulses. Here, $\tau = T_E/2$, where T_E is the echo time
4.3	DTI diffusivity ellipsoid indicating diffusivities $(D_{\parallel}, D_{\perp 1}, D_{\perp 2})$ and the orientation angles $(\theta_F, \phi_F, \psi_F)$
4.4	ADTI diffusivity ellipsoid indicating diffusivities $(D_{\parallel}, D_{\perp})$ and the orientation angles (θ_F, ϕ_F)
4.5	(a) A schematic of a typical echo-planar imaging sequence for gradient echo. (b) The k-space trajectory for the EPI sequence
4.6	(a) Single RF pulse with slice select gradient. (b) 12 RF pulses of the spatio-spectral pulse sequence with the slice select gradients
5.1	Rician distribution at different SNRs (SNR = m/σ). Distribution are generated by (a) varying m and fixing σ at 1.0 and (b) varying σ and fixing m at 2.5
5.2	Plot of (a) the normalized MR signal and (b) its square for the ADTI model with respect to the gradient direction angles (θ, ϕ) with the mean fiber direction is at $(\theta_F, \phi_F) = (0^{\circ}, 0^{\circ})$. The gray scale represents the corresponding signal value
5.3	Plot of the sensitivity values and their square for the ADTI model with respect to gradient direction angles (θ, ϕ) . Shown in the figure are sensitivity values and their squares w.r.t. D_{\parallel} ((a) and (b)), D_{\perp} ((c) and (d)), θ_F ((e) and (f)) and ϕ_F ((g) and (h)). The mean fiber direction is at $(\theta_F, \phi_F) = (0^{\circ}, 0^{\circ})$. The gray scale represents the corresponding sensitivity values or its square

5.4	Variation of the sensitivity values and the normalized MR signal w.r.t. diffusion gradient direction angles (θ, ϕ) for nearly axisymmetric case for the DTI model. Shown in the figure are sensitivity values w.r.t. (a) D_{\parallel} , (b) $D_{\perp 1}$, (c) $D_{\perp 2}$, (d) θ_F , (e) ϕ_F , (f) ψ_F and (g) the normalized MR signal. The mean fiber direction is at $(\theta_F, \phi_F) = (90^{\circ}, 0^{\circ})$	80
5.5	Variation of the squares of sensitivity values and the normalized MR signal w.r.t. diffusion gradient direction angles (θ, ϕ) for nearly axisymmetric case for the DTI model. Shown in the figure are squares of sensitivity values w.r.t. (a) D_{\parallel} , (b) $D_{\perp 1}$, (c) $D_{\perp 2}$, (d) θ_F , (e) ϕ_F , (f) ψ_F and (g) the normalized MR signal. The mean fiber direction is at $(\theta_F, \phi_F) = (90^{\circ}, 0^{\circ})$.	81
5.6	Variation of the sensitivity values and the normalized MR signal w.r.t. diffusion gradient direction angles (θ, ϕ) for non-axisymmetric case for the DTI model. Shown in the figure are sensitivity values w.r.t. (a) D_{\parallel} , (b) $D_{\perp 1}$, (c) $D_{\perp 2}$, (d) θ_F , (e) ϕ_F , (f) ψ_F and (g) the normalized MR signal. The mean fiber direction is at $(\theta_F, \phi_F) = (90^{\circ}, 0^{\circ})$	82
5.7	Variation of squares of the sensitivity values and the normalized MR signal w.r.t. diffusion gradient direction angles (θ, ϕ) for non-axisymmetric case for the DTI model. Shown in the figure are squares of sensitivity values w.r.t. (a) D_{\parallel} , (b) $D_{\perp 1}$, (c) $D_{\perp 2}$, (d) θ_F , (e) ϕ_F , (f) ψ_F and (g) the normalized MR signal. The mean fiber direction is at $(\theta_F, \phi_F) = (90^{\circ}, 0^{\circ})$.	83
5.8	Gradient directions (white circles) on a 2D opened hemisphere showing a reformulated scheme (for P = 3). Mean fiber orientation is at $(\theta_F, \phi_F) = (0^{\circ}, 0^{\circ})$. The gray scale underlay shows the normalized MR signal variation due to changing gradient directions (θ, ϕ)	88
5.9	Robust optimization results for the ADTI model with Rician CRLB for $b=1000~{\rm smm^{-2}}$ with $P=3$ rings for fiber orientations within a cone of axis along the z-axis and cone angle $\Lambda=35^{\circ}$. (a) Gradient directions (white circles) an opened hemisphere with gray scale equal to the normalized MR signal. (b) Comparison of performance curves	90
5.10	Variation of normalized hypervolume of uncertainty for 30-direction optimal gradient schemes for ADTI model. The cone angles vary as ($\Lambda = [10^{\circ} - 90^{\circ}]$) and Rician noise case is selected. Noise level, $\sigma = 0.1$. Normalization reference is MF30 gradient scheme	91
5.11	Plot of the ratio of hypervolumes for OPT30 w.r.t. MF30 scheme optimized using Gaussian noise assumption and for the DTI model. The contour line at unity value shows the cone of angles within which the optimization performance is improved	92

5.12	Optimized Gradient schemes for the ADTI diffusion model under the following optimality criteria: optimize for all parameter ((a) Rician and (b) Gaussian), diffusivities only ((c) Rician and (d) Gaussian) and fiber orientation only ((e) Rician and (f) Gaussian). MF30 scheme is shown in (g). The fiber orientation, $(\theta_F, \phi_F) = (0^{\circ}, 0^{\circ})$. The gray scale values represent the normalized MR signal and the white circles are the locations of the diffusion gradient unit vector on an opened unit hemisphere	98
5.13	Optimized Gradient schemes for the DTI diffusion model under the following optimality criteria: optimize for all parameter ((a) Rician and (b) Gaussian), diffusivities only ((c) Rician and (d) Gaussian) and fiber orientation only ((e) Rician and (f) Gaussian). The fiber orientation, $(\theta_F, \phi_F) = (90^{\circ}, 0^{\circ})$. The gray scale values represent the normalized MR signal and the white circles are the locations of the diffusion gradient unit vector on an opened unit hemisphere.	96
5.14	Performance curves for the ADTI diffusion model for optimization w.r.t. all parameters ((a) Rician and (b) Gaussian), diffusivities ((c) Rician and (d) Gaussian) and angular parameters ((e) Rician and (f) Gaussian)	100
5.15	Performance plots for the DTI diffusion model for optimization w.r.t. all parameters ((a) Rician and (b) Gaussian), diffusivities ((c) Rician and (d) Gaussian) and angular parameters ((e) Rician and (f) Gaussian). Gray scale values indicate the ratio of CRLB-based hypervolume of OPT30 by MF30 and the contour lines are at unity ratio	101
6.1	Comparison of the estimated and true values of the normalized MR signal (E) for the cases of Rician and Gaussian fit to the distribution of S/S_0 and S/m_0 . Simulations are run at (a) NEX = 2 and (b) NEX = 4	104
6.2	Variation of the estimated σ_E of the noisy normalized MR signal (\hat{E}) for the cases of Rician and Gaussian fits to the distributions of S/S_0 and S/m_0 respectively. Simulations are run at (a) NEX = 2 and (b) NEX = 4	105
6.3	Variation of ratio of hypervolume of uncertainty $(D_{OPT}/D_{MF}, D = \sqrt{\det{(\Sigma_{CR})}})$ for ADTI model from Monte Carlo simulations w.r.t. angular deviation (α) at $\sigma = 0.1$, $\Lambda = 35^{\circ}$. Gaussian case with LS estimator (a) and Rician case with LS (b), LSC (c) and ML (d) estimators	112
6.4	Effect of varying b-factor on the diffusion gradient optimization. Performance indices (a) normalized hypervolume for successful trials (μ_{r1}) , (b) percentage success rate (P_S) , (c) effective SNR (eSNR) and (d) normalized variance of FA (σ_{FA}^2) are shown for different b-factors and for both the optimized gradient schemes (OPT) and the MF30 scheme (MF)	116

6.5	Effect of varying number of diffusion gradients (N) on the diffusion gradient optimization. Normalized hypervolume for successful trials (μ_{r1}) ((a) and (b)), effective SNR (eSNR) ((c) and (d)) and normalized variance of FA (σ_{FA}^2) ((e) and (f)) are shown for different N and for both the optimized gradient schemes (OPT) and the MF-based schemes (MF). Figures (a), (c) and (e) are for $b = 1000$ s mm ⁻² , whereas figures (b), (d) and (f) are for $b = 2500$ s mm ⁻²	117
6.6	Effect of varying cone angle (Λ) on diffusion gradient optimization. Performance indices (a) normalized hypervolume for successful trials, (μ_{r1}) , (b) percentage success rate (P_S) , (c) effective SNR (eSNR) and (d) normalized variance of FA (σ_{FA}^2) are shown for different Λ and for both the optimized gradient schemes (OPT) and the MF30 scheme (MF)	119
7.1	(a) T1 coronal view of the cervical spinal cord and brain stem near the C1 - C2 vertebral region. The boxed region is selected manually and further magnified in (b) (e). (b) T2 coronal image showing the segmented spinal cord within the initial ROI in (a) after removal of the CSF surrounding the spinal cord by MD thresholding. (c) T2 coronal image showing the selected white matter ROI voxels in (b) after removal of gray matter voxels by FA thresholding. Similarly, the brain stem region is first manually selected in (a), and then thresholded in two stages, (d) and (e), to extract the ROI voxels	128
7.2	Optimized gradient scheme (white circles) for 30 gradient directions on a 2D opened hemisphere for cone angles (a) $\Lambda=35^{\circ}$ (b) $\Lambda=90^{\circ}$ (completely uncertain fiber orientation case). Underlying grayscale image shows the normalized MR signal levels over the hemisphere changing with respect to the diffusion gradient direction (θ, ϕ) . Mean fiber orientation is at $(0^{\circ}, 0^{\circ})$.	129
7.3	Region of interest (ROI) voxel distributions with respect to hypervolume ratio (D_{OPT30}/D_{MF30}) for different subjects. D_{OPT30} and D_{MF30} are square roots of the determinants of covariance matrix of parameter estimation $(\sqrt{\det \Sigma})$ for estimation (Est.) and $\sqrt{\det \Sigma}$ for prediction (Pred.)) for OPT30 and MF30 schemes respectively. Figs. (a) to (e) correspond to subject number 1 to 5. Majority of the ROI voxels for each subject are in the less than unity range indicating an overall uncertainty reduction in the parameter estimation	132
7.4	Distributions of relative differences for various estimated quantities under the DTI and ADTI model. Differences of (a) $\lambda_r = (\lambda_2 + \lambda_3)/2$ and D_{\perp} , (b) λ_1 and D_{\parallel} , (c) FA (d) MD, (e) θ_F and (f) ϕ_F are shown. These results are based on the voxels in the cervical spinal cord white matter tracts (C1-C2 region) from five subject data collected using the MF30 gradient scheme.	136

7.5	riber tracking based on simulated fiber bundle surrounded by isotropic medium	138
7.6	(a) Coronal view, (b) sagittal view and (c) axial view of T2-weighted image of the cervical spinal cord with the seed ROI shown in red	139
7.7	3D fiber tracking shown in the cervical spinal cord region using the DTIS-tudio software	139
7.8	Distribution of 30 gradient directions (white circles) on a opened unit hemisphere shown with an underlay image of the normalized MR signal at $b=2062~\mathrm{smm^{-2}}$ and FA = 0.9	144
7.9	ROI voxel distribution with respect to hypervolume ratio (D_{OPT30}/D_{MF30}) based on the ADTI datasets from MF30 and OPT30 gradient scheme for one healthy subject. Estimated $P_S=72.2\%$ and $\mu_{r1}=0.742$ for 36 ROI voxels. Estimation is based on the covariance of estimates and prediction is based on the Rician CRLB formulation	145
7.10	Distributions of optimized diffusion gradient directions (indicated by white circles) on an opened unit hemisphere. Underlying grayscale image shows the normalized MR signal levels over the hemisphere changing with respect to the diffusion gradient direction (θ_F, ϕ_F) . Optimized gradients are shown for the ADTI model in (a) and the non-axisymmetric DTI model in (b) for healthy white matter tracts with FA = 0.745, MD = 0.818 × 10 ⁻³ mm ² s ⁻¹ . For the pathological case (cervical spinal cord in ALS patients), optimized gradients are shown for the ADTI model in (c) and the non-axisymmetric DTI model in (d) with FA = 0.45, MD = 0.96 × 10 ⁻³ mm ² s ⁻¹ . For all cases, the fiber orientation angle is $(\theta_F, \phi_F) = (0^{\circ}, 0^{\circ})$	148
7.11	An illustration of the FACT algorithm applied to a 2D distribution of fiber orientations. Tracks are shown in orange. Each box represents a pixel with the fiber orientation shown by the arrow. True fiber orientation is along the vertical. Light red pixels are ones with more uncertain fiber orientation. The green pixels are the seed (ROI) pixels. Only tracks penetrating the seed pixels are retained	153
A.1	Flowchart for the processing of the preliminary DTI data to compute the cone angle (Λ) and the mean of ADTI model parameters in the spinal cord tract region	170
A.2	General overview of the overall gradient and b-factor optimization scheme. Flowcharts for simulated annealing, robust optimization and b-factor optimization are shown in Figs. A.3–A.6	173

A.3	Flowchart describing the simulated annealing algorithm to find the sub- optimal solution (not using the cone angle information). $\Omega = \{g_i; i \in [1, N]\}$, N is the number of gradient directions $(N = 30)$. g_i is the i th gradient direction vector: $\mathbf{g}_i \equiv [g_{xi}, g_{yi}, g_{zi}] \equiv [\theta_i, \phi_i]$. Cost function, $S = \det \Sigma_{CR, full}$ or $\det \Sigma_{CR, partial}$. S is a function of Ω . S_0 is the initial value of cost function for gradient scheme Ω_0 and it is later updated in every iteration. 'rand' is a function that generates random numbers between 0 and 1 with uniform probability. The flowchart for the decision box for stopping criteria is shown in Fig. A.4	174
A.4	Flowchart for the stopping criteria in the simulated annealing algorithm. Here, NtryT = number of trials at a fixed temperature T, max_NtryT = maximum limit of NtryT, Nsucc = success count, max_Nsucc = maximum limit of Nsucc, Nrej = consecutive rejection count, max_Nrej = maximum limit of Nrej, T = temperature(simulated), min_T = minimum limit of T, $cool(T) = cooling$ method for T	175
A.5	Flowchart for the robust optimization procedure for the gradient directions utilizing the cone angle information of fiber orientations. $\Omega = \{g_i; i \in [1, N]\}$, N is the number of gradient directions $(N = 30)$. g_i is the i th gradient direction vector. Cost function, $S = \det \Sigma_{CR, full}$ or $\det \Sigma_{CR, partial}$ iter = number of iterations, iterMax = maximum limit of iter, del = absolute relative change in the cost function (abs $(S - S_0/S_0)$), delMin = minimum limit of del, osc = number of oscillations in the cost function, oscMax = maximum limit of osc	176
A.6	Flowchart for the robust optimization of gradient directions and b -factor using simulated annealing algorithm utilizing the cone angle information of fiber orientations. Here, $\Omega = \{g_i; i \in [1, N]\}$, N is the number of gradient directions $(N = 30)$. g_i is the i th gradient direction vector: $g_i \equiv [g_{xi}, g_{yi}, g_{zi}] \equiv [\theta_i, \phi_i]$. Cost function, $S = \det \Sigma_{CR, full}$ or $\det \Sigma_{CR, partial}$. S is a function of Ω . S_0 is the initial value of cost function for gradient scheme Ω_0 and it is later updated in every iteration. The flowchart for the decision box for stopping criteria is shown in Fig. A.4	177
A.7	Flowchart for the processing of the multiple DTI 4D volume datasets obtained by using the optimized protocol and compared to the MF30 protocol	.179
B.1	Diffusion gradient directions (white circles) for Subject 1 optimized using prior structural information. The underlay shows the normalized MR signal w.r.t. gradient direction angles (θ, ϕ)	180
B.2	Diffusion gradient directions (white circles) for Subject 2 optimized using prior structural information. The underlay shows the normalized MR signal w.r.t. gradient direction angles (θ, ϕ)	182

В.3	Diffusion gradient directions (white circles) for Subject 3 optimized using prior structural information. The underlay shows the normalized MR signal w.r.t. gradient direction angles (θ, ϕ)	183
B.4	Diffusion gradient directions (white circles) for Subject 4 optimized using prior structural information. The underlay shows the normalized MR signal w.r.t. gradient direction angles (θ, ϕ)	184
B.5	Diffusion gradient directions (white circles) for Subject 5 optimized using prior structural information. The underlay shows the normalized MR signal w.r.t. gradient direction angles (θ, ϕ)	185
B.6	Diffusion gradient directions (white circles) for Subject 1 optimized using completely uncertain fiber orientation. The underlay shows the normalized MR signal w.r.t. gradient direction angles (θ, ϕ)	186

LIST OF SELECTED ABBREVIATIONS

ADTI axisymmetric diffusion tensor imaging

CRLB Cramer-Rao lower bound

CSF cerebrospinal fluid

DTI diffusion tensor imaging

DWI diffusion-weighted imaging

eSNR effective signal-to-noise ratio

FA fractional anisotropy

FACT fiber assignment by continuous tracking

FID free induction decay

LS least-squares

MD mean diffusivity

MF minimum force

MLE maximum likelihood estimator

MRI magnetic resonance imaging

NEX number of excitations

PGSE pulsed gradient spin-echo sequence

RF radio frequency

ROI region of interest

SE-EPI spin-echo echo-planar imaging

LIST OF SELECTED SYMBOLS

 T_R time of repetition, ms

 T_E time of echo, ms

 T_1 longitudinal magnetization recovery time constant, ms

 T_2 transverse magnetization decay time constant, ms

 γ gyromagnetic ratio, rad s⁻¹T⁻¹

 δ diffusion encoding gradient pulse width, ms

 Δ time interval between diffusion encoding gradient pulses, ms

b b-factor or diffusion sensitivity factor, s mm⁻²

D diffusion tensor matrix, mm² s⁻¹

 D_{\parallel} longitudinal diffusivity in ADTI model, mm² s⁻¹

 D_{\perp} transverse diffusivity in ADTI model, mm² s⁻¹

 θ_F zenith angle for fiber orientation in ADTI model, rad

 ϕ_F azimuthal angle for fiber orientation angle in ADTI model, rad

E normalized MR signal or echo attenuation, dimensionless

 Σ_{CR} Cramer-Rao lower bound of the covariance matrix of estimated parame-

ters, unit depends on the diffusion model

X sensitivity matrix, unit depends on the diffusion model

 σ noise standard deviation in normalized MR signal, dimensionless

N number of gradient directions, dimensionless

 Λ cone angle of fiber directions, deg

 P_S percentage success rate, %

 μ_{r1} mean ratio of hypervolumes, dimensionless

CHAPTER 1

Introduction

1.1 Neuronal connectivity

The human body comprises of a complex network of neural connections between different organs and the nervous system. Through these neural connections, the functioning of the different organs is controlled by the central nervous system (CNS). The CNS comprising of the brain and the spinal cord itself contain neural networks by which different regions of the CNS communicate with each other. The neural connections are formed by a large number of nerve cells consisting of a cell body and a tail-like structure called axon. Axons are specialized structures responsible for conducting action potentials (neural electrical impulses) from a nerve cell to another. Axons connect with other nerve cells via synapses. Bundles of axons or axonal fiber tracts (or neural fiber tracts) within the brain, the spinal cord and the peripheral nervous system provide a communication network for transmitting a plethora of control signals to a variety of organs. The integrity of the neural network formed by the neural fiber tracts is extremely important for the normal functioning of the human body. Thus, there is a need for non-invasive methods for imaging the neural fiber tracts for proper evaluation of the health of the tracts and the diagnosis of pathology.

The integrity of the neural network can be analyzed by neuronal connectivity studies which can either be structural (based on neuro-anatomy) or functional (based on neurophysiology) studies. Some of the techniques based on measuring neuro-physiological phenomena (as critically discussed in [1,2]) are Electroencephalography (EEG, which measures the electrophysiology in the brain), Magnetoencephalography (MEG, which measures the induced magnetic field caused by the electrophysiology in the brain), functional Magnetic Resonance Imaging (fMRI, which measures the hemodynamic response (blood oxygen level dependent (BOLD) signal [3]), generally in the brain) and Fludeoxyglucose (FDG) Positron Emission Tomography (FDG-PET, which measures the metabolic absorption rate in the whole body), O-15 PET (measures cerebral blood flow). It should be noted that physiological phenomena are largely due to changes in the nerve cell body rather than the fiber tracts themselves and the connectivity is established in different parts of the nervous system by either analyzing the temporal correlation of these physiological processes or testing a hypothesis based on a cause-effect relation (causality). Hence, it's an indirect way of establishing neuronal connectivity as compared to a more direct way in neuro-anatomical imaging.

Early techniques in neuro-anatomical imaging were ex vivo and only applicable postmortem, such as tract tracing using fluorescent dyes (for example, [4]). However, recent advances in imaging technology especially in magnetic resonance imaging, have provided completely non-invasive in vivo methods for studying neuronal connectivity anatomically. To understand the anatomy of fiber tracts, there is a need to precisely and accurately visualize the fibers causing little or no damage to the structure. Stejskal and Tanner [5, 6] showed that nuclear magnetic resonance (NMR) can be used to obtain information about diffusion of water molecules when confined within restrictive boundaries. They demonstrated that by applying a pair of diffusion-encoding gradients in a spin-echo experiment, the NMR signal can be weighted by an additional attenuation factor that depends on the diffusivity of water molecules. After the advent of magnetic resonance imaging (MRI), the use of the Stejskal-Tanner pulse sequence [5] (or sequences based on it) during MR imaging would be known as Diffusion-Weighted MRI (DW-MRI or DWI). An important observation from the DWI is that the MR signal attenuation due to diffusion depends on the direction of the diffusion-encoding gradient. Thus, applying diffusion-encoding gradients along the direction of high water diffusivity produces higher MR signal attenuation compared to along any other direction. Hence, DWI can be used to measure diffusion anisotropy.

In the axon bundles in nerve fibers, the water molecules follow preferential movement along the fiber direction. This preferential movement is due to barriers to molecular motion such as myelin (fat) sheath in neural fibers that causes restricted or hindered diffusion towards the boundary of the fibers and unrestricted diffusion along the longitudinal direction of the fiber. Such anisotropy in the local diffusion process can be measured by DWI to infer tissue microstructure in the neural fibers. By optimally selecting the strength and directions of the diffusion-encoding gradient, neural fiber tracts can be more precisely demarcated. This leads to a more comprehensive study of the neural fiber tracts and helps to improve the DWI protocols in clinical studies.

1.2 Diffusion-weighted imaging

In diffusion-weighted imaging, the diffusion-weighted MR images are acquired by using specialized pulse sequences such as the Stejskal-Tanner Spin Echo sequence [5] which uses additional diffusion-encoding gradients. This pulse sequence can capture the effect of local water diffusion and attenuate the MR signal according to the diffusion process. It should be noted that the DWI images themselves are less informative. However, from post-processing of the DWI image data, quantities characterizing the diffusion process are estimated which provide more direct information about the imaged structure and are more commonly used in the analysis or diagnosis of diseases. These quantities can either be scalar so as to generate a secondary parametric map or these can be angular information which can be directly used for tracking neural fibers.

The diffusion process can be characterized either by a parametric model or by a nonparametric process, such as defined by a transform of the DWI data. This distinction differentiates the post-processing techniques. For model-based post-processing (e.g., DTI [7], QUAQ (quantitative analysis of q-space) [8], CHARMED (composite hindered and restricted model of diffusion) [9]), the MR signal is modeled by a parametric relation between the signal and diffusion model parameters (such as the local diffusion coefficients or diffusivities and the fiber orientation angles). This is in contrast to non-parametric methods (e.g., diffusion spectrum imaging [10], q-ball imaging [11]), where the signal is processed to obtain probability distributions of quantities of interest. For instance, the orientation distribution function in q-ball imaging is obtained by performing the Funk-Radon transform of the DWI data collected under certain experimental settings [11]. The focus of this work is on model-based methods, such as DTI.

In model-based post-processing approaches, the DWI data is fitted to a diffusion model to extract specific quantitative information. Diffusion tensor imaging (DTI, [7,12]), the most often used model, is based on an anisotropic hindered diffusion model with six parameters, and yields a local "apparent diffusion tensor", whose principal eigenvector provides the fiber orientation. DTI model uses a single tensor to characterize diffusion within the fiber tracts and as such it reconstructs a single (unidirectional) fiber bundle within each volume element (voxel) of the image. The DTI model can be modified by assuming axisymmetric diffusion inside fibers (ADTI), reducing the number of model parameters to four. A physics-based approach, called QUAQ (quantitative analysis of q-space [8]), models fibers as impermeable axisymmetric cylinders, and uses the solution of the diffusion equation inside a cylinder which also contains four parameters.

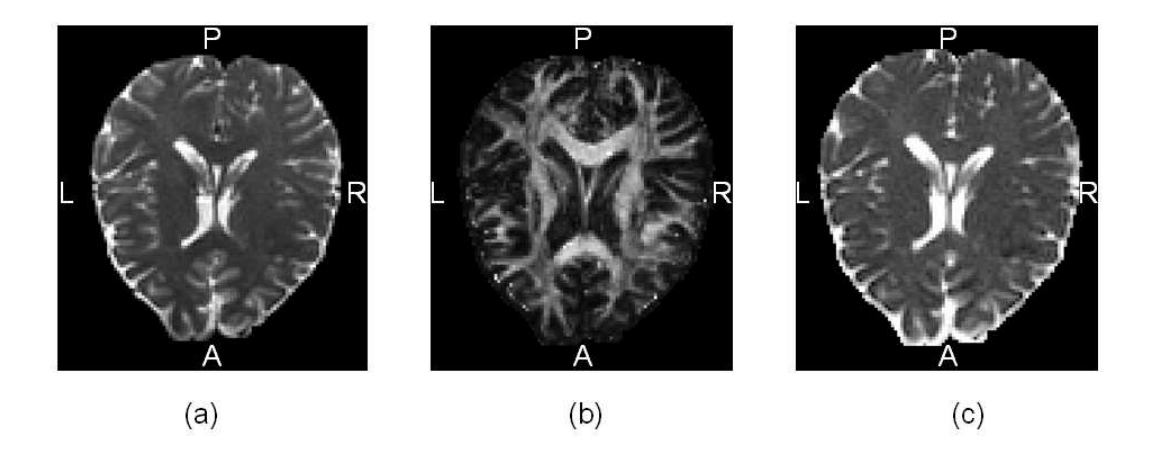
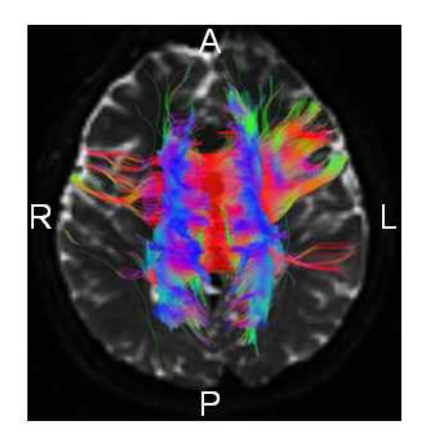


Figure 1.1. (a) T_2 -weighted image, (b) fractional anisotropy (FA) map and (c) mean diffusivity (MD) map. The data for these images are acquired using a DTI protocol (with MF30 gradient scheme and $b = 1000 \text{ s} \text{ mm}^{-2}$) and the images are processed using FSL software package (Analysis Group, FMRIB, Oxford, UK).

For neuronal connectivity, diffusivities and fiber orientation maps are investigated since these can indicate presence and connection of fibers in the imaged region. For example, a secondary quantity computed based on the DTI processing is fractional anisotropy (FA) which is a dimensionless number represented by a ratio of diffusion coefficients as defined in [13]. It is indicative of the local diffusion anisotropy (see Fig. 1.1(b)). FA images are widely used in connectivity studies (for example, [14]). Another scalar quantity derived from the DWI data is the mean diffusivity (MD) which provides an average of diffusivities calculated from the apparent diffusion tensor. The MD is more indicative of local diffusion isotropy (see Fig. 1.1(c)). For fiber tractography (or tracking), fiber orientation information as well as other diffusion coefficient based quantities (such as FA) are collected as the output of DWI post-processing and used in tractographic algorithms ([15,16]) (see Fig. 1.2). Since fiber tractography is a secondary processing stage, its precision and accuracy (and, in general, quality) depends on the precision and accuracy of the post-processing results of DWI.



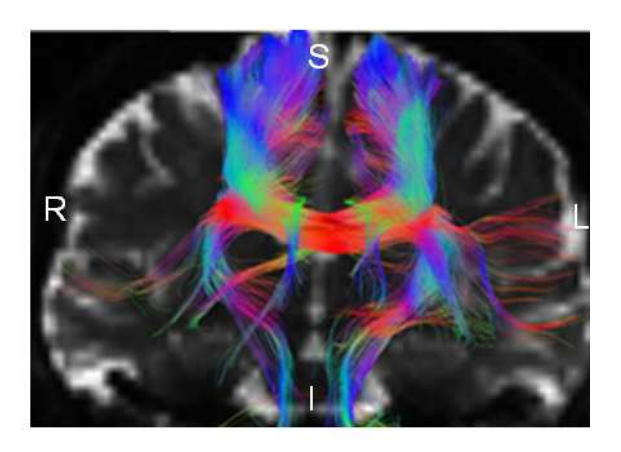


Figure 1.2. Fiber tracking through Corpus Callosum (a) Axial view, (b) Coronal view. The fibers shown are 3D reconstructed streamline fibers projected onto the 2D image views. The color coding indicates the fiber orientation on the RGB scale, namely, red is right(R)-left(L), blue is superior(S)-inferior(I) and green is anterior(A)-posterior(P) orientations respectively. Note that the axial and coronal views are not on the same scale. The data for these images are acquired using a DTI protocol (with MF30 gradient scheme and b = 1000 s mm⁻²) and fiber tracking is performed using MedINRIA software package (Asclepios Research Project, INRIA Sophia Antipolis, France). For interpretation of the references to color in this and all other figures, the reader is referred to the electronic version of this dissertation.

In DWI, there are a number of MRI experimental parameters that can be optimally chosen to improve the precision of the estimated fiber orientation and the diffusion model parameter. These include the diffusion-encoding gradient strength, gradient directions and timing parameters, such as the diffusion gradient pulse duration and time interval between the diffusion gradients. Several optimization criteria and gradient-encoding schemes have been discussed in [17]. DWI protocol optimization can also be based on a specific structure to be imaged. If adequate knowledge about the structure is available, optimal schemes based on the *a priori* knowledge can be designed.

1.3 Optimizing DWI protocols

In the formulation of an optimization problem, it is required to define the optimized parameters, the optimization cost function which is minimized during the optimization procedure, other additional parameters which are part of the formulation but not varied, constraints on the optimized parameters and finally the prior knowledge of the parameters of the problem. After the optimization problem is formulated, the next steps include the development and implementation of the algorithm that solves the optimization problem and computes the optimized parameters. Finally, the performance of the optimized parameters is validated using either simulations or experiments.

A DWI experimental protocol consists of a prescribed list of settings for the different experimental parameters to be used during imaging. For a Stejskal-Tanner spin-echo pulse sequence, these include parameters related to the diffusion-encoding gradient (its strength, direction and timings). In the context of the optimization problem, these are the optimized parameters. However, a variety of cost functions have been defined by researchers which address different aspects of the DWI experiment. The optimization problem depends on the post-processing of the DWI data. Since the focus is on model-based post-processing (especially DTI), I will discuss some of the optimization done for the DTI protocol.

A number of DTI diffusion gradient optimization techniques have been proposed previ-

ously. Numerically optimized schemes (minimum force, minimum energy, minimum condition number), heuristic schemes (orthogonal encoding) and geometric schemes (icosahedral polyhedra) are approaches that only optimize diffusion gradient directions [17]. There are schemes based on optimizing the specific cost function, such as in [18–21]. Hasan et al. [17] summarized several DTI-based or model-independent optimization cost function to be minimized (variance for the diffusion tensor components, condition number [19], force [22], Coulomb energy) and compared the resulting schemes via Monte Carlo simulations. Besides diffusion gradient directions, optimization can also be on the selection of the diffusion gradient strength, pulse duration and pulse interval between diffusion gradients and number of diffusion gradient directions, as shown by Alexander et al. [23] and Brihuega-Moreno [24]. In DTI, the diffusion gradient strength and the timing parameters are combined into b-factor [12].

In the discussion so far, the various DTI protocol optimization mentioned focus on the selection of the optimization cost function while not exploring the use of prior knowledge of the diffusion model parameters which can be effectively used to improve the optimization performance. Use of the prior knowledge constrains the optimization problem. Hence, the prior should be chosen cautiously so as to not overly constrain the problem.

Typically, the prior knowledge of the imaged structure can be utilized for optimization. For example, in spinal cord tracts in normal healthy subjects, the nerve fibers are mostly in the superior-inferior orientation and enclosed within a narrow range of fiber angles. To illustrate this point, DTI data was collected using standard protocol and analyzed in the cervical spinal cord region of a healthy adult.

Fig. 1.3(a) shows the coronal view of the spinal cord/brain stem region. The underlying image is a T₂-weighted MRI image used for demarcation of the spinal cord region (dark region) within the cerebrospinal fluid (CSF) surroundings (bright regions). The overlying arrows show the fiber orientation (projected on the 2D image) estimated using DTI at each pixel of the image. The distribution of the deviation angle α w.r.t. the average orientation of the nerve fibers is plotted in Fig. 1.3(b). It is observed that the majority (\sim 85%) of the fiber orientations is contained within a narrow range of fiber angles (cone

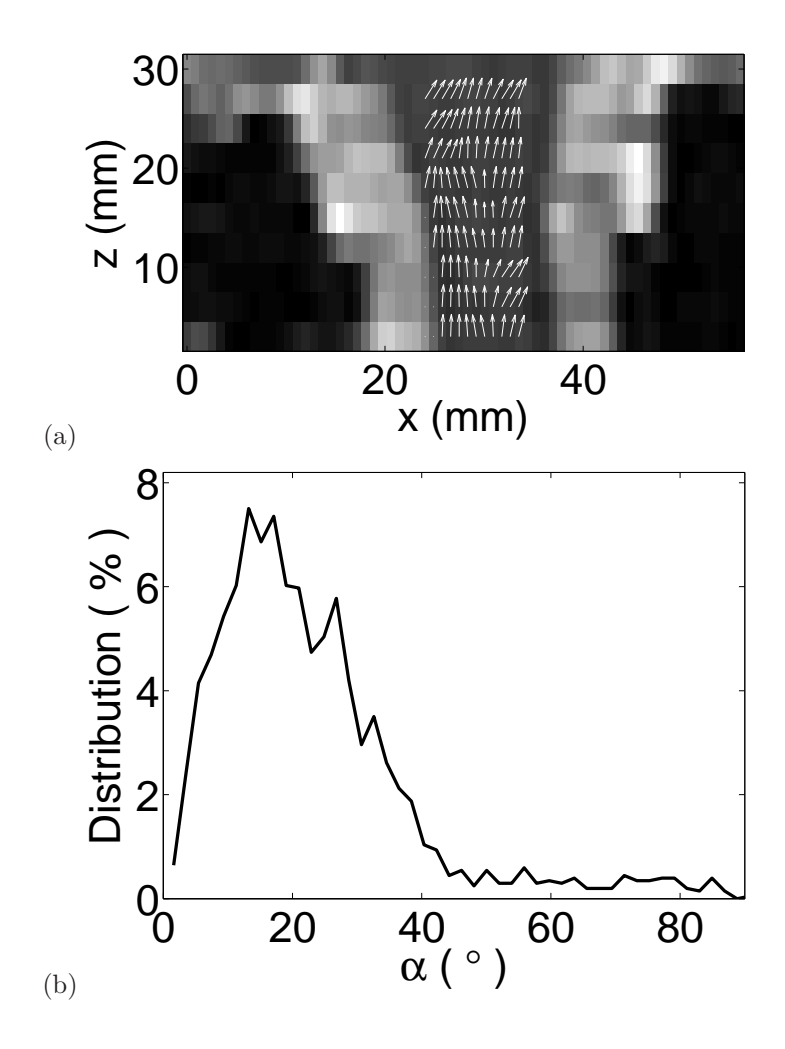


Figure 1.3. DTI results on a healthy adult human in the cervical spinal cord/brainstem region. (a) Fiber orientations estimated by DTI superimposed over a T₂-weighted image, (b) distribution of the angle between the fiber orientations and the mean fiber orientation. of half-angle 35°).

1.4 Motivation and scope of research

Tissue structural information is well documented from anatomical studies for both healthy ([25]) and pathological tissues ([26]). The available knowledge of expected structure can be represented by mathematical models. For a simple case, the structure can be modeled as a cone of structural projections with a specified mean orientation and a range of orientation angles about the mean orientation, as shown for the spinal cord nerve fibers case in Fig. 1.3. The mean and range values for the cone model can be obtained from previous DTI studies (as was performed for Fig. 1.3 and other studies such as

[27, 28]). Similar cone-based structural model can also be applied to other tissues that show directional nature with long range projections (without sharp bending) and where the structural information necessary for the model is available from previous DTI studies, such as median nerves in the wrist [29], optic nerves in the brain [30], peroneal nerves in the leg [31] and muscle fibers [32]. Apart from the structural information, diffusivity properties of the tissue can also be obtained from previous DTI studies. Hence, there is a prevalence of tissues in the human body with available a priori structural information and this information can be effectively exploited to optimize the DTI protocol.

The research work in this thesis focuses on utilizing the prior information of the imaged tissue available from previous studies to optimally select the DTI experimental parameters (gradient directions and the b-factor) so as to improve the precision (or reduce uncertainty) of the estimated diffusion model parameters. The optimization framework developed in this work is based on D-optimality [33, 34] which minimizes the determinant of the Cramer-Rao lower bound (CRLB) of the covariance matrix of the estimated model parameters. The use of prior information constrains the optimization problem to improve the precision of the parameter estimation. Such optimized protocol will lead to more precise estimation of FA, MD and improved fiber tracking.

The optimized DTI protocol can be applied to a number of scenarios. It can be used for aging related studies of normal subjects where the structural orientation of the tissue remain consistent and diffusivities for different age groups can be obtained from previous DTI studies, for example, changes in cervical spinal cord white matter organization in normal subjects and the correlation with function such as dexterity as demonstrated in [35]. A second scenario for the application of the optimized protocol could be assessment of nerve regeneration [36]. In this case, the expected orientation angles of the growing nerve fibers can be based on previous DTI studies on normal subjects and thus a prior information based optimized protocol can be used to monitor the regeneration process. A third scenario could be in the application to the detection of neurodegenerative diseases, such as multiple sclerosis (MS). MS results in demyelination of nerve fibers causing reduced capability to conduct nerve impulses. Also, MS lesions that are caused due to

scarring result in transection of fiber tracts. Thus, in MS, the FA values show a significant decrease as compared to normal subjects [37,38]. The DTI protocol can be optimized at a reduced FA value corresponding to MS (rather than normal subjects) and can be used to improve the detectability of MS.

Although a number of studies have been reported on the optimization of DTI experimental parameters (as summarized by Hasan et al. [17]), few have utilized the prior structural information. Two recent works on using prior information for DTI protocol optimization are Peng et al. [21] and Gao et al. [39]). Both of them used the cone model for fiber orientations. However, each of their techniques have certain shortcomings that I intend to address in this research work. Their techniques have very specific cost functions, thus lacking flexibility in selecting the diffusion model parameters for which the protocol is optimized. The optimization framework developed here provides a number of choices to select the optimization cost function, such as optimizing for improved precision of all diffusion model parameters, diffusivities only, fiber orientation angles only, variance of FA, variance of MD, etc. All of these cost functions are derived from the CRLB formulation. Moreover, diffusion-weighted images suffer from low SNR and since these are magnitude images, the DTI measurement noise is non-additive Rician rather than additive Gaussian which has been used in these previous works. This research work develops both the Rician and Gaussian CRLB-based optimization frameworks. Finally, the previous works have largely used the tensor-based diffusion model for the optimization. However, the framework developed in this work can optimize for any diffusion model (DTI, ADTI, CHARMED, QUAQ etc.) although focus has been on DTI only. Thus, this work aims to provide a more generalized optimization framework for the experimental protocol.

1.5 Outline

This thesis is mainly divided into three sections. The first section comprising of Chapters 2-4 consists of a review of the various DWI (and other neuroimaging) techniques, then a brief description of MRI and DWI principles.

The second section is mainly in Chapter 5 where the theoretical framework of the DWI protocol optimization is described in details. This chapter introduces the concept of CRLB and its use for optimal design of experiments. Also, various noise models, such as Rician and Gaussian noises, and their corresponding CRLB definitions are derived in this chapter. The optimization algorithm is also described here. An aspect of DWI optimization for improvement in the precision of selective diffusion model parameters is also introduced. Finally, optimized gradient schemes for DTI and ADTI models are generated and there performance analyzed.

Finally, the third section which are in Chapters 6 and 7 discuss the simulation results and the spinal cord ADTI study on human subjects. Chapter 6 discusses noise characterization, the simulation results for the effect of various experimental parameters on the estimation of diffusion model parameters and performance of various estimators. Chapter 7 describes the human study for spinal cord ADTI where the gradient scheme optimization procedure and the validation process are described in details. Next, a study on the effect of optimization on fiber tracking is presented. Finally, an experimental technique for optimizing both the b-factor and the gradient directions is given which optimizes the experimental parameters for improved precision of selected diffusion model parameters.

Chapter 8 concludes this thesis by summarizing the results and contributions and discussing future research works that can benefit from the work done in this research.

CHAPTER 2

A review of current techniques in neuroimaging

2.1 Neuronal connectivity: DWI and other competing technologies

Neuronal connectivity can be classified as structural, functional or effective. While structural connectivity is a more direct visualization of neural connections, functional and effective connectivity are related to neurophysiological processes mainly originating from the nerve cell body instead of the axons. Functional connectivity is defined as the temporal correlations between spatially remote neurophysiological events while effective connectivity is defined as the influence one neural system exerts over another, either at a synaptic or cortical level [40].

At a conceptual level, both functional and effective connectivity can be observed using either neuroimaging (such as fMRI, O-15 PET) or electrophysiology (such as EEG, MEG) [40]. However, at the practical level, neuroimaging and electrophysiological methods are fundamentally different due to difference in time scales and the measured neurophysiological phenomenon. It is important to note that functional connectivity only provides a statistical correlation-based relationship without any causal implications, while effective connectivity measures causal neural connections that can decipher the directionality of

the neural processes. However the causal relations are generally based on an assumption of a causality model or framework, such as structural equation modeling [41], dynamic causal modeling [42], Granger causality mapping [43], multivariate autoregressive modeling [44].

Neuroimaging methods in fMRI measure hemodynamic response (BOLD contrast [45]) and in O-15 PET measure cerebral blood flow [46], while electrophysiological methods in EEG measure volume conduction [47] or associated effects, such as induced magnetic field due to volume conduction in MEG [48]. Volume conduction is caused by spike-trains of neural electrical impulses in active cortical regions. Neuroimaging methods have better spatial resolution (for example, in fMRI, sub-millimeter voxels can be imaged) than temporal resolution (for example, in fMRI, temporal resolutions are of the order of seconds). However, electrophysiological methods have better temporal resolution (order of milliseconds), but poor spatial resolution (tens of millimeters of separability of cortical sources).

For studying structural connectivity, techniques can be either based on imaging or histological studies. One of the histological method for neuroanatomical studies is tract tracing which involves injecting the tissue sample with lipophilic flourecent dyes [4] and tracing the labelled neural tracts. This technique is applicable post-mortem and the tissue staining process generally takes times of the order of more than 24 hours. In the context of the research work in this thesis, neuroimaging techniques can be broadly classified into MRI-based and non-MRI based methods. MRI-based neuroimaging methods include T₁-weighted MRI, T₂-weighted MRI, MR microscopy (MRM) and finally DWI. While T₁ and T₂ weighted MRI are currently part of routine clinical MRI, MR microscopy and DWI are generally research protocols. MRM is essentially ultra high resolution (order of 10–100 microns) MRI which involves the use of ultra-high magnetic field (e.g., 9.4 or 11.7 Tesla) and very high gradients [49]. In-vivo MR microscopy is limited to small animals. MRM is also reported on excised human tissue samples (post-mortem) from the cortical region [50]. Amongst non-MRI based methods, X-ray based computed tomography (CT) methods with contrast enhancement have been reported for neural tracking [51]. Another

research reported use of scanning electron microscopy (SEM) along with reconstruction techniques to explore neural connections [52].

With the improvements in MRI technology, diffusion-weighted imaging is more frequently used for neuroanatomical imaging. Neural fiber tracts can be traced in-vivo from one region of the brain to another completely non-invasively and within a reasonable scan time (order of tens of minutes). Thus, DWI provides the anatomical aspect to neuroimaging which is not present in neurophysiology-based methods. Functional or effective connectivity studies can be either validated or augmented by structural connectivity studies based on DWI. Integration of DWI-based information with functional or effective connectivity is fast becoming a means of studying different neurological processes as well as diseases such as Alzheimer's disease [53] or accessing tumors [54].

2.2 Applications of DWI

After introducing the various techniques in neuroimaging which are contemporary to DWI-based methods, I will focus on DWI and its various applications. DWI in an MR imaging method where the MR signal is sensitize to the local diffusion process. Structures in nerve (axonal) fiber tracts are highly organized and oriented in a particular direction. Owing to myelin sheath covering the axons, the self-diffusion of water molecules in these structures is anisotropic in nature with high diffusivity along the direction of fibers and low otherwise. DWI can measure the diffusion anisotropy by collecting a series of DW images at different gradient directions. The diffusion anisotropy can be modeled by a diffusion tensor as in DTI ([7]) or using non-parametric methods as in q-ball imaging ([11]).

In DTI, after the acquisition of DWI data, the diffusion tensor is estimated on a voxelby-voxel basis. Next, two types of secondary post-processing can be conducted to obtain knowledge of neuronal connectivity. The first processing is computation of scalar quantities that are representative of the local diffusion process, such as the eigenvalues of the diffusion tensor, mean diffusivity, fractional and relative anisotropy [13]. These scalar metrics can be used for further quantitative analysis in studying connectivity. These have been used for detection of stroke [55] and multiple sclerosis [56]. The second processing is fiber tracking which is generally the visual representation of reconstructed nerve fiber tracts. Fiber tracking uses the local fiber orientation (in the form of direction angles) calculated from the DWI data processing and applies either deterministic tracking ([16, 57, 58]) or probabilistic tracking algorithms ([59, 60]). Deterministic tracking algorithms estimate a streamline fit using continuous tracking to reconstruct the fibers using local fiber orientation information and additional constraints (on FA, for example). This algorithm require a seed region to initiate the tracks. Probabilistic methods provide probability maps of connectivity of a seed region to the rest of the brain (or specified targets in the brain). Two common techniques are "FACT" (fiber assignment by continuous tracking, [16] used by DTIStudio software package) which gives deterministic reconstructed fiber tracks and "Probtrack" [59] (part of FSL package) which provides a quantitative voxel-by-voxel probability of connection of seed to targets. Tracking can also be performed by using thresholded FA maps which are projected on to a standard space and computing statistical quantities such as mean, variance or Z-score as shown in Tract-Based Spatial Statistics (TBSS |14|) method.

Based on the scalar metrics derived from the post-processing of DWI data (such as FA, MD, diffusivities) or fiber connectivity information, DWI can be applied for the diagnosis of pathology. For example, DTI-based metrics have been used as biomarkers for detecting spinal cord diseases, such as multiple sclerosis [56], amyotrophic lateral sclerosis [61], aging and spondylosis-related changes [62], as well as spinal cord compression [27]. Many of these studies involve characterizing the difference in the DTI-based biomarkers between normal and pathological population which helps to identify the range of values of these metrics. In the context of DWI protocol optimization in this thesis, such prior knowledge of range of values can be used to optimize the DWI protocol to diagnose specific diseases.

Applications of DWI can also be based on the imaged target organs in the body. DWI can be for neuroimaging in the brain, spinal cord and the peripheral nervous system. DWI can also be extended to any tissue which exhibit an organized and oriented structure,

such as skeletal muscle fibers. DWI applications for skeletal muscle fibers are especially interesting in this context since the DWI protocol optimization discussed in the thesis can be extended for imaging muscle tissues. Some of the recent work conducted on DWI of muscle include use of DTI-based fiber tracking for in vivo three-dimensional (3D) architecture of skeletal muscles in mice hind leg [63], application of DTI fiber tracking in human skeletal muscle and test the cause of the heterogeneity in pennation angle (fiber orientation) [64] and creating biomechanical models of the quadriceps mechanism in humans using DTI fiber tracking information [32]. The DTI-based fiber tracking provides information on the local orientation of the muscle fibers (pennation), fiber length and cross-section of the fiber bundles. These information correlate to muscles physiological cross sectional area which can be used to predict the muscular force produced by the muscle [32].

The work in this thesis will focus on the spinal cord. DTI has been used for studies on the spinal cord [65–67] and have shown promising results. Ries et al. [65] applied DTI to subjects suffering from narrowing of the cervical canal and observed substantial differences in diffusion characteristics to detect lesions in the spine. Mottershead et al. [66] demonstrated the existence of a strong correlation between myelin content and axonal density with diffusion anisotropy. Ducreux et al. [67] reconstructed 3D fiber tracts to visualize the deformation of the posterior spinal cord lemniscal and corticospinal tracts. DTI has been proven to be a valuable diagnosis tool for spinal cord diseases, such as multiple sclerosis [56], amyotrophic lateral sclerosis [61], aging and spondylosis-related changes [62], as well as spinal cord compression [27].

ADTI diffusion model has been used in the cervical spinal cord experiment in this work. Previously, the axisymmetric diffusion assumption has been used by Anderson [68] to estimate fiber diffusion properties through high angular resolution diffusion imaging (HARDI), and by Assaf et al. [9] with the composite hindered and restricted model of diffusion (CHARMED) to model diffusion in intra-axonal compartments. The mean of the secondary and tertiary eigenvalues of the diffusion tensor has also been used previously to compute the transverse diffusivity to investigate regional differences in white matter

tracts in the cervical spinal cord funiculli in humans [69], as well as in rat spinal cord studies [70, 71].

2.3 Prior work on DWI protocol optimization

DTI protocol can be broadly divided into selection of the b-factor (which combines diffusion gradient strength and the timing parameters) and selection of the diffusion gradient directions. For the diffusion gradient directions, a number of gradient scheme have been discussed by Hasan et al. [17]. These gradient scheme are either selected based on geometry (such as icosahedral polyhedra) or heuristics (orthogonal encoding) or numerical optimization (by minimizing a cost function, such as minimum energy, minimum force). Some other examples of numerically optimized gradient scheme is discussed next. Papadakis et al. [18] isolated the effect of gradient directions from the weighting b-factor for the diffusion tensor estimation. They defined an "index of DTI", which relates the variance of the measured data to the total variance of the measured tensor components and used it as a measure of optimality of the diffusion gradient directions. Skare et al. [19] proposed the condition number as a means of studying the noise propagation, and showed improvements in the estimation of the FA by minimizing condition number of the transformation matrix for a given gradient scheme. Batchelor et al. [20] showed that noise propagation in DTI is anisotropic and used the standard deviation of FA as a measure of optimality. Variance of FA was also used by Peng and Arfanakis [21] to compare several gradient schemes. Hasan et al. [17] used several DTI-based or model-independent optimization metrics to be minimized (variance for the ADT components, condition number [19], force [22], Coulomb energy) and compared the resulting schemes via Monte-Carlo simulations. A common gradient directions optimization scheme is the minimum force (MF) based scheme by Jones et al. [22]. They proposed that in absence of any prior knowledge of the tensor to be estimated, gradients can be uniformly distributed in 3-D gradient space by minimizing Coulomb's force between unit charges on a sphere where charges represent the gradient directions. The MF-based gradient schemes do not assume

any DTI signal model. Besides diffusion gradient directions, optimization can also be on the selection of the diffusion gradient strength, pulse duration and pulse interval between diffusion gradients and number of diffusion gradient directions, as proposed by Alexander et al. [23].

So far I discussed optimization by the selection of cost function. Next, I will discuss optimization using prior knowledge of the structure. Thus, these will fall under constrained optimization procedures. Work on the optimization of estimation of DTI model parameters using prior structural information has been previously discussed by Peng et al. [21], Gao et al. [39] and Yanasak et al. [72]. Each of these works attempted to improve certain aspects of the DTI model parameter estimation. Peng et al. [21] reduced the total variance of FA by using a 30° cone of fibers as a prior structural information for the fiber bundles in the corticospinal tract. Gao et al. [39] showed an optimization procedure based on simulated annealing to simultaneously optimize various DTI experimental parameters. They used 20° cone configurations in their procedure and proposed to apply it to neonatal DTI. Simulated annealing is a stochastic minimization technique [73] which is based on the annealing process (slow cooling process) in metallurgy and is known to be robust with respect to local minima problems common in gradient-based minimization methods. Yanasak et al. [72] proposed a gradient scheme to improve the precision of angular measurements in DTI. They showed that restricting the zenith angles of diffusion gradient directions within certain bands can improve the precision of angular measurements significantly.

In this thesis, I have extensively used CRLB to derive the cost function to predict the uncertainty of the diffusion model parameters so that an optimized DWI protocol parameters can be obtained. CRLB is defined by both the noise and the signal model. Use of CRLB has been previously demonstrated by Brihuega-Moreno et al. [24] for the optimal selection of b-values (or b-factors) by minimizing the CRLB of diffusion coefficient with respect to the b-values. They assumed Gaussian noise model for magnitude MR images in the definition of CRLB. However, the Rician noise model is a more accurate noise model for magnitude MR image data. Alexander [23] demonstrated the use of

Rician CRLB in the optimization of acquisition parameters based on the CHARMED model [9]. Both the Rician CRLB [23,74]) and the Gaussian CRLB has been derived and analyzed in this work. Through this work a number of scenarios of signal and noise models have been analyzed. For each case, the CRLB and the cost function has been obtained and optimization was validated, either by simulations or by DTI experiments.

CHAPTER 3

Basic principles of nuclear magnetic resonance imaging

3.1 Nuclear magnetic resonance and signal generation

Atoms with an odd number of protons and/or neutrons (odd mass number) have nuclear spin angular momentum. The nucleus of these atoms can be considered as spinning charged sphere which can possess small magnetic moment. In biological specimen, the most common nucleus that is used for NMR is Hydrogen (1 H) which has a single proton. It is abundantly found in water (1 H2O) and fat or other organic molecules. Examples of other common nuclei used in MR studies are Phosphorus (31 P), Sodium (23 Na), Carbon (13 C).

From a quantum mechanical perspective [75, 76], the spin angular momentum of a nucleus is quantized and can exist in only certain states. For hydrogen, the nuclear spin can take only two quantum states of angular momentum which are given by $\hbar I_z$, where $I_z = \pm 1/2$ and \hbar is the reduced Planck's constant ($\hbar = 1.054 \times 10^{-34} \text{ J s}$). Thus, two populations of spins of hydrogen nuclei can exist in a specimen. In the absence of any external magnetic field, the spin populations are equal in number and cancel each other's magnetic moments. Thus, the net magnetic dipole moment of the overall

population is zero. When the specimen is exposed to a constant external magnetic field, B_0 (with magnitude B_0 and direction along +Z-axis in the laboratory reference frame by convention), the spins tend to align with the field in either parallel or anti-parallel fashion and attain potential energy due to the interaction between magnetic moment and the external applied field, B_0 (Fig. 3.1 (a)). Since, the spins are at two distinct states of angular momentum (and thus magnetic moment), the application of the external field, B_0 , results in spins at two distinct potential energy levels separated by an energy gap, ΔE , given by $\Delta E = \gamma \hbar B_0$, where γ is gyromagnetic ratio (Fig. 3.1 (b)).

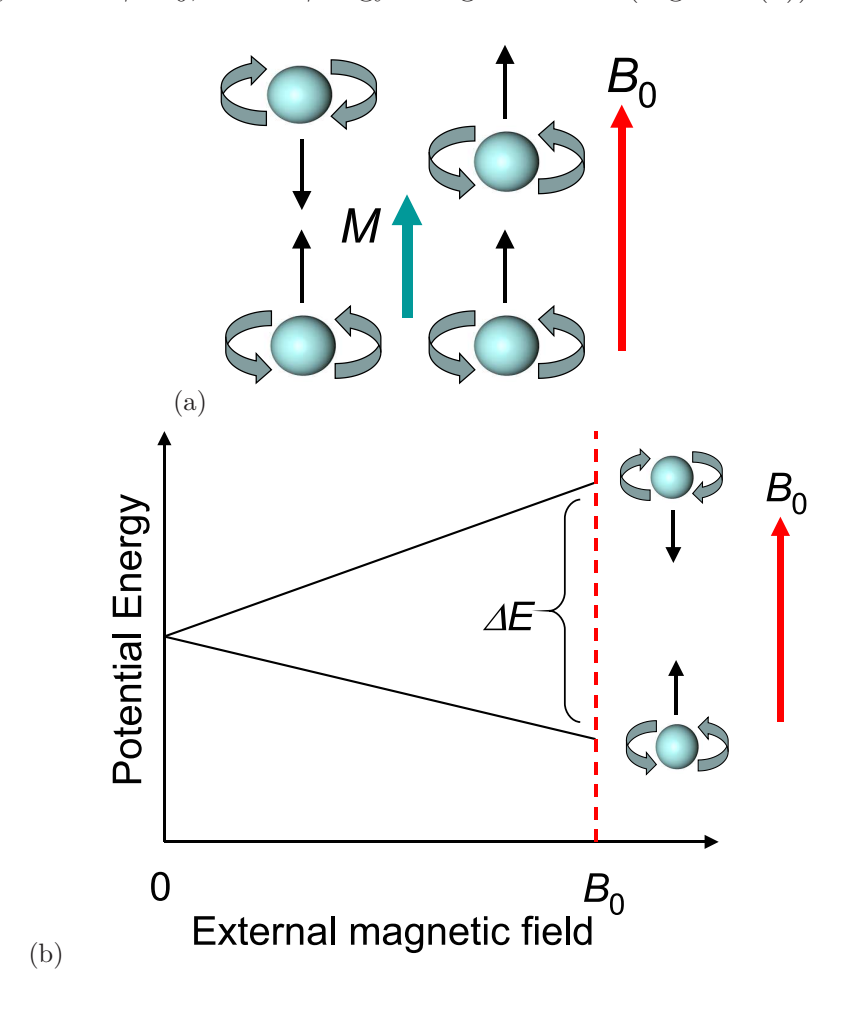


Figure 3.1. (a) Alignment of spins with B_0 (most are parallel, while some can be antiparallel to B_0 . M is the net magnetization vector. (b) Separation of spin energy into low and high levels when subjected to B_0 .

Although, the spins tend to occupy the lower energy state (parallel), the energy gap, ΔE , is easily overcome due to the thermal energy of the nuclei (from body temperature). The ratio of the spin population in the two energy states in presence of an external

magnetic field can be given by $n_+/n_- = e^{\Delta E/kT}$, where n_+ , n_- are the spin populations at lower and higher energy states respectively and k is the Boltzmann constant ($k = 1.38 \times 10^{-23} \text{J K}^{-1}$). Typically, this corresponds to about 3 parts per million per Tesla at 310 K temperature of excess lower energy spins. This excess spin population causes a net magnetic moment along the direction of the applied field. Sum total of the magnetic moments in a voxel (or volume element) is denoted by net magnetization, M, which is a vector and it is also aligned with the applied magnetic field, B_0 , at equilibrium. Thus, at equilibrium, only longitudinal magnetization exist.

Any longitudinal magnetization (along B_0) due to magnetic resonance is difficult to measure since it's contribution can not be distinguished from that of B_0 while taking field measurements. In order to generate and measure a unique MR signal, the net magnetization, M, needs to be reoriented or flipped away from the longitudinal direction. To achieve this flip, spins in the lower energy state must be shifted to the higher energy state by providing energy equal to ΔE . Based on quantum mechanical model, the frequency equivalent of ΔE is called Larmor frequency, ω_0 . Magnetic resonance is exhibited when external magnetic field at frequency equal to Larmor frequency, ω_0 , is applied to a spin system thereby causing energy transfer from the source field to the spin system. Larmor frequency is given by,

$$\omega_0 = \gamma B_0$$
 or
$$f = \frac{\gamma}{2\pi} B_0$$
 (3.1)

,where ω_0 is known as the Larmor frequency and γ is gyromagnetic ratio. For 1H , $\gamma/2\pi$ = 42.576 Mhz T⁻¹.

The net magnetization, M, and the applied external magnetic field, B_0 , follow a relation given by the Bloch's equation (without the relaxation and diffusion terms),

$$\frac{d\mathbf{M}}{dt} = \mathbf{M} \times \gamma \mathbf{B_0} \tag{3.2}$$

Since, the net magnetization (M) is related to the angular momentum of the spins, the solution to Bloch's equation gives the angular frequency with which spins would precess

about B_0 if not aligned with it. And it turns out to be the same as Larmor frequency, ω_0 . Thus, the rate at which the spins precess about the direction of the external static magnetic field, B_0 , is also given by the Larmor frequency, ω_0 .

Going back to the process of flipping the magnetization vector, an additional external high frequency (radio frequency, RF) magnetic field pulse, B_1 (apart from the static magnetic field, B_0) tuned to the Larmor frequency, ω_0 , when applied transverse to B_0 , would cause the spins and the net magnetization, M, to flip towards the transverse direction of B_0 (Fig. 3.2 (a)). Since the RF field is at frequency ω_0 , it carries energy equivalent to ΔE which is necessary to transfer spins to the higher energy state. While flipping the spins, the spins and net magnetization, M, would follow a precessing motion about B_0 at frequency ω_0 . This can be explained using Eq. 3.2 in the context of B_1 where B_1 creates a torque that rotates the M vector towards the transverse direction (Fig. 3.2(b)). Generally, B_1 is of the order of a few Gauss in strength and milliseconds in duration.

$$\mathbf{B_1} = B_1 \cos(\omega_0 \ t)\mathbf{i} - B_1 \sin(\omega_0 \ t)\mathbf{j}$$
(3.3)

where B_1 is the magnitude of B_1 and \mathbf{i} , \mathbf{j} are the unit vectors along +X and +Y directions in laboratory reference frame and t is the time. If the RF pulse is applied to spins at equilibrium, then right after flipping, the spins would have phase coherence (i.e., the spins are rotating in phase). Also, the net magnetization vector, \mathbf{M} , is nutated towards the X-Y plane. By careful design, an RF pulse can be applied to flip \mathbf{M} completely to 90°. Thus, \mathbf{M} will have no longitudinal component. Such an RF pulse is called a 90° pulse.

The MR signal is a measure of the transverse magnetization and is collected after the RF pulse is turned off. In absence of the RF pulse, magnetization relaxation initiates and the net magnetization, M, tends to return to the equilibrium state and towards the B_0 direction. The relaxation process consists of the growth of the longitudinal magnetization and it is accompanied by the decay of the transverse magnetization (Fig. 3.2 (c)). The former follows T_1 -recovery (Fig. 3.3 (a)), while latter follows T_2 -decay (Fig. 3.3 (b)). T_1 -recovery corresponds to spin-lattice relaxation where the spins return to lower energy state while releasing energy, ΔE , to the surrounding lattice. T_2 -decay, on the other hand,

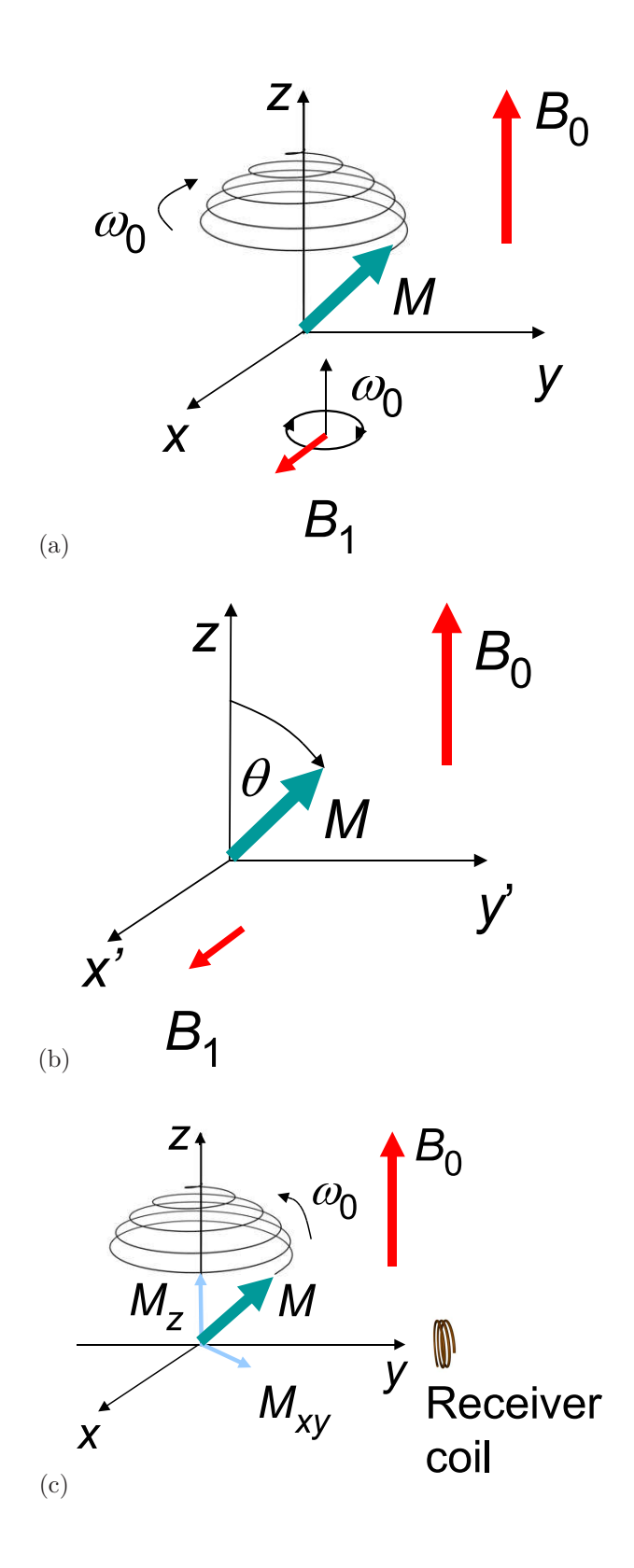


Figure 3.2. (a) M when RF pulse, B_1 , is applied as seen in the laboratory reference frame (b) M nutated by flip angle θ as seen in the rotating reference frame. (c) M during relaxation after RF pulse is turned off as seen in the laboratory reference frame. $M_{\rm Z}$ and $M_{\rm XY}$ are the longitudinal and transverse magnetizations respectively.

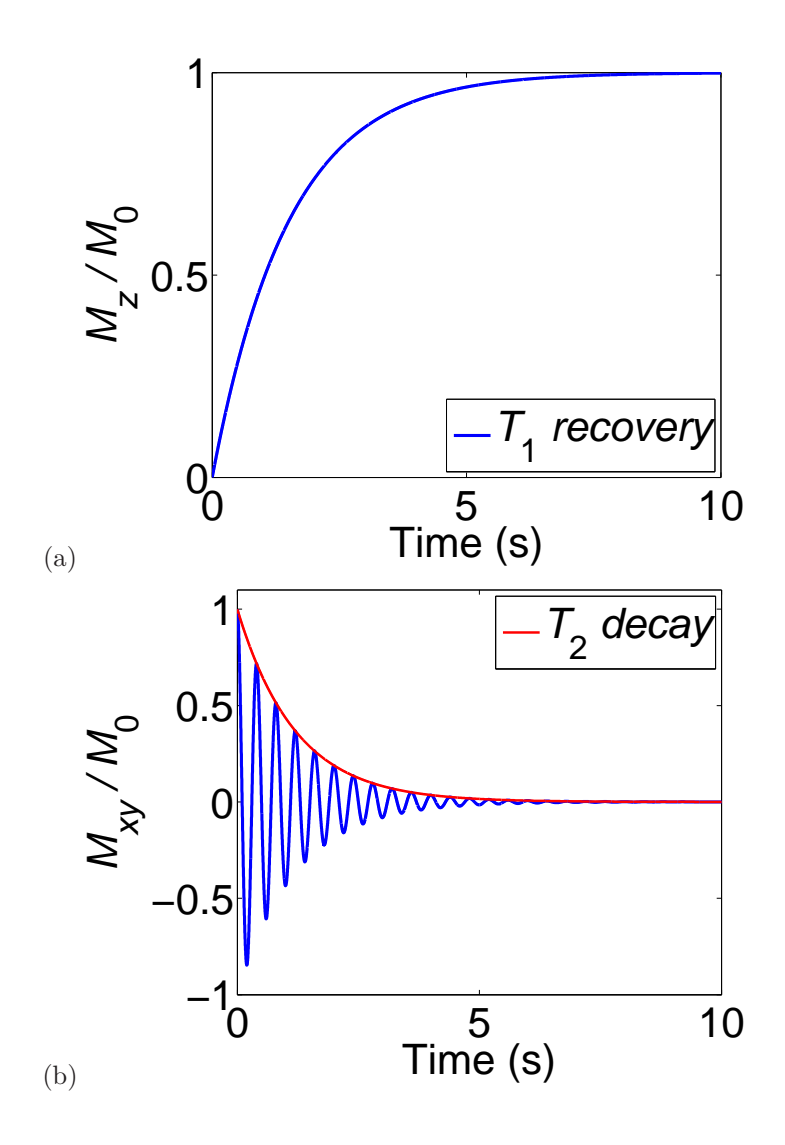


Figure 3.3. (a) T_1 recovery of longitudinal magnetization and (b) T_2 decay of transverse magnetization. M_0 is the equilibrium magnetization.

corresponds to the dephasing of the precessing spins while returning to lower energy states. The dephasing can be attributed to spin-spin interactions owing to local field interactions due to individual magnetic fields of each spin. When the RF pulse is applied to spins in equilibrium, then the moment after the RF pulse is turned off, the spins are in phase coherence (or in phase). However, due to the spin-spin interactions, the phase coherence is lost resulting in the T_2 -decay of transverse magnetization. The time constant characterizing the return of the magnetization vector along the longitudinal direction is called T_1 , while the time constant characterizing the decay of the magnetization vector component in the transverse plane is called T_2 . In human tissue, T_1 values range from 180–2000 ms (at 1 T) whereas for T_2 values, the range is 40–300 ms (at 1 T) [77]. The

MR signal is proportional to the magnitude of the transverse magnetization which is in turn dependent on the density of the nucleus in the volume of the specimen as well as the relaxation time constants. Thus, the contrast mechanism in the MR signal between tissues is mainly dictated by the spin density and the relaxation time constants (T_1 and T_2). Additional signal weighting can be achieved by specialized pulse sequences, such as diffusion-weighting, which is described in the next chapter. The signal right after the excitation pulse (90° pulse) is known as free induction decay (FID). The signal can be represented mathematically by,

$$S(x,y) = K\rho(x,y)[1 - e^{-T_R/T_1(x,y)}]e^{-T_E/T_2(x,y)}$$
(3.4)

where S(x,y) is the signal at (x,y) location, ρ is density of the nuclei, T_1 and T_2 are the relaxation and decay time constants, respectively. K is any other gain constants lumped together, such as digitizer gain, coil sensor gain. T_R is the pulse repetition time which corresponds to the time after which the sequence of RF excitation signal is repeated to take measurement at different locations in the specimen. T_E is echo time and it corresponds to the time at which the data is acquired. Echoes will be discussed later.

In practice, the resonant frequency is not uniform all through the specimen due to main field inhomogeneity, susceptibility effects, chemical shifts and the application of the linear gradient field itself. Due to additional dephasing effects on the spins, these effects cause additional loss of the transverse magnetization resulting in a faster decay rate and a shorter time constant (called T_2^*) as compared to the T_2 decay. The expression for the MR signal is updated as,

$$S(x,y) = K\rho(x,y)[1 - e^{-T_R/T_1(x,y)}]e^{-T_E/T_2^*(x,y)}$$
(3.5)

3.2 MR Imaging

MR imaging method can be classified into two main types, namely, 2D multi-slice and 3D volumetric. In 2D multi-slice imaging, the images are obtained from exciting slices of the target object (using slice-selective RF excitation and linear gradient field) while in

3D volumetric imaging, the whole object is excited (using nonselective RF excitation). Following the RF excitation, the spins are spatially encoded with slightly different resonant frequencies and phases by using linear gradient magnetic fields. The MR signal measured by the receiver coil is finally due to the summation of the signals from all the spatially encoded spins. After the measurement of the MR signal, image reconstruction is performed which can also be of two types, namely, projection-reconstruction and 2D Fourier transform methods. I will focus on the 2D multi-slice and 2D Fourier transform based imaging since this is commonly used in diffusion-weighted imaging.

3.2.1 Slice selection

For 2D multi-slice MR imaging, the signal is collected from specific slices excited by applying special RF pulses and linear gradient fields transverse to slicing plane. In order to excite a slice perpendicular to the longitudinal axis (Z-axis), of thickness Δz , the gradient $G_z(z)\mathbf{k}$ is turned on which provides spatial encoding along Z-direction (\mathbf{k} is the unit vector along +Z direction). $G_z = \partial B_z/\partial z$, $\omega = \gamma B_z$ and thus, slice frequency bandwidth, $\Delta \omega_z = \gamma G_z \Delta z$. Alongside, $\mathbf{B_1}$ must be applied and be tuned to the Larmor frequencies of the spins only in the slice of interest. Since the slice requires a frequency band ($\Delta \omega_z$) which is equal to $\gamma G_z \Delta z$, B_1 (magnitude of B_1) has to be designed to carry a frequency band that matches the frequencies in the slice (Fig. 3.4). This is commonly achieved by providing a sinc-modulated RF pulse. The B_1 excitation takes the form of,

$$\mathbf{B_1} = B_1(t)\cos(\omega_0 t)\mathbf{i} - B_1(t)\sin(\omega_0 t)\mathbf{j}$$
(3.6)

3.2.2 2D Fourier transform method for imaging

After the slice selection process, it can be assumed that all of the signal comes from spins in the slice section only. The spins in the slice plane (X-Y plane) are further spatially encoded for frequency and phase such that the signal collected can be represented in k-space. k-space represents the spatial frequency domain corresponding to Fourier transform of an image in spatial variables, (x, y, z). Since this is a 2D process, only x, y

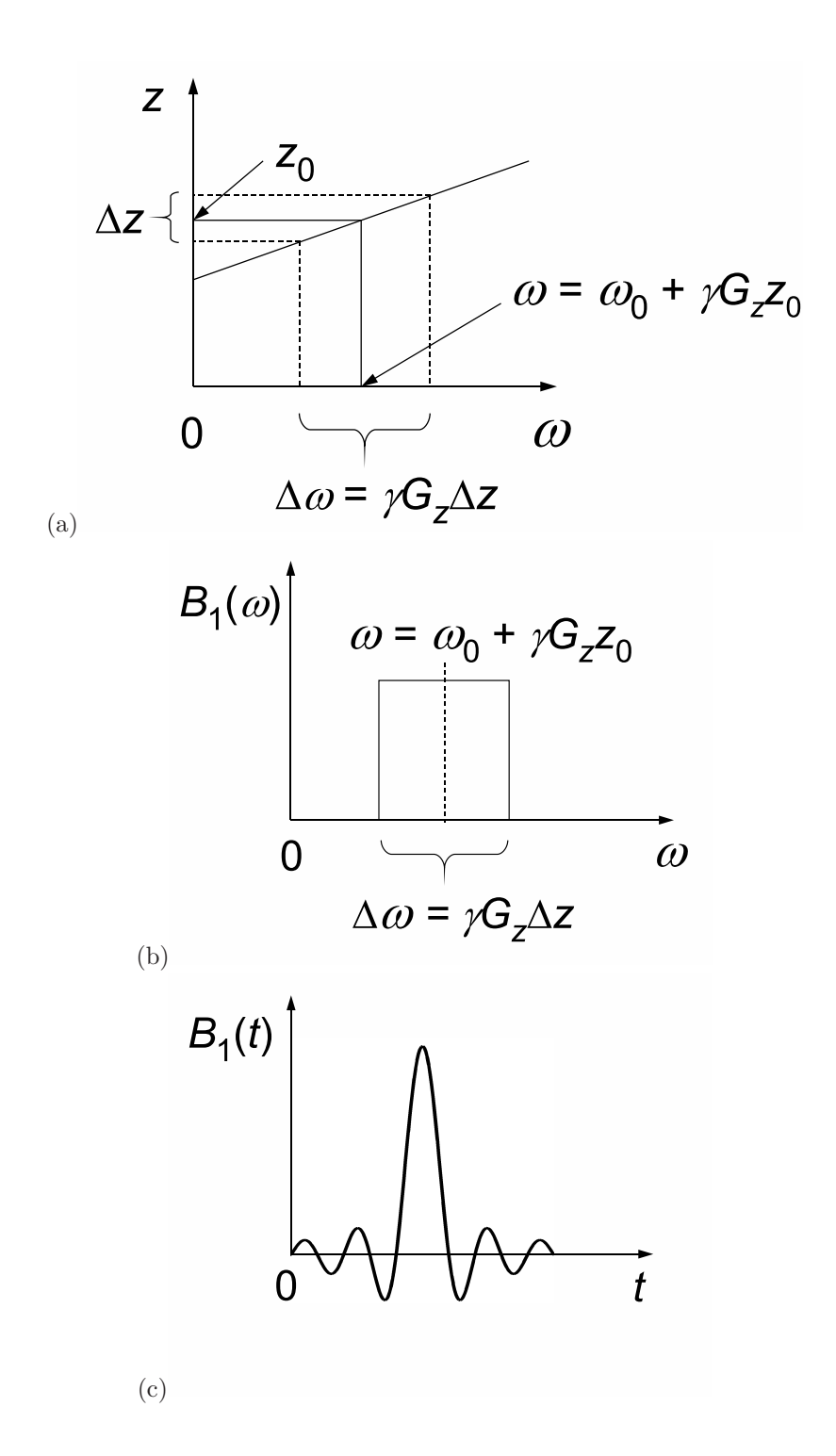


Figure 3.4. Schematic showing slice (Δz) selection in z-direction using G_z field in (a) and the sinc-modulated B_1 RF signal in frequency (b) and time (c) domains respectively.

variables are used in the expression assuming z to be fixed. The measured demodulated

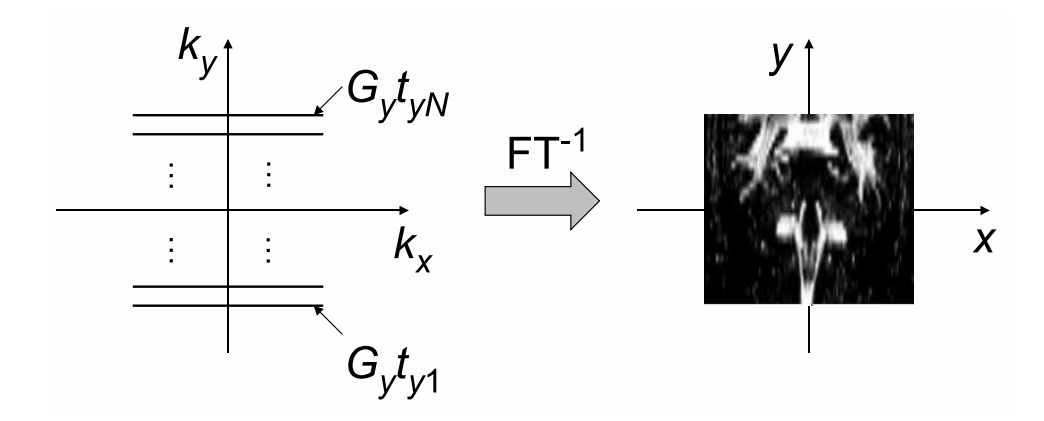


Figure 3.5. Schematic showing k-space imaging using 2D Fourier transform method.

MR signal can be expressed as,

$$s(t, t_y) = \int_x \int_y m(x, y) e^{-i\gamma G_y y t_y} e^{-i\gamma G_x x t} dx dy$$

= $\mathbf{F_{2D}} \{ m(x, y) \}, \ k_x = (\gamma/2\pi) G_x t, \ k_y = (\gamma/2\pi) G_y t_y$ (3.7)

where F_{2D} refers to the 2D Fourier transform in k-space and k_x and k_y represent the spatial frequencies (Fig. 3.5).

3.2.3 Phase encoding

From Eq. 3.7, it is seen that phase encoding of the spins can be achieved by applying a gradient along the +Y-direction, G_y ($G_y = \partial B_z/\partial y$), for a fixed time interval, t_y . This step warps the spins and provides the necessary phase offset (and thus sets the spatial frequency k_y) required for the Fourier transform representation (in Eq. 3.7) before signal measurement (data acquisition) is performed. Note that in Eq. 3.7, G_y is assumed to be constant. For a more general representation of phase encoding,

$$k_y = (\gamma/2\pi) \int_0^{t_y} G_y(t')dt'$$
(3.8)

where $G_y(t')$ is the gradient along +Y-direction varying with time, t'.

3.2.4 Frequency encoding

After the phase encoding step, the spins are set to a particular spatial frequency, k_y , along the Y-direction. However, in order to differentiate between the spins along the

X-direction (Fig. 3.6), spins are frequency encoded by applying a gradient along the +X-direction, G_x ($G_x = \partial B_z/\partial x$), such that $\omega(x) = \gamma(B_0 + G_x x) = \omega_0 + \gamma G_x x$. The measured MR signal, $s(t, t_y)$, is a function of time and the time dependence is reflected in $k_x = (\gamma/2\pi)G_x t$. During data acquisition, sampling of the time-dependent MR signal represents sampling of k-space along the k_x spatial frequency.

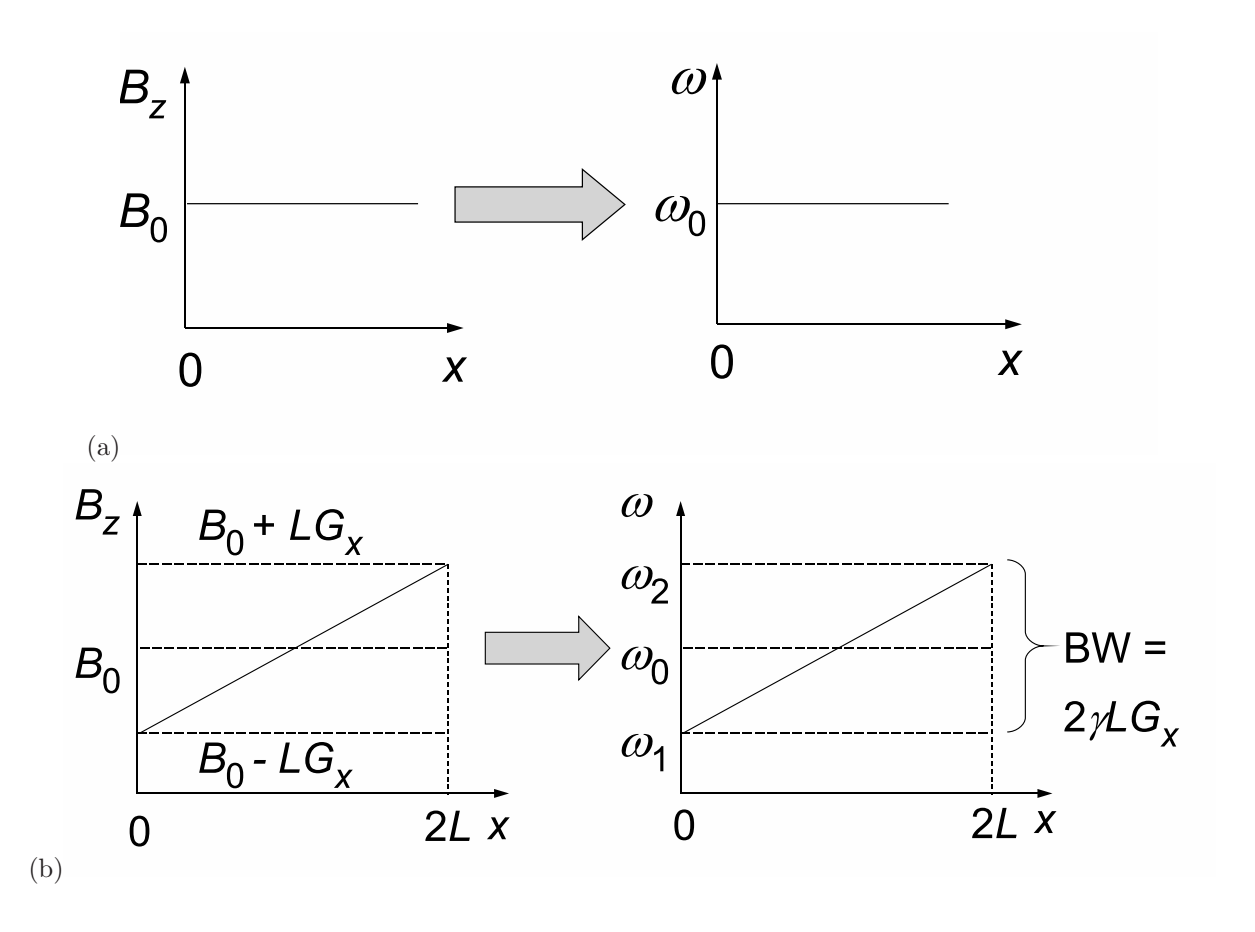


Figure 3.6. (a) Schematic showing absence of spatial encoding when no gradient field is used. (b) Schematic showing encoding of a fixed length (2L) in x-direction using gradient field, G_x .

3.3 Using echoes

During the frequency encoding of spins, the k-space is often sampled from the most negative to the most positive spatial frequency value. In terms of the gradient, this can be achieved by placing a dephasing gradient lobe of negative field strength preceding the main gradient (rephasing) lobe of positive field strength. The time at which the phase

accumulation due to the dephasing lobe is canceled by that of the rephasing lobe is the time of echo (T_E) which is also the time at which the center of k-space is reached. This kind of echo is called gradient echo since such an echo can cancel the effect of dephasing caused by itself. Generally, the sampling of k-space is symmetric about the center of k-space such that the dephasing lobe is half the time duration as the rephasing lobe (as shown in Fig. 3.7). Gradient echo based sequences are fast, but still produce T_2^* -weighted images since the gradient echo does not compensate for the MR signal loss due to field inhomogeneity sources.

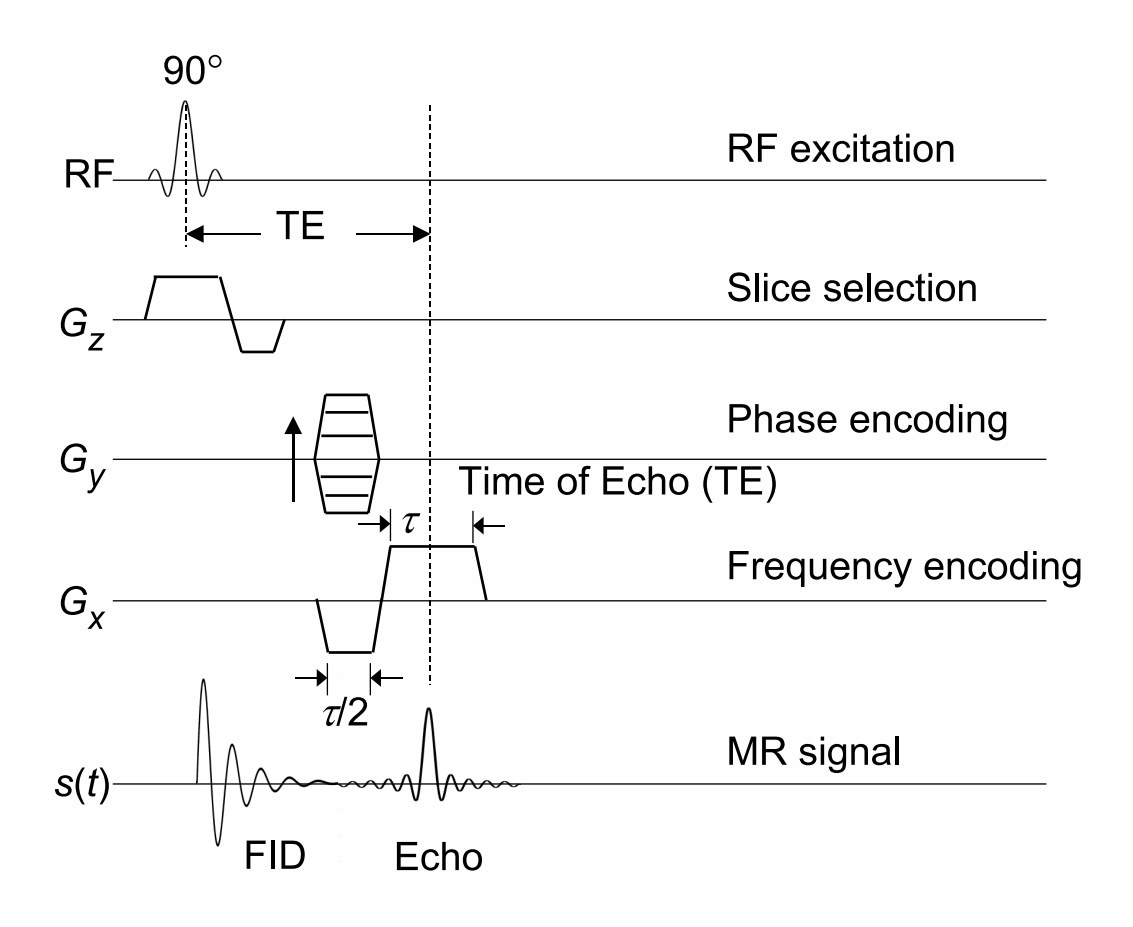


Figure 3.7. Gradient echo pulse sequence diagram showing the timings of the slice selection, phase-encoding and frequency-encoding gradients.

Spin-echo sequences are used to cancel the effect of field inhomogeneity at a voxel. Spin-echo pulse sequence is a specialized pulse sequence where the additional dephasing due to field inhomogeneity sources is reversed by application of a second RF pulse with 180 flip angle. As shown in Fig. 3.8, the initial signal dies at a rate given by the T_2^* decay. Then, a 180° pulse is applied which causes phase reversal and after a time called echo

time (T_E) , the spins undergo complete rephasing (constructive interference) to produce an MR signal called spin-echo. The spin-echo signal is stronger and the signal level is only limited by the intrinsic T_2 decay (as shown in Fig. 3.8) as compared to T_2^* decay in absence of any spin-echo sequence.

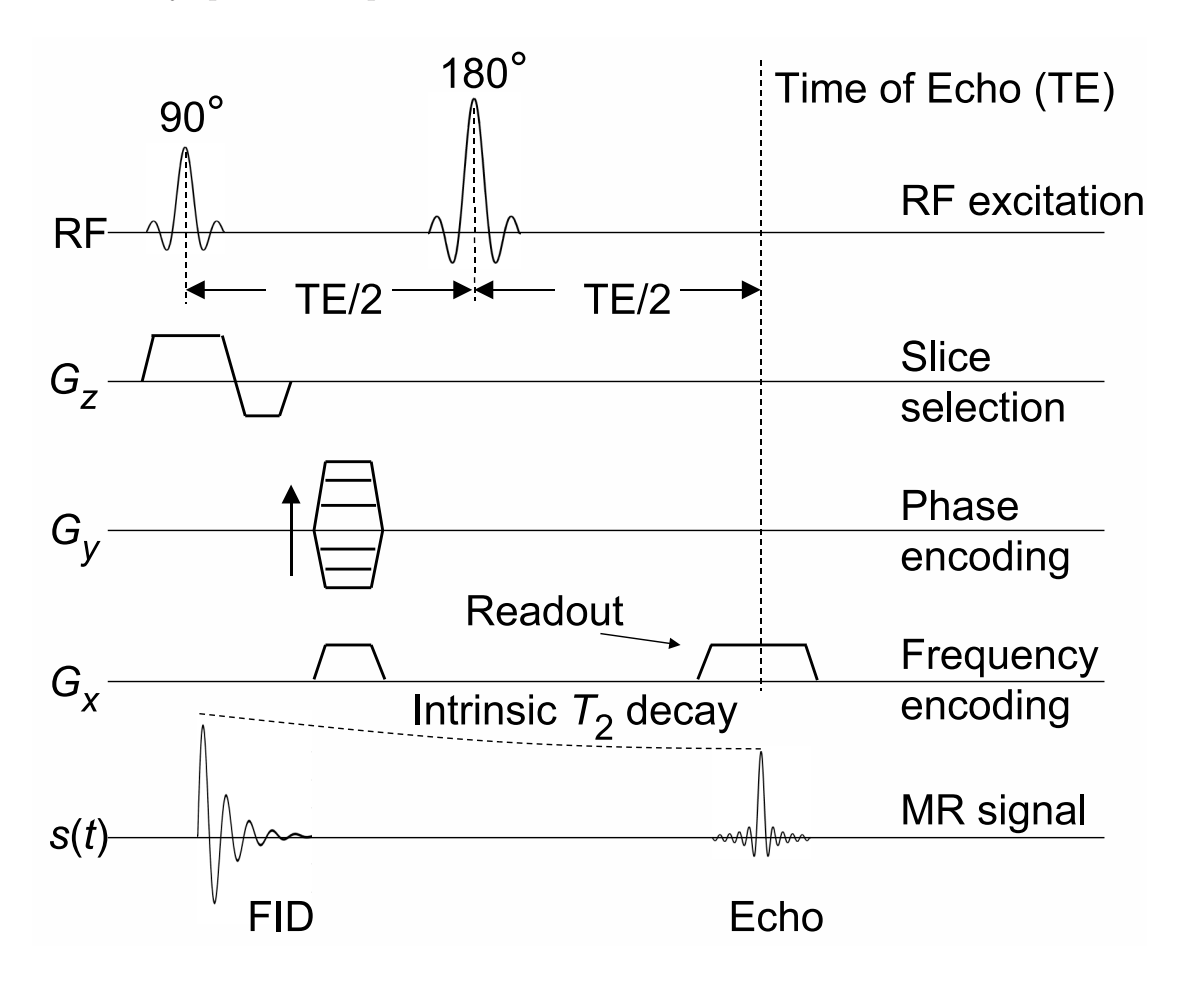


Figure 3.8. Spin-echo pulse sequence diagram showing the timings of the slice selection, phase-encoding and frequency-encoding gradients.

3.4 T_1 and T_2 weighting

As shown in Eq. 3.4, the signal at any location can be represented in terms of the density of the nuclei or spins (ρ) , T_1 and T_2 . When a spin-echo sequence is used, the signal expression remains the same as Eq. 3.4 even though the field inhomogeneity sources are taken into consideration.

In order to obtain T_1 -weighted images, $T_R \approx T_1$ of the target tissue and T_E is short

such that,

$$S(x,y) \approx K\rho(x,y)[1 - e^{-T_R/T_1(x,y)}]$$
 (3.9)

This is a fast scan and typical $T_E=20~\mathrm{ms}$ and $T_R=600~\mathrm{ms}$ for $B_0=1.5~\mathrm{T}$.

For a T_2 -weighted image, T_R is much longer than the T_1 in the target tissue and $T_E \approx T_2$ of target tissue. Signal is represented as,

$$S(x,y) \approx K\rho(x,y)e^{-T_E/T_2(x,y)}$$
(3.10)

These are long scans due to longer T_R and typical $T_R=2500$ ms and $T_E=80$ ms at $B_0=1.5$ T.

CHAPTER 4

Concepts in diffusion-weighted MRI

4.1 Self-diffusion of water in nervous tissue

Water (H₂O) molecules (hence, protons H⁺ in water) exhibit self diffusion. Molecular self-diffusion is different from regular diffusion since the diffusion of particles occurs within itself (i.e., the diffusing particle, protons in this case, and the medium are the same) and it is due to the kinetic energy of the particle from thermal agitation (Brownian motion). Fig. 4.1 (a) depict the case of Brownian motion of water molecules for a healthy axon fiber where it can be observed that the preferential movement of water along the fiber orientation and restricted motion in the transverse direction. Note, in this case, an impermeable axon boundary has been defined. Alternately, a semi-permeable boundary can also be defined. Fig. 4.1 (b) shows a case of a ruptured axon fiber and its effect on the movement of water molecules. It can be seen that at the location of the rupture, the water molecules are less restricted in motion towards the transverse direction to fiber orientation. These examples show that the molecular self-diffusion delineates the tissue microstructure due to its preferential movement.

Bundles of nerve fibers form tracts in the central nervous system (e.g., corticospinal or pyramidal tract travel between the cerebral cortex and the spinal cord) or nerves in the peripheral nervous system (e.g., common peroneal nerve in the legs). Myelinated nerve fibers are covered by layers of specialized membrane known as myelin, which contain lipids (fats) and provide natural barrier to the movement of water molecules. A bundle of nerve fibers can be treated as bundles of tubes carrying water. At microscopic length scale, which is of the size of the diameter of nerve fibers, the water diffusion is isotropic but restricted or hindered by barriers. However, at macroscopic length scale (such as few millimeters as in the spatial resolution of MRI), the diffusion process can be modeled as homogeneous, unrestricted and anisotropic [7], such as in DTI/ADTI. In QUAQ [8], on the other hand, diffusion is modeled as a spatially restricted but isotropic process representing impermeable cylinders of water.

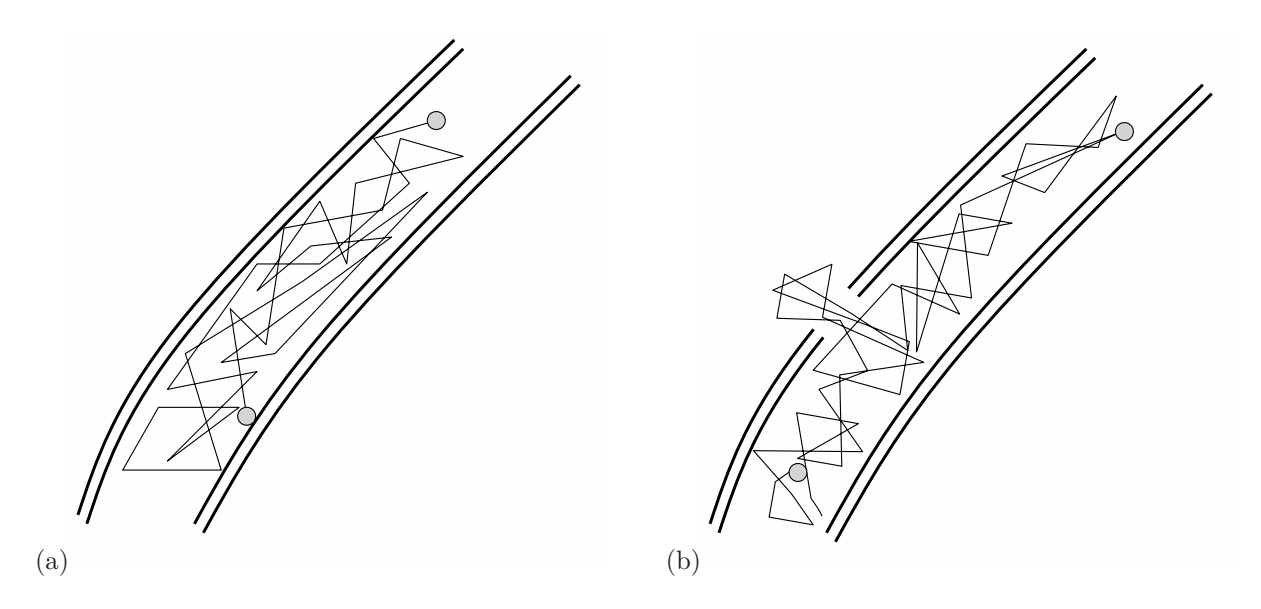


Figure 4.1. Brownian motion of water molecules in (a) a healthy axon fiber and (b) an axon fiber with a rupture.

Principles of molecular diffusion are governed by Fick's laws. Fick's first law relates the diffusive flux (amount of particles passing through a fixed area in a short time) with the concentration gradient and the constant of proportionality is defined as the diffusion coefficient.

$$\boldsymbol{J} = -D\nabla c \tag{4.1}$$

where J is the diffusive flux vector (unit: mol mm⁻² s⁻¹), c is the concentration (unit: mol mm⁻³) of the particles at a position (x, y, z), D is the diffusion coefficient or diffusivity (unit: mm² s⁻¹) and ∇ is the derivative operator $(\nabla = (\mathbf{i}\partial/\partial x, \mathbf{j}\partial/\partial y, \mathbf{k}\partial/\partial z))$. Fick's first law shows that whenever a spatial concentration gradient is created, the par-

ticles will diffusion in the opposite direction to the concentration gradient to equalize the concentrations. Combining the law of conservation of mass (continuum principle) with Fick's first law, Fick's second law of diffusion is obtained. The second law shows the effect of diffusion on changes in concentration, c, with time, t.

$$\frac{\partial c}{\partial t} = \nabla \cdot (D\nabla c) \tag{4.2}$$

For constant D with respect to space, the above equation simplifies to $\partial c/\partial t = D\nabla^2 c$, where $\nabla^2 = \nabla \cdot \nabla$.

Historically, the first mathematical description of Brownian motion and its relation with molecular diffusion was done by Albert Einstein (in 1905 [78]). Einstein provided a statistical description of the Fick's second law of diffusion and defined a probability of finding a particle at a position at a particular time when under diffusion. His work showed that Brownian motion of particles in a fluid medium was a thermodynamic phenomenon which can be characterized statistically by a probability function. Einstein reformulated Fick's second law as [78, 79],

$$\frac{\partial \Psi(\boldsymbol{r},t)}{\partial t} = D\nabla^2 \Psi(\boldsymbol{r},t) \tag{4.3}$$

where $\Psi(\mathbf{r},t)$ is the probability of finding a particle at position \mathbf{r} at time t. Let the conditional probability (or propagator), $P_s(\mathbf{r}_0|\mathbf{r},t)$, be the probability that a particle starting at \mathbf{r}_0 would diffuse to \mathbf{r} in time t and that $\Psi(\mathbf{r},t) = \int \Psi(\mathbf{r}_0,0) P_s(\mathbf{r}_0|\mathbf{r},t)$, such that,

$$\frac{\partial P_s}{\partial t} = D\nabla^2 P_s \tag{4.4}$$

Solving the reformulated Fick's law for a freely diffusing particle under the initial condition $P_s(\mathbf{r}_0|\mathbf{r},t) = \delta(\mathbf{r}-\mathbf{r}_0)$, (δ being the Dirac delta function in this case),

$$P_s(\mathbf{r}_0|\mathbf{r},t) = (4\pi Dt)^{-3/2} \exp\left[-\frac{(\mathbf{r}-\mathbf{r}_0)^2}{4Dt}\right]$$
(4.5)

Thus, the root mean squared distance traveled after a time t during free diffusion in any direction is given by $\sqrt{2Dt}$. Einstein also defined the diffusion coefficient, D = kT/b where k is the Boltzmann's constant, T is the temperature and b is the drag coefficient. Torrey [80] later included the diffusion term in the famous Bloch equation using the results from Einstein's work (see Eq. 4.6).

4.2 Pulsed gradient spin echo sequence for diffusion quantification

Stejskal and Tanner [5,6] proposed the famous pulsed gradient spin-echo (PGSE) experiment to quantify diffusivity (or diffusion coefficient) of fluids using NMR. In this experiment, a pair of diffusion-encoding gradients is placed on both sides of the 180° RF pulse. A typical example with rectangular gradient pulse is shown in Fig. 4.2. In absence of diffusion, the phase accumulation in the spins due to the first gradient pulse is canceled by the second gradient pulse resulting in only a T_2 -weighted signal. However, due to diffusive movement of spins, the MR signal suffers additional attenuation which can be expressed as a function of diffusivity. PGSE experiment is a generic experiment for the quantification of diffusivity of fluids since it follows the physics of diffusion and links it with the signal acquisition process.

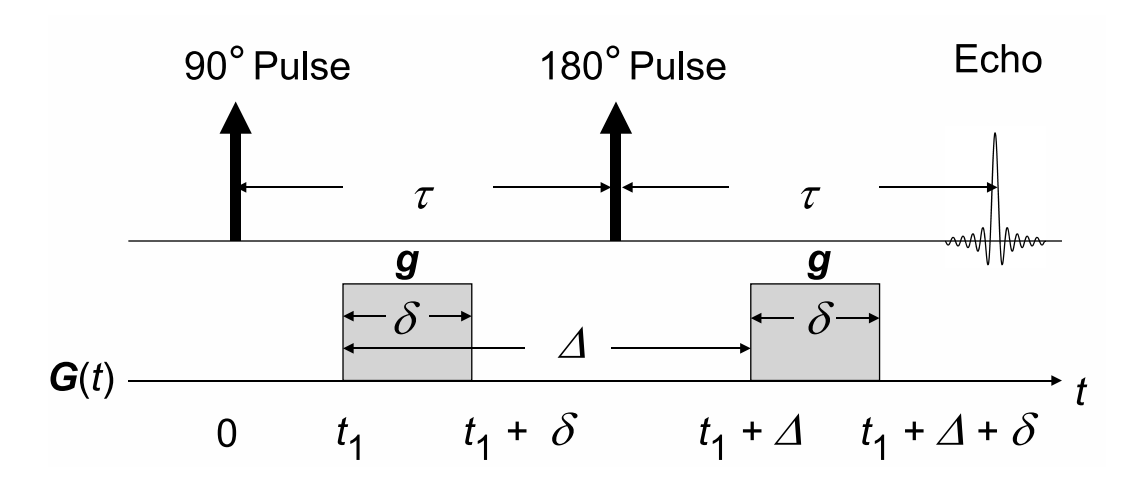


Figure 4.2. Schematic of the PGSE sequence showing only the timing of the diffusion-encoding gradient and the RF pulses. Here, $\tau = T_E/2$, where T_E is the echo time.

Torrey introduced the diffusion term in Bloch's equation [80] which is given by

$$\frac{\partial \boldsymbol{M}(\boldsymbol{r},t)}{\partial t} = \gamma \boldsymbol{M}(\boldsymbol{r},t) \times \boldsymbol{B} + \frac{M_0 - M_z}{T_1} \mathbf{k} - \frac{M_{xy}}{T_2} \mathbf{n} + \nabla \cdot D \nabla \boldsymbol{M}(\boldsymbol{r},t)$$
(4.6)

where M(r,t) is the net magnetization vector at a position r at time t, B is the applied magnetic field (along the +Z direction, k), D is the diffusivity. M_0 , M_z are the initial magnetization and the longitudinal magnetization (along the +Z direction) component

respectively. M_{xy} is the transverse magnetization component perpendicular (along the **n** direction) to the applied field \boldsymbol{B} . T_1 , T_2 are the relaxation time constants. ∇ is the gradient operator. Note that the velocity term in the Bloch Torrey equation (Eq. 4.6) is ignored.

Eq. 4.6 assumes diffusion to be isotropic and uniform, hence, representing the microscopic nature of self-diffusing water molecules. The transverse component of the magnetization vector, M_{xy} , after application of a gradient ($\mathbf{G}(t) = \{g_x(t), g_y(t), g_z(t)\}$), is given by,

$$M_{xy}(\mathbf{r},t) = m(\mathbf{r},t) \exp\left[-(j\omega_0 + \frac{1}{T_2})t\right]$$
(4.7)

$$\frac{\partial m(\boldsymbol{r},t)}{\partial t} = -j\gamma(\boldsymbol{r}\cdot\boldsymbol{G}(t))\ m(\boldsymbol{r},t) + D\nabla^2 m(\boldsymbol{r},t)$$
(4.8)

where $\nabla^2 = \nabla \cdot \nabla$, is the Laplacian operator.

The solution for $m(\mathbf{r}, t)$ in Eq. 4.8 when D = 0 is of the form [75],

$$m(\mathbf{r}, t) = A \exp(-j\gamma \mathbf{r} \cdot \mathbf{F}(t))$$
(4.9)

where

$$\boldsymbol{F}(t) = \int_0^t \boldsymbol{G}(t') dt'$$
 (4.10)

The G(t) is assumed to be only a function of time, t, and is constant in space and A is a constant. When $D \neq 0$, $A \to A(t)$ in Eq. 4.9 assuming D is only a function of time, t, and is constant within the imaging voxel space. Substituting Eq. 4.9 in Eq. 4.8 and simplifying,

$$\frac{\partial A(t)}{\partial t} = -\gamma^2 D(\mathbf{F}(t) \cdot \mathbf{F}(t)) A(t) \tag{4.11}$$

Thus,

$$\ln\left[\frac{A(t)}{A(0)}\right] = -\gamma^2 D \int_0^t \left[\mathbf{F}(t') \cdot \mathbf{F}(t') \right] dt'$$
$$= -\gamma^2 D \int_0^t \left[\left(\int_0^{t'} \mathbf{G}(t'') dt'' \right) \cdot \left(\int_0^{t'} \mathbf{G}(t'') dt'' \right) \right] dt'$$
(4.12)

where A(t) and A(0) are the echo signal intensities at times t and t=0 respectively.

For a spin echo sequence, let the 90° pulse be applied at time t = 0, and the 180° pulse be applied at time $t = \tau$. The gradient, $\mathbf{G}(t)$, can be turned on as follows (shown in Fig.

4.2):

$$G(t) = \begin{cases} 0, & 0 < t \le t_1 \\ g, & t_1 < t \le t_1 + \delta \\ 0, & t_1 + \delta < t < \tau \\ 0, & \tau \le t \le t_1 + \Delta \\ g, & t_1 + \Delta < t \le t_1 + \Delta + \delta \\ 0, & t_1 + \Delta + \delta < t \le 2\tau \end{cases}$$

$$(4.13)$$

where g is a constant vector not dependent on time. Thus, a pair of diffusion-encoding gradients is applied on both sides of the 180° pulse. Note that in practice, a perfect rectangular gradient pulse is not possible and generally a trapezoid pulse is practical which has a rising and falling edge (whose slope is decided by the slew rate of the MRI scanner).

The integral, F(t), is calculated for the different time intervals as follows:

The integral,
$$\boldsymbol{F}(t)$$
, is calculated for the different time intervals as follows:
$$\boldsymbol{F}(t) = \int_0^t \boldsymbol{G}(t') \mathrm{d}t' = \begin{cases} 0, & 0 < t \le t_1 \\ \boldsymbol{g}(t-t_1), & t_1 < t \le t_1 + \delta \\ \boldsymbol{g}\delta, & t_1 + \delta < t < \tau \\ -\boldsymbol{g}\delta, & \tau \le t \le t_1 + \Delta \\ -\boldsymbol{g}\delta + \boldsymbol{g}(t-t_1-\Delta), & t_1 + \Delta < t \le t_1 + \Delta + \delta \\ 0, & t_1 + \Delta + \delta < t \le 2\tau \end{cases}$$

Note that at time, $t=\tau$, the 180° pulse causes phase reversal.

Using Eq. 4.14 in Eq. 4.12 and simplifying the results leads to the famous Stejskal-Tanner diffusion equation for echo signal attenuation, as given by,

$$A(t = 2\tau) = A(0)\exp\left[-\gamma^2 g^2 \delta^2 \left(\Delta - \frac{\delta}{3}\right)D\right] = A(0)\exp(-bD)$$
 (4.15)

where g = |g| (magnitude of the g vector). Note that when the diffusion gradient is turned off (g = 0), the spin-echo signal intensity is simply the T_2 -weighted signal. It should be noted that imaging gradients also contribute to the diffusion sensitization of the MR signal although their contribution can be considered negligible when relatively large diffusion-encoding gradients are applied [81]. Thus, even the T_2 -weighted reference image is slightly diffusion-weighted. However, when imaging gradients are also considerably large, such as in MR microscopy, the diffusion coefficient has to be accurately estimated by considering the effect of imaging gradients.

4.3 Propagator formalism

Since self-diffusion of water molecules can be hindered by barriers (such as myelin sheath in nerve fibers) or restricted spatially, a formalism is necessary where appropriate boundary conditions can be applied on diffusion. In this case, the probabilistic approach to describing diffusion in space and time is favorable as was introduced by Einstein while explaining Brownian motion. Such approach can be used to represent both restricted and unrestricted (or free) diffusion.

The propagator is defined by the probability $P(\mathbf{r}_0|\mathbf{r},t)$ that a particle initially at position \mathbf{r}_0 will have moved to a position \mathbf{r} after a time interval t. The echo signal attenuation, E, [6, 82] in terms of the propagator is given by,

$$E(\boldsymbol{g},t) = \int_{V_0} P_0(\boldsymbol{r}_0) \int_V P(\boldsymbol{r}_0|\boldsymbol{r},t) \exp[-j\gamma\delta(\boldsymbol{r}-\boldsymbol{r}_0)\cdot\boldsymbol{g}] dV dV_0$$
(4.16)

where g is the diffusion-encoding gradient and $g \equiv \{g_x, g_y, g_z\}$. Note that the above expression of the echo attenuation assumes narrow gradient pulse, i.e., $\Delta \gg \delta$ such that the average displacements during the gradient pulse is negligible compared with the average displacements between the gradient pulses. $P_0(\mathbf{r}_0)$ is the probability of the diffusing particle at \mathbf{r}_0 at the time of the first gradient pulse. γ is the gyromagnetic ratio and δ is the duration the diffusion gradient pulse.

This relation can be approximated assuming r_0 does not affect the echo attenuation. This holds true for narrow pulsed field approximation where the diffusion pulse duration is small enough so that diffusion during the encoding period is ignored. Also, omitting the integral for $P_0(r_0)$ gives a Fourier relationship between the echo attenuation and the propagator as given [6],

$$E(\boldsymbol{g},t) = \int_{V} P_{a}(\boldsymbol{r},t) \exp[-j\gamma \delta \boldsymbol{r} \cdot \boldsymbol{g}] dV$$
 (4.17)

where $P_a(\mathbf{r},t) = P(0|\mathbf{r},t)$. The solution of echo attenuation relies on obtaining an expression for the propagator $P_a(\mathbf{r},t)$ and then applying the Fourier relation to obtain the expected echo attenuation, E.

Callahan [83] suggested the use of q-space formulation to represent the echo attenuation and making use of the Fourier relation with respect to the propagator. Here, q represents the reciprocal space vector corresponding to the displacement vector $(r - r_0)$ in a Fourier transform pair. The echo attenuation has been rewritten as [83],

$$E(\boldsymbol{q}, \Delta) = \int \int \rho(\boldsymbol{r}_0, 0) P(\boldsymbol{r}_0 | \boldsymbol{r}, \Delta) \exp[j2\pi \boldsymbol{q} \cdot (\boldsymbol{r} - \boldsymbol{r}_0)] d\boldsymbol{r}_0 d\boldsymbol{r}$$
(4.18)

where $\rho(\mathbf{r}_0,0)$ is the starting spin density. The reciprocal space vector \mathbf{q} is defined as a function of the diffusion gradient as $(2\pi)^{-1}\gamma\delta\mathbf{g}$. For the case of the restricted diffusion of diffusivity, D, confined within a pore of size a, the echo attenuation can be approximated by a Fourier relation [83], $E(\mathbf{q}, \Delta \to \infty) = |S(\mathbf{q})|^2$, where $S(\mathbf{q})$ is the Fourier transform of $\rho(\mathbf{r})$. This is under the assumption that $\Delta \gg a^2/D$ such that $P(\mathbf{r}_0|\mathbf{r},\Delta\to\infty)\to\rho(\mathbf{r})$ and also $\rho(\mathbf{r}_0,0)\to\rho(\mathbf{r}_0)$. Physically, the assumption $\Delta\gg a^2/D$ means that sufficient time is given between the diffusion encoding gradient pulses for the diffusing water molecules to reach the impermeable boundary of the pore, otherwise for shorter Δ , the diffusion will become unrestricted. The Fourier relation explains the famous diffusive diffraction pattern seen in PGSE experiments with small impermeable pores of uniform size [83].

So far I have shown that the echo attenuation is the Fourier transform of the propagator over space. Thus, in order to obtain an expression for the echo attenuation, the expression of the propagator has to be available. The propagator is generally solved from Fick's law by applying appropriate boundary conditions required by the problem ([83]). The Fick's law can be applied directly to the propagator $(P(\mathbf{r}_0|\mathbf{r},t))$,

$$D\nabla^2 P = \frac{\partial P}{\partial t} \tag{4.19}$$

This is equation can be solved using standard eigenmode expansion, the initial condition that $P(\mathbf{r}_0|\mathbf{r},t=0) = \delta(\mathbf{r}_0-\mathbf{r})$ and proper boundary conditions.

4.4 Parametric DWI

In complex structures, such as nerve fibers, it is difficult to characterize the exact nature of diffusion on a macroscopic length scale. Hence, a number of parametric models have been suggested to interpret the echo attenuation signal observed in the PGSE experiment. Three of such types are described in the following subsections, namely, DTI, ADTI and QUAQ.

4.4.1 DTI formulation

At macroscopic length scales, diffusion can be modeled as an anisotropic and homogeneous process [7]. Diffusion anisotropy can be represented by a rank 2 tensor (also called a dyad). A rank 2 tensor is a 3×3 matrix. The generalization to 3D anisotropic diffusion process is best understood from Fick's first law. From Fick's first law, it is known that $J = -D\nabla c$, where J is the diffusive flux, c is the concentration at a position and ∇c gives the concentration gradient vector. For an isotropic diffusion case where D is a scalar quantity, the diffusive flux, J, is along the direction of the concentration gradient vector, ∇c . However, when diffusion is anisotropic, a diffusion tensor, D is used in place of the scalar D and Fick's first law becomes, $J = -D \cdot \nabla c$. Now, the diffusive flux, J, need not be along the direction of the concentration gradient vector, ∇c , and this direction is governed by the tensor operation (D) on the concentration gradient vector (∇c) . An analogy of such an anisotropy is stress tensor and force relation. It is known that stress can be tensile (normal) and shear (tangential). Thus, force (F) exerted due to stress (T) on a surface (s) is given by, $F = T \cdot s$ where the force (F) need not be in the direction of the surface normal s.

The use of diffusion tensor was presented by Basser *et al.* [7, 12] who also introduced the technique Diffusion Tensor Imaging (DTI). In the case of axonal fiber tracts, the tensorial

notation interprets the hindrance of diffusion of water molecules in the transverse direction to the fiber orientation (due to semi-permeable myelin sheath membrane) as anisotropic diffusion and the eigenvectors of the tensor matrix indicate the principal directions of diffusion. However, this model does not consider restricted diffusion as will be discussed later.

The DTI signal formulation can be derived by generalizing Eq. 4.12 and using a diffusion tensor D for the diffusion process. Thus,

$$\ln\left[\frac{A(t)}{A(0)}\right] = -\gamma^2 \int_0^t \left[\mathbf{F}(t') \cdot \mathbf{D} \cdot \mathbf{F}(t') \right] dt'$$
$$= -\gamma^2 \int_0^t \left[\left(\int_0^{t'} \mathbf{G}(t'') dt'' \right) \cdot \mathbf{D} \cdot \left(\int_0^{t'} \mathbf{G}(t'') dt'' \right) \right] dt'$$
(4.20)

The above step can be written using matrix form as [12],

$$\ln\left[\frac{A(t)}{A(0)}\right] = -\gamma^2 \int_0^t \left[\mathbf{F}(t')^T \mathbf{D} \mathbf{F}(t') \right] dt'$$

$$= -\gamma^2 \int_0^t \left[\mathbf{F}(t') \mathbf{F}(t')^T \right] dt' : \mathbf{D}^{\text{eff}}$$

$$= -\mathbf{b} : \mathbf{D}^{\text{eff}}$$
(4.21)

where \mathbf{b} is the \mathbf{b} -matrix and \mathbf{D}^{eff} is the "effective" diffusion tensor. ":" is the generalized dot product (applicable to tensors). T represents the transpose operation. The effective diffusion tensor gives an equivalent tensorial representation of the diffusion process for the time period $[0, T_E]$ assuming a medium with a fixed diffusion tensor during this time. Thus, \mathbf{D}^{eff} has no time dependence although the actual diffusion process is time-dependent. Also, the tensor is assumed to have no spatial variation within the voxel. The effective diffusion tensor can be written as a product of the \mathbf{b} -matrix and \mathbf{D}^{eff} as

$$\ln\left[\frac{A(t)}{A(0)}\right] = -\sum_{i=1}^{3} \sum_{j=1}^{3} b_{ij} D_{ij}^{\text{eff}}$$
(4.22)

where b_{ij} and D_{ij}^{eff} are the ijth elements of the **b** and the \mathbf{D}^{eff} matrix respectively. For the PGSE sequence given in Fig. 4.2, the DTI equation can be rewritten in matrix form

as,

$$\ln \left[\frac{A(T_E)}{A(0)} \right] = -\gamma^2 \delta^2 \left(\Delta - \frac{\delta}{3} \right) \boldsymbol{g}^T \boldsymbol{D}^{\text{eff}} \boldsymbol{g}$$

$$= -\gamma^2 \delta^2 \left(\Delta - \frac{\delta}{3} \right) g^2 \hat{\boldsymbol{g}}^T \boldsymbol{D}^{\text{eff}} \hat{\boldsymbol{g}}$$

$$= -b \, \hat{\boldsymbol{g}}^T \boldsymbol{D}^{\text{eff}} \hat{\boldsymbol{g}}$$
(4.23)

where \hat{g} is the unit column vector along the gradient direction and $\hat{g} \equiv [\hat{g}_x, \hat{g}_y, \hat{g}_z]^T$. b is the b-factor and g is the gradient column vector as defined before. This is the classic echo signal formulation for the DTI model. For the sake of simplicity of notation, \mathbf{D}^{eff} will be written as \mathbf{D} only although wherever applicable, the proper tensor will be used.

From a probabilistic standpoint, as was introduced earlier in this chapter, Eq. 4.23 shows that water molecules follow simple anisotropic unrestricted diffusion governed by a 3D Gaussian probability distribution of displacement, $P(\mathbf{r}_0|\mathbf{r},t)$.

$$P(\boldsymbol{r}_0|\boldsymbol{r},t) = \frac{1}{\sqrt{(4\pi t)^3 |\boldsymbol{D}|}} \exp\left[-\frac{(\boldsymbol{r}-\boldsymbol{r}_0)^T \boldsymbol{D}^{-1} (\boldsymbol{r}-\boldsymbol{r}_0)}{4t}\right]$$
(4.24)

This shows that the diffusion tensor is proportional to the 3D variance of the probability of displacements. This result has been shown by a number of researchers [6, 7].

The effective diffusion tensor matrix (D) is a symmetric 3×3 matrix with six unique parameters which quantifies the anisotropic diffusion within each voxel in the 3D space.

$$\mathbf{D} = \begin{bmatrix} D_{xx} & D_{xy} & D_{xz} \\ D_{xy} & D_{yy} & D_{yz} \\ D_{xz} & D_{yz} & D_{zz} \end{bmatrix}$$
(4.25)

and $\hat{\boldsymbol{g}} = [\hat{g_x} \ \hat{g_y} \ \hat{g_z}]^T$ = the diffusion gradient direction unit vector (column vector) written in matrix format. The expression for the echo signal attenuation was defined as [7],

$$E(\mathbf{g}) = \frac{A(T_E)}{A(0)} = \exp\left(-b\hat{\mathbf{g}}^T \mathbf{D}\hat{\mathbf{g}}\right)$$

$$= \exp\left[-b\left(\hat{g}_x^2 D_{xx} + \hat{g}_y^2 D_{yy} + \hat{g}_z^2 D_{zz} + 2\hat{g}_x \hat{g}_y D_{xy} + 2\hat{g}_x \hat{g}_z D_{xz} + 2\hat{g}_y \hat{g}_z D_{yz}\right)\right]$$
(4.26)

In a fiber, there is preferential diffusion along the longitudinal direction which gives the fiber orientation. Thus, after estimating the D matrix from the DWI data using the model in (4.23), the fiber orientation is given by the direction of principal eigenvector of the D matrix. Thus, from eigen decomposition,

$$\mathbf{DE} = \mathbf{E}\Lambda \tag{4.27}$$

where **E** is the matrix of eigenvectors (column vectors) $(\mathbf{e_1}, \mathbf{e_2}, \mathbf{e_3})$ and Λ is the eigenvalue matrix,

$$\mathbf{E} = [\mathbf{e_1} | \mathbf{e_2} | \mathbf{e_3}] \tag{4.28}$$

$$\Lambda = \begin{bmatrix}
\lambda_1 & 0 & 0 \\
0 & \lambda_2 & 0 \\
0 & 0 & \lambda_3
\end{bmatrix}$$
(4.29)

If $\lambda_3 > \lambda_2 > \lambda_1$, then $\mathbf{e_3}$ is the principal eigenvector and the fiber orientation is given by the direction of $\mathbf{e_3}$. The diffusion coefficient along this direction will be given by the eigenvalue, λ_3 . For the sake of clarity, it is assumed that principal fiber direction is along the +Z-axis of the diffusion space and define, $D_{\parallel} = \lambda_3, D_{\perp 1} = \lambda_2, D_{\perp 2} = \lambda_1$.

From the perspective of model parameter estimation, for the DTI formulation, the model is composed of the 6 diffusion coefficients of the effective diffusion tensor matrix. Also, an additional A(0) signal is required. However, these model parameters are dependent of the coordinate axis. To obtain a set of parameters which are independent of the coordinate axis, the set of eigenvalues and the Euler angles as model parameters are collected. Thus, if the set of model parameters is defined as β , then, $\beta \equiv \{D_{\parallel}, D_{\perp 1}, D_{\perp 2}, \theta_F, \phi_F, \psi_F\}$, where $D_{\parallel}, D_{\perp 1}, D_{\perp 2}$ are the longitudinal and transverse diffusivities and θ_F, ϕ_F, ψ_F are the Euler angles. This is also a 6-parameter model. The diffusion process could be best described by an diffusion ellipsoid diagram shown in Fig. 4.3.

Decomposing D into its eigenvectors and eigenvalues,

$$\mathbf{D} = \mathbf{R}^T \mathbf{D}_0 \mathbf{R}$$
, where $\mathbf{D}_0 = \begin{bmatrix} D_{\perp 2} & 0 & 0 \\ 0 & D_{\perp 1} & 0 \\ 0 & 0 & D_{\parallel} \end{bmatrix}$ (4.30)

and $\mathbf{R} = R(\theta_F, \phi_F, \psi_F)$ represents the combined rotation matrix which can be decomposed into component rotation matrices as shown.

$$\mathbf{R} = R_z(\psi_F) * R_y(\theta_F) * R_z(\phi_F)$$
(4.31)

$$R_y(\theta_F) = \begin{bmatrix} \cos(\theta_F) & 0 & -\sin(\theta_F) \\ 0 & 1 & 0 \\ \sin(\theta_F) & 0 & \cos(\theta_F) \end{bmatrix}$$
(4.32)

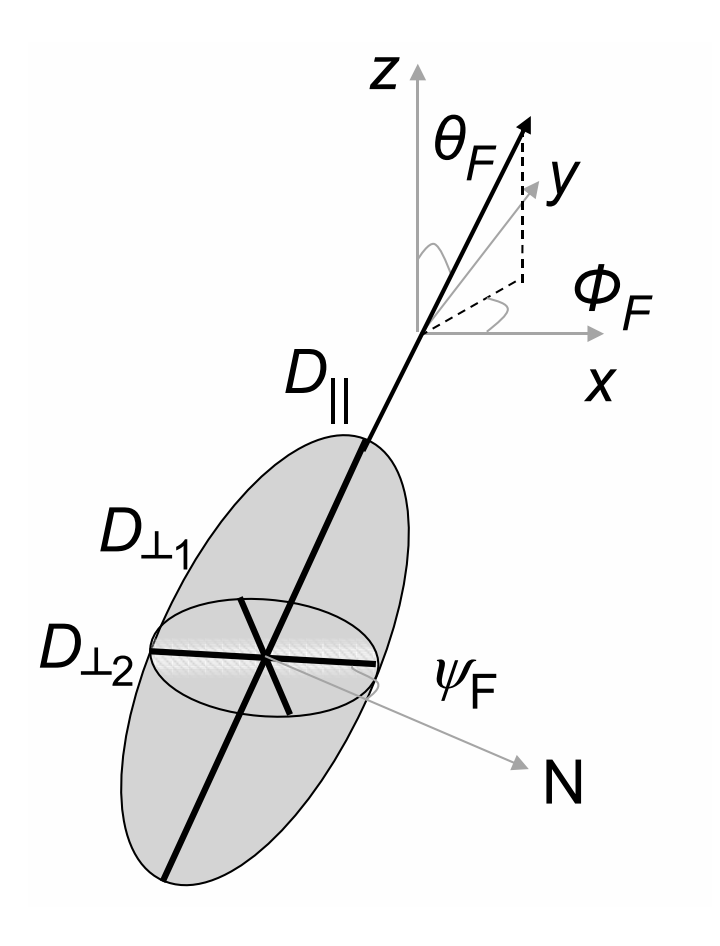


Figure 4.3. DTI diffusivity ellipsoid indicating diffusivities $(D_{\parallel}, D_{\perp 1}, D_{\perp 2})$ and the orientation angles $(\theta_F, \phi_F, \psi_F)$.

$$R_z(\phi_F) = \begin{bmatrix} \cos(\phi_F) & \sin(\phi_F) & 0\\ -\sin(\phi_F) & \cos(\phi_F) & 0\\ 0 & 0 & 1 \end{bmatrix}$$

$$(4.33)$$

$$R_z(\psi_F) = \begin{bmatrix} \cos(\psi_F) & \sin(\psi_F) & 0\\ -\sin(\psi_F) & \cos(\psi_F) & 0\\ 0 & 0 & 1 \end{bmatrix}$$
(4.34)

4.4.2 ADTI formulation

For axisymmetric DTI model [8, 84, 85], transverse diffusivity is assumed isotropic (Fig. 4.4). Thus, $D_{\perp 1} = D_{\perp 2} = D_{\perp}$. Also, $D_{\parallel} \geq D_{\perp}$ and ψ_F is identically zero. This leads to a 4-parameter model. Let $\boldsymbol{\beta}$ be the parameter set, $\boldsymbol{\beta} \equiv \{D_{\parallel}, D_{\perp}, \theta_F, \phi_F\}$. \boldsymbol{D} is decomposed into its eigenvalues and eigenvectors as:

$$\mathbf{D} = \mathbf{R}^T \mathbf{D}_0 \mathbf{R}, \text{ where } \mathbf{D}_0 = \begin{bmatrix} D_{\perp} & 0 & 0 \\ 0 & D_{\perp} & 0 \\ 0 & 0 & D_{\parallel} \end{bmatrix}$$
(4.35)

and \mathbf{R} is the transpose of the matrix of eigenvectors. If $\mathbf{R} = \mathbf{I}$, a 3 × 3 identity matrix, then $\mathbf{D} = \mathbf{D}_0$ and the fiber orientation, given by the principal eigenvector direction, is along the +Z-direction. So, for the fiber orientation to be at the spherical coordinates (θ_F, ϕ_F) , the tensor (\mathbf{D}_0) will also be oriented along the fiber direction. Thus, in case of a fiber oriented at the spherical coordinates (θ_F, ϕ_F) , $\mathbf{R} = R(\theta_F, \phi_F)$ will be the rotation matrix which reorients the coordinate axis along the fiber direction. It can be decomposed into component rotation matrices as shown.

$$\mathbf{R} = R_y(\theta_F) R_z(\phi_F) \tag{4.36}$$

$$R_y(\theta_F) = \begin{bmatrix} \cos(\theta_F) & 0 & -\sin(\theta_F) \\ 0 & 1 & 0 \\ \sin(\theta_F) & 0 & \cos(\theta_F) \end{bmatrix}$$

$$(4.37)$$

$$R_z(\phi_F) = \begin{bmatrix} \cos(\phi_F) & \sin(\phi_F) & 0\\ -\sin(\phi_F) & \cos(\phi_F) & 0\\ 0 & 0 & 1 \end{bmatrix}$$
(4.38)

The expression for the echo attenuation or the normalized MR signal for the ADTI model in matrix format can be simplified as,

$$E = \exp\left(-b\hat{\mathbf{g}}^T \mathbf{D}\hat{\mathbf{g}}\right)$$

$$= \exp\left(-b\hat{\mathbf{g}}^T \mathbf{R}^T \mathbf{D}_0 \mathbf{R}\hat{\mathbf{g}}\right)$$

$$= \exp\left(-b(\mathbf{R}\hat{\mathbf{g}})^T \mathbf{D}_0 \mathbf{R}\hat{\mathbf{g}}\right)$$

$$= \exp\left(-b\hat{\mathbf{g}}'^T \mathbf{D}_0\hat{\mathbf{g}}'\right)$$
(4.39)

where column vector $\hat{\boldsymbol{g}}' = \mathbf{R}\hat{\boldsymbol{g}}$ and $\hat{\boldsymbol{g}}' \equiv [\hat{g}_x', \hat{g}_y', \hat{g}_z']^T$ and $\hat{\boldsymbol{g}} \equiv [\hat{g}_x, \hat{g}_y, \hat{g}_z]^T$ as before. T is the transpose of a matrix. b is the b-factor. Expanding the exponent,

$$\hat{\mathbf{g}}^{\prime T} \mathbf{D}_0 \hat{\mathbf{g}}^{\prime} = \hat{g}_z^2 D_{\parallel} + (\hat{g}_x^2 + \hat{g}_y^2) D_{\perp}$$
(4.40)

Since **R** is the transpose of the matrix of eigenvectors which reorients the coordinate axis along the fiber, $\hat{g}' = \mathbf{R}\hat{g}$ is the projection of the gradient direction \hat{g} on to the eigen directions. Let \hat{f} be the unit column vector along the fiber direction given by spherical coordinates (θ_F, ϕ_F) . Then, projection of the gradient direction on the fiber direction,

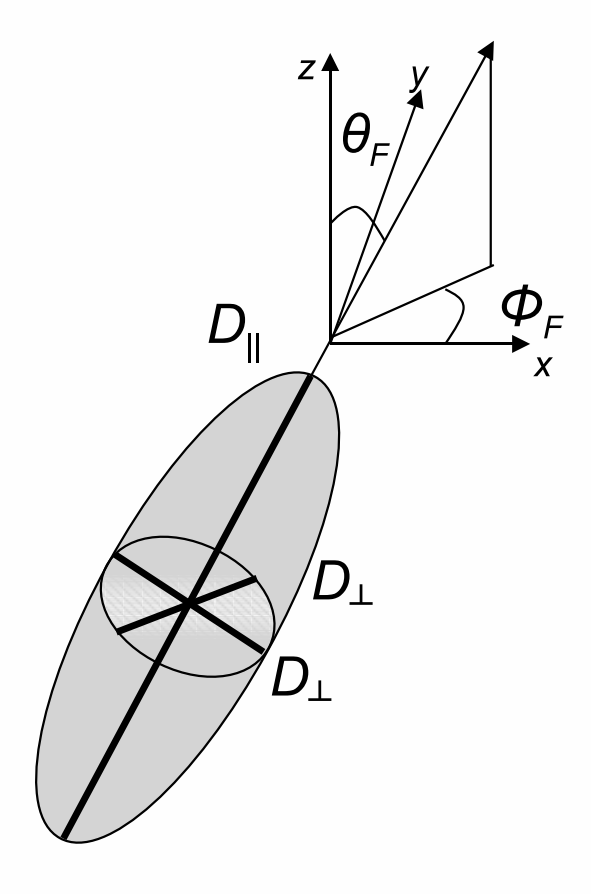


Figure 4.4. ADTI diffusivity ellipsoid indicating diffusivities $(D_{\parallel}, D_{\perp})$ and the orientation angles (θ_F, ϕ_F) .

 $g_{\parallel} = \hat{\boldsymbol{g}}^T \hat{\boldsymbol{f}}$, is the same as \hat{g}_z . And the transverse component is given by, $g_{\perp} = \sqrt{\hat{g}_x^2 + \hat{g}_y^2}$. Thus, the ADTI signal equation can be rewritten as,

$$E = \exp\left(-b(g_{\parallel}^{2}D_{\parallel} + g_{\perp}^{2}D_{\perp})\right)$$
 (4.41)

Also, $g_{\perp}^2 = 1 - g_{\parallel}^2$. D_{\parallel} and D_{\perp} are the diffusion coefficients in the parallel and perpendicular directions to the fiber orientation, respectively.

4.4.3 QUAQ formulation

In quantitative analysis of q-space [8] (QUAQ), the diffusion process is modeled by unrestricted diffusion on the longitudinal direction to the fiber and restricted diffusion along transverse direction. Each fiber population is assumed to consist of an impermeable

cylindrical shape, with self-diffusion coefficient D inside the cylinder (and no diffusion outside), an average or "apparent" radius a and orientation angles in spherical coordinates of the individual fibers (ϕ_F, θ_F) . The MR signal attenuation is formulated in the q-space, where q is the reciprocal space vector [83] corresponding to a position r. The echo attenuation at time, Δ , in terms of q is given by,

$$E(\mathbf{q}, \Delta) = E_{\parallel}(q_{\parallel}, \Delta) E_{\perp}(q_{\perp}, \Delta) \tag{4.42}$$

where $E_{\parallel}(q_{\parallel}, \Delta)$ and $E_{\perp}(q_{\perp}, \Delta)$ are the contributions due to the longitudinal and transverse components of diffusion respectively. Here, $q_{\parallel} = \gamma \delta g_{\parallel}/2\pi$, $g_{\parallel} = \boldsymbol{g} \cdot \boldsymbol{f}$ and \boldsymbol{f} is the unit vector along the fiber direction defined in spherical coordinates by (θ_F, ϕ_F) . And, $q_{\perp} = \sqrt{1 - q_{\parallel}^2}$.

For the longitudinal unrestricted diffusion, the simple Gaussian propagator can be used and the echo attenuation is given by,

$$E_{\parallel}(q_{\parallel}) = \exp\left[-4\pi^2 \left(\Delta - \frac{\delta}{3}\right) D q_{\parallel}^2\right] \tag{4.43}$$

For the transverse restricted diffusion, the solution for the echo attenuation for a cylindrical pore using the propagator formalism is shown in [8, 83]. The narrow pulse-width assumption has been applied in the derivation ($\Delta \gg \delta$). Since the transverse component of echo attenuation is being calculated, the coordinate axis is aligned with the fiber orientation such that the cylinder is along Z-axis with (r, θ) as the cylindrical coordinates with respect to the central axis. The echo attenuation for the transverse component is given by[8],

$$E_{\perp}(q_{\perp}) = 4 \left(\frac{J_0'(2\pi a \ q_{\perp})}{2\pi a \ q_{\perp}} \right)^2 + 4 \sum_{k=1}^{\infty} \left(\frac{2\pi a \ q_{\perp} J_0'(2\pi a \ q_{\perp})}{(2\pi a \ q_{\perp})^2 - \beta_{0,k}^2} \right)^2 \exp\left(-\beta_{0,k}^2 \frac{D\Delta}{a^2} \right)$$

$$+8 \sum_{n=1}^{\infty} \sum_{k=1}^{\infty} \left(\frac{2\pi a \ q_{\perp} J_n'(2\pi a \ q_{\perp})}{(2\pi a \ q_{\perp})^2 - \beta_{n,k}^2} \right)^2 \frac{\beta_{n,k}^2}{\beta_{n,k}^2 - n^2} \exp\left(-\beta_{n,k}^2 \frac{D\Delta}{a^2} \right)$$

where $q_{\perp} = \gamma \delta g_{\perp}/2\pi$ and $g_{\perp}^2 = 1 - g_{\parallel}^2$. $\beta_{n,k}$ is the kth root of the first derivative of the Bessel function of order n, J_n , such that $(J'_n(\beta_{n,k}) = 0)$ [8].

While, in DTI, the diffusion tensor that is estimated is an "apparent" or "effective" diffusion tensor that approximates the actual diffusion process in each voxel as a unre-

stricted (barrier-free) anisotropic diffusion process, in QUAQ, the actual isotropic diffusion process within a network of impermeable cylinders is considered. Hence, in DTI, the estimated diffusivities strongly depend on the acquisition parameters, while, in QUAQ, the estimated parameters have a physical interpretation in direct correlation with the physical problem under investigation.

4.5 Non-parametric DWI

An alternate method of analyzing the diffusion-weighted data is by solving for the conditional probability function $(P(r_0|r,t))$ or the propagator for the diffusion process as is without using a parametric model for the propagator. Such methods are known as q-space imaging (QSI) or diffusion spectrum imaging (DSI) [86]. In QSI, the sampling is performed in the Fourier space of displacements, i.e., q-space over a regular grid. The reconstruction is performed via Fast Fourier transform and a discrete representation of the probability function is obtained [87]. The need for QSI arose due to the need to resolve fiber crossings where a simple single fiber model can not provide accurate results. QSI requires dense sampling on the 3D Cartesian grid (thus is very time consuming) and uses large pulsed gradients. Total scan time depends on the number of samples of the q-space and thus depends on the number of diffusion-weighted images acquired which is significantly higher for non-parametric DWI than model-based DWI (such as DTI). For example, a typical full brain DTI with 15 diffusion directions can be around 2 min (for $T_R=6.4~\mathrm{s},\,\mathrm{NEX}=1),\,\mathrm{while}$ a full brain QSI (such as Q-ball imaging) with 252 directions can be around 27 min [11] (for $T_R = 6.4$ s, NEX = 1). Due to long scan times, QSI is not clinically viable. Since the focus is on resolving the fiber orientations in a crossing fiber situation, a cumulative probability with respect to the propagator called orientation distribution function (ODF, $\phi(\hat{\mathbf{x}})$) is estimated.

$$\phi(\hat{\mathbf{x}}) = \int_0^\infty P(\alpha \hat{\mathbf{x}}) d\alpha \tag{4.44}$$

where $\hat{\mathbf{x}}$ is the unit vector in the direction of displacement vector \mathbf{x} . Hence, the ODF is the radial projection of the propagator on to a unit sphere. It has higher values

at a particular orientation when the presence of a fiber is more probable. The ODF can be obtained by acquiring data on spherical shells in q-space and reconstructing the ODF using fitting methods as in high angular resolution diffusion imaging (HARDI [88]) or transform methods, such as Funk-Radon transform in Q-ball imaging (QBI [11]). Although a non-parametric approach is applied in the estimation of the propagator and the ODF, the interpretation of the ODF often involves fitting the ODF to model-based functions (e.g., spherical harmonics [89, 90]) in order to identify fiber tracts.

4.6 Experimental DTI protocol used in this work

4.6.1 Pulse sequence

For the DTI experiment, the sequence used is based on the PGSE experiment suggested by Stejskal and Tanner but with a number of modifications. The sequence is a spin-echo echoplanar imaging (SP-EPI) sequence. This sequence belongs to the fast imaging methods. Since the DTI models unrestricted diffusion, the narrow pulse assumption ($\Delta \gg \delta$) is not required in the pulse sequence [82]. The following are the salient features of the DTI pulse sequence used in the GE Signa HDx 3T scanner (GE Healthcare, Waukesha, WI):

- 1. Use of echo-planar imaging: Echo planar imaging is one of the fast imaging methods in MRI and it was first introduced by Mansfield [91]. The use of EPI drastically reduced the MRI scan times and made imaging large parts of the body possible within a tolerable amount of scan time. In EPI, the k-space plane is sufficiently sampled to reconstruct an image after a single RF excitation. The planar k-space sampling is done by alternating the readout gradient which produces a train of gradient echoes and phase encoding the echoes using intermediate short gradient pulses (blips). Fig. 4.5 shows the schematic for a typical EPI sequence along with the k-space trajectory for MR signal acquisition.
- 2. Use of spatio-spectral RF pulse: In a conventional RF pulse (such as the 90° pulse), the spin flip is achieved by a single pulse. Additionally, for slice selection, the slice

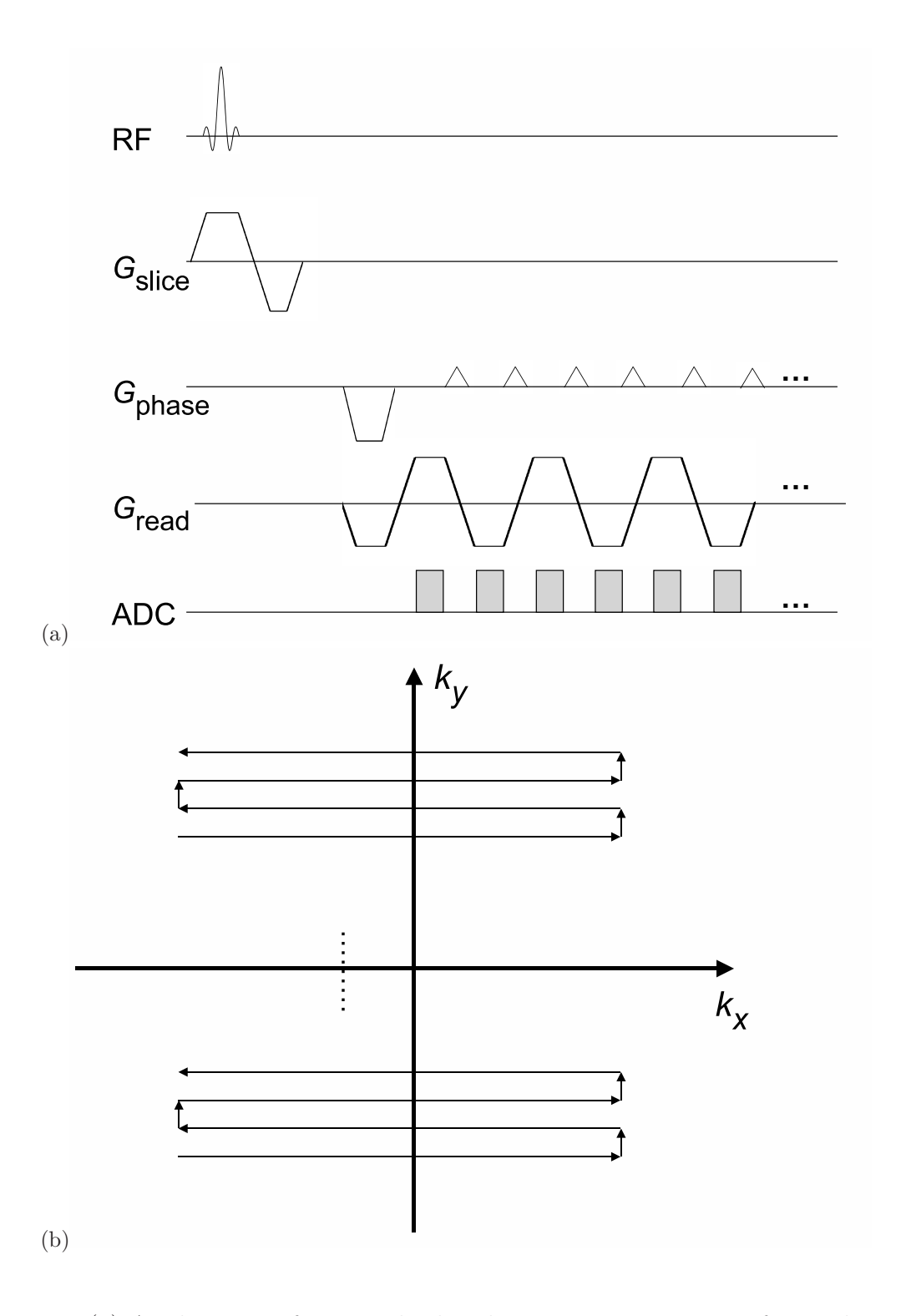


Figure 4.5. (a) A schematic of a typical echo-planar imaging sequence for gradient echo. (b) The k-space trajectory for the EPI sequence.

selected gradient (G_z) is turned on in case of 2D multi-slice MR imaging. However, the chemical shift effect where protons in the fat (or molecules other than water) precess at a slightly different Larmor frequency as compared to protons in water leads to image artifacts, such as ghosting [92]. In order to minimize this effect, a spatially as well as spectrally (frequency) selective RF pulse sequence is used [92]. The spectral selection is done using a sequence of RF pulses (instead of a single RF pulse) where each RF pulse is tuned at the Larmor frequency of protons in water and the pulses are spaced at time intervals equal to half of the time period corresponding to the frequency difference between Larmor frequencies of protons in water and fat [92]. This way the RF excitation of protons in fat is suppressed. Note that the effective flip angle of the combined RF pulse sequence is the cumulative sum of the individual flip angles. Fig. 4.6 shows the traditional single RF pulse and 12 pulse spatio-spectral pulse sequence used in the GE scanner for DTI experiments. Flip angles of the RF pulses in the spatio-spectral pulse in Fig. 4.6(b) add up to 90°.

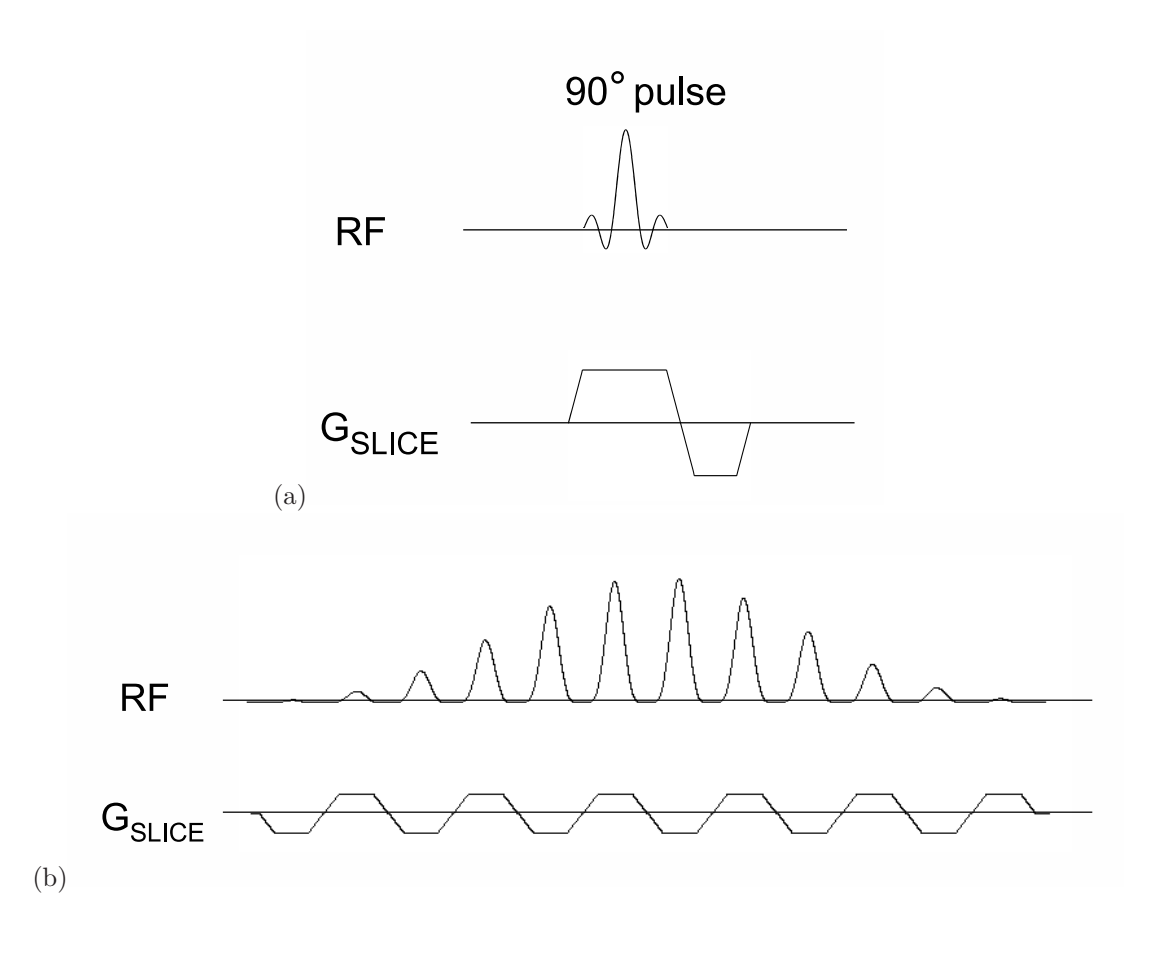


Figure 4.6. (a) Single RF pulse with slice select gradient. (b) 12 RF pulses of the spatio-spectral pulse sequence with the slice select gradients.

3. Use of dual spin-echo: Diffusion-weighted imaging is prone to field gradient eddy current effects due to the fast switching of strong gradient fields. Such switching induces eddy current on the conductive surfaces of the MRI scanner and the current can linger even after the switching event is past. The presence of eddy current causes spatial magnetic field distortion which results in phase error during k-space sampling resulting in numerous image artifacts, such as contraction, dilation, shift, shear and ghosting. The problem could be severe in diffusion-weighted imaging since diffusion-weighting is performed with varying gradient field strengths and could result in image misregistration between the diffusion-weighted images [93]. In a dual-spin echo sequence, a second 180° pulse is applied so as to refocus the spins twice. Such a twice-refocused spin-echo sequence is less prone to field gradient eddy current effects. Eddy current effect is generally modeled as an exponential decay with a decay constant. If the eddy current decays slowly, then during readout the eddy current induced residual field will attenuate the MR signal additionally. This effect is also more pronounced in EPI sequences. The pulse durations (δs) can be optimally selected to completely cancel the effect of eddy currents at a particular decay constant |93|, thereby reducing the eddy current induced residual field effect on the MR signal. After twice refocusing, the eddy current build-up at the time of acquisition is reduced to zero. In the DTI framework, such modifications in the pulse sequence results in a modified expression of the b-factor and the b-factor has to be recalculated in terms of the new timing parameters. Although analytical expressions of the b-factor exists under different assumptions of the timing parameters (for example, [94]), on the GE scanner, the b-factor is numerically estimated [95] by using the definition of the b-matrix which is based on gradient waveform integration equation shown in Eq. 4.21: $\mathbf{b} = \gamma^2 \int_0^{TE} \left[\mathbf{F}(t') \mathbf{F}(t')^T \right] dt'$. The integration based technique, however, assumes piecewise linear segments of the gradient waveform. During the DTI experiment, the user prescribes a b-factor for the scan. Using the integration technique [95], the calculated b-factor is matched with the userprescribed b-factor to estimate the gradient strengths along the different gradient coordinate axes. The calculated b-factor is adjusted iteratively until the value is within a tolerance range of the prescribed b-factor.

4.6.2 Experimental settings

Apart from the standard settings for Spin-Echo pulse sequence such as T_E , T_R , diffusion-related experimental parameters are the b-factor, the diffusion-encoding gradient directions (vector \mathbf{g}) and the number of gradient directions (N). Since b-factor is a function of the diffusion-encoding gradient strength (G), diffusion pulse duration (δ) and pulse separation or diffusion time (Δ), these can also be separately set during experiments. Note that the time of echo, T_E , is dependent on the selection of the Δ and δ . And for the dual-spin echo sequence, an effective b-factor based on the individual timing parameters is calculated and used in the DTI model. From an optimization perspective, in this work, focus is on the diffusion-encoding gradient vector, \mathbf{g} , and its distribution in gradient space (or \mathbf{q} -space). Also, the selection of the b-factor on the whole and its influence on the estimation performance is investigated without going into the dependence of the b-factor on the individual timing parameters.

4.7 Fiber assignment by continuous tracking

Estimated diffusion model parameters in DTI (or ADTI) can be used to track white matter connectivity from a seed region to the rest of the imaged tissue by estimating white matter tract trajectories. In general, fiber tracking algorithms can be based on a deterministic framework, such as ones proposed by Mori et al. [16], Conturo et al. [58] and Basser et al. [96], or on a probabilistic framework, such as ones proposed by Poupon et al. [97], Parker et al. [98] and Behrens et al. [59]. While deterministic algorithms are fast and more often used clinically [99], probabilistic techniques could potentially be more accurate (for example, as shown by Behrens et al. [59]) but tend to be computationally intensive (hence slow) and generally require more data. A commonly used deterministic fiber tracking algorithm is fiber assignment by continuous tracking or FACT. Alternately,

a common example of probabilistic fiber tracking is implemented in the software package FSL which is called "probtrack" [59, 100] which uses the estimates of posterior probabilities of local fiber orientations obtained from "Bayesian Estimation of Diffusion Parameters Obtained using Sampling Techniques" (BEDPOST) [59, 101] to calculate a probabilistic connectivity map from a seed to different targets in the imaged structure.

The general notion for the deterministic fiber tracking based on DTI is to define a seed region (for example, a seed voxel) in image space and trace a streamline by following the direction of the principal eigenvector of the diffusion tensor (which represents the direction of the fastest diffusion within a voxel) from the seed voxel to other voxels within the 3D image under certain constraints based on the local diffusion anisotropy and curvature of the estimated streamlines. Mathematically, this is equivalent to solving an ordinary differential equation (ODE) numerically for a curve in 3D space given an initial condition (seed) [96,99] and where the unit tangent vector at a point on the trajectory is equated to the principal eigenvector of the estimated diffusion tensor. The numerical integration for solving the ODE can be a first order method (as in the Euler's method [16]) or higher order method (as in the Runge-Kutta method [96]).

FACT method introduced by Mori et al. [16, 102] is one of the most common methods for deterministic fiber tracking. The tracking is initiated from seed points (generally voxel center) and the direction of the track is changed from the current voxel's principal eigenvector direction to that of the neighboring voxel at the point on the boundary of the voxels where the track leaves the voxel and enters the next. This ensures that tracks are reconstructed more realistically than by merely connecting the centers of the voxels [16]. The tracking algorithm uses a brute-force approach where tracks originate from seed points from the uniformly sampled 3D image space (for example, voxel centers). From this ensemble of reconstructed fibers, specific tracks are visualized by selecting specific ROI which the tracks originate from or pass through [102, 103]. The FACT method is implemented in the DTIStudio software [103] which is used for the fiber tracking analysis in this work. FACT-based tracking has been previously used for visualizing white matter connectivity for in vivo DTI experiments, such as in the human brain for

cortical association tracts [104] and corpus callosum [105] and in the spinal cord for detecting spinal cord compression [27] and astrocytomas [67].

In the FACT algorithm, generation of arbitrary tracks is restricted by constraining the trajectory paths with thresholds based on the local diffusion anisotropy (FA threshold) and curvature of the evolving fiber track (curvature threshold). High FA threshold makes sure that tracking is performed within the highly anisotropic white matter regions and not the low anisotropy gray matter or CSF. The curvature threshold ensures that sharp changes in the fiber track are avoided [102]. Selection of the threshold values is generally based on previous studies in the region of interest and is user defined, although studies on the sensitivity of these thresholds to the fiber tracking result can help select the thresholds more robustly [106].

While FACT-based fiber tracking provides a visual interpretation of the white matter tracts in the form of estimated streamlines, certain tract-based metrics can also be defined to quantify the quality of the tracked fibers and compare across subjects. Correia et al. [107] defined a number of such metrics. DTIStudio computes some of these metrics as part of the output of the tracking analysis, such as, the total number of fibers tracked (TF), the average number of fibers per voxel in the tracked fibers (AF) and the average length of fibers tracked (AL). These metrics can be ROI specific (calculated for tracks that are either originating from or passing through the ROI voxels) or for the whole image. The length-based metrics (AL) and number of fibers based metrics (TF, AF) provide independent information about the white matter integrity [107]. For example, higher AL indicates longer fiber tracks and thus better long range white matter connectivity and integrity. On the other hand, higher TF indicates more fiber tracks from the ROI and thus indicates better chance of connectivity. AF indicates the track density with respect to an ROI. These metrics have been previously used for fiber tracking analyses, such as in studying age-related degradation in the central nervous system where both TF and AF showed good correlation (negative correlation) with age for different white matter tracts [108]. FACT-based algorithms are commonly used for clinical studies and hence this work will explore the effect of gradient optimization on FACT-based fiber tracking.

CHAPTER 5

Optimization of gradient scheme in diffusion-weighted imaging

The gradient scheme in diffusion-weighted imaging consists of the diffusion gradient directions and the b-factor which is calculated based on the parameters related to the gradient strength and time durations. In this work, I have focused on the optimal selection of the gradient directions. However, I have also studied the b-factor optimization. The optimization is based on D-optimality [33, 34] which minimizes the Cramer-Rao lower bound (CRLB) on the estimation variance and uses the Fisher information matrix [109]. The optimization procedure will only improve precision (or reduce estimation uncertainty). The procedure assumes that the parameter estimator is unbiased, i.e., there is no difference (or no bias) between the expected and true values of the parameters. In case the estimation is actually biased, minimizing the CRLB could still minimize the uncertainty in the estimation, but the analytical CRLB will not be equal to the actual lower bound of the uncertainty. The effect of the optimization on the bias depends on the problem formulation, especially the signal and the noise model. The optimization is applied to DTI (and ADTI) signal model which assumes that the diffusion phenomenon in the nerve fibers strictly as an unrestricted diffusion and is described by a three-dimensional Gaussian distribution. Another signal model, called the QUAQ model, assumes that the diffusion occurs in impermeable tubes with unrestricted diffusion along the direction of the tube and restricted diffusion in the transverse direction. The noise model can be considered as Gaussian (at SNR > 5) or in general Rician. The Gaussian noise model, which is more popular, has a simpler formulation than the Rician model. Both noise models have been considered in this work.

5.1 General concepts in parameter estimation and optimization

5.1.1 Cramer-Rao Lower Bound

Given the model-based normalized MR signal E and the variance σ^2 of the noise in the MRI data, the experimental measurement of the normalized MR signal (noisy signal), \hat{E} , follows a probability distribution function (pdf), $p(\hat{E}|E,\sigma^2)$. For a set of N diffusion-weighted images with different gradients, the joint pdf for the measurement column vector $(\hat{E} = [\hat{E}_1, \hat{E}_2, \hat{E}_3, ..., \hat{E}_N]^T)$ will be

$$p(\hat{\mathbf{E}}) = \prod_{i=1}^{N} p(\hat{E}_i | E_i, \sigma^2)$$
(5.1)

assuming each measurement of the normalized MR signal, \hat{E}_i , to be independent and having the same variance (σ^2) but different model signals, E_i . The model signal, E_i , depends on the diffusion model parameters, denoted by a column vector of parameters $\boldsymbol{\beta} := [\beta_1, \beta_2, \beta_3, ..., \beta_M]^T$ (for M diffusion model parameters), as well as the MRI experimental parameters, denoted by $\boldsymbol{\alpha}$ vector. Thus, $p(\hat{\boldsymbol{E}})$ can be rewritten as $p(\hat{\boldsymbol{E}}|\boldsymbol{\beta}, \boldsymbol{\alpha})$. The experimental parameters $(\boldsymbol{\alpha})$ can be separated into the b-factor and the set of gradient directions or gradient scheme. Each ith gradient direction, \boldsymbol{g}_i , can be represented as $\boldsymbol{g}_i \equiv \{g_{xi}, g_{yi}, g_{zi}\} \equiv \{\theta_i, \phi_i\}$. The (θ_i, ϕ_i) representation is preferred since there are fewer parameters in this form. In matrix form, the gradient scheme consisting of N gradient directions, Ω , is defined as, $\Omega := [\theta_1, \theta_2, \theta_3, ..., \theta_N, \phi_1, \phi_2, \phi_3, ..., \phi_N]^T$. Thus, $\boldsymbol{\alpha} := [b, \Omega]^T$.

The Cramer-Rao Lower Bound (CRLB) [109] on the variance of the estimated model

parameters $(\hat{\boldsymbol{\beta}} = [\hat{\beta}_1, \hat{\beta}_2, \hat{\beta}_3, ..., \hat{\beta}_M]^T)$ can be given by the inequality,

$$\Sigma(\hat{\beta}) - \mathbf{I}^{-1}(\beta) \ge 0 \tag{5.2}$$

where $\Sigma(\hat{\boldsymbol{\beta}})$ is the covariance matrix of the diffusion model parameter estimates $(\hat{\boldsymbol{\beta}})$ defined as,

$$\Sigma(\hat{\boldsymbol{\beta}}) = \langle (\hat{\boldsymbol{\beta}} - \langle \hat{\boldsymbol{\beta}} \rangle)(\hat{\boldsymbol{\beta}} - \langle \hat{\boldsymbol{\beta}} \rangle)^T \rangle$$
 (5.3)

where $\langle \ \rangle$ is the expectation operation. $\mathbf{I}(\boldsymbol{\beta})$ is the Fisher information matrix for the true parameters $(\boldsymbol{\beta})$ and ' $\geq \mathbf{0}$ ' refers to a matrix being positive semidefinite. The Cramer-Rao covariance lower bound is given by,

$$\Sigma_{CR}(\boldsymbol{\beta}) = \mathbf{I}^{-1}(\boldsymbol{\beta}) \tag{5.4}$$

and the jkth element of the Fisher information matrix is defined as,

$$[\mathbf{I}(\boldsymbol{\beta})]_{jk} = -\langle \frac{\partial^2 \ln p(\hat{\boldsymbol{E}})}{\partial \beta_j \partial \beta_k} \rangle \tag{5.5}$$

where β_j and β_k are the jth and kth diffusion model parameters from β , respectively. The expectation operation ($\langle \ \rangle$) is taken with respect to $p(\hat{E})$ (Eq. 5.1). Both $j \in [1, M]$ and $k \in [1, M]$, where M is the number of diffusion model parameters in β . The Fisher information matrix is a function of $p(\hat{E})$ and thus depends both on β and α . So, $I(\beta)$ can be rewritten as $I(\beta, \alpha)$. Thus, $\Sigma_{CR}(\beta)$ can also be written as $\Sigma_{CR}(\beta, \alpha)$ and depends on both the diffusion model parameters and the MRI experimental parameters. By optimizing the experimental parameters (α), the covariance bound on the diffusion model parameter estimates can be minimized. This covariance bound is achieved by any unbiased and minimum variance estimator. Thus, an optimal experimental design can be obtained. As shown later, using determinant of the CRLB matrix as a cost function for the optimization problem, an overall minimal uncertainty can be achieved in the estimation.

5.1.2 Sensitivity matrix

As will be discussed later, the definition of CRLB (and the Fisher information matrix) involves the sensitivity matrix (X) which is essentially Jacobian matrix of the signal at

different gradients with respect to the different diffusion model parameters. The jkth element of the sensitivity matrix, X, is given by,

$$[\mathbf{X}]_{ij} := \frac{\partial E(\boldsymbol{\beta}; \mathbf{g}_i; b)}{\partial \beta_i}$$
 (5.6)

where $i \in [1, N]$ and $j \in [1, M]$, N and M are the number of gradient directions used in the DTI experiment and the number of diffusion model parameters respectively. In matrix form, the sensitivity matrix can be defined as,

$$\boldsymbol{X} = \begin{bmatrix} \frac{\partial E(\boldsymbol{\beta}; \boldsymbol{g}_{1}; b)}{\partial \beta_{1}} & \frac{\partial E(\boldsymbol{\beta}; \boldsymbol{g}_{1}; b)}{\partial \beta_{2}} & \dots & \frac{\partial E(\boldsymbol{\beta}; \boldsymbol{g}_{1}; b)}{\partial \beta_{M}} \\ \frac{\partial E(\boldsymbol{\beta}; \boldsymbol{g}_{2}; b)}{\partial \beta_{1}} & \frac{\partial E(\boldsymbol{\beta}; \boldsymbol{g}_{2}; b)}{\partial \beta_{2}} & \dots & \frac{\partial E(\boldsymbol{\beta}; \boldsymbol{g}_{2}; b)}{\partial \beta_{M}} \\ \dots & \dots & \dots & \dots \\ \frac{\partial E(\boldsymbol{\beta}; \boldsymbol{g}_{N}; b)}{\partial \beta_{1}} & \frac{\partial E(\boldsymbol{\beta}; \boldsymbol{g}_{N}; b)}{\partial \beta_{2}} & \dots & \frac{\partial E(\boldsymbol{\beta}; \boldsymbol{g}_{N}; b)}{\partial \beta_{M}} \end{bmatrix}$$
(5.7)

Sensitivity matrices are critical to the definition of CRLB since it links the covariance bound to the sensitivities of the signal with respect to different model parameters. Although sensitivity matrix depend exclusively on the signal model, but, as will be shown later, modified sensitivity matrices for Rician noise case would also depend on the noise variance. In later sections, the detailed formulation for the sensitivity matrix for ADTI and DTI model is given. For signal models with simple analytical expressions, such as ADTI and DTI, the sensitivity matrices are computed analytically. Otherwise, the sensitivities can be calculated numerically.

5.1.3 Noise models

MRI images are reconstructed from the complex k-space data by taking the magnitude of the Fourier inverse of the k-space data. Assuming that both the real and imaginary part of the Fourier inverse data contain Gaussian noise, the noise in the magnitude images is Rician in nature. Thus, if x is the noisy signal following Rician pdf, then $x = ||x_c||$ (magnitude of the complex signal, x_c), where $x_c = m + n_r + jn_i$ and m is the magnitude of the complex signal without noise and n_r and n_i are Gaussian noise signals with zero mean and σ^2 variance. Through a rotation of the quadrature detector [110], all the signal intensity is shifted to the real component of the complex signal. Thus, the imaginary

component of the signal is only noise, n_i , and has a zero mean and σ^2 variance. The Rician pdf is given by [111, 112],

$$p(x|m,\sigma) = \frac{x}{\sigma^2} \exp(-\frac{x^2 + m^2}{2\sigma^2}) I_0(\frac{xm}{\sigma^2})$$
 (5.8)

where x is the random variable following the Rician pdf which is defined by the two parameters, the magnitude (m) and variance (σ^2) . I_0 is the zero order modified Bessel function of the first kind. Note that x, m and σ are strictly non-negative. An important observation regarding the Rician pdf is that the mean and the variance of the Rician pdf depend on both the m and σ parameters, as given by,

Mean
$$(x) = \sigma \sqrt{\frac{\pi}{2}} L_{1/2}(\frac{-m^2}{2\sigma^2})$$
 (5.9)

$$Var(x) = 2\sigma^2 + m^2 - \frac{\pi\sigma^2}{2} L_{1/2}^2(\frac{-m^2}{2\sigma^2})$$
 (5.10)

where L is the Laguerre polynomial. $L_{1/2}$ can be written in terms of the modified Bessel functions as,

$$L_{1/2}(x) = \exp(\frac{x}{2})[(1-x)I_0(\frac{-x}{2}) - xI_1(\frac{-x}{2})]$$
(5.11)

where I_0 and I_1 are the modified Bessel functions of the zero and first order respectively. There are two important approximations to the Rician pdf which depend on the SNR. At very low SNR (when $m \sim 0$), the Rician pdf reduces to Rayleigh distribution which is given by,

$$p(x|\sigma) = \frac{x}{\sigma^2} \exp(\frac{-x^2}{2\sigma^2})$$
 (5.12)

On the other hand, at high SNR $((m/\sigma) > 5)$ [113, 114], the noise tends to be more Gaussian (Fig. 5.1) following the pdf given by,

$$p(x|m,\sigma) = \frac{1}{\sqrt{2\pi\sigma^2}} \exp(-\frac{(x-m)^2}{2\sigma^2})$$
 (5.13)

Fig. 5.1 shows different Rician pdf when m and σ are varied. It is interesting to observe the non-central nature of the Rician pdf. The pdf becomes more Gaussian as the signal level (m) increases or the noise level (σ) decreases. From these plots, it can be observed that when a Gaussian pdf is assumed at low SNR instead of the Rician pdf, the mean value of the pdf is affected and this shows as a bias in the estimated parameters of the pdf.

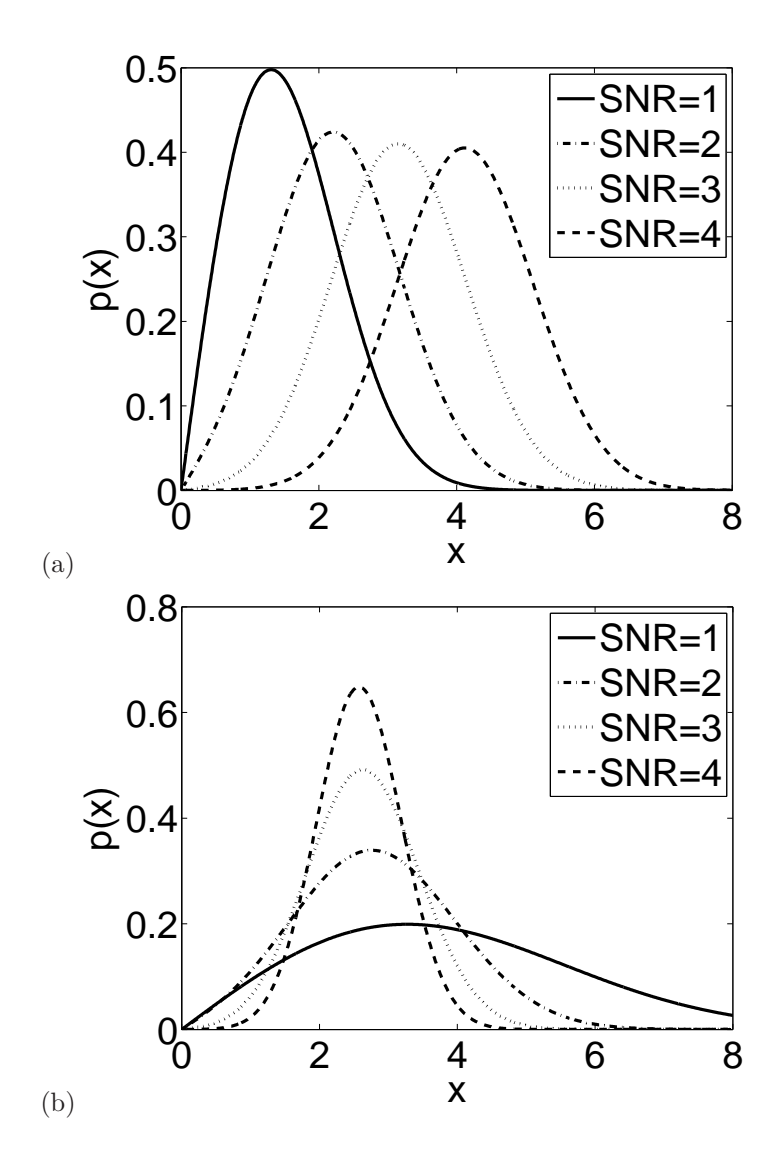


Figure 5.1. Rician distribution at different SNRs (SNR = m/σ). Distribution are generated by (a) varying m and fixing σ at 1.0 and (b) varying σ and fixing m at 2.5.

5.1.4 Choice of estimators for different noise models

The selection of estimator for the parameter estimation largely depends on the amount of information available about the estimation problem. In case when the noise model is not known, a least-squares estimator is preferred. For a non-linear signal model, a non-linear least-squares estimator can be used for estimation such as least-squares estimator based on the Levenberg-Marquardt (LM) algorithm [115, 116].

In this work, both the Rician and the Gaussian noise cases have been considered. For the Gaussian noise case (which is generally assumed in absence of any noise information), a least-squares estimator (LS) based on the LM algorithm is used. Since for the Rician case the parameter estimates are biased due to the non-linear nature in which Rician noise is injected into the signal, two methodologies were followed. From previous works such as Henkelman [110], Gudbjartsson, Patz [113], Koay, Basser [114], a correction scheme has been suggested to remove the bias in the estimation. For the first method, a correction scheme suggested by Gudbjartsson, Patz [113] is used since the assumption is that the data SNR are high enough (SNR>3) to assume a Gaussian noise. So, the correction fixes the bias only and does not affect the variance of the estimates. This estimator will be called least-squares with correction (LSC). The second methodology is based on probabilistic methods and the maximum likelihood estimator (MLE) for the Rician noise model is used. Such estimators have been discuss previously by Sijbers et. al. [117] and these require the knowledge of the noise model explicitly. The advantage of using MLE is that there is no need to apply any bias correction to the data since the correction is inherent in the estimator.

5.1.5 Relation with FA, MD and α

The minimization of the determinant of CRLB provides an optimized gradient scheme with respect to the uncertainty in the estimation of diffusion model parameters. Since the diffusion model parameters are sometimes not the quantities of interest, it would be important to find the relation of the performance of the schemes (in terms of CRLB) with clinical biomarkers used for the identification of diseases, such as FA, MD and the fiber angular deviation (α). FA and MD are functions of only the longitudinal and transverse diffusivities in the diffusion model. FA is a dimensionless, normalized quantity that indicates the local anisotropy in the imaging target [13]. MD, on the other hand, is the mean of the diffusivities (trace of the diffusion tensor divided by 3). Finally, the angular deviation is the deviation from the mean fiber orientation. This is a single quantity that represents the angular position of the fiber in the voxel with respect to the mean fiber orientation, instead of the two fiber direction parameters (θ_F, ϕ_F). FA, MD and the angular deviation are quantities that can be interpreted more easily in a pathological condition than the diffusion model parameters.

In this section, the relationship of the performance of the diffusion gradient scheme with the variances of FA, MD and angular deviation is studied. For the DTI model, MD is defined as

$$MD = \frac{D_{\parallel} + D_{\perp 1} + D_{\perp 2}}{3} = D_{av}$$
 (5.14)

and FA is defined as [13],

$$FA = \sqrt{\frac{3(D_{\parallel} - D_{av})^2 + (D_{\perp 1} - D_{av})^2 + (D_{\perp 2} - D_{av})^2}{D_{\parallel}^2 + D_{\perp 1}^2 + D_{\perp 2}^2}}$$
(5.15)

where D_{\parallel} , $D_{\perp 1}$ and $D_{\perp 2}$ are the eigenvalues of the diffusion tensor, \mathbf{D} . By convention, D_{\parallel} is the diffusivity along the fiber orientation and $D_{\perp 1}$ and $D_{\perp 2}$ are the transverse diffusivities. For the ADTI model, the expressions for FA and MD are simplified by setting $D_{\perp 1} = D_{\perp 2} = D_{\perp}$, as given by

$$FA = \frac{D_{\parallel} - D_{\perp}}{\sqrt{D_{\parallel}^2 + 2D_{\perp}^2}} \tag{5.16}$$

and

$$MD = \frac{D_{\parallel} + 2D_{\perp}}{3} = D_{av} \tag{5.17}$$

The angular deviation (α) is defined as

$$\alpha = \cos^{-1}(\mathbf{f} \cdot \mathbf{f}_0) \tag{5.18}$$

where f represents the voxel fiber direction unit vector and f_0 is the mean fiber direction unit vector defined as the average fiber orientation in voxels in the region of interest. Fiber direction is the direction of the principal eigenvector of the diffusion tensor matrix, D. The dot operation (\cdot) represents the scalar product.

The propagation of uncertainty principle is used to find the variance of FA, MD and α in terms of the variance bounds from the CRLB matrix. Assuming each metric, f (FA or MD) is expanded by Taylor series expansion upto first order, for the DTI model, the expansion is given by,

$$f \approx f_0 + D_{\parallel} \frac{\partial f}{\partial D_{\parallel}} + D_{\perp 1} \frac{\partial f}{\partial D_{\perp 1}} + D_{\perp 2} \frac{\partial f}{\partial D_{\perp 2}}$$
 (5.19)

Thus.

$$\sigma_{f}^{2} \geq \sigma_{D_{\parallel}}^{2} \left(\frac{\partial f}{\partial D_{\parallel}}\right)^{2} + \sigma_{D_{\perp 1}}^{2} \left(\frac{\partial f}{\partial D_{\perp 1}}\right)^{2} + \sigma_{D_{\perp 2}}^{2} \left(\frac{\partial f}{\partial D_{\perp 2}}\right)^{2} + 2 cov(D_{\parallel}, D_{\perp 1}) \frac{\partial f}{\partial D_{\parallel}} \frac{\partial f}{\partial D_{\perp 1}} + 2 cov(D_{\parallel}, D_{\perp 2}) \frac{\partial f}{\partial D_{\perp 1}} \frac{\partial f}{\partial D_{\perp 2}} + 2 cov(D_{\parallel}, D_{\perp 2}) \frac{\partial f}{\partial D_{\parallel}} \frac{\partial f}{\partial D_{\perp 2}}$$

$$(5.20)$$

where cov() is the covariance function.

For FA, the variance can be computed from Eqs. 5.15 and 5.20. The following can be computed easily from the FA definition (Eq. 5.15),

$$\frac{\partial FA}{\partial D_{\parallel}} = (2 A - B - C - 2 D_{\parallel} FA^{2})/(2 SS FA)$$
 (5.21)

$$\frac{\partial FA}{\partial D_{\perp 1}} = (2 B - A - C - 2 D_{\perp 1} FA^2)/(2 SS FA)$$
 (5.22)

$$\frac{\partial FA}{\partial D_{\perp 2}} = (2 C - B - Q - 2 D_{\perp 2} FA^2)/(2 SS FA)$$
 (5.23)

where

$$A = D_{\parallel} - D_{av}$$

$$B = D_{\perp 1} - D_{av}$$

$$C = D_{\perp 2} - D_{av}$$

$$SS = D_{\parallel}^2 + D_{\perp 1}^2 + D_{\perp 2}^2$$
(5.24)

For MD, the expressions are simpler than that of FA as shown below (Eq. 5.14).

$$\frac{\partial MD}{\partial D_{\parallel}} = \frac{\partial MD}{\partial D_{\perp 1}} = \frac{\partial MD}{\partial D_{\perp 2}} = \frac{1}{3}$$
 (5.25)

For variance of angular deviation, the first-order Taylor series approximation is given by

$$\sigma_{\alpha}^{2} \ge \sigma_{\theta_{F}}^{2} \left(\frac{\partial \alpha}{\partial \theta_{F}}\right)^{2} + \sigma_{\phi_{F}}^{2} \left(\frac{\partial \alpha}{\partial \phi_{F}}\right)^{2} \tag{5.26}$$

where

$$\frac{\partial \alpha}{\partial \theta_F} = -\frac{\cos(\phi_F)\cos(\theta_F)}{\sqrt{1 - (\cos(\phi_F)\sin(\theta_F))^2}} \tag{5.27}$$

and

$$\frac{\partial \alpha}{\partial \phi_F} = \frac{\sin(\phi_F)\sin(\theta_F)}{\sqrt{1 - (\cos(\phi_F)\sin(\theta_F))^2}}$$
 (5.28)

This is assuming that the covariance between θ_F and ϕ_F is zero. Note that the expression for the variance is the same for DTI and ADTI model, since α only depends on the θ_F , ϕ_F parameters (in \mathbf{f}) and \mathbf{f}_0 does not depend on the model.

The variances and covariances of the diffusion parameters are replaced by the bounds obtained from the CRLB of the variance of the parameters. For DTI, the model parameters are $\beta = \{D_{\parallel}, D_{\perp 1}, D_{\perp 2}, \theta_F, \phi_F, \psi_F\}$. The CRLB matrix can be decomposed into diagonal and off-diagonal matrices as follows,

$$\Sigma_{CR} = \Sigma_1 + \Sigma_2 + \Sigma_3 \tag{5.29}$$

where,

$$\Sigma_{1} = \begin{bmatrix} \sigma_{D_{\parallel}}^{2} & 0 & 0 & 0 & 0 & 0 \\ 0 & \sigma_{D_{\perp 1}}^{2} & 0 & 0 & 0 & 0 \\ 0 & 0 & \sigma_{D_{\perp 2}}^{2} & 0 & 0 & 0 \\ 0 & 0 & 0 & \sigma_{\theta_{F}}^{2} & 0 & 0 \\ 0 & 0 & 0 & 0 & \sigma_{\phi_{F}}^{2} & 0 \\ 0 & 0 & 0 & 0 & 0 & \sigma_{\psi_{F}}^{2} \end{bmatrix}$$

$$(5.30)$$

and

$$\Sigma_{2} = \begin{bmatrix} 0 & cov(D_{\parallel}, D_{\perp 1}) & cov(D_{\parallel}, D_{\perp 2}) & cov(D_{\parallel}, \theta_{F}) & cov(D_{\parallel}, \phi_{F}) & cov(D_{\parallel}, \psi_{F}) \\ 0 & 0 & cov(D_{\perp 1}, D_{\perp 2}) & cov(D_{\perp 1}, \theta_{F}) & cov(D_{\perp 1}, \phi_{F}) & cov(D_{\perp 1}, \psi_{F}) \\ 0 & 0 & 0 & cov(D_{\perp 2}, \theta_{F}) & cov(D_{\perp 2}, \phi_{F}) & cov(D_{\perp 2}, \psi_{F}) \\ 0 & 0 & 0 & 0 & cov(\theta_{F}, \phi_{F}) & cov(\theta_{F}, \psi_{F}) \\ 0 & 0 & 0 & 0 & 0 & cov(\phi_{F}, \psi_{F}) \\ 0 & 0 & 0 & 0 & 0 & 0 \end{bmatrix}$$

$$(5.31)$$

and $\Sigma_3 = \Sigma_2^T$, where T is the transpose operation.

Thus, the variance bounds of the estimates are computed from CRLB, Σ_{CR} , as follows:

$$\begin{split} \sigma_{D_{\parallel}}^2 &= \Sigma_{CR}[1,1]; \sigma_{D_{\perp 1}}^2 = \Sigma_{CR}[2,2]; \sigma_{D_{\perp 2}}^2 = \Sigma_{CR}[3,3] \\ &cov(D_{\parallel},D_{\perp 1}) = \Sigma_{CR}[1,2] \\ &cov(D_{\perp 1},D_{\perp 2}) = \Sigma_{CR}[2,3] \\ &cov(D_{\parallel},D_{\perp 2}) = \Sigma_{CR}[1,3] \end{split} \tag{5.32}$$

Also, the variance bounds of θ_F and ϕ_F are obtained as

$$\sigma_{\theta_F}^2 = \Sigma_{CR}[4, 4]; \sigma_{\phi_F}^2 = \Sigma_{CR}[5, 5]$$
 (5.33)

Similarly, for the ADTI model, the model parameters $\beta = \{D_{\parallel}, D_{\perp}, \theta_F, \phi_F\}$. The Σ_{CR} can also be written in expanded matrix form as

$$\Sigma_{CR} = \Sigma_1 + \Sigma_2 + \Sigma_3 \tag{5.34}$$

where

$$\Sigma_{1} = \begin{bmatrix} \sigma_{D_{\parallel}}^{2} & 0 & 0 & 0 \\ 0 & \sigma_{D_{\perp}}^{2} & 0 & 0 \\ 0 & 0 & \sigma_{\theta_{F}}^{2} & 0 \\ 0 & 0 & 0 & \sigma_{\phi_{F}}^{2} \end{bmatrix}$$

$$(5.35)$$

and

$$\Sigma_{2} = \begin{bmatrix} 0 & cov(D_{\parallel}, D_{\perp}) & cov(D_{\parallel}, \theta_{F}) & cov(D_{\parallel}, \phi_{F}) \\ 0 & 0 & cov(D_{\perp}, \theta_{F}) & cov(D_{\perp}, \phi_{F}) \\ 0 & 0 & 0 & cov(\theta_{F}, \phi_{F}) \\ 0 & 0 & 0 & 0 \end{bmatrix}$$
(5.36)

and $\Sigma_3 = \Sigma_2^T$, where T is the transpose operation.

Thus, the variance bounds of the estimates are computed from CRLB, Σ_{CR} , as follows:

$$\sigma_{D_{\parallel}}^{2} = \Sigma_{CR}[1, 1]; \sigma_{D_{\perp}}^{2} = \Sigma_{CR}[2, 2]; cov(D_{\parallel}, D_{\perp}) = \Sigma_{CR}[1, 2]$$
 (5.37)

And, the variance bounds of θ_F and ϕ_F are obtained as,

$$\sigma_{\theta_F}^2 = \Sigma_{CR}[3,3]; \sigma_{\phi_F}^2 = \Sigma_{CR}[4,4]$$
 (5.38)

5.2 CRLB for different noise models

5.2.1 Rician noise case

In case of DTI data, the Rician noise model is incorporated as follows: the magnitude data is computed from the complex data

$$E_c = (E(\boldsymbol{\beta}; \boldsymbol{\alpha}) + n_r) + jn_i \tag{5.39}$$

where $E(\boldsymbol{\beta}; \boldsymbol{\alpha})$ is the modeled MR signal (real quantity), n_r, n_i are zero mean and σ^2 variance Gaussian distributions, $\boldsymbol{\beta}; \boldsymbol{\alpha}$ are the diffusion model parameters and experimental parameters respectively, as defined before. It should be noted that the complex signal

is rotated by a rotation of the quadrature detector towards the real axis [110, 114]. Hence, the imaginary component only contains the noise while the real component contains the signal and the noise. The measured signal is $\hat{E} = \parallel E_c \parallel$ which has a Rician pdf given by,

$$p(\hat{E}|E(\boldsymbol{\beta};\boldsymbol{\alpha}),\sigma^2) = \frac{\hat{E}}{\sigma^2} I_0(\frac{E\hat{E}}{\sigma^2}) \exp(-\frac{\hat{E}^2 + E^2}{2\sigma^2})$$
 (5.40)

When a set of N measurements is taken at different diffusion-encoding gradient directions (\boldsymbol{g} vectors), the measurement vector, $\hat{\boldsymbol{E}} = \{\hat{E}_i, i \in [1, N]\}$, follows a multivariate Rician distribution $p(\hat{\boldsymbol{E}}|\boldsymbol{\beta}; \boldsymbol{\alpha}) \sim R(\mu(\boldsymbol{\beta}; \boldsymbol{\alpha}), \mathbf{C}(\boldsymbol{\beta}; \boldsymbol{\alpha}))$ where $\mu(\boldsymbol{\beta}; \boldsymbol{\alpha})$ is the mean vector of expected value of the measured normalized MR signal, $\hat{\boldsymbol{E}}$, and $\mathbf{C}(\boldsymbol{\beta}; \boldsymbol{\alpha})$ is the covariance matrix of measurements.

The jkth element of the Fisher information matrix for Rician pdf [118] can be shown to be

$$[\mathbf{I}(\boldsymbol{\beta}, \boldsymbol{\alpha})]_{jk} = \sum_{i=1}^{N} \frac{1}{\sigma^4} \frac{\partial E_i}{\partial \beta_j} \frac{\partial E_i}{\partial \beta_k} (E_i^2 - Z_i)$$
 (5.41)

where

$$Z_{i} = \int_{0}^{\infty} E_{i}^{2} I_{1}^{2} \left(\frac{E_{i}\hat{E}}{\sigma^{2}}\right) I_{0}^{-2} \left(\frac{E_{i}\hat{E}}{\sigma^{2}}\right) p(\hat{E}) d\hat{E}$$
 (5.42)

and $p(\hat{E}) = p(\hat{E}|E, \sigma^2)$ (Rician pdf). I_0 and I_1 are the zero-order and first-order modified Bessel functions of the first kind respectively. Eq. 5.41 can be rewritten using $Z_i = W_i^2$,

$$[\mathbf{I}(\boldsymbol{\beta}, \boldsymbol{\alpha})]_{jk} = \sum_{i=1}^{N} \frac{1}{\sigma^4} \left\{ (E_i - W_i) \frac{\partial E_i}{\partial \beta_j} \right\} \left\{ (E_i + W_i) \frac{\partial E_i}{\partial \beta_k} \right\}$$
(5.43)

Since Z_i are all positive as seen in Eq. 5.42, W_i are all real-valued. Let X_1 and X_2 be the modified model sensitivity matrices and their ijth elements are defined as follows:

$$[\boldsymbol{X}_1]_{ij} := (E_i - W_i)\partial E_i/\partial \beta_j \tag{5.44}$$

$$[\mathbf{X}_2]_{ij} := (E_i + W_i)\partial E_i/\partial \beta_j \tag{5.45}$$

In matrix-expanded form, the modified sensitivity matrices can be written as,

$$\boldsymbol{X}_{1} = \begin{bmatrix} (E_{1} - W_{1})\partial E_{1}/\partial \beta_{1} & (E_{1} - W_{1})\partial E_{1}/\partial \beta_{2} & \dots & (E_{1} - W_{1})\partial E_{1}/\partial \beta_{M} \\ (E_{2} - W_{2})\partial E_{2}/\partial \beta_{1} & (E_{2} - W_{2})\partial E_{2}/\partial \beta_{2} & \dots & (E_{2} - W_{2})\partial E_{2}/\partial \beta_{M} \\ \dots & \dots & \dots & \dots \\ (E_{N} - W_{N})\partial E_{N}/\partial \beta_{1} & (E_{N} - W_{N})\partial E_{N}/\partial \beta_{2} & \dots & (E_{N} - W_{N})\partial E_{N}/\partial \beta_{M} \end{bmatrix}$$
(5.46)

and

$$\boldsymbol{X}_{2} = \begin{bmatrix} (E_{1} + W_{1})\partial E_{1}/\partial \beta_{1} & (E_{1} + W_{1})\partial E_{1}/\partial \beta_{2} & \dots & (E_{1} + W_{1})\partial E_{1}/\partial \beta_{M} \\ (E_{2} + W_{2})\partial E_{2}/\partial \beta_{1} & (E_{2} + W_{2})\partial E_{2}/\partial \beta_{2} & \dots & (E_{2} + W_{2})\partial E_{2}/\partial \beta_{M} \\ \dots & \dots & \dots & \dots \\ (E_{N} + W_{N})\partial E_{N}/\partial \beta_{1} & (E_{N} + W_{N})\partial E_{N}/\partial \beta_{2} & \dots & (E_{N} + W_{N})\partial E_{N}/\partial \beta_{M} \end{bmatrix}$$

$$(5.47)$$

 X_1 and X_2 are both $N \times M$ matrices and depend on β , Ω and the b-factor. $i \in [1, N]$ and $j \in [1, M]$. Also $E_i = E(\mathbf{g}_i; b; \boldsymbol{\beta})$ corresponds to the *i*th diffusion-weighted signal obtained using the diffusion gradient \mathbf{g}_i , b-factor and parameter set $\boldsymbol{\beta}$. In terms of the original sensitivity matrix (X), the modified sensitivity matrices can be written as,

$$X_1 = \mathbf{E}_1 X$$

$$X_2 = \mathbf{E}_2 X$$
(5.48)

where

$$\mathbf{E}_{1} = \begin{bmatrix} (E_{1} - W_{1}) & 0 & \dots & 0 \\ 0 & (E_{2} - W_{2}) & \dots & 0 \\ \dots & \dots & \dots & \dots \\ 0 & 0 & \dots & (E_{N} - W_{N}) \end{bmatrix}$$
(5.49)

and

$$\mathbf{E}_{2} = \begin{bmatrix} (E_{1} + W_{1}) & 0 & \dots & 0 \\ 0 & (E_{2} + W_{2}) & \dots & 0 \\ \dots & \dots & \dots & \dots \\ 0 & 0 & \dots & (E_{N} + W_{N}) \end{bmatrix}$$
 (5.50)

and

$$\boldsymbol{X} = \begin{bmatrix} \frac{\partial E_1}{\partial \beta_1} & \frac{\partial E_1}{\partial \beta_2} & \cdots & \frac{\partial E_1}{\partial \beta_M} \\ \frac{\partial E_2}{\partial \beta_1} & \frac{\partial E_2}{\partial \beta_2} & \cdots & \frac{\partial E_2}{\partial \beta_M} \\ \cdots & \cdots & \cdots & \cdots \\ \frac{\partial E_N}{\partial \beta_1} & \frac{\partial E_N}{\partial \beta_2} & \cdots & \frac{\partial E_N}{\partial \beta_M} \end{bmatrix}$$
(5.51)

Eq. 5.43 can be written as,

$$\mathbf{I}(\boldsymbol{\beta}, \boldsymbol{\alpha}) = \frac{1}{\sigma^4} (\boldsymbol{X}_1^{\mathrm{T}} \boldsymbol{X}_2) \tag{5.52}$$

Thus, the corresponding Rician CRLB in matrix form is given as,

$$\Sigma_{CR}(\boldsymbol{\beta}, \boldsymbol{\alpha}) = \mathbf{I}^{-1}(\boldsymbol{\beta}, \boldsymbol{\alpha}) = \sigma^4(\boldsymbol{X}_1^{\mathrm{T}} \boldsymbol{X}_2)^{-1}$$
(5.53)

Note that $(\mathbf{X}_1^{\mathrm{T}}\mathbf{X}_2)$ is an $M \times M$ matrix. Using the determinant identity, $\det(r\mathbf{Q}) = r^M \det(\mathbf{Q})$ and also $\det(\mathbf{Q}^{-1}) = 1/\det(\mathbf{Q})$ for an $M \times M$ matrix \mathbf{Q} and a scalar r, the

determinant of Eq. 5.53 gives,

$$\det \mathbf{\Sigma}_{CR} = \det \left(\sigma^4 (\mathbf{X}_1^T \mathbf{X}_2)^{-1} \right) = \frac{\sigma^{4M}}{\det \left(\mathbf{X}_1^T \mathbf{X}_2 \right)}$$
 (5.54)

5.2.2 Gaussian noise case at high SNR

At high SNR, the Gaussian approximation holds good. In such a case, an additive white Gaussian noise case with zero mean and σ^2 variance is considered. The observed signal can be expressed as,

$$\hat{E} = E(\boldsymbol{\beta}; \boldsymbol{\alpha}) + n \tag{5.55}$$

where n is zero mean and σ^2 variance Gaussian distribution and

$$p(\hat{E}|E(\boldsymbol{\beta};\boldsymbol{\alpha}),\sigma^2) = \frac{1}{\sqrt{2\pi\sigma^2}} \exp(-\frac{(\hat{E}-E)^2}{2\sigma^2})$$
 (5.56)

When a set of N measurements is taken at different diffusion-encoding gradient directions (\boldsymbol{g} vectors), the measurement vector, $\hat{\boldsymbol{E}} = \{\hat{E}_i, i \in [1, N]\}$, follows a multivariate Gaussian distribution $p(\hat{\boldsymbol{E}}|\boldsymbol{\beta};\boldsymbol{\alpha}) \sim N(\mu(\boldsymbol{\beta};\boldsymbol{\alpha}),\mathbf{C}(\boldsymbol{\beta};\boldsymbol{\alpha}))$ where $\mu(\boldsymbol{\beta};\boldsymbol{\alpha})$ is the mean vector of expected value of the measured normalized MR signal, $\hat{\boldsymbol{E}}$, and $\mathbf{C}(\boldsymbol{\beta};\boldsymbol{\alpha})$ is the covariance matrix of measurements.

For normally distributed measurements, $p(\hat{E}; \beta; \alpha)$ has a mean vector $\mu(\beta; \alpha)$ and covariance matrix $\sigma^2 I$. Since the measurements are uncorrelated and has the same variance, σ^2 , the covariance matrix is a diagonal matrix with σ^2 as the diagonal element. The jkth element of the Fisher information matrix can be computed by [109],

$$[\mathbf{I}(\boldsymbol{\beta}; \boldsymbol{\alpha})]_{jk} = \left[\frac{\partial \mu(\boldsymbol{\beta}; \boldsymbol{\alpha})}{\partial \beta_j}\right]^T \frac{1}{\sigma^2} I\left[\frac{\partial \mu(\boldsymbol{\beta}; \boldsymbol{\alpha})}{\partial \beta_k}\right]$$
(5.57)

where I is identity matrix of size $N \times N$, N being the number of DTI images acquired. T represents transpose operation. $j, k \in [1, M]$ where M is the number of diffusion model parameters (for example, M = 4 for ADTI).

Since the covariance bound is given by $\Sigma_{CR}(\boldsymbol{\beta}; \boldsymbol{\alpha}) = \mathbf{I}^{-1}(\boldsymbol{\beta}; \boldsymbol{\alpha})$ and simplifying Eq. 5.57 [109],

$$\Sigma_{CR} = \sigma^2 (\boldsymbol{X}^{\mathrm{T}} \boldsymbol{X})^{-1} \tag{5.58}$$

where X is called the model sensitivity matrix. Sensitivity matrix, X, are based on the partial derivatives of the model $E(\boldsymbol{\beta}; \boldsymbol{\alpha})$ w.r.t. the parameters: $\eta_j(\boldsymbol{\beta}; \boldsymbol{\alpha}) := \partial E(\boldsymbol{\beta}; \boldsymbol{\alpha}) / \partial \beta_j$ with $j \in [1, M]$.

For N diffusion-encoding gradient directions used during DTI experiment, a sequence of N diffusion-encoded images is collected. The sensitivity matrix $\mathbf{X} \in \mathbb{R}^{N \times M}$ is defined as $\mathbf{X}(\boldsymbol{\beta}; \boldsymbol{\alpha}) := (X_{i,j})_{N \times M}$ where $X_{i,j} := \eta_j(\boldsymbol{g}_i; b; \boldsymbol{\beta})$ [119].

From Eq. 5.58, applying determinant operation on both sides of the equations,

$$\det \Sigma_{CR} = \frac{\sigma^{2M}}{\det (\mathbf{X}^{\mathrm{T}} \mathbf{X})}$$
 (5.59)

5.2.3 Interpretation of CRLB

The determinant of CRLB (Σ_{CR}) corresponds to the product of the variance bounds of the estimated parameters, assuming the parameters to be orthogonal to each other. It is proportional to the bound on the hypervolume of uncertainty in the estimation of β parameters, the hypervolume being defined as the product of the standard deviations of the estimated parameters. The lower the hypervolume, the smaller will be the overall uncertainty of estimation. From Eq. 5.54, it can be observed that the cost function is a function of both experimental noise (σ) and the model sensitivity matrices (X_1 and X_2). For the Gaussian case (Eq. 5.59), the relation between the sensitivity matrix and noise variance is decoupled [119]. However, this is not the case for the Rician noise model (Eq. 5.54) since the modified sensitivity matrices (X_1 and X_2) depend on σ^2 also.

The model sensitivity matrices are functions of the gradient scheme (Ω) , the b-factor and the estimation parameter set (β) . Thus, in order to reduce the determinant of Σ_{CR} by optimizing the gradient scheme (Ω) only, the gradient scheme should be chosen to maximize the determinant of $X_1^T X_2$ (or minimize $1/\det(X_1^T X_2)$), assuming a fixed σ , thereby creating an experimental design for which the bound of the hypervolume of uncertainty $(\sqrt{\det \Sigma_{CR}})$ is minimized. If a bound on uncertainty can be optimized by design, then any minimum variance unbiased (MVU) and efficient estimator [109] can be shown to attain the bound asymptotically while performing the parameter estimation. Such a determinant-optimal or simply D-optimal [33, 34] experimental design forms the

basis for designing optimal ADTI experiments in this work.

5.2.4 Sensitivity matrix computation

The definition of the CRLB involves the sensitivity matrix which is the Jacobian matrix of the signal with respect to the model parameters at different gradient directions. The following show the derivation for the sensitivity matrix for the ADTI and DTI model.

ADTI model

The expression for the normalized MR signal, E, for the ADTI model can be written as,

$$E = \exp(-b(g_{\parallel}^2 D_{\parallel} + g_{\perp}^2 D_{\perp}))$$
 (5.60)

where $g_{\parallel} = \boldsymbol{g} \cdot \boldsymbol{f}$ and \boldsymbol{f} is the unit vector along the fiber direction defined in spherical coordinates $(\theta_{\rm F}, \phi_{\rm F})$. Also, $g_{\perp}^2 = 1 - g_{\parallel}^2$. The ADTI diffusion model parameter set, $\boldsymbol{\beta} = \{D_{\parallel}, D_{\perp}, \theta_F, \phi_F\}$.

A row of the sensitivity matrix, X, is defined as,

$$[\mathbf{X}]_{i.} = \begin{bmatrix} \frac{\partial E_i}{\partial D_{\parallel}} & \frac{\partial E_i}{\partial D_{\perp}} & \frac{\partial E_i}{\partial \theta_F} & \frac{\partial E_i}{\sin(\theta_F)\partial\phi_F} \end{bmatrix}$$
(5.61)

Using Eq. 5.60 and 5.61,

$$\frac{\partial E}{\partial D_{\parallel}} = -bg_{\parallel}^2 E \tag{5.62}$$

$$\frac{\partial E}{\partial D_{\perp}} = -bg_{\perp}^2 E \tag{5.63}$$

$$\frac{\partial E}{\partial \theta_F} = -bE(2g_{\parallel})(D_{\parallel} - D_{\perp})(\sin(\theta)\cos(\theta_F)\cos(\phi - \phi_F) - \cos(\theta)\sin(\theta_F)) \quad (5.64)$$

$$\frac{\partial E}{\sin(\theta_F)\partial\phi_F} = -bE(2g_{\parallel})(D_{\parallel} - D_{\perp})(\sin(\theta)\sin(\phi - \phi_F))$$
(5.65)

where θ, ϕ are the spherical coordinate angles for the gradient direction ($g \equiv \{\theta, \phi\}$). To account for the curvature of the spherical coordinate system, the partial derivative w.r.t. ϕ_F is divided by $\sin(\theta_F)$. Since the *b*-factor is fixed, the gradients are sampled on a sphere of constant radius. These analytical expressions provide considerable insight into the sensitivity of the MR signal w.r.t. to the diffusion model parameters. The first

observation is that all the sensitivities (derivatives) are weighted by the signal and the b-factor. Thus, gradients sampling the regions of high signal or where high b-factor is used will always provide better estimates of the parameters. However, high b-factor causes the signal to reduce due to more signal attenuation. Hence, there has to be a compromise solution between the choice of signal level and the b-factor. Next, for the diffusivities, the sensitivities are proportional to the projections of the gradient direction vector onto the fiber direction, i.e., g_{\parallel} and g_{\perp} . Thus, the sampling locations selected along the longitudinal direction will lead to a more sensitive estimation of D_{\parallel} and the ones along the transverse direction lead to a more sensitive estimation of D_{\perp} . For the angular parameters, the interpretation is not direct. Apart from signal and b-factor, the sensitivities w.r.t. angular parameters are also proportional to the difference of the diffusivities $(D_{\parallel} - D_{\perp})$, which is indicative of the local diffusion anisotropy.

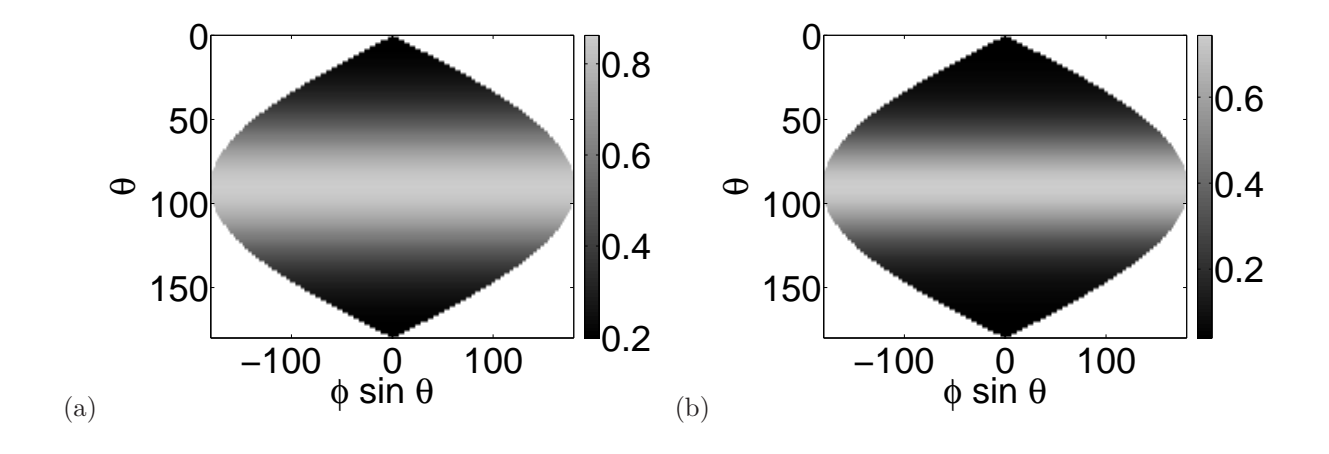


Figure 5.2. Plot of (a) the normalized MR signal and (b) its square for the ADTI model with respect to the gradient direction angles (θ, ϕ) with the mean fiber direction is at $(\theta_F, \phi_F) = (0^{\circ}, 0^{\circ})$. The gray scale represents the corresponding signal value.

Figs. 5.2 and 5.3 show the variation of the normalized MR signal and the sensitivities (and squares) with changing gradient directions (given by θ , ϕ). The following model parameters are used to generate the sensitivity and normalized MR plots: $D_{\parallel}=1.62\times 10^{-3}~\mathrm{mm^2~s^{-1}},\ D_{\perp}=0.148\times 10^{-3}~\mathrm{mm^2~s^{-1}},\ \theta_F=0^{\circ},\ \phi_F=0^{\circ},\ \sigma=0.1$ (FA = 0.9, MD = 0.638 × 10⁻³ mm² s⁻¹), $b=1000~\mathrm{s~mm^{-2}}$. The axisymmetric nature of the signal model shows up nicely on the plot for MR signal. The axisymmetry is also observed in the sensitivities w.r.t. D_{\parallel} and D_{\perp} , but not in the sensitivity for angular

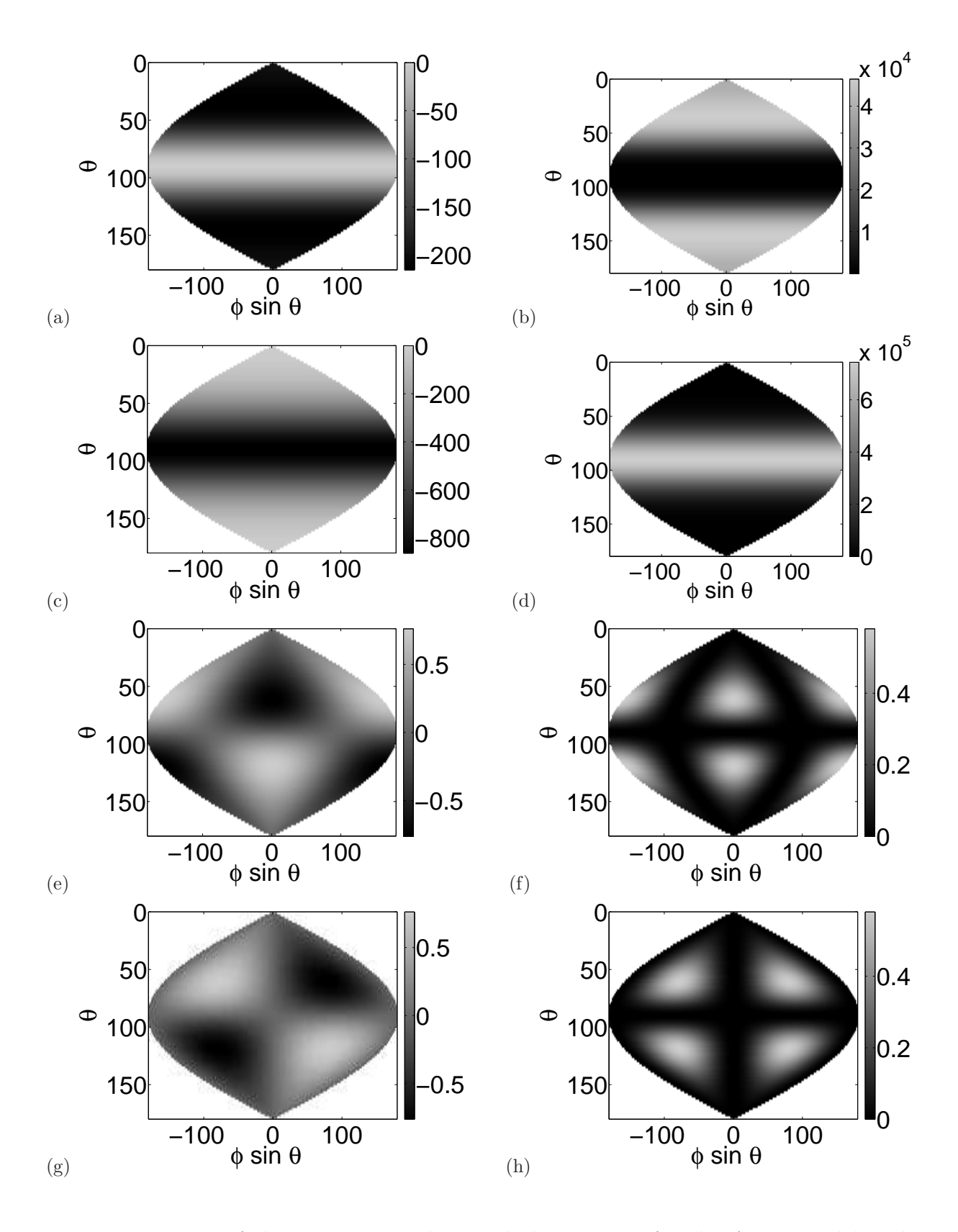


Figure 5.3. Plot of the sensitivity values and their square for the ADTI model with respect to gradient direction angles (θ, ϕ) . Shown in the figure are sensitivity values and their squares w.r.t. D_{\parallel} ((a) and (b)), D_{\perp} ((c) and (d)), θ_F ((e) and (f)) and ϕ_F ((g) and (h)). The mean fiber direction is at $(\theta_F, \phi_F) = (0^{\circ}, 0^{\circ})$. The gray scale represents the corresponding sensitivity values or its square.

parameters. The squares of the sensitivities are also shown to demonstrate the model axisymmetry and also since the definition of CRLB uses the square of the sensitivity matrices (i.e., $\mathbf{X}_1^T \mathbf{X}_2$ for Rician case and $\mathbf{X}^T \mathbf{X}$ for Gaussian case), the square of the sensitivity determines the optimized gradient distribution based on the CRLB.

DTI model

In this section, the sensitivity matrix computation is shown for the general 6-parameter non-axisymmetric DTI or simply DTI case. Here, $\beta = \{D_{\parallel}, D_{\perp 1}, D_{\perp 2}, \theta_F, \phi_F, \psi_F\}$ and number of estimation parameters (M) is 6. The normalized MR signal, E, is represented in terms of the diffusion model and experimental parameters as

$$E = e^{-bg^T \mathbf{R}^T \mathbf{D}_0 \mathbf{R}g} ag{5.66}$$

The DTI model sensitivity matrix is composed of partial derivatives of the signal with respect to parameters. A row of the sensitivity matrix, X, is given by,

$$[\mathbf{X}]_{i.} = \begin{bmatrix} \frac{\partial E_i}{\partial D_{\parallel}} & \frac{\partial E_i}{\partial D_{\perp 1}} & \frac{\partial E_i}{\partial D_{\perp 2}} & \frac{\partial E_i}{\partial \theta_F} & \frac{\partial E_i}{\sin(\theta_F)\partial\phi_F} & \frac{\partial E_i}{\partial\psi_F} \end{bmatrix}$$
(5.67)

The partial derivatives are analytically computed using signal equation Eq. 5.66 as follows:

$$\frac{\partial E}{\partial D_{\parallel}} = -bE\boldsymbol{g}^T \boldsymbol{R}^T \frac{\partial \boldsymbol{D}_0}{\partial D_{\parallel}} \boldsymbol{R} \boldsymbol{g}$$
 (5.68)

where

$$\frac{\partial \mathbf{D}_0}{\partial D_{\parallel}} = \begin{bmatrix} 0 & 0 & 0 \\ 0 & 0 & 0 \\ 0 & 0 & 1 \end{bmatrix} \tag{5.69}$$

This follows from the definition of the signal model (Eq. 5.66) and that \mathbf{D}_0 is only dependent on the diffusivities $(D_{\parallel}, D_{\perp 1}, D_{\perp 2})$. Similarly,

$$\frac{\partial E}{\partial D_{\perp 1}} = -bE \boldsymbol{g}^T \boldsymbol{R}^T \frac{\partial \boldsymbol{D}_0}{\partial D_{\perp 1}} \boldsymbol{R} \boldsymbol{g}$$
 (5.70)

where

$$\frac{\partial \mathbf{D}_0}{\partial D_{\perp 1}} = \begin{bmatrix} 0 & 0 & 0 \\ 0 & 1 & 0 \\ 0 & 0 & 0 \end{bmatrix} \tag{5.71}$$

$$\frac{\partial E}{\partial D_{\perp 2}} = -bE \boldsymbol{g}^T \boldsymbol{R}^T \frac{\partial \boldsymbol{D}_0}{\partial D_{\perp 2}} \boldsymbol{R} \boldsymbol{g}$$
 (5.72)

where

$$\frac{\partial \mathbf{D}_0}{\partial D_{\perp 2}} = \begin{bmatrix} 1 & 0 & 0 \\ 0 & 0 & 0 \\ 0 & 0 & 0 \end{bmatrix} \tag{5.73}$$

For the partial derivatives with respect to Euler angle parameters $(\theta_F, \phi_F, \psi_F)$, the chain rule for the derivatives is applied as follows:

$$\frac{\partial E}{\partial \theta_F} = -bE \boldsymbol{g}^T \left(\frac{\partial \boldsymbol{R}}{\partial \theta_F}^T \boldsymbol{D}_0 \boldsymbol{R} + \boldsymbol{R}^T \boldsymbol{D}_0 \frac{\partial \boldsymbol{R}}{\partial \theta_F} \right) \boldsymbol{g}$$
 (5.74)

where

$$\frac{\partial \mathbf{R}}{\partial \theta_F} = R_z(\psi_F) \frac{\partial R_y(\theta_F)}{\partial \theta_F} R_z(\phi_F)$$
(5.75)

and

$$\frac{\partial R_y(\theta_F)}{\partial \theta_F} = \begin{bmatrix}
-\sin(\theta_F) & 0 & -\cos(\theta_F) \\
0 & 0 & 0 \\
\cos(\theta_F) & 0 & -\sin(\theta_F)
\end{bmatrix}$$
(5.76)

For computing the partial derivative with respect to ϕ_F , the reduction in the latitudinal distance of the sphere due to the curvature has to be considered. Thus, an additional $\sin(\theta_F)$ must be divided as shown:

$$\frac{\partial E}{\sin(\theta_F)\partial\phi_F} = \frac{-bE}{\sin(\theta_F)} \boldsymbol{g}^T \left(\frac{\partial \boldsymbol{R}}{\partial\phi_F}^T \boldsymbol{D}_0 \boldsymbol{R} + \boldsymbol{R}^T \boldsymbol{D}_0 \frac{\partial \boldsymbol{R}}{\partial\phi_F} \right) \boldsymbol{g}$$
(5.77)

where

$$\frac{\partial \mathbf{R}}{\partial \phi_F} = R_z(\psi_F) R_y(\theta_F) \frac{\partial R_z(\phi_F)}{\partial \phi_F}$$
(5.78)

and

$$\frac{\partial R_z(\phi_F)}{\partial \phi_F} = \begin{bmatrix} -\sin(\phi_F) & \cos(\phi_F) & 0\\ -\cos(\phi_F) & -\sin(\phi_F) & 0\\ 0 & 0 & 0 \end{bmatrix}$$
 (5.79)

Finally, the partial derivative computed with respect to ψ_F is as follows:

$$\frac{\partial E}{\partial \psi_F} = -bE \boldsymbol{g}^T \left(\frac{\partial \boldsymbol{R}}{\partial \psi_F}^T \boldsymbol{D} \boldsymbol{R} + \boldsymbol{R}^T \boldsymbol{D} \frac{\partial \boldsymbol{R}}{\partial \psi_F} \right) \boldsymbol{g}$$
 (5.80)

where

$$\frac{\partial \mathbf{R}}{\partial \psi_F} = \frac{\partial R_z(\psi_F)}{\partial \phi_F} R_y(\theta_F) R_z(\phi_F) \tag{5.81}$$

and

$$\frac{\partial R_z(\psi_F)}{\partial \psi_F} = \begin{bmatrix} -\sin(\psi_F) & \cos(\psi_F) & 0\\ -\cos(\psi_F) & -\sin(\psi_F) & 0\\ 0 & 0 & 0 \end{bmatrix}$$
 (5.82)

Since, by definition, ψ_F (the third Euler angle) is the angle that the x-axis of the rotated transverse diffusion plane makes with the line of nodes, this rotation is not on a spherical latitude and the division by $\sin(\theta_F)$ is not required.

Note that the earlier analysis of the ADTI case was performed at $\theta_F = 0^{\circ}$. But, this value cannot be used for the DTI case since at $\theta_F = 0^{\circ}$, ϕ_F and ψ_F are indistinguishable. Using the definition of rotation matrix (\mathbf{R}) above,

$$R_y(\theta_F) = I \tag{5.83}$$

$$\mathbf{R} = R_z(\psi_F) * R_y(\theta_F) * R_z(\phi_F) = R_z(\psi_F) * R_z(\phi_F) = R_z(\psi_F + \phi_F)$$
 (5.84)

where I represents the identity matrix of size 3×3 . The problem with the above condition is that the derivatives of E w.r.t. ϕ_F and ψ_F become equal and $\mathbf{X}^T\mathbf{X}$ has a rank less than M (number of parameters, ie, 6). From the definition of CRLB, the CRLB becomes indefinite. This problem can be solved by computing the derivatives at an angle other than $\theta_F = 0^\circ$, say $\theta_F = 90^\circ$.

The variation of the signal and the partial derivatives with respect to different DTI model parameters under an axisymmetric and non-axisymmetric condition are shown in Figs. 5.4 and 5.6 and their squares in Figs. 5.5 and 5.7 . The parameters values used to generate the sensitivities and the normalized MR signal for the axisymmetric case in Fig. 5.4 are: $D_{\parallel}=2\times10^{-3}~\mathrm{mm^2~s^{-1}},\ D_{\perp1}=0.2\times10^{-3}~\mathrm{mm^2~s^{-1}},\ D_{\perp2}=0.1999\times10^{-3}~\mathrm{mm^2~s^{-1}},\ \theta_F=90^\circ,\ \phi_F=0^\circ,\ \psi_F=0^\circ(\mathrm{FA}=0.891,\mathrm{MD}=0.8\times10^{-3}~\mathrm{mm^2~s^{-1}}),\ b=1000~\mathrm{s~mm^{-2}},\ N=30.$ For the non-axisymmetric case in Fig. 5.6, the parameter values used are: $D_{\parallel}=2\times10^{-3}~\mathrm{mm^2~s^{-1}},\ D_{\perp1}=0.2\times10^{-3}~\mathrm{mm^2~s^{-1}},\ D_{\perp2}=0.05\times10^{-3}~\mathrm{mm^2~s^{-1}},\ \theta_F=90^\circ,\ \phi_F=0^\circ,\ \psi_F=0^\circ(\mathrm{FA}=0.935,\mathrm{MD}=0.75\times10^{-3}~\mathrm{mm^2~s^{-1}}),\ b=1000~\mathrm{s~mm^{-2}},\ N=30.$ The axes of the plot represents the diffusion gradient direction in spherical coordinates, i.e., θ and ϕ on a unit sphere. For the nearly axisymmetric case, the plots look similar to the ADTI sensitivity plots.

This validates that the DTI formulation can incorporate the axisymmetric case also. Note that these cases are slightly non-axisymmetric (or nearly axisymmetric) so that the CRLB matrix is not singular. For a perfectly axisymmetric case, η_{ψ_F} will vanish making the CRLB matrix singular since its determinant will be zero. For the non-axisymmetric case, the normalized MR signal and the sensitivities w.r.t. to diffusivities are no longer axisymmetric as expected. Thus, the DTI formulation provides for a more general model although being more complicated than the ADTI formulation. Similar to the ADTI case, variation of the square of the sensitivities and the normalized MR signal can indicate how the final distribution of the optimized gradient distribution will be. CRLB is inversely proportional to the determinant of the square of the sensitivity matrix and thus optimal gradient directions will sample regions in the gradient space where the product of the sensitivities will be higher.

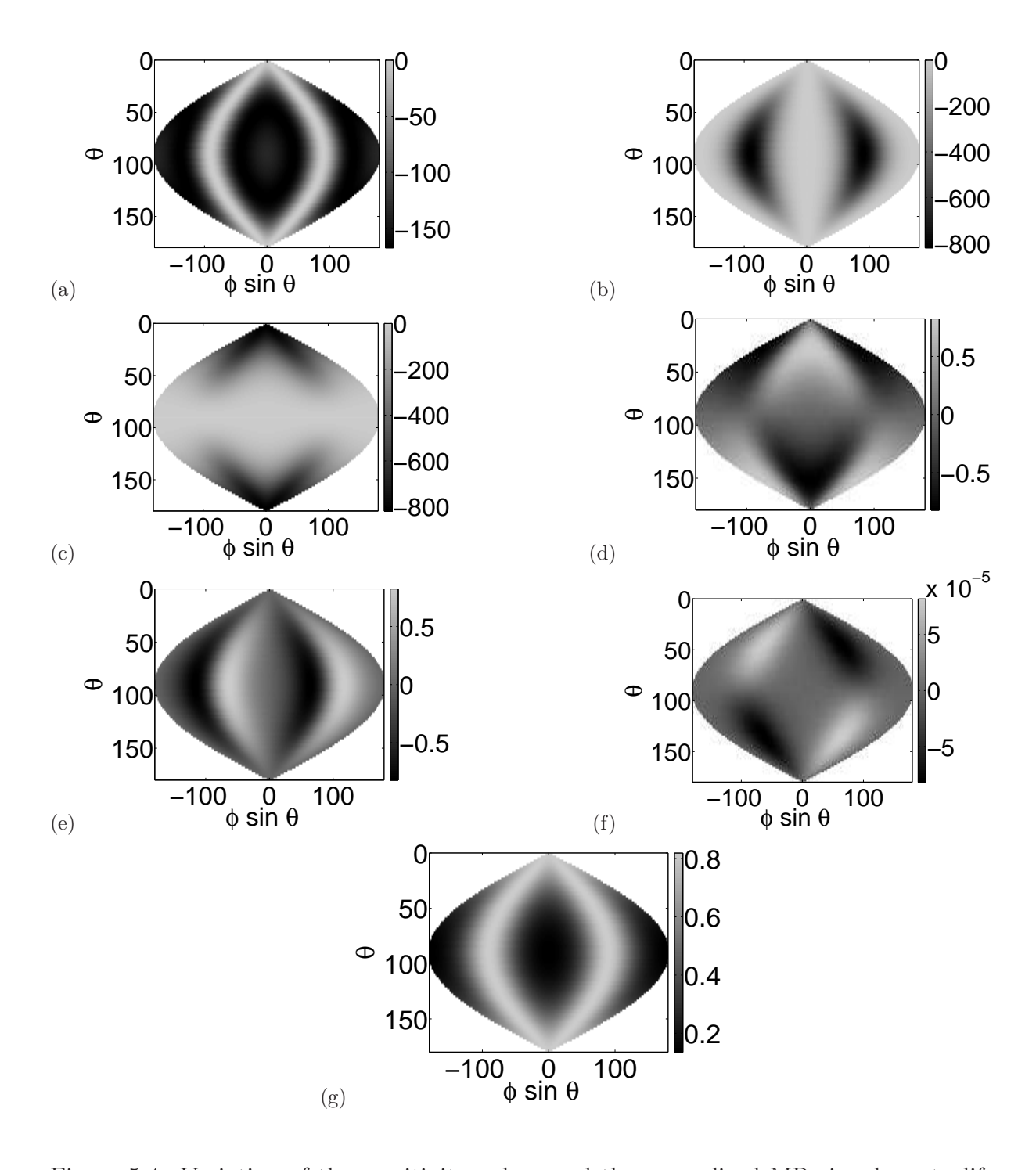


Figure 5.4. Variation of the sensitivity values and the normalized MR signal w.r.t. diffusion gradient direction angles (θ, ϕ) for nearly axisymmetric case for the DTI model. Shown in the figure are sensitivity values w.r.t. (a) D_{\parallel} , (b) $D_{\perp 1}$, (c) $D_{\perp 2}$, (d) θ_F , (e) ϕ_F , (f) ψ_F and (g) the normalized MR signal. The mean fiber direction is at $(\theta_F, \phi_F) = (90^{\circ}, 0^{\circ})$.

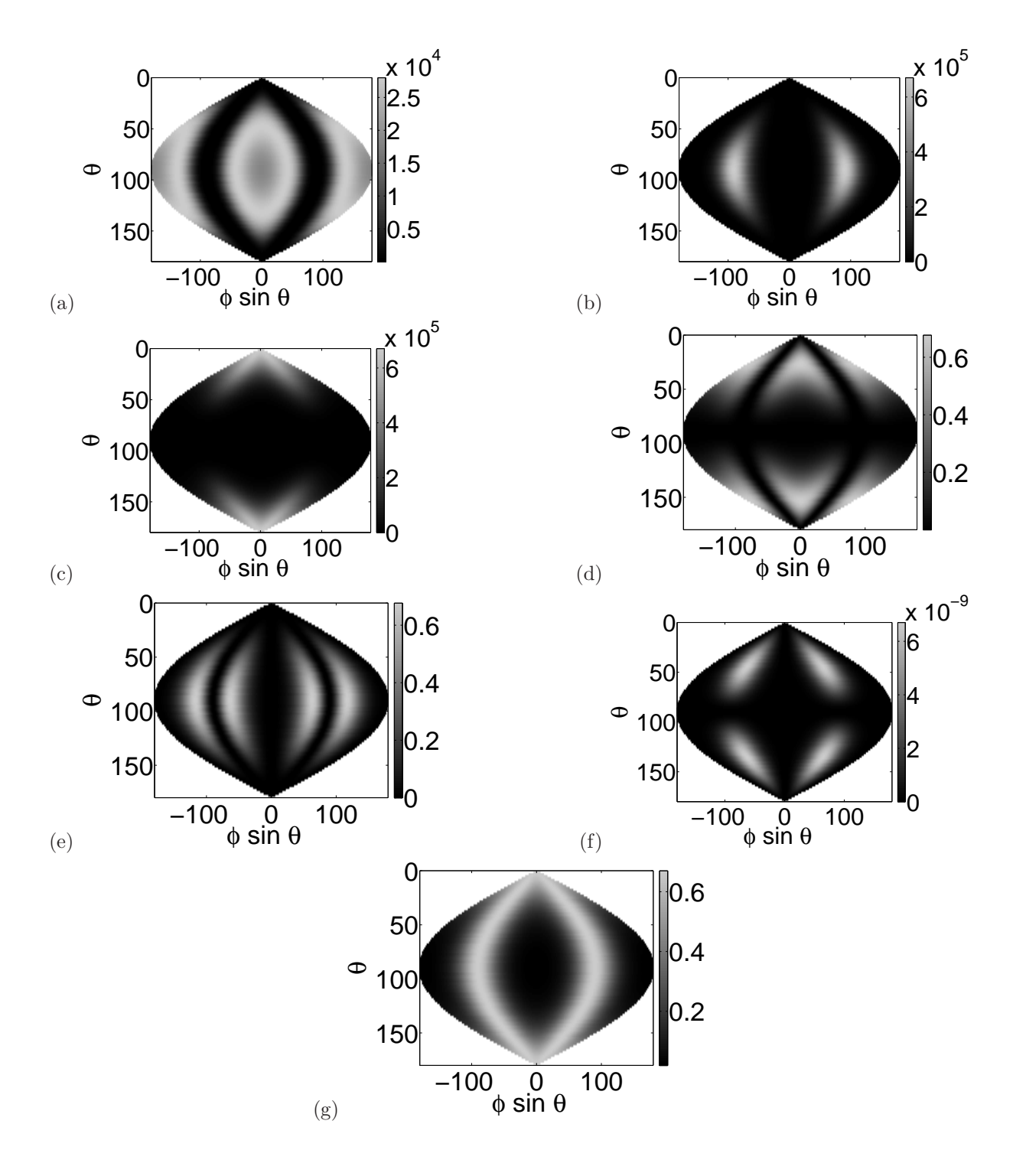


Figure 5.5. Variation of the squares of sensitivity values and the normalized MR signal w.r.t. diffusion gradient direction angles (θ, ϕ) for nearly axisymmetric case for the DTI model. Shown in the figure are squares of sensitivity values w.r.t. (a) D_{\parallel} , (b) $D_{\perp 1}$, (c) $D_{\perp 2}$, (d) θ_F , (e) ϕ_F , (f) ψ_F and (g) the normalized MR signal. The mean fiber direction is at $(\theta_F, \phi_F) = (90^{\circ}, 0^{\circ})$.

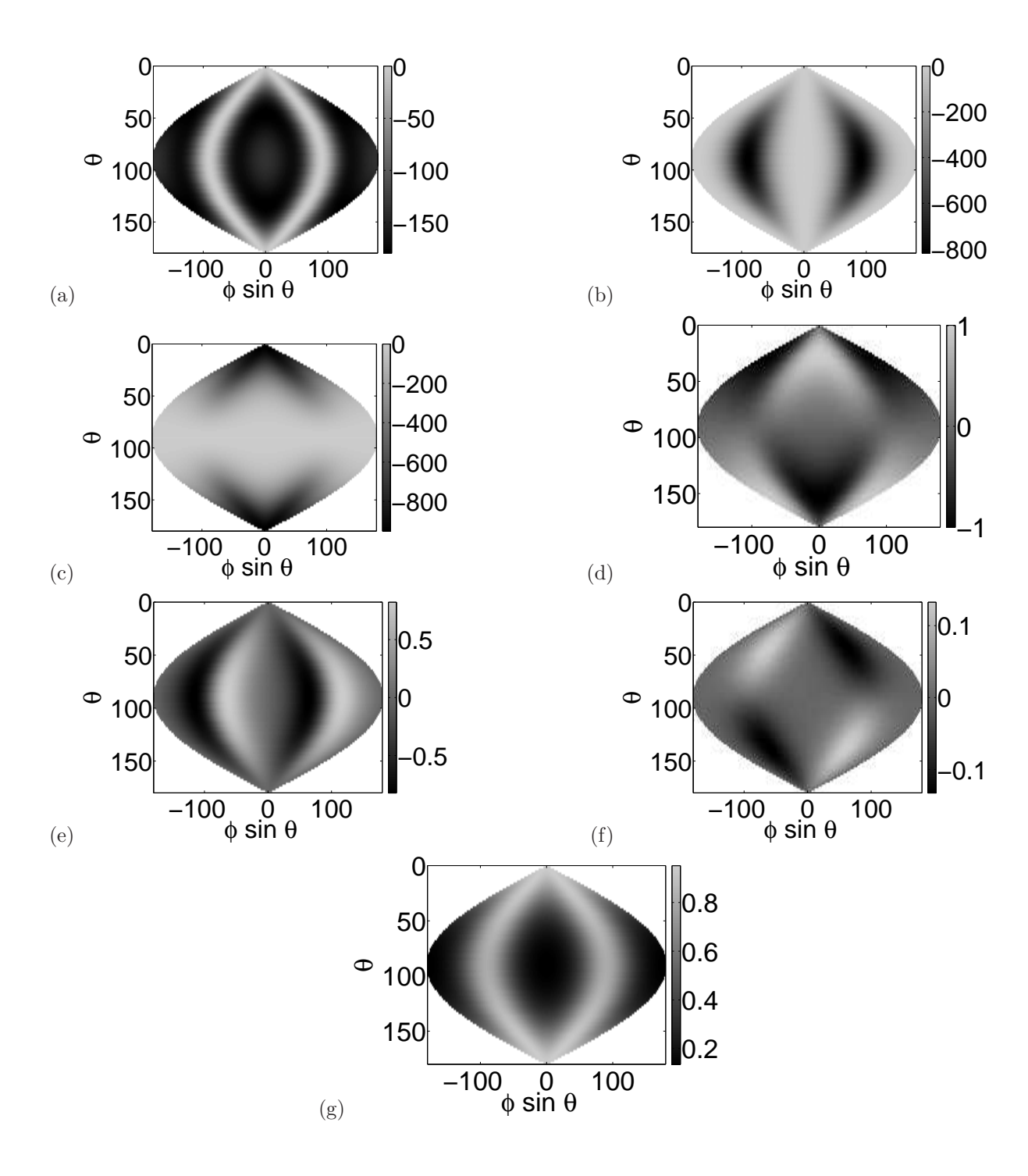


Figure 5.6. Variation of the sensitivity values and the normalized MR signal w.r.t. diffusion gradient direction angles (θ, ϕ) for non-axisymmetric case for the DTI model. Shown in the figure are sensitivity values w.r.t. (a) D_{\parallel} , (b) $D_{\perp 1}$, (c) $D_{\perp 2}$, (d) θ_F , (e) ϕ_F , (f) ψ_F and (g) the normalized MR signal. The mean fiber direction is at $(\theta_F, \phi_F) = (90^{\circ}, 0^{\circ})$.

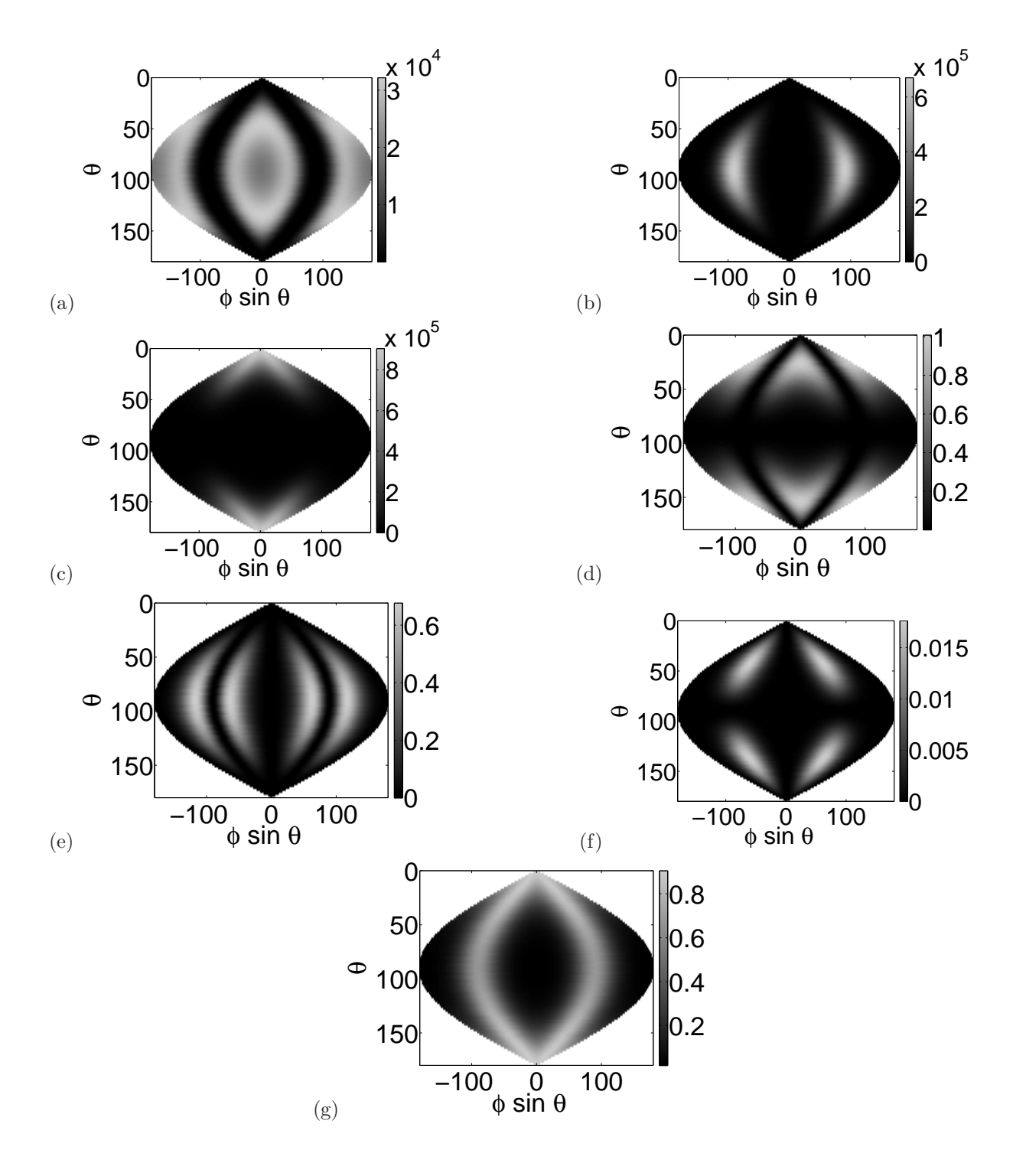


Figure 5.7. Variation of squares of the sensitivity values and the normalized MR signal w.r.t. diffusion gradient direction angles (θ, ϕ) for non-axisymmetric case for the DTI model. Shown in the figure are squares of sensitivity values w.r.t. (a) D_{\parallel} , (b) $D_{\perp 1}$, (c) $D_{\perp 2}$, (d) θ_F , (e) ϕ_F , (f) ψ_F and (g) the normalized MR signal. The mean fiber direction is at $(\theta_F, \phi_F) = (90^{\circ}, 0^{\circ})$.

5.3 Partitioning CRLB matrix for optimized estimation of selected parameters

Generally, in an estimation problem, such as the estimation of DTI/ADTI model parameters, there are only certain parameters that are of interest and the rest can be assumed to be "nuisance" parameters which are although estimated, but are not used or is not of interest for further analysis. In the case of DTI, if the analysis is based on determining the FA or MD in the voxel, only the diffusivities are of interest. Similarly, if the purpose of the analysis is fiber tracking, only angular parameters, such as θ_F , ϕ_F are of interest. Thus, a gradient optimization scheme that can optimize the model parameter estimation to reduce the uncertainty of selective parameters is highly desirable.

In the context of DTI/ADTI model parameter estimation, there are two kinds of parameters, namely, diffusivity and angular parameters. I will focus on each of the kind of parameters individually and come up with the gradient scheme optimization for selective parameter estimation of each kind. The basic idea is factorization of the CRLB matrix and optimize for the determinant of the sub-matrix which carries the variances of the parameters of interest. This has been discussed in [33, 120]. Based on the discussion on the derivation of the CRLB matrix, the Rician CRLB is given by

$$\Sigma_{CR} = \sigma^4 (\boldsymbol{X}_1^{\mathrm{T}} \boldsymbol{X}_2)^{-1} \tag{5.85}$$

and the Gaussian CRLB is given by

$$\Sigma_{CR} = \sigma^2 (\boldsymbol{X}^{\mathrm{T}} \boldsymbol{X})^{-1} \tag{5.86}$$

where X, X_1 and X_2 are the sensitivity matrices. Columns of these matrices contain partial derivatives with respect to diffusion model parameters computed at different experimental settings, such as diffusion gradients.

Let a row of the sensitivity matrix be

$$[\mathbf{X}]_{i.} = \begin{bmatrix} \frac{\partial E_i}{\partial \beta_1} & \dots & \frac{\partial E_i}{\partial \beta_{M_1}} & \frac{\partial E_i}{\partial \beta_{M_1+1}} & \dots & \frac{\partial E_i}{\partial \beta_M} \end{bmatrix}$$
(5.87)

where the vertical line divides the matrix into partial derivatives of M_1 diffusivities and $M - M_1$ angular parameters. Thus, the $\mathbf{X}^{\mathrm{T}}\mathbf{X}$ can be partitioned into four sub-matrices,

as given by

$$\boldsymbol{X}^{\mathrm{T}}\boldsymbol{X} = \begin{bmatrix} A_1 & A_2 \\ A_3 & A_4 \end{bmatrix} \tag{5.88}$$

where A_1 , A_2 , A_3 and A_4 are the sub-matrices after matrix squaring. Here, A_1 is the autocorrelation matrix of the partial derivatives with respect to only diffusivities and A_4 is the autocorrelation matrix of the partial derivatives with respect to only angular parameters. A_2 and A_3 are cross-correlation matrices between the diffusivity and angular matrices. Similarly, the CRLB matrix can be partitioned into four sub-matrices as given by,

$$\Sigma_{CR} = \begin{bmatrix} B_1 & B_2 \\ B_3 & B_4 \end{bmatrix} = \sigma^2 \begin{bmatrix} A_1 & A_2 \\ A_3 & A_4 \end{bmatrix}^{-1}$$
 (5.89)

where B_1 and B_4 are the CRLB sub-matrices with respect to only diffusivity and angular parameters, respectively. Thus, in order to minimize the CRLB of estimation variance of diffusivities only, determinant of B_1 can be minimized instead of the entire CRLB matrix. Using Woodbury's matrix inversion formula [120, 121], B_1 is computed as,

$$B_1 = \sigma^2 (A_1 - A_2 A_4^{-1} A_3)^{-1} \tag{5.90}$$

The inversion is under the condition that A_4 is not singular (i.e., $\det(A_4) \neq 0$). Scharf et al. [120] shows another way of partitioning the CRLB matrix which is applicable only to Gaussian CRLB case. However, Eq. 5.90 is a more general form of partitioning the CRLB matrix and is useful for Rician CRLB case where the non-symmetric matrix is partitioned, as given by

$$\boldsymbol{X}_{1}^{\mathrm{T}}\boldsymbol{X}_{2} = \begin{bmatrix} A_{1} & A_{2} \\ A_{3} & A_{4} \end{bmatrix}$$
 (5.91)

Here X_1 and X_2 are the modified sensitivity matrices which can also be split into the partial derivatives of the diffusivity and angular parameters as shown for the sensitivity matrix (X) case.

5.3.1 Diffusivities

For DTI case, model parameters are $\beta = \{D_{\parallel}, D_{\perp 1}, D_{\perp 2}, \theta_F, \phi_F, \psi_F\}$. In order to optimize the gradient scheme only for the diffusivities, CRLB matrix is partitioned to contain

the variance of only diffusivities. Thus, the sensitivity matrix is partitioned to separate the diffusivities as given

$$[\mathbf{X}]_{i.} = \begin{bmatrix} \frac{\partial E_i}{\partial D_{\parallel}} & \frac{\partial E_i}{\partial D_{\perp 1}} & \frac{\partial E_i}{\partial D_{\perp 2}} & \frac{\partial E_i}{\partial \theta_F} & \frac{\partial E_i}{\sin(\theta_F)\partial\phi_F} & \frac{\partial E_i}{\partial\psi_F} \end{bmatrix}$$
(5.92)

Next, using Eq. 5.90, the B_1 matrix will only contain the variances of the diffusivities. Finally, the cost function for the optimization of gradient directions becomes $det(B_1)$.

For ADTI model, the parameter set is $\beta = \{D_{\parallel}, D_{\perp}, \theta_F, \phi_F\}$. Thus, to optimize the diffusivities, the sensitivity matrix is partitioned as

$$[\mathbf{X}]_{i.} = \begin{bmatrix} \frac{\partial E_i}{\partial D_{\parallel}} & \frac{\partial E_i}{\partial D_{\perp}} & \frac{\partial E_i}{\partial \theta_F} & \frac{\partial E_i}{\sin(\theta_F)\partial\phi_F} \end{bmatrix}$$
(5.93)

As before, using Eq. 5.90, the B_1 matrix is computed and the cost function is the determinant of the B_1 matrix.

For Rician CRLB matrix, the partitioning is similar except that instead of X, modified sensitivity matrices (X_1 and X_2) are partitioned individually using Eq. 5.91 and Eq. 5.90 is used to compute the B_1 matrix.

5.3.2 Angular parameters

For DTI model, selective optimization for angular parameters is done by partitioning the sensitivity matrix as

$$[\mathbf{X}]_{i.} = \begin{bmatrix} \frac{\partial E_i}{\partial \theta_F} & \frac{\partial E_i}{\sin(\theta_F)\partial \phi_F} & \frac{\partial E_i}{\partial D_{\parallel}} & \frac{\partial E_i}{\partial D_{\perp 1}} & \frac{\partial E_i}{\partial D_{\perp 2}} & \frac{\partial E_i}{\partial \psi_F} \end{bmatrix}$$
(5.94)

Note that only the θ_F , ϕ_F parameters are considered in the angular parameters set since these directly affect the fiber orientation and α . ψ_F is treated as a nuisance parameter along with the diffusivities. Finally, B_1 is computed according to Eq. 5.90 and the optimization cost function is $\det(B_1)$.

For ADTI model, the sensitivity matrix is also partitioned to separate the angular parameters as given by

$$[\mathbf{X}]_{i.} = \begin{bmatrix} \frac{\partial E_i}{\partial \theta_F} & \frac{\partial E_i}{\sin(\theta_F)\partial \phi_F} & \frac{\partial E_i}{\partial D_{\parallel}} & \frac{\partial E_i}{\partial D_{\perp}} \end{bmatrix}$$
(5.95)

As before, using Eq. 5.90, the B_1 matrix is computed and the cost function is the determinant of the B_1 matrix.

Rician CRLB case is handled as mentioned in the previous section, but with the new partitions of the modified sensitivity matrices.

5.4 Gradient scheme optimization framework

The proposed optimization framework is based on D-optimality and its application for the design of optimal experiments [33,34]. As described earlier, optimization is defined by optimal selection of experimental parameters by minimizing the determinant of CRLB matrix. The analysis has focussed on optimizing the gradient scheme (Ω) for different signal models (such as DTI, ADTI) and noise models (Rician and Gaussian). For the DTI model ([7]), the rotationally invariant diffusion model parameters are $\beta = \{D_{\parallel}, D_{\perp 1}, D_{\perp 2}, \theta_F, \phi_F, \psi_F\}$ (M = 6). For the ADTI model, from axisymmetry assumption, the model parameters are $\beta = \{D_{\parallel}, D_{\perp}, \theta_F, \phi_F\}$ (M = 4).

The optimal diffusion gradient scheme is obtained by solving the following equation,

$$\Omega_{\text{opt}} = \arg \left[\min_{\Omega} \left(\max_{\{\theta_{F}, \phi_{F}\} \in \Lambda} f \right) \right]$$
(5.96)

where $f := 1/\det(\mathbf{X}_1^T\mathbf{X}_2)$ (for the Rician noise case) or $f := 1/\det(\mathbf{X}^T\mathbf{X})$ (for the Gaussian noise case). Since f is a scaled form of $\det \Sigma_{CR}$, minimizing f is equivalent to minimizing $\det \Sigma_{CR}$. In Eq. 5.96, the maximum value of f (worst case of f) within a cone (Λ) that includes the majority of fiber directions is searched and then this value is minimized w.r.t. the gradient scheme (Ω) to reach the optimal gradient design (Ω_{opt}). The formulation is robust since the gradient scheme is optimal for an uncertainty range of fiber orientations. The a priori structural information is incorporated in Eq. 5.96 by measuring Λ from preliminary DTI scan on a subject. Since the optimization is local in parameter space, the mean values of diffusion model parameters (β) (also obtained from preliminary DTI scan) are used to calculate f.

5.4.1 Reformulation of the gradient scheme

To reduce the computation time for gradient scheme optimization, the definition of the gradient scheme is reformulated as $\Omega = \{(\theta_r, \Delta\phi_r, N_r); r \in [1, P]\}$, where P is the number of rings, each located at inclination angle (θ_r) with azimuthal offset angle $(\Delta\phi_r)$ and N_r uniformly distributed points [84, 85]. Under this formulation, the number of optimization parameters is greatly reduced. For example, for a 30-gradient direction problem (Fig. 5.8), instead of defining Ω in 60 variables, $\Omega = \{(\theta_i, \phi_i); i \in [1, 30]\}$, it can be redefined in 9 variables, $\Omega = \{(\theta_r, \Delta\phi_r, N_r); r \in [1, 3]\}$ for P = 3 (3-ring configuration). P is selected by trying a number of configurations (such as P = 3, 4, 5, 6 and 7) and choosing the best in terms of cost function, i.e., the one that gives the minimum cost function. This framework helps improve the optimization speed significantly (when P is less) and also provides flexibility in designing complex schemes (for large P).

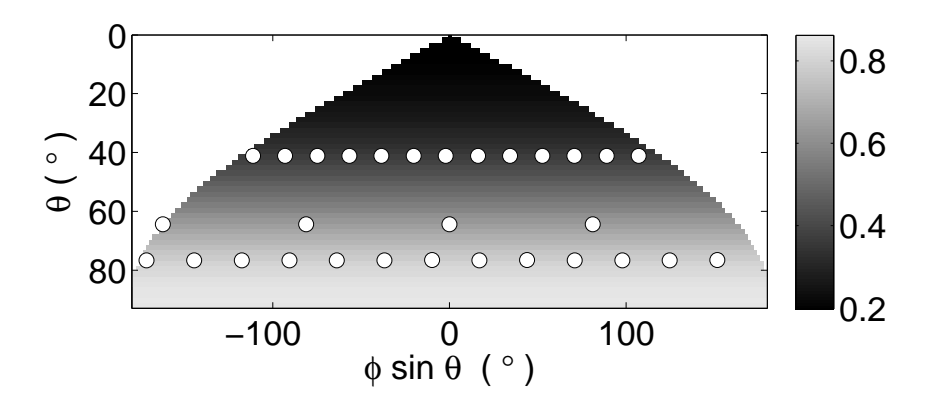


Figure 5.8. Gradient directions (white circles) on a 2D opened hemisphere showing a reformulated scheme (for P = 3). Mean fiber orientation is at $(\theta_F, \phi_F) = (0^{\circ}, 0^{\circ})$. The gray scale underlay shows the normalized MR signal variation due to changing gradient directions (θ, ϕ) .

The representation of the gradient scheme in a ring-like formation originates from the observation that upon application of the axisymmetric condition on the diffusion model such that the diffusion in the plane transverse to the fiber direction is isotropic, the optimal sampling locations in the gradient space collapse onto axisymmetric rings about the mean fiber direction [39, 72, 119]. This phenomenon can be seen in analytical derivations as well as by numerical simulations. Thus, sets of gradient directions can be grouped into ring-like distribution and defined as given in the reformulated definition of Ω . Although this representation puts constraints on the gradient distribution, by adding additional parameters such as $\Delta \phi_r$ in the definition of Ω , even non-axisymmetric cases can be represented. So, a range of distribution patterns of gradient directions can be achieved by the reformulated gradient scheme.

5.4.2 Algorithm

The robust optimization problem defined in Eq. (5.96) is solved for the DTI and ADTI models. A preliminary optimization using $\theta_{\rm F}=0^{\circ}$ and $\Lambda=0$ is performed to provide a starting point, $\Omega_0:=\arg\left[\min_{\Omega}f\right]$, for the robust optimization algorithm. This strategy is preferred to choosing an arbitrary gradient scheme and results in shorter computational times. For the computation of Ω_0 , a simulated annealing method, which performs a stochastic exploration of the sampling space controlled by a temperature parameter (T), is implemented using the full set of variables [122]. Simulated annealing is a stochastic minimization technique [73] which is based on the annealing process (slow cooling process) in metallurgy and is known to be robust with respect to local minima problems common in gradient-based methods. Details of this algorithm are given in Appendix A (Fig. A.3 and Fig. A.4). Solutions satisfying the T-dependent Metropolis criterion [73] are accepted, while others are rejected. The exploration stage is necessary to avoid local optima (the cost function f is nonconvex), and the step-size for exploration is progressively reduced after a maximum number of rejection steps are reached [119].

In the second stage, the robust optimization problem (Eq. 5.96) is solved using the reduced-order parameterization with P rings. The ring locations, $\{\theta_i \in [0, \pi/2]; i \in [1, P]\}$, and number of points, $\{N_i \in [1, N-P]; i \in [1, P-1]\}$, are initialized based on the clustering of the q-space sampling scheme Ω_0 . These parameters are optimized by iterating on possible values for N_i and P and using a deterministic gradient-based "minimax" algorithm [123] for θ_i . Eq. (5.96) is solved iteratively by updating the parameters of Ω until the changes in these parameters do not change the cost function significantly. The optimization is implemented in Matlab (Mathworks Inc., Natick, MA) using routines

from the Optimization Toolbox.

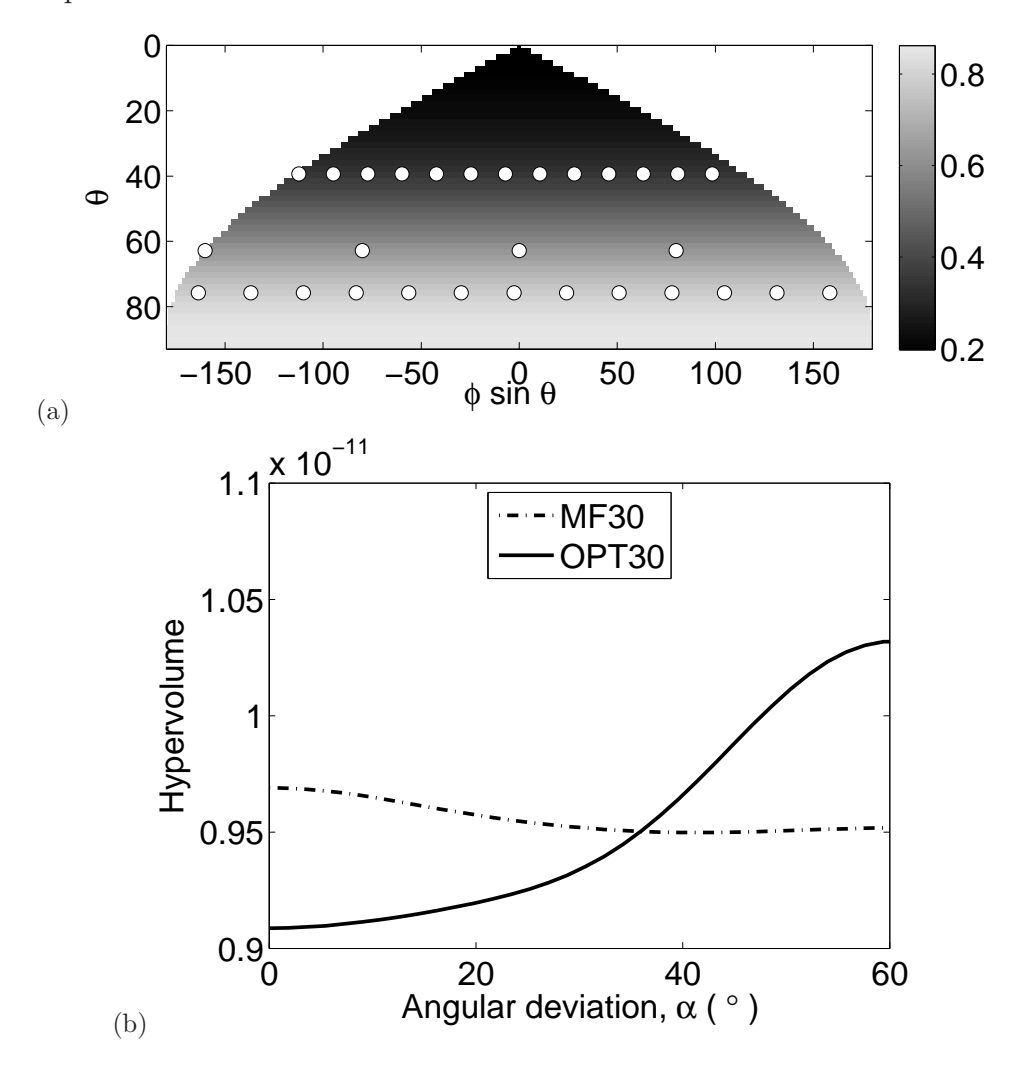


Figure 5.9. Robust optimization results for the ADTI model with Rician CRLB for $b = 1000 \text{ s} \text{ mm}^{-2}$ with P = 3 rings for fiber orientations within a cone of axis along the z-axis and cone angle $\Lambda = 35^{\circ}$. (a) Gradient directions (white circles) an opened hemisphere with gray scale equal to the normalized MR signal. (b) Comparison of performance curves.

5.4.3 Optimization Efficiency

ADTI model

Eq. 5.54 (Rician noise case) or Eq. 5.59 (Gaussian noise case) can be used to predict the performance of the diffusion-encoding gradient scheme (Ω) before performing the ADTI experiment. A gradient scheme has a better performance when det Σ_{CR} is lower with respect to another scheme. Also, a scheme is more robust (in terms of fiber angular deviation (α) from the mean fiber orientation) than another scheme when det Σ_{CR} is

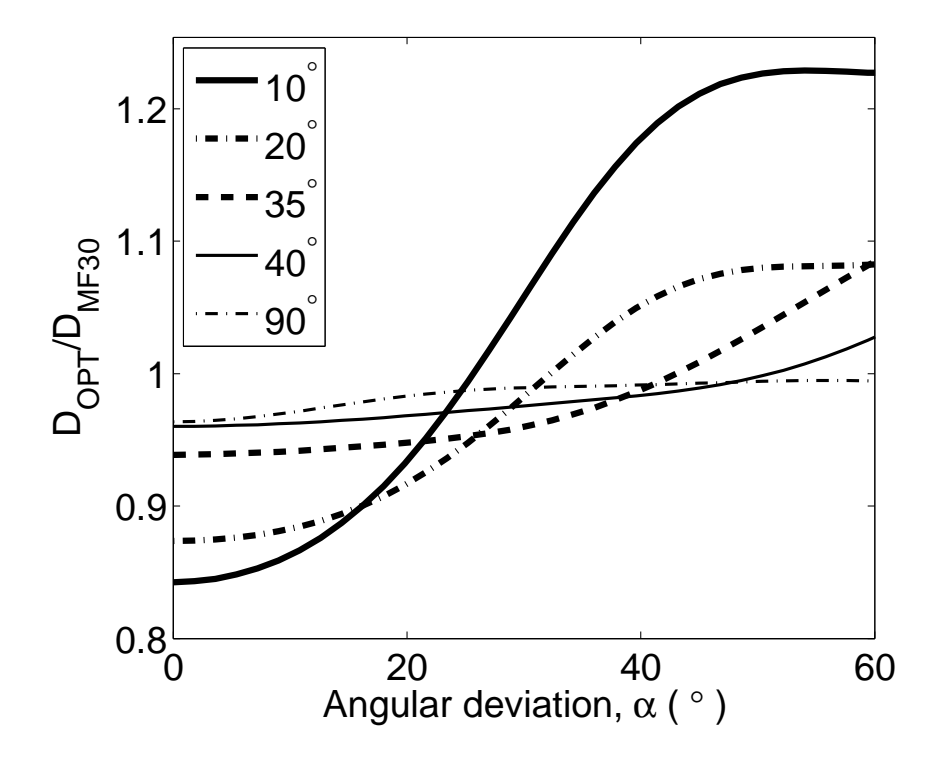


Figure 5.10. Variation of normalized hypervolume of uncertainty for 30-direction optimal gradient schemes for ADTI model. The cone angles vary as $(\Lambda = [10^{\circ} - 90^{\circ}])$ and Rician noise case is selected. Noise level, $\sigma = 0.1$. Normalization reference is MF30 gradient scheme.

low over a broader range of α . This performance range (of α) is determined by the value of the cone angle (Λ) used during the optimization procedure.

Fig. 5.10 shows the variation of normalized hypervolume of uncertainty $(D_{OPT}/D_{MF30}, D_{OPT} = \sqrt{\det \Sigma_{CR,OPT}}, D_{MF30} = \sqrt{\det \Sigma_{CR,MF30}})$ for the optimal 30-direction gradient schemes at different cone angles (Λ). Normalization is w.r.t. hypervolume of uncertainty for the MF30 scheme. The MF30 is a 30-direction MF technique-based gradient scheme [22] which does not use any a priori angle information (Λ). For smaller cone angles ($\Lambda = 10^{\circ}$), the performance of the optimized gradient scheme is better than MF30 only when the fiber orientation is close to the mean fiber orientation ($\alpha = 0^{\circ}$). As the cone angle is increased, the performance becomes worse and eventually at $\Lambda = 90^{\circ}$ (completely uncertain case) D_{OPT}/D_{MF30} remains always less than unity, albeit close to unity, indicating a mildly improved performance compared to that of MF30.

DTI model

The performance prediction of an optimized gradient scheme for DTI case is done by computing the determinant of CRLB (at some fixed noise, σ^2) for different values of θ_F and ϕ_F . Only these two parameters are chosen since the scheme is made robust with respect to a range of fiber orientations. Thus to verify if the robustness is achieved, the CRLB is computed in a range of fiber orientations given in terms of θ_F and ϕ_F . The Fig. 5.11 shows the 2D performance plots for a non-axisymmetric diffusion case under Gaussian noise.

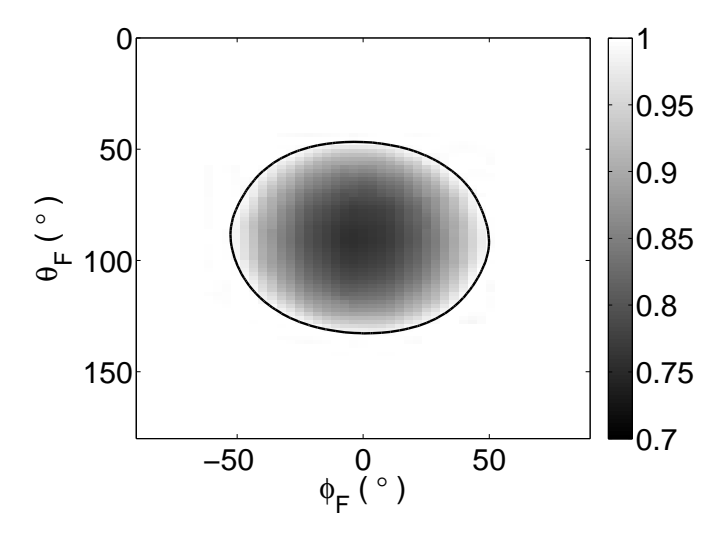


Figure 5.11. Plot of the ratio of hypervolumes for OPT30 w.r.t. MF30 scheme optimized using Gaussian noise assumption and for the DTI model. The contour line at unity value shows the cone of angles within which the optimization performance is improved.

The interpretation of the Fig. 5.11 is straightforward. Since a reduced uncertainty for a range of fiber orientations is desired when compared to the performance of the standard scheme such as MF30, it is verified if the robust optimal scheme is theoretically robust (based on the CRLB) in performance within an angular deviation defined by Λ from the mean fiber orientation. Fig. 5.11 shows the plot of the ratio of the cost function (det Σ_{CR}) for the optimized scheme w.r.t. MF30 scheme. The optimization is performed at $\Lambda = 35^{\circ}$. Thus, the ratio should be less than unity for angles within the cone angle range as observed in Fig. 5.11. Note, the true fiber orientation is at $(\theta_F, \phi_F) = (90^{\circ}, 0^{\circ})$. Since Λ is specified during optimization and its value collected from the preliminary DTI

scan on the subject, the robust optimization is subject specific, and thus more accurate.

5.4.4 *b*-factor optimization

In the discussion so far, I focussed on the optimization of the gradient directions to minimize the cost function (i.e., determinant of Σ_{CR}) within a range of fiber orientation. However, in all of these cases, the *b*-factor has been kept constant. In this section, I discuss the optimization of the *b*-factor as well as the gradient scheme using a modified form of Eq. 5.96. Here the *b*-factor is included as an optimized parameter in the optimization problem which can be written as,

$$\alpha_{\text{opt}} = \arg \left[\min_{b,\Omega} \left(\max_{\{\theta_{F}, \phi_{F}\} \in \Lambda} f \right) \right]$$
 (5.97)

where, $\boldsymbol{\alpha} \equiv [b, \Omega]$, $f := 1/\det(\boldsymbol{X}_1^T \boldsymbol{X}_2)$ (for Rician noise case) or $f := 1/\det(\boldsymbol{X}^T \boldsymbol{X})$ (for Gaussian noise case). Note that the sensitivity matrix, \boldsymbol{X} (and the modified sensitivity matrices, \boldsymbol{X}_1 and \boldsymbol{X}_2) are functions of both the gradient scheme (Ω) and the b-factor.

Under this optimization scheme, the b-factor is considered on the whole rather than considering its individual components, such as the diffusion gradient strength, gradient pulse durations and the diffusion pulse interval. While optimizing for the b-factor, it will be assumed that the values that are obtained are achievable and within limits of the MRI scanner. This results in additional constraint on the optimization problem. A change in the b-factor could be accomplished by changing any of its components. But, it is preferred that the change in the b-factor is caused by the change in the diffusion gradient strength only, while keeping the timing parameters fixed. However, in general, the diffusion gradients are set at the maximum by the hardware already. Thus, the b-factor needs to increased by increasing the pulse duration or the inter-pulse intervals. This leads to increase of T_E . In addition to longer diffusion gradients, the SNR will drop in the diffusion-weighted images. This limits the upper value of b-factor on clinical scanners.

Inclusion of b-factor in the optimization framework result in a modified algorithm for the framework. The modifications include:

- 1. Using simulated annealing method for the combined optimization of the b-factor and the gradient scheme: the algorithm discussed previously uses a preliminary exploratory stage based on simulated annealing method [73] to avoid the local minima problem (see Appendix A (Fig. A.3 and Fig. A.4) for flowchart of the optimization procedure) and then uses the reformulated gradient scheme (discussed in the section 'Reformulation of the gradient scheme' and Appendix A (Fig. A.5)) to search for the optimized gradient scheme. When the b-factor is included in the optimization, the local minima problem is severe since the b-factor scales the model parameter sensitivities directly and thus has more influence over the CRLB matrix than the gradient directions. Hence, when optimizing for the b-factor, a simulated annealing method with slower cooling rate and finer step size adjustment is used (see Appendix A (Fig. A.6 for flowchart and detailed steps)).
- 2. No use of the reformulated gradient scheme: Owing to local minima problem and significant variations in the echo signals while changing the b-factor, the reformulated gradient scheme could pose additional constraints and as such is not used.
- 3. No use of the exploitation stage: In the previous algorithm, the second stage based on the reformulated gradient scheme used a gradient descent-based method to reach an optimal location quickly. However, due to local minima issues, the gradient descent technique could not be applied.

From the derivation of the sensitivity matrix for both the ADTI and DTI model, it is observed that sensitivities are proportional to the b-factor and hence if the b-factor is varied, the optimization algorithm will attain higher b-factors to reduce the CRLB variance. On the other hand, regions where determinant of CRLB matrix is low generally correspond to regions where signal levels are high for a fixed b-factor. But, in order for the signal level to be high, the b-factor has to be low. Thus, there is a definite region where an optimal b-factor which satisfies both the high signal criterion as well as the high sensitivity criterion is attained by the optimization algorithm.

In optimizing the b-factor, an important observation is that at high b-factor values, the

signal will be low and as such the SNR will also be low. Under such conditions, the Rician noise model and use of the maximum likelihood estimator is most appropriate. However, the SNR can be improved by increasing the number of excitations and thus using more averaging to reduce the noise. So, at high b-factor, even though the signal level is low, but a good SNR can be obtained by averaging of more images. The disadvantage of this method is that the total scan time greatly increases. Still, the most common practice while using high b-factor is increasing the number of averages in the MR data acquisition.

5.4.5 Additional constraints on FA and MD in gradient scheme optimization

After discussing the gradient scheme optimization and the b-factor optimization, in this section, I will discuss the inclusion of additional constraints on FA and MD into the optimization problem. The optimization cost function (determinant of Σ_{CR}), so far, was computed for a fixed value of diffusion model parameters and optimized within a range of fiber directions. This notion can be extended to FA and MD values range as well. In other words, the cost function can be optimized within a range of both fiber directions as well as a range of FA and MD values. The range of FA and MD essentially sets a constraint on the diffusivity values. The optimization problem can now be modified as follows,

$$\alpha_{\text{opt}} = \arg \left[\min_{b,\Omega} \left(\max_{C} f \right) \right]$$
 (5.98)

where constraints are denoted by C and given by,

$$C \equiv \{\theta_{F}, \phi_{F}\} \in \Lambda \& FA \in [FA_{0}, FA_{1}] \& MD \in [MD_{0}, MD_{1}]$$
 (5.99)

where, as before, $f := 1/\det(\mathbf{X}_1^T\mathbf{X}_2)$ (for Rician noise case) or $f := 1/\det(\mathbf{X}^T\mathbf{X})$ (for Gaussian noise case). The range of FA values is given by $[FA_0, FA_1]$ and the range of MD values is given by $[MD_0, MD_1]$. Also, the fiber angular range is given, as before, by $\{\theta_F, \phi_F\} \in \Lambda$, where Λ is the cone of fiber orientations. This is the optimization problem formulation in a very generalized form and could incorporate prior information of both the fiber orientation as well as the diffusivities (in the form of FA and MD). The

optimization algorithm is the same as the one used for b-factor optimization. However, due to a large number of constraints, the computation time for the optimization is much higher as compared to just optimizing the gradient directions.

5.5 Comparison of optimized gradient schemes and their predicted performances

This section presents a comparison of spatial distributions and the predicted performances for various optimized schemes. Both ADTI and DTI diffusion model and Rician and Gaussian noise model have been considered for the gradient optimization.

For the ADTI case, the parameter values and noise level used for the gradient optimization process are: $D_{\parallel}=1.62\times10^{-3}~\mathrm{mm^2~s^{-1}}, D_{\perp}=0.148\times10^{-3}~\mathrm{mm^2~s^{-1}}, \theta_F=0^{\circ},$ $\phi_F=0^{\circ},\ \sigma=0.1.$ This corresponds to FA = 0.9, MD = 0.638 × 10⁻³ mm² s⁻¹ Experimental settings are : $b=1000~\mathrm{s~mm^{-2}},\ N=30$. Prior structural information used: $\Lambda=35^{\circ}$.

For the DTI case, the parameter values and noise level used for the gradient optimization process are: $D_{\parallel}=2.2\times10^{-3}~\mathrm{mm^2~s^{-1}},~D_{\perp1}=0.4\times10^{-3}~\mathrm{mm^2~s^{-1}},$ $D_{\perp2}=0.3657\times10^{-3}~\mathrm{mm^2~s^{-1}},~\theta_F=90^\circ,~\phi_F=0^\circ,~\psi_F=0^\circ,~\sigma=0.1.$ This corresponds to FA = 0.802, MD = 0.989 × 10⁻³ mm² s⁻¹ Experimental settings are : $b=1000~\mathrm{s~mm^{-2}},~N=30$. Prior structural information used: $\Lambda=35^\circ$.

5.5.1 Distribution of gradient directions

Fig 5.12 shows the optimized gradients distribution on an opened unit hemisphere for the ADTI diffusion model and Rician and Gaussian noise models under different optimality criteria. The MF30 scheme is also shown for comparison. The CRLB-based D-optimality criterion is inversely related to the determinant of the square of the sensitivity matrices. Hence, by minimizing the determinant of the CRLB for the gradient directions, the optimization framework distributes these gradients in regions where the square of the sensitivity is higher. Determinant of the square of the sensitivity matrices is propor-

tional to the product of the individual parameter sensitivities, such as sensitivities w.r.t. $D_{\parallel}, D_{\perp}, \theta_F$ and ϕ_F for ADTI, and the optimization framework looks for regions where the majority of the model sensitivities are high. Referring to the sensitivity plots in Fig. 5.3 which shows the spatial variation of the sensitivities caused due to the prior assumption of the fiber structure, for the all parameters case, the region transverse to the fiber orientation corresponds to higher overall square sensitivity values and hence are sampled more in this region by optimization (shown in Fig. 5.12 (a) and (b)). For the diffusivity only case, both the regions transverse and towards the fiber orientation are sampled (shown in Fig. 5.12 (c) and (d)) and for the angular parameters only case, only transverse region is sampled after gradient optimization (shown in Fig. 5.12 (e) and (f)). Note that the sensitivity being a function of the normalized MR signal which is also higher transverse to the fiber orientation also influences the distribution of the gradient directions, pushing these towards the transverse direction. Results of Rician and Gaussian cases are similar but Rician CRLB optimized cases are more dispersed than the Gaussian CRLB optimized cases which could be due to the rescaling of the sensitivity matrix in the Rician case as shown in Eq. 5.48. MF30 (Fig. 5.12 (g)) scheme uniformly samples the gradient space since it does not use any optimization based on prior structural knowledge.

Fig. 5.13 shows the distribution of the optimized gradient directions on an opened sphere for the DTI model. Here the true fiber orientation is along +X-zxis to avoid the singularity in the CRLB definition when the fiber is at +Z-axis. While the reasoning for the distribution is same as in the ADTI case, i.e., regions of higher overall square sensitivities are selected by the optimization framework, the distribution is consistently towards the transverse orientation, even for the diffusivities only case. This can be explained from the sensitivity plots for the DTI model (see Figs. 5.4 – 5.7) where the square sensitivities of most of the DTI model parameters (except for D_{\parallel}) are higher transverse to the fiber orientation. This effect is less pronounced in the ADTI since it has fewer diffusion model parameters.

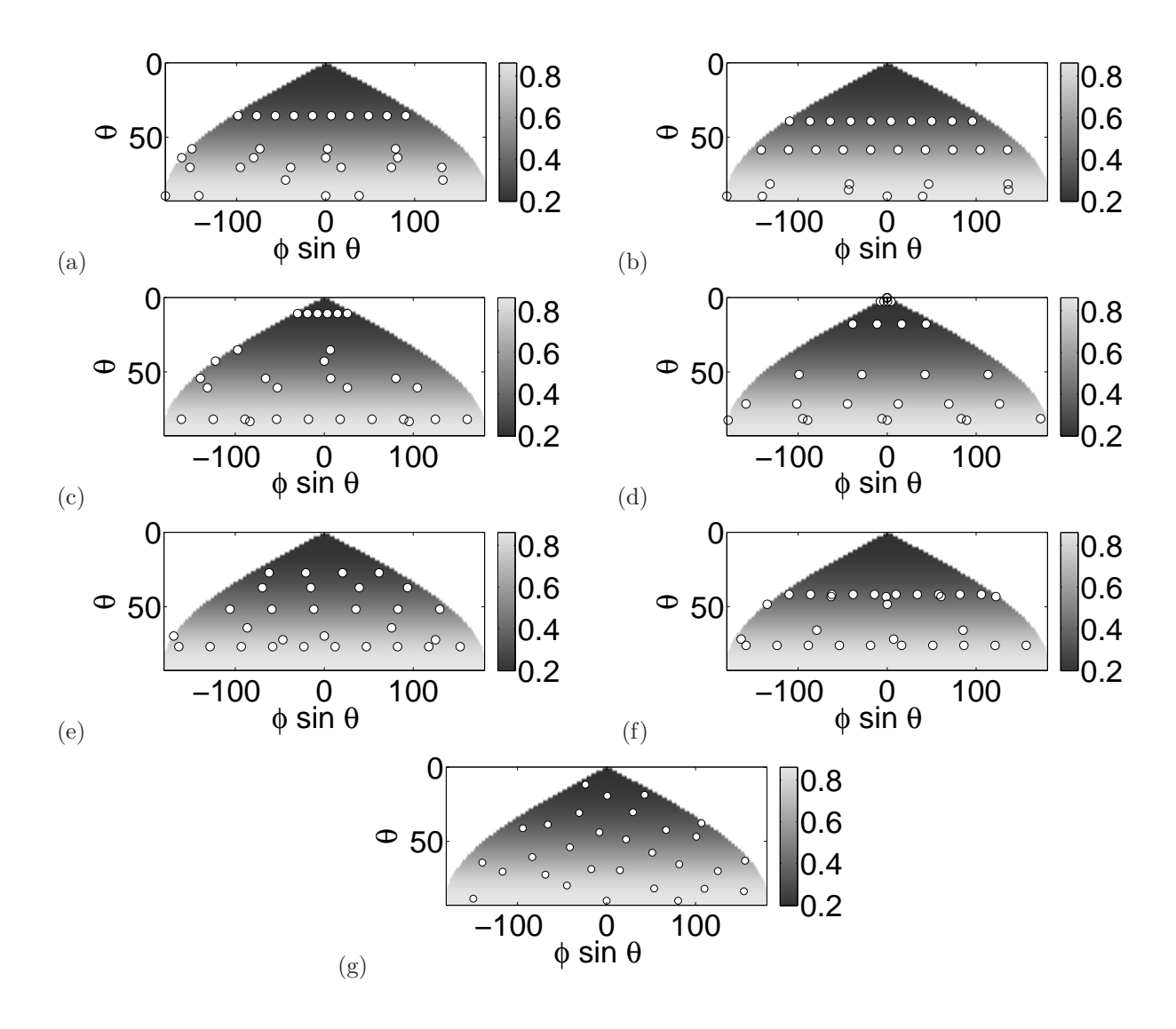


Figure 5.12. Optimized Gradient schemes for the ADTI diffusion model under the following optimality criteria: optimize for all parameter ((a) Rician and (b) Gaussian), diffusivities only ((c) Rician and (d) Gaussian) and fiber orientation only ((e) Rician and (f) Gaussian). MF30 scheme is shown in (g). The fiber orientation, $(\theta_F, \phi_F) = (0^{\circ}, 0^{\circ})$. The gray scale values represent the normalized MR signal and the white circles are the locations of the diffusion gradient unit vector on an opened unit hemisphere.

5.5.2 Performance curves

Fig. 5.14 shows the performance curves of various optimized gradient schemes for the ADTI model. The CRLB-based hypervolume has been reduced for the OPT30 scheme compared to the MF30 scheme in the desired angular deviation from the fiber orientation defined by the cone angle during optimization. The curve is smooth for the all parameter case, but fluctuates for the diffusivities only or angular parameters only cases within the cone angle even though there is reduction in the hypervolume compared to MF30.

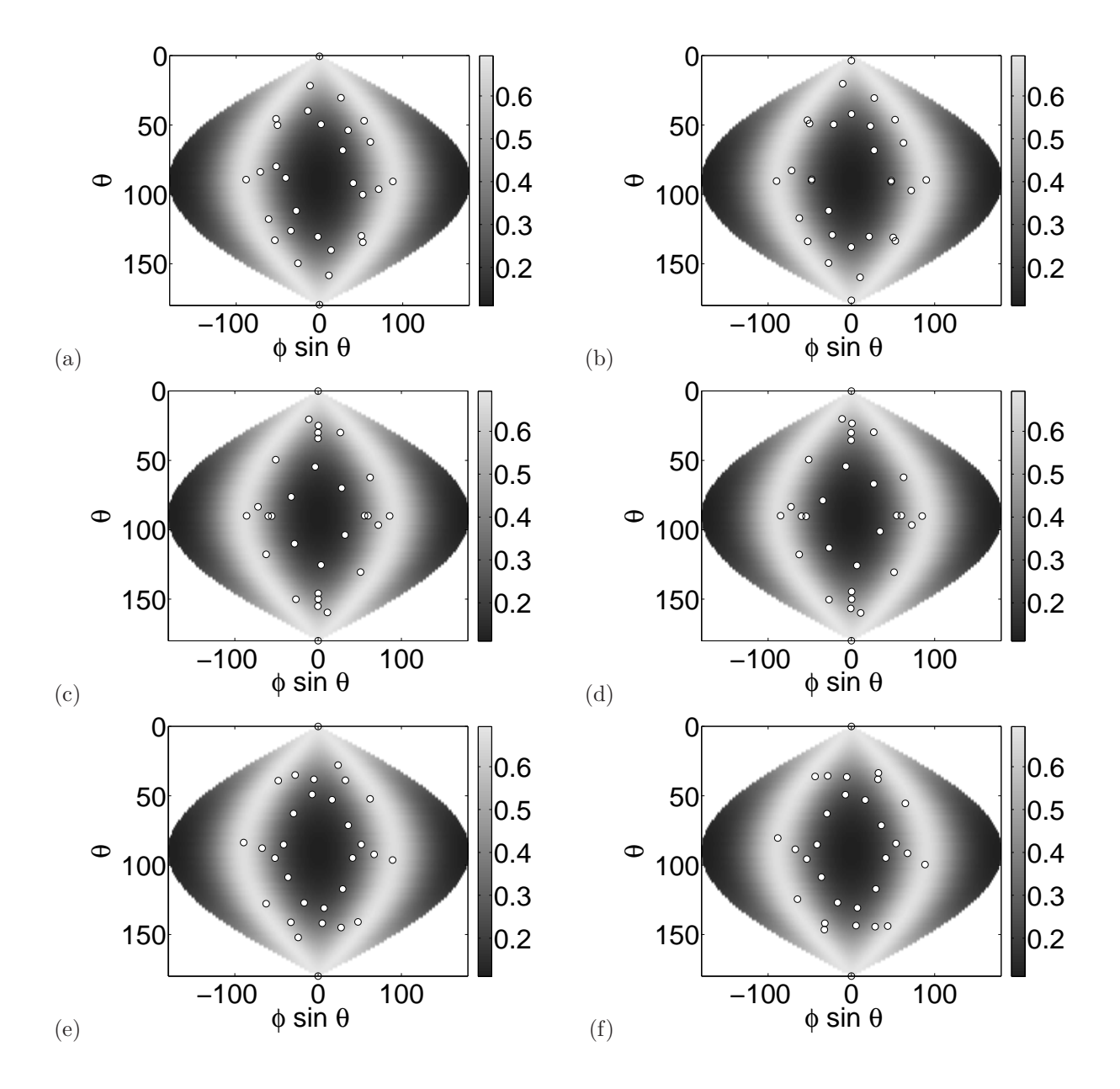


Figure 5.13. Optimized Gradient schemes for the DTI diffusion model under the following optimality criteria: optimize for all parameter ((a) Rician and (b) Gaussian), diffusivities only ((c) Rician and (d) Gaussian) and fiber orientation only ((e) Rician and (f) Gaussian). The fiber orientation, $(\theta_F, \phi_F) = (90^{\circ}, 0^{\circ})$. The gray scale values represent the normalized MR signal and the white circles are the locations of the diffusion gradient unit vector on an opened unit hemisphere.

Fig. 5.15 shows the performance plots of various optimized gradient schemes for the DTI model. The contour line indicates the unity ratio level which coincides with the cone angle set during optimization. Thus, a optimized scheme perform as designed within the cone angle. The reduction is more significant for the all parameter case (Fig. 5.15 (a) and (b)) than other cases (Fig. 5.15 (c) - (f)). The region of overall higher square sensitivities

is more when more diffusion parameters are selected for improved precision since there is a possibility of more overlapping regions of higher individual sensitivities which is not the case for fewer model parameters, such as diffusivities only or angular parameters only cases.

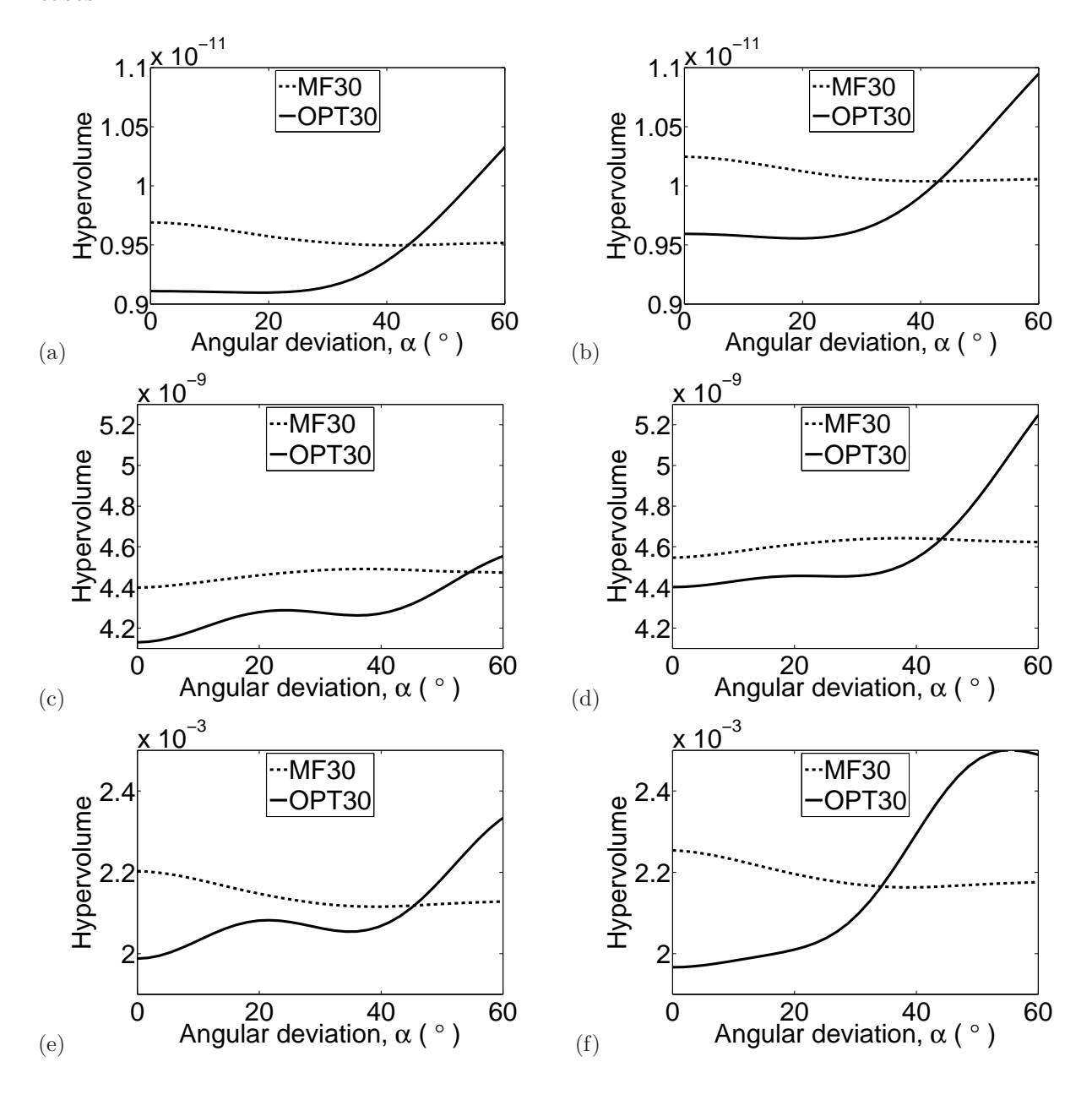


Figure 5.14. Performance curves for the ADTI diffusion model for optimization w.r.t. all parameters ((a) Rician and (b) Gaussian), diffusivities ((c) Rician and (d) Gaussian) and angular parameters ((e) Rician and (f) Gaussian).

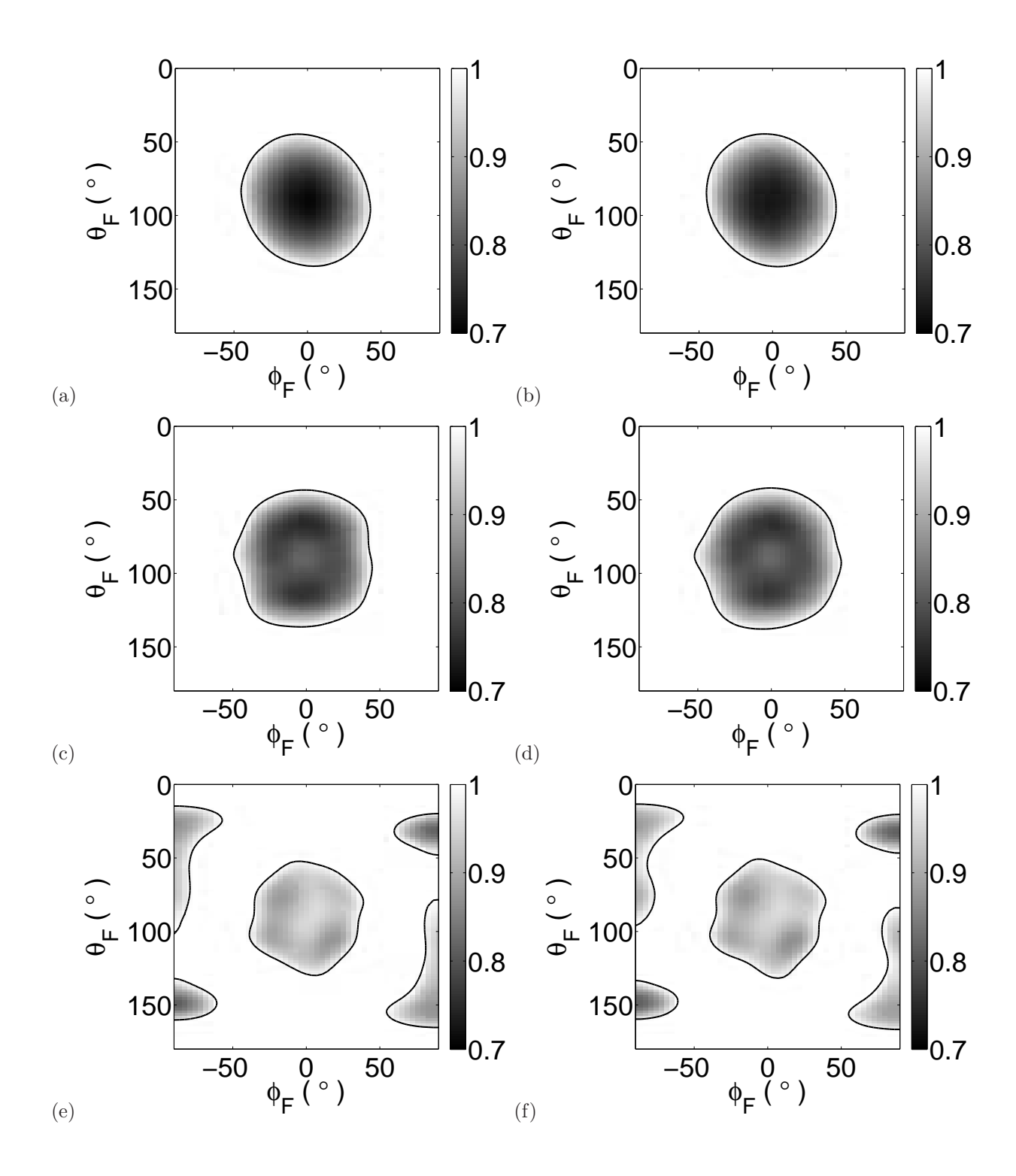


Figure 5.15. Performance plots for the DTI diffusion model for optimization w.r.t. all parameters ((a) Rician and (b) Gaussian), diffusivities ((c) Rician and (d) Gaussian) and angular parameters ((e) Rician and (f) Gaussian). Gray scale values indicate the ratio of CRLB-based hypervolume of OPT30 by MF30 and the contour lines are at unity ratio.

CHAPTER 6

Evaluation of estimation performance by simulations

In this chapter, various Monte Carlo simulations are performed to (a) evaluate the noise models, (b) evaluate the performance of different parameter estimators and (c) evaluate the effect of the non-optimized experimental parameters in terms of performance indices. Finally, simulations are performed to study the performance of the optimized gradient schemes for the ADTI and the DTI models with Rician and Gaussian noise models. Cases for gradient optimization based on selected model parameters are also considered, such as diffusivities only or angular parameters for fiber directions only, for different diffusion and noise models.

6.1 Noise characterization

The normalized MR signal (or echo attenuation) due to diffusion is defined as the ratio of two magnitude MR signals obtained with and without the application of diffusion gradients respectively. Assuming that measured complex MR signals contain additive white Gaussian noise, the corresponding magnitude MR signals (MR image intensities) will contain Rician noise [110,114] and the normalized MR signal being defined as the ratio of two magnitude MR signals will follow a ratio pdf of two Rician distributed random variables. The ratio pdf can be approximated by a Rician pdf or a Gaussian pdf.

In this section, an evaluation of the Rician approximation of the ratio pdf is performed and sources of error are analyzed. For comparison, the Gaussian approximation is also included in the evaluation.

6.1.1 Method

Let the measured (noisy) normalized MR signal, E, be defined as $E = S/S_0$, where S and S_0 are the measured magnitude MR signals with and without diffusion-weighting. Let $S_c = m + n_r + jn_i$ and $S = |S_c|$, where S_c is the measured complex MR signal with diffusion-weighting, n_r , n_i are $N(0,\sigma)$ (Gaussian pdf). Also, $S_{0c} = m_0 + n_{0r} + jn_{0i}$ and $S_0 = |S_{0c}|$ where S_{0c} is the measured complex MR signal without diffusion-weighting, n_{0r} , n_{0i} are $N(0,\sigma_0)$ (Gaussian pdf). Thus, $S \sim R(m,\sigma)$ and $S_0 \sim R(m_0,\sigma_0)$ are the Rician pdfs of the measured magnitude signals.

For the simulations, a set of values for m, m_0 , σ , σ_0 are selected. Also, each realization of the random variables can be averaged simulating the number of excitations (NEX) in MRI experiments. 10^6 realizations of S and S_0 are generated to compute the realizations of E. In the first simulation, the distribution of E is fitted to a Rician pdf by the method of moments (matching the expected value and the variance) to estimate m_E and σ_E for the pdf of E. In the second simulation, S_0 is considered a fixed non-random variable equal to m_0 under the assumption $m_0 >> \sigma_0$ and the E is regenerated and fitted to a Rician pdf by the method of moments to estimate m_E and σ_E for the pdf of E. The distribution of E from both simulations are also fitted to Gaussian pdfs by the method of moments to estimate m_E and σ_E for the Gaussian fit.

For both simulations, $m_0 = 697$ and $\sigma_0 = 100$. These values are estimated from the T2-weighted MR signals for the cervical spinal cord region in the white matter tract voxels for one subject (imaging protocol is given in the next chapter) based on techniques described in [124]. In ADTI or DTI model, the range of the normalized MR signal values is limited by the maximum and minimum diffusivities for a fixed b-factor. The intermediate values of the signal are obtained due to variation in the diffusion gradient direction. The limits of m can be calculated using, $m = m_0 \exp(-bD)$, where b is the

b-factor and D is the diffusivity. From previous studies, two values for the diffusivity D, $1.62 \times 10^{-3} \text{ mm}^2 \text{ s}^{-1}$ and $0.1485 \times 10^{-3} \text{ mm}^2 \text{ s}^{-1}$ were selected. This gives the range of m as $m \in \{0.1979m_0, 0.8620m_0\}$. Both simulations are performed at 10 values in this range of m values. Each of the simulations are repeated for NEX = 2 and 4.

6.1.2 Results

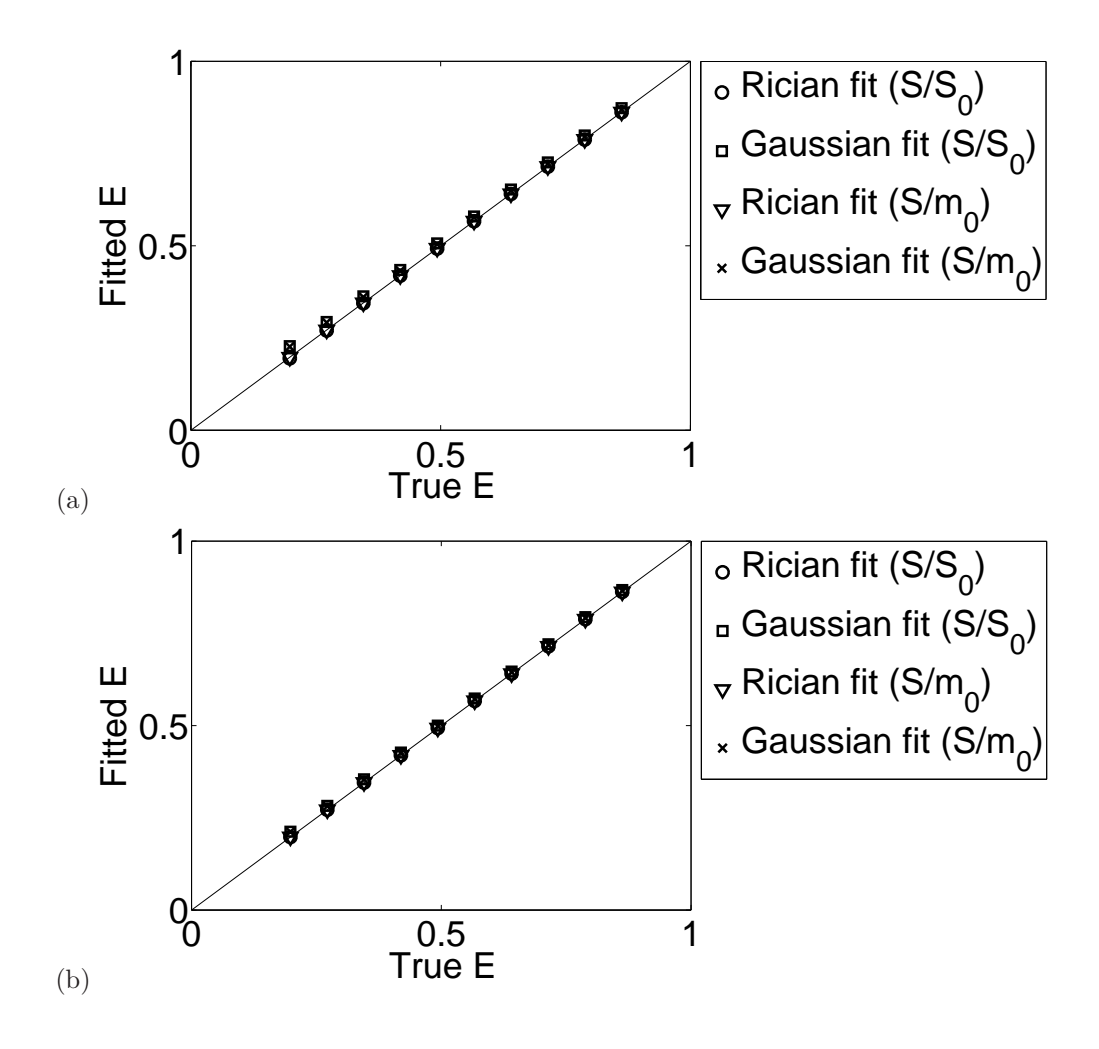


Figure 6.1. Comparison of the estimated and true values of the normalized MR signal (E) for the cases of Rician and Gaussian fit to the distribution of S/S_0 and S/m_0 . Simulations are run at (a) NEX = 2 and (b) NEX = 4.

Fig 6.1 shows the comparison of the estimated and true values of the normalized MR signal (E) for the cases of Rician and Gaussian fits to the distribution of S/S_0 and S/m_0 . For each case of NEX, the mean and the standard deviation (SD) of the relative difference of the estimated normalized MR signal (E) with respect to the true value of E,

i.e., $E-(m/m_0)$, are calculated. For NEX = 2, the mean and the SD of relative difference are $(-1.02\pm0.75)\times10^{-3}$ (for the Rician fit of S/S_0), $(1.52\pm0.62)\times10^{-2}$ (for the Gaussian fit of S/S_0), $(-2.89\pm6.89)\times10^{-5}$ (for the Rician fit of S/m_0) and $(1.23\pm0.71)\times10^{-2}$ (for the Gaussian fit of S/m_0). For NEX = 4, the mean and the SD of relative difference are $(-2.27\pm1.26)\times10^{-4}$ (for the Rician fit of S/S_0), $(7.42\pm2.87)\times10^{-3}$ (for the Gaussian fit of S/S_0), $(-4.49\pm7.05)\times10^{-5}$ (for the Rician fit of S/m_0) and $(6.02\pm3.38)\times10^{-3}$ (for the Gaussian fit of S/m_0). It is clear from these results that the Rician fit is better than the Gaussian fit of S/S_0 as the Gaussian fit is more biased as seen from the mean values of the relative difference. A similar trend is seen for the case of Rician fit of S/m_0 compared to the Gaussian fit. The bias reduces with increasing NEX from 2 to 4.

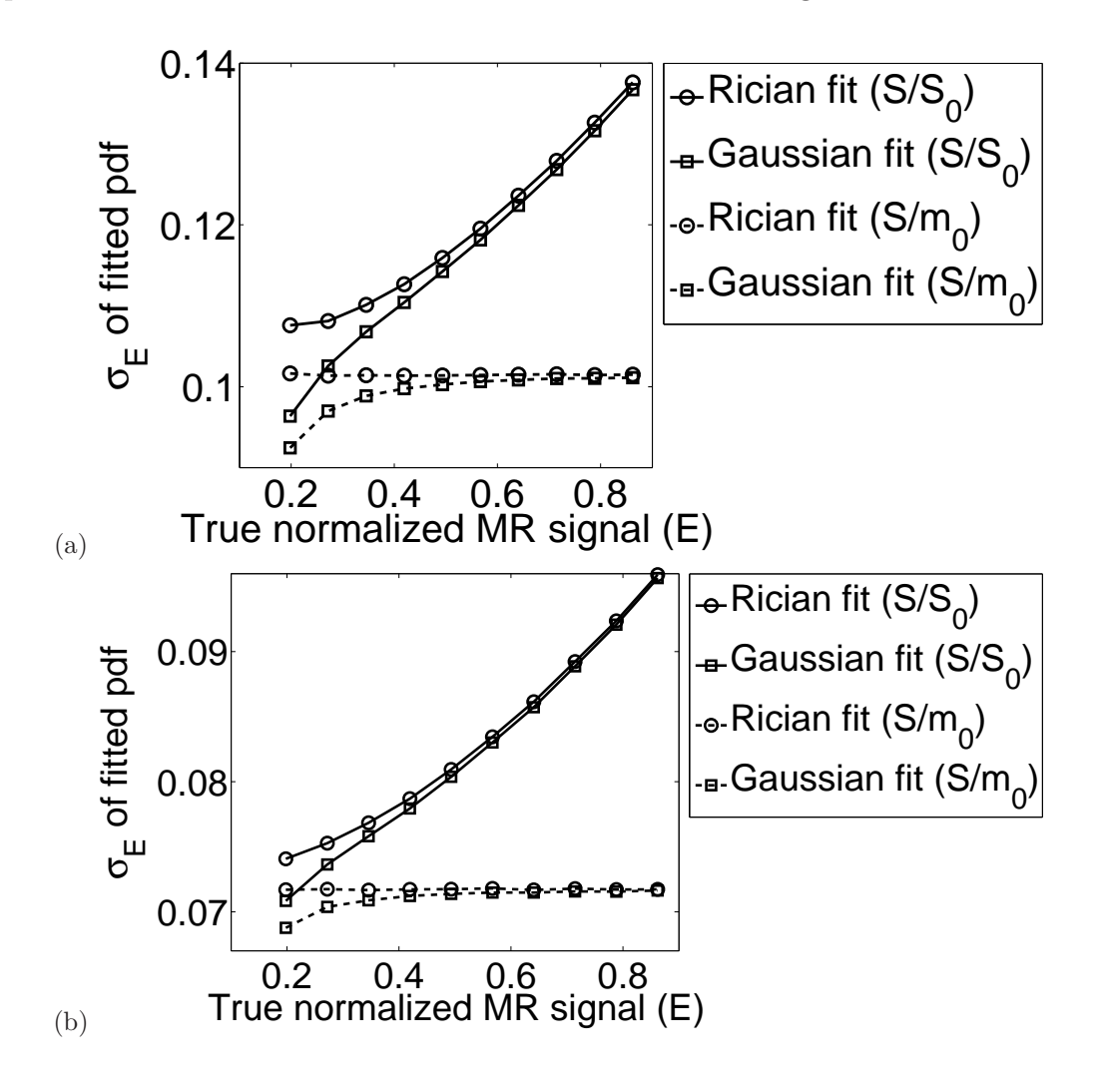


Figure 6.2. Variation of the estimated σ_E of the noisy normalized MR signal (\hat{E}) for the cases of Rician and Gaussian fits to the distributions of S/S_0 and S/m_0 respectively. Simulations are run at (a) NEX = 2 and (b) NEX = 4.

Fig. 6.2 shows the variation of the estimated σ_E for the noisy normalized MR signal for the cases of Rician and Gaussian fits to the distributions of S/S_0 and S/m_0 respectively at two values of NEX. These results indicate that while using the distribution of S/S_0 for the noisy normalized MR signal, the estimated σ_E increases with respect to the value of the true normalized MR signal E. This is true for both the Rician fit and Gaussian fit to the S/S_0 distributions. The Gaussian fit underestimates σ_E compared to the Rician fit of S/S_0 in general and more so at lower signal levels. For the NEX = 4 case, σ_E is further decreased indicating that more averaging could reduce the dependence of σ_E on E. However, when assuming $m_0 >> \sigma_0$ such that S/S_0 can be approximated to S/m_0 , the estimated σ_E for the Rician fit does not change with the true normalized MR signal. However, for the Gaussian fit of the distribution of S/m_0 , the σ_E parameter is again underestimated, the effect becoming worse at lower signal levels. In this work, I used the S/m_0 distribution and select the value of $\sigma_E = 0.1$ (for NEX = 2 case) based on the result of these simulations. However, in order to use the S/S_0 distribution and fit a Rician distribution to it, a signal-dependent σ_E has to be used. The covariance matrix definition in the CRLB formulation has to be corrected to incorporate this effect.

6.1.3 Discussion

S and S_0 are both signals with a Rician pdf since these are obtained from magnitude MR images. The exact nature of the distribution of S/S_0 has not been explored in these simulations. However, the effect of fitting the distribution of S/S_0 to a Rician and a Gaussian pdf has been demonstrated. While fitting these distributions to that of S/S_0 results in the dependence of the σ_E on the true normalized MR signal, the estimated value of E is largely unaffected since the bias shown in the estimates is negligible. The dependence of σ_E on E is further reduced by increasing NEX during signal acquisition.

In this work, it is assumed that $m_0 >> \sigma_0$ such that S/S_0 is approximately equal to S/m_0 and the Rician fit of this distribution is more appropriate. The value of m_0 is measured by a single acquisition of S_0 at NEX = 2. As shown in the simulations, using the assumption $m_0 >> \sigma_0$, σ_E can be assumed constant with respect to E. Thus, in

the CRLB formulation, the covariance matrix (Σ) of the measurements of the normalized MR signal (E) can be assumed to be $\sigma_E \mathbf{I}$ (i.e., $\Sigma = \sigma_E \mathbf{I}$), where \mathbf{I} is an identity matrix of size $N \times N$, with N being the number of measurements (equal to the number of diffusion gradient directions in the DTI experiment). However, using this assumption, the CRLB will underestimate the bound of the covariance of parameter estimation. To correct the CRLB formulation, the covariance matrix of the measurements can be redefined as a diagonal matrix to include the dependence of σ_E on E, i.e., ijth term of the covariance matrix becomes, $[\Sigma]_{ij} = {\sigma_{E_i}}$ for i = j, 0 otherwise}.

6.2 Performance of Estimators

Different estimators selected to perform the parameter estimation are evaluated for precision (uncertainty) and accuracy (bias) in the estimation of the model parameters. The selection of the estimator is essential since the performance of the model parameter estimation is determined by the estimator although the performance can be predicted analytically using the CRLB formulation. The CRLB gives a bound on the estimation uncertainty which is attained when the estimator is minimum variance, unbiased and efficient [109]. However, this is only true asymptotically (for infinite signal samples and infinitesimally small tolerance settings of the estimator). In reality, a finite tolerance setting is set for the convergence to the final solution and also a finite number of signal samples are available for the parameter estimation. Thus, estimator performance in terms of its precision and accuracy needs to be evaluated by means, such as Monte Carlo simulations and proper settings for tolerances has to be made before using the estimator for the analysis of experimental data.

DTI data being MRI magnitude data always contain Rician noise. However, if a high SNR is assumed (SNR > 5), the Gaussian approximation is reasonable. This approximation simplifies the analysis significantly and hence is more popular although inaccurate. In the simulations, different scenarios of signal and noise models are considered and the corresponding analysis is presented for them. In this section, the performance of different

estimators, namely least-squares (LS), least-squares with bias correction (LSC) and maximum likelihood estimator (MLE), are evaluated in terms of its uncertainty (precision) and the bias (accuracy) in the estimation of diffusion model parameters.

For the estimator performance evaluation, ADTI signals (using a particular gradient scheme) are injected with noise (Rician or Gaussian) and a number of trials are simulated where in each trial the parameter estimation is performed by different estimators. After the estimation, the estimation covariance matrix and its determinant are computed. Also the bias is calculated from the true parameter values. A total of 20000 realizations of the ADTI signal are generated for each set of parameter values. The following parameter values are used for the simulation: ADTI diffusion model parameters: D_{\parallel} = 1.62 × $10^{-3}~{\rm mm^2~s^{-1}},~D_{\perp}=0.148\times10^{-3}~{\rm mm^2~s^{-1}},~\phi_F=0^{\circ},~\theta_F=90^{\circ},~\sigma=0.1.~{\rm FA}=0.000$ $0.9, \mathrm{MD} = 0.638 \times 10^{-3}~\mathrm{mm^2~s^{-1}}$ Experimental settings are : $b = 1000~\mathrm{s~mm^{-2}}, \, N = 30.0$ Two gradient schemes are used: MF30 and OPT30. OPT30 is the optimized gradient scheme obtained at the same parameter values and a cone angle of $\Lambda=35^{\circ}$. Same bfactor and N are used for the optimization. Note that the θ_F is set to 90° since at 0°, the distribution of θ_F is one-sided and non-symmetric. Thus, to display the full distribution of θ_F , the fiber is directed towards the +X axis instead of the +Z axis. The estimators were: LS, LSC and MLE (for the Rician noise case) and LS only (for the Gaussian noise case). For each estimator, the settings are: maximum number of iterations = 10^5 , tolerance in variable values $= 10^{-6}$, use Levenberg-Marquardt algorithm. The purpose of this simulation exercise is to study the estimation performance of each estimator in terms of the uncertainty (standard deviation in the model parameter estimates), bias (mean signed difference (MSD)) and overall uncertainty (hypervolume of uncertainty = determinant of covariance matrix).

6.2.1 Rician noise

For the Rician noise case, noise is injected in the complex signal and ADTI signal is the magnitude of the noisy complex signal. Although the MLE seems to be the most suitable estimator for this noise model, use of LS and LSC is also considered due to their popularity

in usage. Tables 6.1, 6.2 and 6.3 show the estimation results (parameter estimates, the mean signed difference (MSD = mean($\hat{\beta} - \beta$), where $\hat{\beta}$ and β are the estimated and true values of the model parameters) and the hypervolume of uncertainty ($\sqrt{\det(\Sigma)}$) for the three estimators and for both MF30 and OPT30 gradient schemes. The performance of MLE is the best in terms of bias correction in the Rician noise injected data. Although, MLE does not have the lowest hypervolume of uncertainty, which is obtained for the LS case. This is because the estimator cost function in LS is the square of fitting error and it will give the better result for covariance matrix. However, there is more bias in the LS case as compared to MLE case. LSC estimator has better bias correction as compared to LS, but is worse in the uncertainty. Its performance is somewhat in between LS and MLE. Based on these simulations, MLE is most suitable for Rician noise based data since it can achieve comparable precision with higher accuracy.

Table 6.1. Simulation results for the least-squares (LS) estimator performance assuming Rician noise model

R	True	MF30		OPT30	
β		Est.	MSD	Est.	MSD
$D_{\parallel}(\times 10^{-3} \text{ mm}^2 \text{ s}^{-1})$	1.620	1.564 ± 0.125	-0.057	1.571 ± 0.133	-0.049
$D_{\perp}(\times 10^{-3} \text{ mm}^2 \text{ s}^{-1})$	0.149	0.143 ± 0.037	-0.006	0.142 ± 0.038	-0.006
$\theta_F(^\circ)$	90.000	89.982 ± 2.775	-0.018	89.985 ± 2.636	-0.015
$\phi_F(^\circ)$	0.000	0.025 ± 2.741	0.025	-0.008 ± 2.647	-0.008
Hypervolume ($\times 10^{-11}$)		0.970		0.931	

MSD is the mean signed difference between estimates and the true values, MSD = mean($\hat{\beta} - \beta$), where $\hat{\beta}$ and β are the estimated and true values of the model parameters. Hypervolume = $\sqrt{\det \Sigma}$, where Σ is covariance matrix of estimates.

6.2.2 Gaussian noise

For the Gaussian noise case, the noise is additive and zero mean, σ^2 variance. So, it should not create any bias in the estimates. Also, under this case, the least-squares estimator is the same as the maximum likelihood estimator [109]. Hence, for this case, only the least-squares estimator performance in shown. The Gaussian approximation holds good for SNR > 5 [114]. This is not always observed in DTI data. However, for other MRI

Table 6.2. Simulation results for the least-squares with bias correction (LSC) estimator performance assuming Rician noise model

З	True	MF30		OPT30	
β		Est.	MSD	Est.	MSD
$D_{\parallel}(\times 10^{-3} \text{ mm}^2 \text{ s}^{-1})$	1.620	$1.620 1.636 \pm 0.136$		1.637 ± 0.144	0.017
$D_{\perp}(\times 10^{-3} \text{ mm}^2 \text{ s}^{-1})$	0.149	0.146 ± 0.038	-0.003	0.146 ± 0.038	-0.003
$\theta_F(^\circ)$	90.000	89.986 ± 2.780	-0.014	89.984 ± 2.647	-0.016
$\phi_F(^\circ)$	0.000	0.028 ± 2.742	0.028	-0.007 ± 2.650	-0.007
Hypervolume ($\times 10^{-11}$)		1.078		1.034	

MSD is the mean signed difference between estimates and the true values, MSD = $\operatorname{mean}(\hat{\beta} - \beta)$, where $\hat{\beta}$ and β are the estimated and true values of the model parameters. Hypervolume = $\sqrt{\det \Sigma}$, where Σ is covariance matrix of estimates.

Table 6.3. Simulation results for the maximum likelihood (ML) estimator performance assuming Rician noise model

a	True	MF30		OPT30	
β		Est.	MSD	Est.	MSD
$D_{\parallel}(\times 10^{-3} \text{ mm}^2 \text{ s}^{-1})$	1.620 1.626 ± 0.140		0.005	1.627 ± 0.141	0.007
$D_{\perp}(\times 10^{-3} \text{ mm}^2 \text{ s}^{-1})$	0.149	0.145 ± 0.038	-0.003	0.145 ± 0.038	-0.003
$\theta_F(^\circ)$	90.000	89.986 ± 2.781	-0.014	89.998 ± 2.670	-0.002
$\phi_F(^\circ)$	0.000	-0.032 ± 2.768	-0.032	0.007 ± 2.634	0.007
Hypervolume ($\times 10^{-11}$)		1.129		1.027	

MSD is the mean signed difference between estimates and the true values, MSD = $\operatorname{mean}(\hat{\beta} - \beta)$, where $\hat{\beta}$ and β are the estimated and true values of the model parameters. Hypervolume = $\sqrt{\det \Sigma}$, where Σ is covariance matrix of estimates.

based analysis where the image has better SNR, Gaussian approximation is commonly used.

6.3 Validation of performance curves

Performance curves are validated by Monte Carlo simulations for the performance of the optimized 30-direction gradient scheme as well as the standard MF30 scheme by estimating the diffusion model parameters using different estimators and computing the covariance and its determinant. This process is repeated for a range of fiber orientation angles and the performance curves based on estimated uncertainties are generated. These are finally compared with the curves generated by CRLB formulation.

Table 6.4. Simulation results for the least-squares (LS) estimator performance assuming Gaussian noise model

$\boldsymbol{\beta}$	True	MF30		OPT30	
β		Est.	MSD	Est.	MSD
$D_{\parallel}(\times 10^{-3} \text{ mm}^2 \text{ s}^{-1})$	1.620	$20 1.634 \pm 0.134$		1.636 ± 0.140	0.016
$D_{\perp}(\times 10^{-3} \text{ mm}^2 \text{ s}^{-1})$	0.149	0.146 ± 0.038	-0.003	0.146 ± 0.038	-0.002
$\theta_F(^\circ)$	90.000	90.020 ± 2.747	0.020	89.987 ± 2.621	-0.013
$\phi_F(^\circ)$	0.000	0.001 ± 2.737	0.001	-0.012 ± 2.625	-0.012
Hypervolume ($\times 10^{-11}$)		1.042		0.993	

MSD is the mean signed difference between estimates and the true values, MSD = $\operatorname{mean}(\hat{\beta} - \beta)$, where $\hat{\beta}$ and β are the estimated and true values of the model parameters. Hypervolume = $\sqrt{\det \Sigma}$, where Σ is covariance matrix of estimates.

For each simulation for each fiber angle, 20000 realizations of the ADTI signal under noise level of $\sigma=0.1$ (Gaussian and Rician) are generated using both standard and optimized gradient schemes. The model parameter values used in the simulation are: $D_{\parallel 0}=1.62\times 10^{-3} \mathrm{mm}^2 \mathrm{s}^{-1}, D_{\perp 0}=0.148\times 10^{-3} \mathrm{mm}^2 \mathrm{s}^{-1}, \theta_F=[90-25]^\circ$ in steps of 5° and $\phi_F=0^\circ$. The optimized gradient scheme was computed at the same parameter values as mentioned except $\theta_F=90^\circ$. Thus, in terms of the angular deviation from the +X axis ($\theta_F=90^\circ$), the range of $\alpha=[0-65]^\circ$.

To verify the robustness of the scheme, the simulations were run at different fiber orientations and hence angular deviations (α) from the original fiber orientation of (90°, 0°) (Fig. 6.3). Three estimators are compared, namely, LS, LSC and MLE. The simulations were run to verify that the predicted improvement in performance shown by the CRLB formulation is also observed in practice with the selected estimators. Also by running the simulation at different angular deviations the robustness of the scheme w.r.t. angular deviation (α) is verified. Finally, the results would also show that predicted performance relate well with the estimated performance and thus to analyze a scheme, a prediction is good enough instead of performing lengthy Monte Carlo simulations.

The prediction represents a bound on the cost function. In practice, for the simulations, the estimated hypervolume $(\sqrt{\det \Sigma})$ would be different from the predicted bound. This difference will depend on the estimator tolerance settings and the number of realizations of the signal. The smaller the tolerance and the larger the number of realizations, the

closer will be the estimation to the CRLB prediction. It will also depend on the choice of the estimator since estimation will approach the predicted bound asymptotically when the estimator is a minimum variance, unbiased and efficient estimator. But, a similar trend is visible in the estimated hypervolume as compared to the hypervolume predicted from the CRLB formulation. These are observed in the Fig. 6.3.

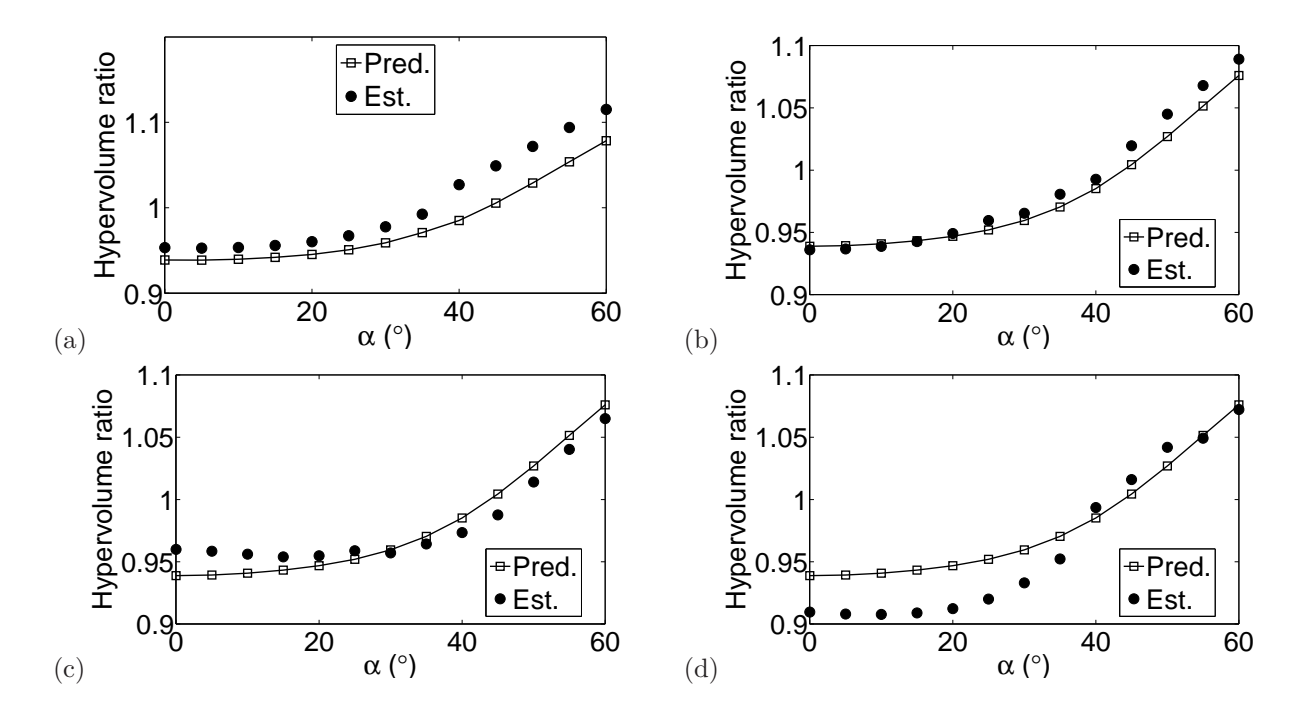


Figure 6.3. Variation of ratio of hypervolume of uncertainty $(D_{OPT}/D_{MF}, D = \sqrt{\det(\Sigma_{CR})})$ for ADTI model from Monte Carlo simulations w.r.t. angular deviation (α) at $\sigma = 0.1$, $\Lambda = 35^{\circ}$. Gaussian case with LS estimator (a) and Rician case with LS (b), LSC (c) and ML (d) estimators.

In Fig. 6.3, the cases of Gaussian and Rician noise models and the effect of optimization on the hypervolume of uncertainty has been demonstrated. For the Gaussian case (Fig. 6.3(a)), the least-squares (LS) estimator has been used and it is seen that the prediction and estimation correlate well. For the Rician noise case (Fig. 6.3(b–d)), the performance is compared for the least-squares estimator(LS) with that of least-squares with noise correction (LSC) and maximum likelihood (ML) estimators. Under similar tolerance settings for each of the estimators, it is observed that MLE has performed well for the optimized scheme. Additionally, it estimates the expected values of the parameters better than LSC estimator since it models noise directly into the estimator as has been shown

in the previous section.

6.4 Simulation for effect of b-factor, N and Λ in ADTI model

Via simulations, the effect of various parameters, including the b-factor, the number of gradient directions (N) and the cone angle (Λ) of fiber directions, on the overall uncertainty of ADTI parameters estimation was investigated. Although the focus is on the optimization of the diffusion gradient directions while keeping b-factor and the number of gradient directions fixed and assuming a certain prior cone angle (Λ) for the fiber directions, these simulations indicates the effect of other non-optimized experimental parameters.

For each simulation, a particular setting of b-factor, N, Λ and the gradient schemes are used and multiple trials are simulated. In each trial, the diffusion model parameters $(D_{\parallel}, D_{\perp}, \theta_F, \phi_F)$ and the noise level (σ) are chosen from a distribution and the cost function based on the Rician CRLB and the variance of FA are computed based on the chosen model parameters. The distribution from which model parameters are chosen incorporate spatial (voxel-to-voxel) variation observed in biological tissues. Finally, after the simulation is completed, performance indices are computed over all trials for each simulation.

6.4.1 Performance indices

Certain indices are defined to assess whether the optimized gradient scheme worked better than a standard (commonly used) gradient scheme, such as MF30 scheme [22]. These are defined in the following:

1) μ_{r1} : the mean ratio of hypervolume of uncertainties in successful trials. $\mu_{r1} = \text{mean}(r1)$, $r1 = D_{OPT}/D_{MF}$, where $D = \sqrt{\det \Sigma_{CR}}$ at each successful trial (r1 < 1) and OPT indicates the optimized scheme and MF indicates the MF-based scheme used as a reference for normalization. Since μ_{r1} is computed in successful trials only, it is always

in the range [0, 1]. A lower μ_{r1} indicates better performance.

- 2) P_S : percentage success rate denotes the number of trials (in percentage) out of total trials where the normalized hypervolume is less than unity (r1 < 1).
- 3) eSNR: effective SNR is defined as the ratio of the mean of all diffusion-weighted signals calculated in all trials over the root mean squared noise values provided in all trials. Since there are different diffusion gradient directions, there are different diffusion-weighting (and signal levels) in the DTI data. Thus, an effective signal level (averaging all diffusion-weighted signals) is used to compute the eSNR. The eSNR can indicate how effectively the diffusion gradients sample the gradient space.
- 4) σ_{FA}^2 : variance of FA is computed using the propagation of error theory [125]. It is computed as a function of the variances of the diffusivities $(D_{\parallel} \text{ and } D_{\perp})$ which are given by the Rician CRLB. It is normalized with respect to the corresponding value for the reference scheme.

6.4.2 Simulation parameters

The following diffusion model parameters and noise levels were used in the simulations (percentage variation are shown in parentheses): $D_{\parallel} = 1.6204 \pm 0.081 \times 10^{-3} \text{ mm}^2 \text{ s}^{-1} (5\%)$; $D_{\perp} = 0.14852 \pm 0.0074 \times 10^{-3} \text{ mm}^2 \text{ s}^{-1} (5\%)$; $(\theta_F, \phi_F) = (0^{\circ}, 0^{\circ})$; $\sigma = 0.1 \pm 0.005 (5\%)$; Rician CRLB; Number of trials = 10000. Other constraints include: $0.6 \leq \text{FA} \leq 1$ and MD $\leq 1.2 \times 10^{-3} \text{ mm}^2 \text{ s}^{-1}$. All varying parameters are uniformly distributed about their mean values.

 $D_{\parallel}=(1.6204\pm0.081)\times10^{-3}~\mathrm{mm^2\,s^{-1}}$ and $D_{\perp}=(0.14852\pm0.0074)\times10^{-3}~\mathrm{mm^2\,s^{-1}}$ was used for the simulation results. These values correspond to high FA voxels (average FA = 0.9) in the white matter tracts between the C1 and C2 levels of the cervical spinal cord. The values of the diffusivity parameters are based on a preliminary DTI data obtained using a standard protocol ($b=1000~\mathrm{s\,mm^{-2}}$ and MF30 gradient scheme). Similar values ($\lambda_1=1.7\times10^{-3}~\mathrm{mm^2\,s^{-1}}, \lambda_2=\lambda_3=0.2\times10^{-3}~\mathrm{mm^2\,s^{-1}}$ and a corresponding FA = 0.87) have been used in previous simulation experiments in the works of Alexander [23], Peng et al. [21] and Gao et al. [39]. The simulations in this work were performed

using diffusivity values with high FA since these values are representative of the white matter tract regions and not are contaminated by the gray matter or CSF regions.

6.4.3 Effect of b-factor

Simulations were run using diffusion model parameters defined previously and varying the b-factor between $b = 1000 \text{ s mm}^{-2}$ and 4500 s mm^{-2} ($b = [1000, 1200, 1500, 2000, 2500, 3000, 3500, 4000, 4500] \text{ s mm}^{-2}$). The cone angle, $\Lambda = 35^{\circ}$ and number of diffusion gradients, N = 30 were used for all the cases. For each case of b-factor, an optimized gradient scheme was generated and its performance indices were computed using MF30 at $b = 1000 \text{ s mm}^{-2}$ as the normalization reference scheme. Similarly, simulations were run with MF30 at different b-factors and the indices were computed with respect to the same reference scheme (i.e., MF30 at $b = 1000 \text{ s mm}^{-2}$).

For both the optimized and MF30 schemes, the performance (based on indices μ_{r1} and P_S) only improves within a certain range of b-factor (Fig. 6.4 (a) and (b)). However, for the optimized case, the range of high performance is broader than the MF30 case. A similar trend is seen for variance of FA. This effect was also demonstrated by Gao et al. [39] where they have showed that when a cone angle of fiber distribution is used for optimizing the diffusion gradient, the b-factor range increased as compared to an un-optimized (MF-based) scheme.

Generally, changes in the b-factor is restricted by the MRI scanner gradient strength limitation and the SNR. It can be clearly seen from the simulation (Fig. 6.4 (c)) that the effective SNR decreases with the increase of the b-factor. However, the optimized scheme shows better SNR compared to MF30 at higher b-factors. A commonly used b-factor in DTI experiment is 1000 s mm⁻² (for example, in [62]) and this was used in the ADTI experiments. The optimized gradient scheme depends on the selection of the b-factor and the performance of the optimized scheme varies with the changes to the b-factor as shown in these simulations.

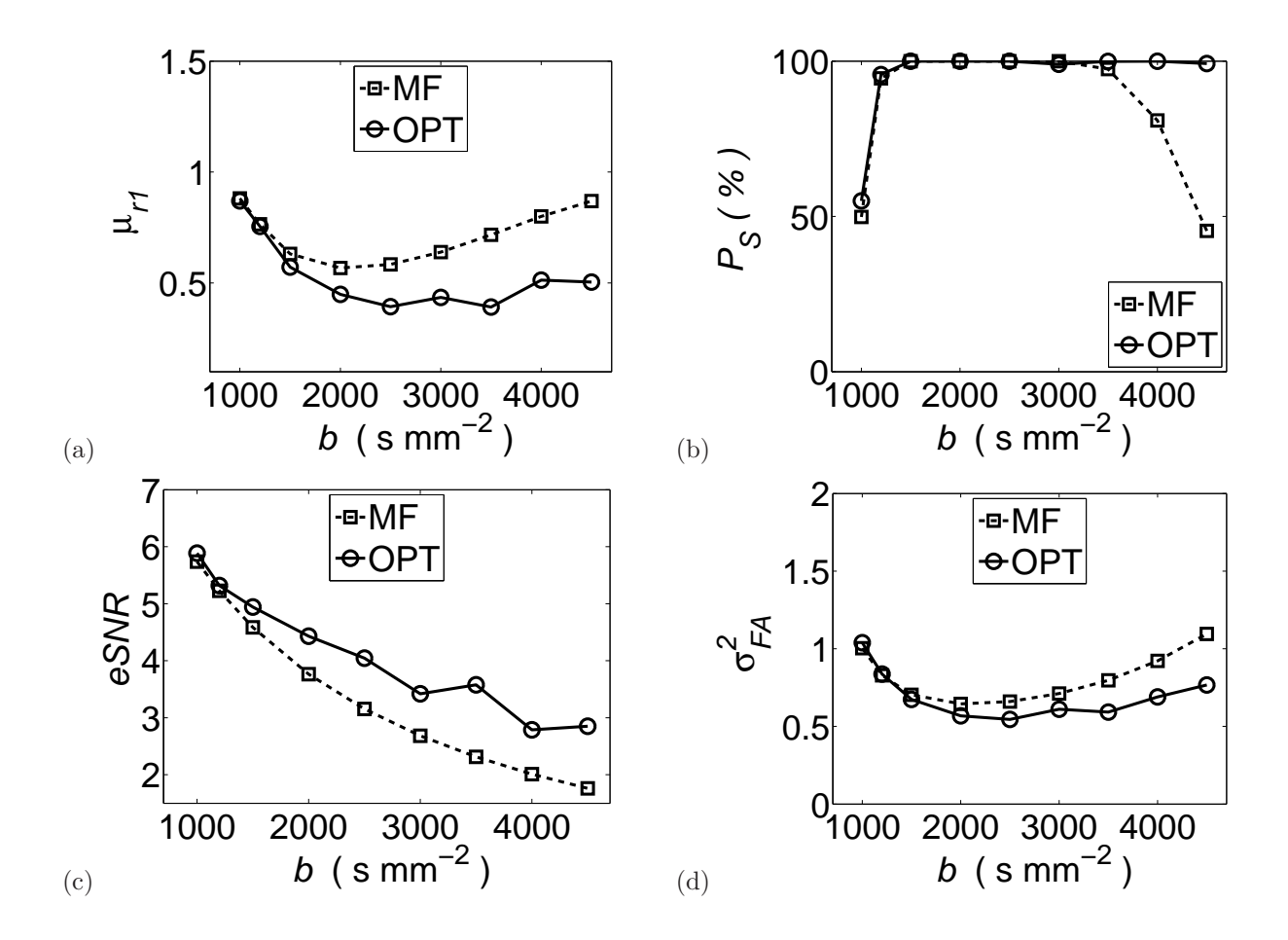


Figure 6.4. Effect of varying b-factor on the diffusion gradient optimization. Performance indices (a) normalized hypervolume for successful trials (μ_{r1}) , (b) percentage success rate (P_S) , (c) effective SNR (eSNR) and (d) normalized variance of FA (σ_{FA}^2) are shown for different b-factors and for both the optimized gradient schemes (OPT) and the MF30 scheme (MF).

6.4.4 Effect of number of diffusion gradient directions (N)

Studies based on DTI showing the effect of number of gradient directions on noise propagation indicate that a higher number of gradient directions is preferred over signal averaging when characterizing noise sensitivity for a DTI gradient scheme [125]. In this section, the effect of number of diffusion gradient directions on the overall performance of the parameter estimation is investigated under the Rician CRLB formulation.

Simulations were run using diffusion model parameters defined previously and a varying number of diffusion gradients (N) from 20 to 80 (N = [20, 30, 40, 50, 60, 80]). For each case of N, an optimized schemes was generated and its performance indices were computed with MF15 (N=15) as a reference. Similarly, the MF-based schemes were simulated at

various N values and MF15 was used as the reference. Two b-factors, $b=1000~{\rm s~mm^{-2}}$ and 2500 s mm⁻² and a cone angle of $\Lambda=35^{\circ}$ in all cases were used.

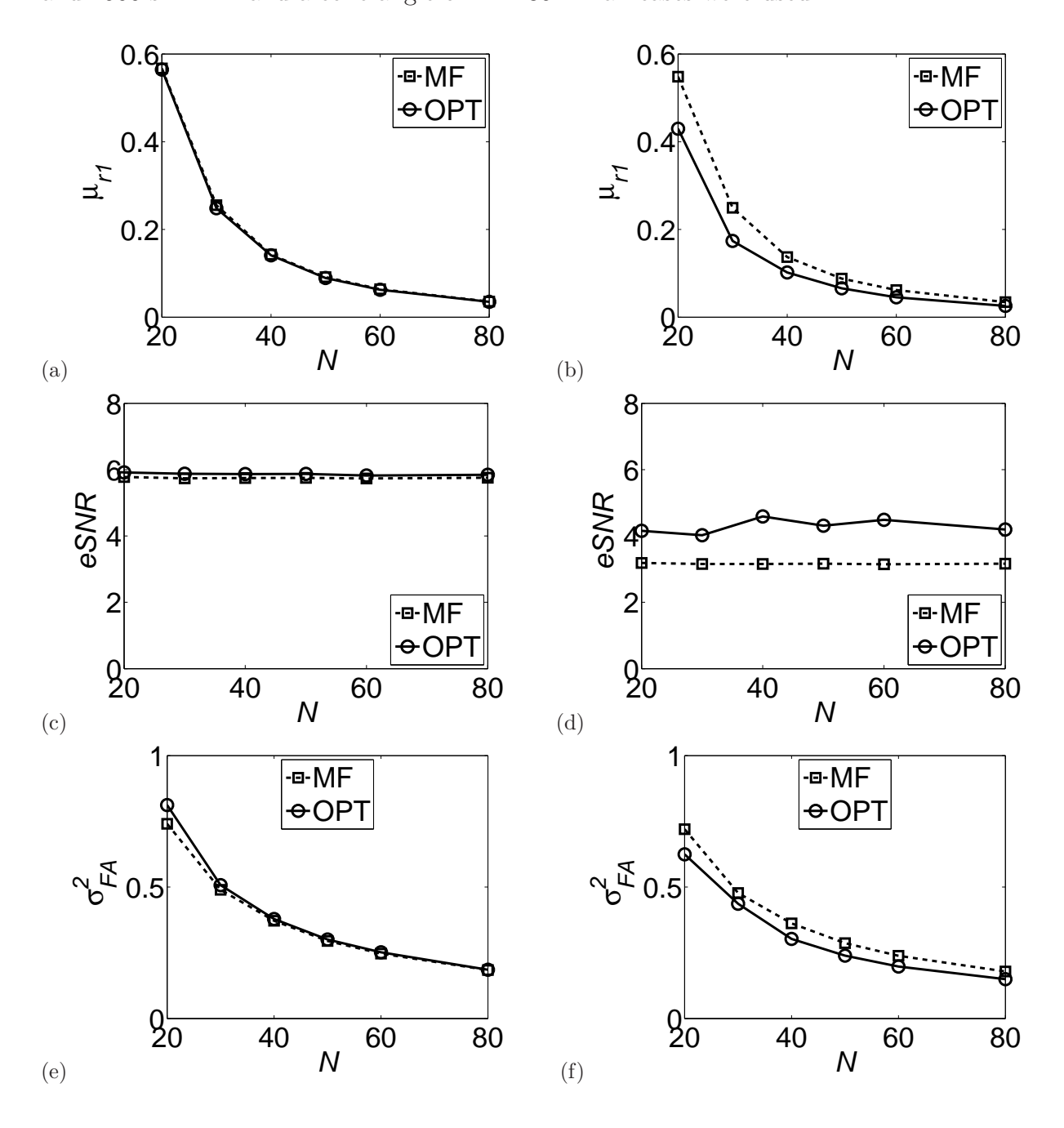


Figure 6.5. Effect of varying number of diffusion gradients (N) on the diffusion gradient optimization. Normalized hypervolume for successful trials (μ_{r1}) ((a) and (b)), effective SNR (eSNR) ((c) and (d)) and normalized variance of FA (σ_{FA}^2) ((e) and (f)) are shown for different N and for both the optimized gradient schemes (OPT) and the MF-based schemes (MF). Figures (a), (c) and (e) are for b = 1000 s mm⁻², whereas figures (b), (d) and (f) are for b = 2500 s mm⁻².

Based on Fig. 6.5, μ_{r1} in general decreases with the increase in N for both the optimized

and MF30 schemes. This is expected since more samples lead to a lower CRLB. But, at a higher b-factor ($b = 2500 \text{ s mm}^{-2}$), better performances are achieved with a lower number of gradients as compared to the corresponding MF case. This result suggests that the number of gradient directions and equivalently the scan time can be reduced to obtain the same performance as the MF scheme. The effective SNR is steady with respect to changes in N. Normalized variance of FA correlates well with μ_{r1} as the number of diffusion gradients increases. N = 30 was selected for the ADTI experiments. This provides good performance with μ_{r1} and also eSNR. This is also a commonly used number of diffusion gradients reported in other studies.

6.4.5 Effect of Cone angle (Λ)

In the diffusion gradient scheme optimization, an *a priori* range of fiber orientation angles is assumed as defined by the cone angle (Λ). It signifies the uncertainty of fiber orientations in the ROI voxels. This uncertainty can vary from a small angle ($\Lambda = 10^{\circ}$) to a completely uncertain case ($\Lambda = 90^{\circ}$). The performance will vary depending on the choice of the Λ parameter during optimization.

For the simulations, diffusion model parameters defined previously were used along with Λ varying from 10° to 90° ($\Lambda = [10\ 20\ 35\ 40\ 60\ 90]^\circ$). A b-factor of 1000 s mm⁻² and N = 30 are used for all simulations. For each value of Λ , an optimized scheme is generated and performance indices are computed with MF30 as a reference. The normalization reference was MF30 with $b = 1000\ \text{s}\,\text{mm}^{-2}$. As shown in Fig. 6.6, μ_{r1} increases with the cone angle. Both P_S and the effective SNR decrease with the increase in the cone angle. But these do not change for MF30. The changes in the performance indices (μ_{r1} and P_S) reach steady state after approximately a cone angle of 40° and remains approximately steady till 90°. At completely uncertain case of $\Lambda = 90^\circ$, the optimized gradient scheme performs similarly as MF30. The variance of FA shows an opposite trend as compared to μ_{r1} . It decreases with the increase in the cone angle (Λ) till about 40° where it reaches a plateau and then begins to increases. No changes are seen for MF30. This could be explained from the fact that when smaller cone angles are used for gradient optimization,

the optimization can get too specific and reduces the uncertainty of the fiber direction parameters (θ_F and ϕ_F) and not diffusivities (D_{\parallel} and D_{\perp}). However, after $\Lambda=40^{\circ}$, this effect is reduced. The variance of FA is a function of the variances of the diffusivities (D_{\parallel} and D_{\perp}). The optimization need not provide a reduction of uncertainty in estimation of both the angular parameters (θ_F and ϕ_F) and the diffusivities (D_{\parallel} and D_{\perp}) concurrently. However, it does provide a scheme with reduced overall uncertainty. This can be explained since D-optimality uses determinant of the CRLB which is essentially the product of the variances of the diffusion model parameters. Thus, although the determinant of CRLB is reduced by optimization, all individual variances are not concurrently reduced.

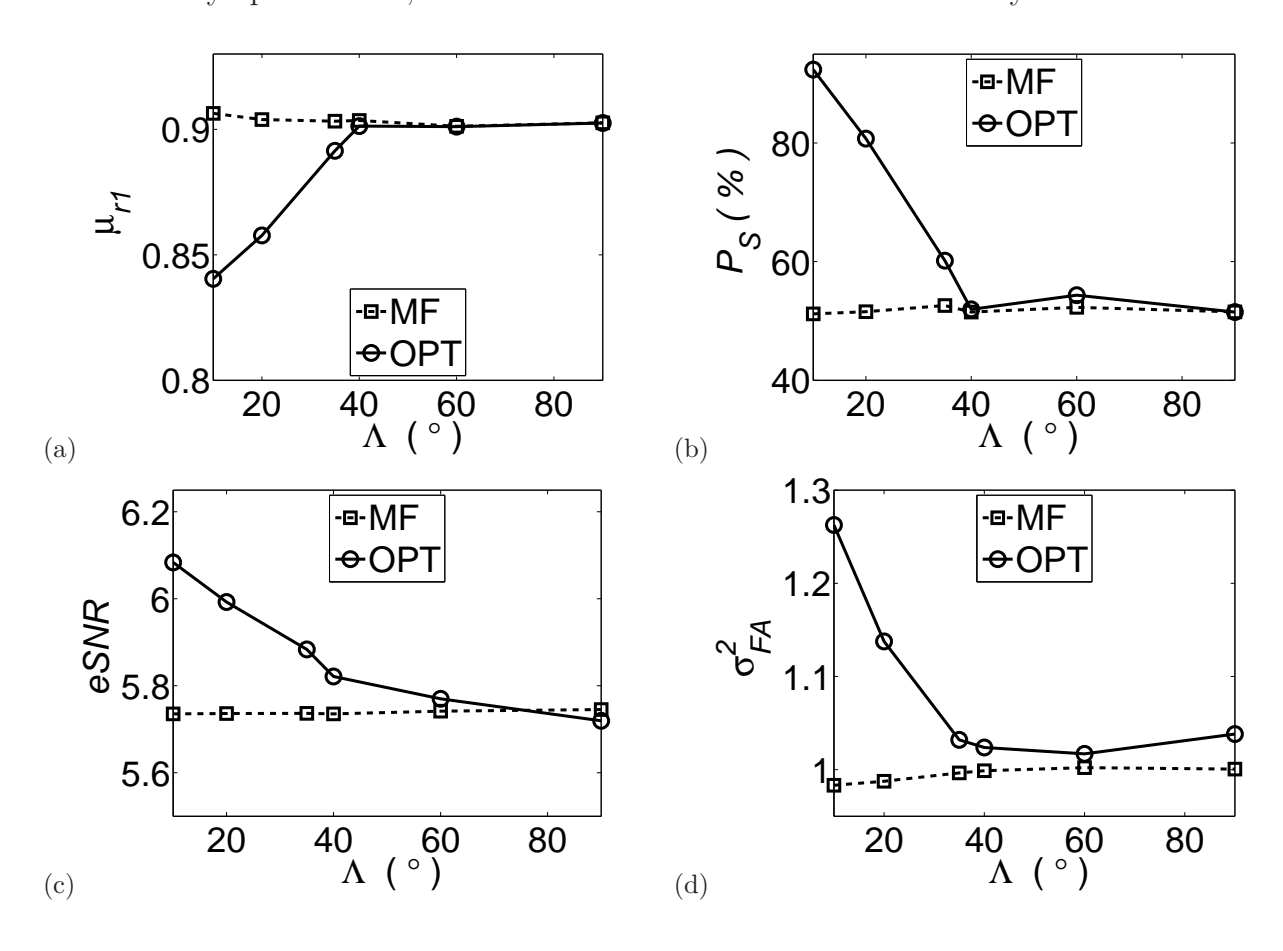


Figure 6.6. Effect of varying cone angle (Λ) on diffusion gradient optimization. Performance indices (a) normalized hypervolume for successful trials, (μ_{r1}), (b) percentage success rate (P_S), (c) effective SNR (eSNR) and (d) normalized variance of FA (σ_{FA}^2) are shown for different Λ and for both the optimized gradient schemes (OPT) and the MF30 scheme (MF).

6.4.6 Selection of b-factor, N and Λ

The selection of the experimental settings for b-factor and the number of gradient directions (N) as well as the prior structural information in cone angle Λ is vital for the performance of the gradient optimization procedure. As shown in the previous section, b-factor can have an optimal value for best estimation performance in uncertainty reduction under the diffusion model parameter values used for the simulation. This observation was exploited in the b-factor optimization in Chapter 5, section "b-factor optimization". Due to hardware constraints on the MRI scanner, the optimal b-factor need not be achievable. Also, it is observed that higher b-factor, lower is the eSNR. Since the cost function (determinant of the CRLB matrix) does not include any SNR term directly, an optimization for b-factor based on CRLB only need not have the best eSNR performance. Based on these arguments, it is suggested that while performing b-factor optimization, an additional constraint on eSNR can be applied to the optimization problem (for example, eSNR > 4). Also, MRI hardware limitations can also be incorporated as a limit on the values b-factor can take during it's optimization.

For the selection of the number of diffusion gradients, it is observed that the higher the number of gradients, the better the estimation performance is in terms of estimation uncertainty. However, more gradients requires a longer acquisition time. N=30 is used commonly and will be used for this work. Also, as shown before, similar estimation performance can be achieved by fewer gradients when gradient optimization is performed. This can be used to reduce the acquisition time.

The prior structural information as given by the cone angle (Λ) is best obtained from a preliminary scan on each subject. A $\Lambda=35^{\circ}$ is generally found in most subjects. Although, smaller cone angle would mean lower uncertainty in the fiber orientation estimation, but performance of the diffusivities estimation is affected at this angle. On the other hand, at higher cone angles, the uncertainty in fiber orientation is affected. Using a preliminary DTI scan makes sure that the subject-to-subject variability is considered during gradient scheme optimization and also that extremes in Λ are not selected, such as $\Lambda=0^{\circ}$ (completely certain fiber orientation) or $\Lambda=90^{\circ}$ (completely uncertain fiber

6.5 Comparison of performance indices for optimized gradient schemes

In this section, gradient schemes designed for the ADTI and the DTI diffusion model with Rician noise and optimized for all parameters, diffusivities only and angular parameters only cases (in Chapter 5, section 5.5) are evaluated in terms of the performance indices, such as P_S , μ_{r1} and eSNR. Also, the CRLB of variance of individual diffusion model parameters and FA, MD and α are compared in the evaluation of the gradient scheme.

A series of simulations are performed for the evaluation with each simulation consisting of a number of trials. At each trial, the normalized MR signal and the sensitivities are calculated based on the Rician CRLB which uses diffusion model parameter values and the experimental settings (b-factor, gradient scheme). Diffusion model parameter values are obtained from a uniform distribution with specified means and variances. This simulates the spatial variation of the diffusion parameter values in a tissue. Experimental settings are kept fixed within a simulation. Simulations are performed for both the OPT30 and MF30 schemes and finally, for each simulation, the performance indices and variance bounds are computed.

For the distribution of diffusion model parameter values, the mean values are specified in Chapter 5, section 5.5 and the standard deviation for diffusivities is 5% of the mean. The fiber angles are uniformly distributed within the cone angle. Also the noise standard deviation is 5% of central value which simulates the spatial variation of the noise parameter, σ , within a tissue.

Three cases of gradient optimization are considered, namely, gradients optimized for all parameters ("All"), for diffusivities only ("Diffusivities only") and for angular parameters ("Angles only") for fiber orientation only.

Table 6.5. Simulation results for the ADTI optimized gradient scheme for Rician noise model

	A	A 11	Diffusivities		Angles only	
			only			
	P_S	μ_{r1}	P_S	μ_{r1}	P_S	μ_{r1}
HyperVol	74.3	0.959	65.8	0.962	84.1	0.950
$\sigma_{D_{ }}^2$	1.1	0.995	71.3	0.980	0.3	0.998
$\sigma_{D_{\perp}}^{2}$	32.3	0.942	70.0	0.884	59.5	0.969
σ_{FA}^2	26.6	0.949	72.8	0.876	42.6	0.976
σ_{MD}^2	4.3	0.999	21.4	0.956	0.0	0.0
$\sigma_{\theta_F}^2$	99.8	0.899	7.2	0.975	71.4	0.949
$\sigma_{\phi_F}^2$	56.0	0.932	7.1	0.957	76.9	0.931
σ_{α}^{2}	65.0	0.925	6.1	0.958	56.8	0.946

6.5.1 ADTI model

In Table 6.5, the simulation results show the effect of using optimized gradients on the variance of the individual diffusion model parameters, FA, MD and α using performance indices. For the "All" parameters case, the overall reduction in the hypervolume of uncertainty (as shown by a 74.3% success rate at 0.959 hypervolume ratio) also results in the reduction of variance of the angular parameters and α . However, the effect on the variance of diffusivities is not significant. The eSNRs are 5.737 for MF30 and 5.859 for OPT30 schemes for this case. For the "Diffusivities only" case, the percentage success is smaller than the "All" parameter case. However, the effect on the variance of D_{\parallel} and D_{\perp} is significant. Since the optimization cost function is to minimize the uncertainties in the diffusivities only, the variances of angular parameters are not reduced sufficiently by gradient optimization. The eSNRs are 5.736 for MF30 and 5.702 for OPT30 for this case. The variance of FA is also reduced sufficiently. But, the variance of MD is not reduced sufficiently. For the "Angles only" case, the reduction in the cost function results in the reduction in the expected variances of θ_F and ϕ_F . This is an expected and a desired result. Effect on the variances of the diffusivities is less significant which is also expected. The eSNRs are 5.740 for MF30 and 5.872 for OPT30 for this case. Except for the "Diffusivities only" case, the eSNR is always improved by gradient optimization.

6.5.2 DTI model

Table 6.6. Simulation results for the DTI optimized gradient scheme for the Rician noise model

	All		Diffusivities		Angles only	
			only			
	P_S	μ_{r1}	P_S	μ_{r1}	P_S	μ_{r1}
HyperVol	100.0	0.759	100.0	0.797	99.6	0.923
$\sigma_{D_{ }}^2$	0.0	0.0	0.0	0.0	32.8	0.962
$\sigma_{D_{\perp 1}}^2$	100.0	0.806	100.0	0.768	81.3	0.957
σ_{D+2}^2	100.0	0.816	100.0	0.688	100.0	0.814
σ_{FA}^{2}	28.1	0.976	25.6	0.952	40.9	0.955
σ_{MD}^2	0.0	0.0	0.0	0.0	40.6	0.965
$\sigma_{\theta_F}^2$	85.9	0.910	78.2	0.809	98.1	0.872
$\sigma_{\phi_F}^2$	89.5	0.911	53.9	0.937	68.1	0.958
σ_{α}^{2}	79.8	0.915	55.7	0.874	92.8	0.921

From the simulation results in Table 6.6, it is observed that while the hypervolume of uncertainty is reduced with $P_S > 99\%$ for all the cases, the reduction is not consistent in all the diffusion model parameters, especially D_{\parallel} and MD where the uncertainty is not reduced for the "All" and the "Diffusivities only" cases compared to MF30. This can be explained referring to the sensitivity plots in Figs. 5.4 - 5.7 where it is observed that the majority of the high square sensitivity regions lie transverse to the fiber orientation (for all parameters except D_{\parallel}) and as such the optimization framework selects the transverse region predominantly. The high square sensitivity region for D_{\parallel} lies towards the fiber orientation which the framework does not sample. This effect is more pronounced in the "All" parameters and "Diffusivities only" cases since here the majority of the higher square sensitivity regions are transverse to the fiber orientation. Interestingly, in a counterintuitive sense, this effect is less observed for the "Angles only" case due to an overlap in the high square sensitivity regions for the fiber angles (θ_F, ϕ_F) and D_{\parallel} (see Figs. 5.4 -5.7). This effect was not significantly observed in the ADTI case since the high sensitivity regions are more overlapping than DTI and hence a common optimal region can be obtained by optimization. Thus, using D-optimality criterion need not optimize the

gradients to improve the precision of all diffusion model parameters simultaneously, but it will reach an overall optimal state w.r.t. the majority of the chosen model parameters. The eSNR values were 4.735 for "All" case, 4.627 for "Diffusivities only" case and 4.485 for the "Angles only" case compared to 4.216 for MF30, indicating an improvement in SNR.

CHAPTER 7

Spinal cord axisymmetric diffusion tensor imaging

7.1 A validation study for gradient scheme optimization

In this section, a diffusion gradient optimization procedure is developed that is based on D-optimality [33,34] for the ADTI model which reduces the overall uncertainty in the estimation of diffusion model parameters in the cervical spinal cord and brain stem region. The optimized gradient scheme is designed to perform within a cone of fiber directions with the mean fiber orientation being the axis of the cone. The cone angle is determined by the *a priori* knowledge of the spinal cord structure obtained from preliminary DTI experiments. The performance of the optimal scheme was compared with the MF-based gradient scheme in terms of various performance indices defined in Chapter 6 previously and also directly comparing the estimated standard deviations of different diffusion model parameters. Also, the Rician noise model [23,74] than Gaussian noise model has been used to improve the estimation accuracy.

7.1.1 Experimental Protocol

To experimentally validate the optimization framework, MRI data was collected with the diffusion gradient directions optimized for a cone of fiber directions with the b-factor and the number of gradient directions fixed (as used in routine MRI experiments). This study was approved by the Institutional Review Board (IRB) for conducting research on human subjects. Five healthy subjects (4 males, 1 female, average age 29 years) participated in this study and provided their signed IRB-approved informed consent. The following steps were performed:

1) Preliminary scan to collect a priori information: A preliminary DTI scan was performed on the upper spinal cord and the brain stem region with a 15-direction MF-based gradient scheme (MF15). The T2 and diffusion-weighted images were acquired using a dual spin-echo EPI sequence on a 3T GE Signa HDx scanner (GE Healthcare, Waukesha, WI), equipped with an 8-channel head coil with the following parameters: 22 contiguous 3-mm axial interleaved slices, $T_R = 7000$ ms, $T_E = 77.4$ ms, matrix size =128 x 128, FOV = 16 cm x 16 cm, number of excitations = 1, parallel imaging acceleration factor = 2, b $= 1000 \text{ s mm}^{-2}$, 15 diffusion gradient directions (MF15) and scan time = 1 min 52 sec. The subject exited the scanner and was scanned again after the optimized gradients were calculated. For the post-processing of the preliminary data, MD, FA, the ADTI model parameters $(D_{\parallel}, D_{\perp}, \theta_F, \phi_F)$ and angular deviation (α) from the mean fiber orientation were computed for each voxel. After visually locating the spinal cord from the T2 image, an automatic ROI voxel selection was performed by applying the following thresholds to extract the spinal cord tracts: FA \geq 0.6 (for high anisotropy), MD \leq 2.5 \times $10^{-3} \rm mm^2~s^{-1}$ (for removing CSF) and α corresponding to 80% of the distribution of fiber orientations (to select majority of the tract voxels). Fig. 7.1 shows the process of selection of the ROI voxels in the white matter tracts of the cervical spinal cord and brain stem regions. For the ROI voxel extraction (shown in Fig. 7.1), a cuboidal region enclosing the spinal cord below the C1 vertebral level and up to the C2 vertebral level was initially selected manually. However, this region contains white matter tracts as well as the gray matter in the spinal cord and CSF in the surroundings. To eliminate the gray matter and CSF region voxels, an FA (FA > 0.6) and MD (MD < 2.5×10^{-3} mm² s⁻¹) based thresholding was applied to the manually selected region. FA values of 0.6 or above have been previously reported [28,69] in the cervical spinal cord region of healthy subjects. The high FA threshold ensures minimal contamination of the ROI voxels with gray matter which cover a significant portion of the spinal cord. The presence of gray matter or CSF in the ROI voxels will result in lower overall FA estimation since gray matter or CSF regions are inherently less anisotropic in terms of diffusion than the white matter tracts. Since the main focus of the study is on normal healthy subjects, this thresholding method worked well in extracting the white matter tracts and reducing contamination by gray matter and CSF regions. Also, for the brain stem region, this method was applied to extract only the healthy white matter tracts (shown in Fig. 7.1). Table 7.1 shows the mean values of diffusivity and the cone (Λ) values used for the design of the optimized gradient table for different subjects.

Table 7.1. Average diffusivities and cone angles from preliminary DTI experiment data of five subjects

Subjects	$D_{\parallel} \times 10^{-3}$	$D_{\perp} \times 10^{-3}$	Λ
	$(mm^2 s^{-1})$	$({\rm mm}^2~{\rm s}^{-1})$	(°)
1	1.819	0.233	35
2	1.494	0.159	35
3	1.388	0.176	35
4	1.791	0.178	35
5	1.909	0.321	40

2) Gradient scheme optimization: The optimized gradient schemes were designed offline based on the information obtained from the preliminary DTI experiment and solving the cost function for robust optimization (minimizing $\det(\Sigma_{CR})$). A b-factor = 1000 s mm⁻² and $\sigma = 0.1$ was selected for the procedure. The selection of noise level (σ) is specific to the MRI scanner used since it depends on the state of the scanner. From previous DTI studies not reported in this paper, σ was found to be approximately 0.1 and has been used in the gradient optimization. Fig. 7.2(a) shows the designed gradient scheme for one of the subjects. The scheme for this subject was designed with $\Lambda = 35^{\circ}$ and the number of rings used in this design was 7 (P = 7, $N_r = \{2, 2, 2, 4, 4, 6, 10\}$).

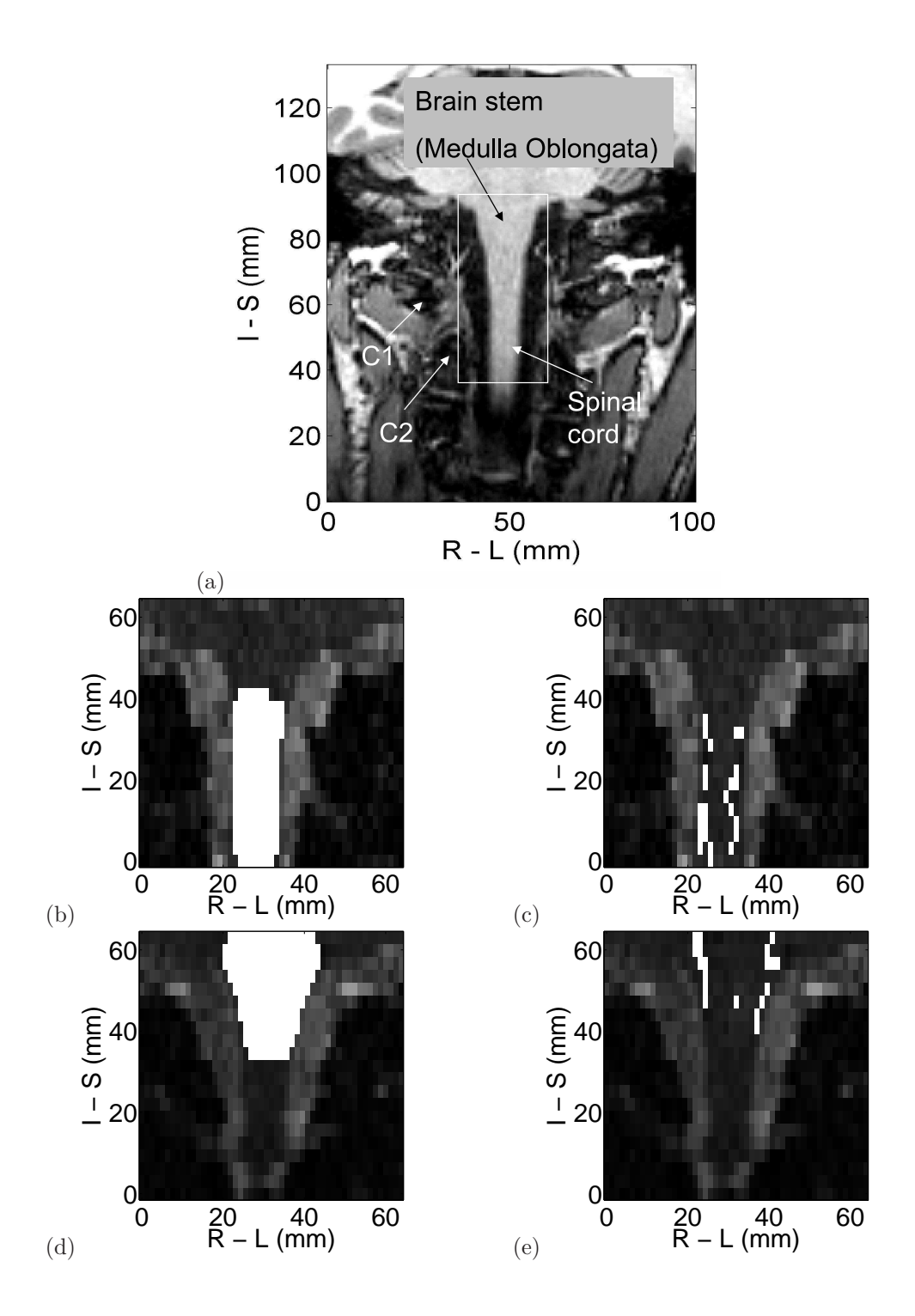


Figure 7.1. (a) T1 coronal view of the cervical spinal cord and brain stem near the C1 - C2 vertebral region. The boxed region is selected manually and further magnified in (b) (e). (b) T2 coronal image showing the segmented spinal cord within the initial ROI in (a) after removal of the CSF surrounding the spinal cord by MD thresholding. (c) T2 coronal image showing the selected white matter ROI voxels in (b) after removal of gray matter voxels by FA thresholding. Similarly, the brain stem region is first manually selected in (a), and then thresholded in two stages, (d) and (e), to extract the ROI voxels.

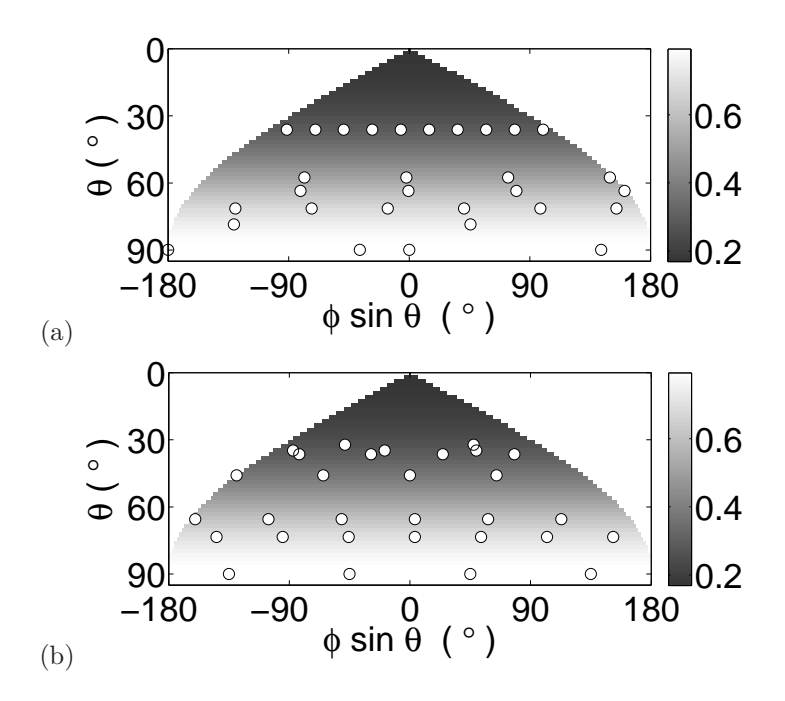


Figure 7.2. Optimized gradient scheme (white circles) for 30 gradient directions on a 2D opened hemisphere for cone angles (a) $\Lambda = 35^{\circ}$ (b) $\Lambda = 90^{\circ}$ (completely uncertain fiber orientation case). Underlying grayscale image shows the normalized MR signal levels over the hemisphere changing with respect to the diffusion gradient direction (θ, ϕ) . Mean fiber orientation is at $(0^{\circ}, 0^{\circ})$.

The procedure took about 20 minutes for each subject.

3) Data collection and analysis with the optimized ADTI protocol: The main ADTI experiment was conducted with the same MRI protocol as the preliminary scan except that the 30-direction optimized diffusion gradient scheme (OPT30) was used and number of excitations = 2 (for additional SNR improvement). The scan time per dataset was 7 min 21 sec. For comparison purpose, an equivalent dataset was acquired with the MF30 gradient scheme. Six data sets were acquired with each gradient scheme on each subject to have sufficient data for covariance computation. For subject-wise post-processing, the data sets were first linearly registered (using FLIRT in FSL [126]) to align the spinal cords. Next, the automatic ROI selection was performed by applying thresholds described in step 1 to identify the common voxels amongst the 12 data sets. The normalized MR signal (E) was calculated by normalizing the diffusion-weighted MR signals with a non-diffusion-weighted $(T_2$ -weighted) value for each ROI voxel.

7.1.2 Statistical Analysis

The sample size was increased from originally 6 data sets (for each gradient scheme) to 6000 data sets using a repetition bootstrap resampling technique [127]. Due to limitations on collecting large amounts of data for each subject, bootstrap resampling techniques are performed to compute statistics of a representative sample set of the subject data. Theoretically, if the subject were to be scanned indefinitely, only then the true values of the parameters can be estimated. However, in reality it is not possible. Via computer simulations, a large data set can be generated. But, in the case of DTI experiment, large dataset can not be collected due to time constraints. Thus, only a representative data set (for example, 6 data sets for each gradient scheme and each subject) is collected and by resampling, a large dataset is generated which can be used to compute statistics, such as the covariance matrix. The resampling technique in this work incorporated a sampling with replacement within the original data sets. For each subject, 6 datasets of 30-direction diffusion-weighted data were collected. Thus, for each diffusion-weighted volume corresponding to a diffusion gradient direction, there are 6 volume data. During repetition bootstrap, secondary datasets of 30-direction diffusion-weighted data are generated by selecting with replacement diffusion-weighted volumes from the 6 original data set. This process can be repeated for 6000 times to generate the bootstrapped datasets. Also, while performing the bootstrapping, the mean of the measured DTI signal from the original datasets was preserved such that the sample mean of the final dataset (with 6000 data) was the same as the original dataset. This ensured that the technique did not inject an artificial bias into the measured DTI signal.

The bootstrapped data from the common voxels (ROI voxels) were used for estimating the diffusion parameters and their mean and covariances. Maximum likelihood estimator (MLE) [117] using the Rician noise model was used for the diffusion parameter estimation. The covariance matrix (for estimated model parameters), its determinant and square root (hypervolume of uncertainty, for example, $D_{OPT} = \sqrt{\det \Sigma_{OPT}}$) were computed at the ROI voxels. The performance indices, P_S and μ_{r1} , and the eSNR were computed over the ROI voxels for each subject data.

Unpaired t-tests (left-tailed and assuming unequal variance) were performed for comparing the estimated hypervolume of uncertainty and the standard deviations (root-mean-squared (RMS)) of the model parameters $(D_{\parallel}, D_{\perp}, \theta_F \text{ and } \phi_F)$ and FA over the ROI voxels. The mean values of diffusivities $(D_{\parallel} \text{ and } D_{\perp})$ and the angular deviations (α) and the standard deviations of model parameters and FA over ROI voxels are also reported.

7.1.3 Results for optimization using cone of fibers obtained from a priori information

The reduction in estimation uncertainty is demonstrated in Fig. 7.3 through the distributions of the ratio of the hypervolumes of uncertainty for five subjects. D_{OPT30} and D_{MF30} are the hypervolumes of uncertainty for the optimized and MF30 schemes respectively. For the estimation, the hypervolumes are computed from the estimated covariance matrix using MLE. For the prediction, these correspond to the hypervolume bound defined by the Rician CRLB. Table 7.2 shows the estimation results on a subject-by-subject basis and supports the following observations:

- 1) Reduction in uncertainty: More than 62% voxels demonstrate estimation uncertainty reduction for all subjects as indicated in P_S in Table 7.2. The mean ratio in successful voxels, μ_{r1} , is much less than unity in all cases showing improvement in overall uncertainty reduction. Table 7.2 also shows that the improvement in uncertainty is accurately predicted based on the CRLB formulation. D_{OPT30} is significantly less than D_{MF30} on three subjects and approach significance in two subjects.
- 2) Standard deviations of model parameters: For the angular model parameters, θ_F and ϕ_F , the standard deviations (RMS) over the ROI voxels always show improvement for the optimized ADTI protocol compared to MF30 scheme (Table 7.4). The t-test shows that the results approach significance. The standard deviations for the diffusivities and FA indicate improvement, but not consistently for all the cases (Table 7.5). The optimization reduces the overall uncertainty but not necessarily the uncertainty for all model parameters concurrently.
 - 3) Mean of the estimates: The mean of the estimates of diffusivity values (D_{\parallel} and

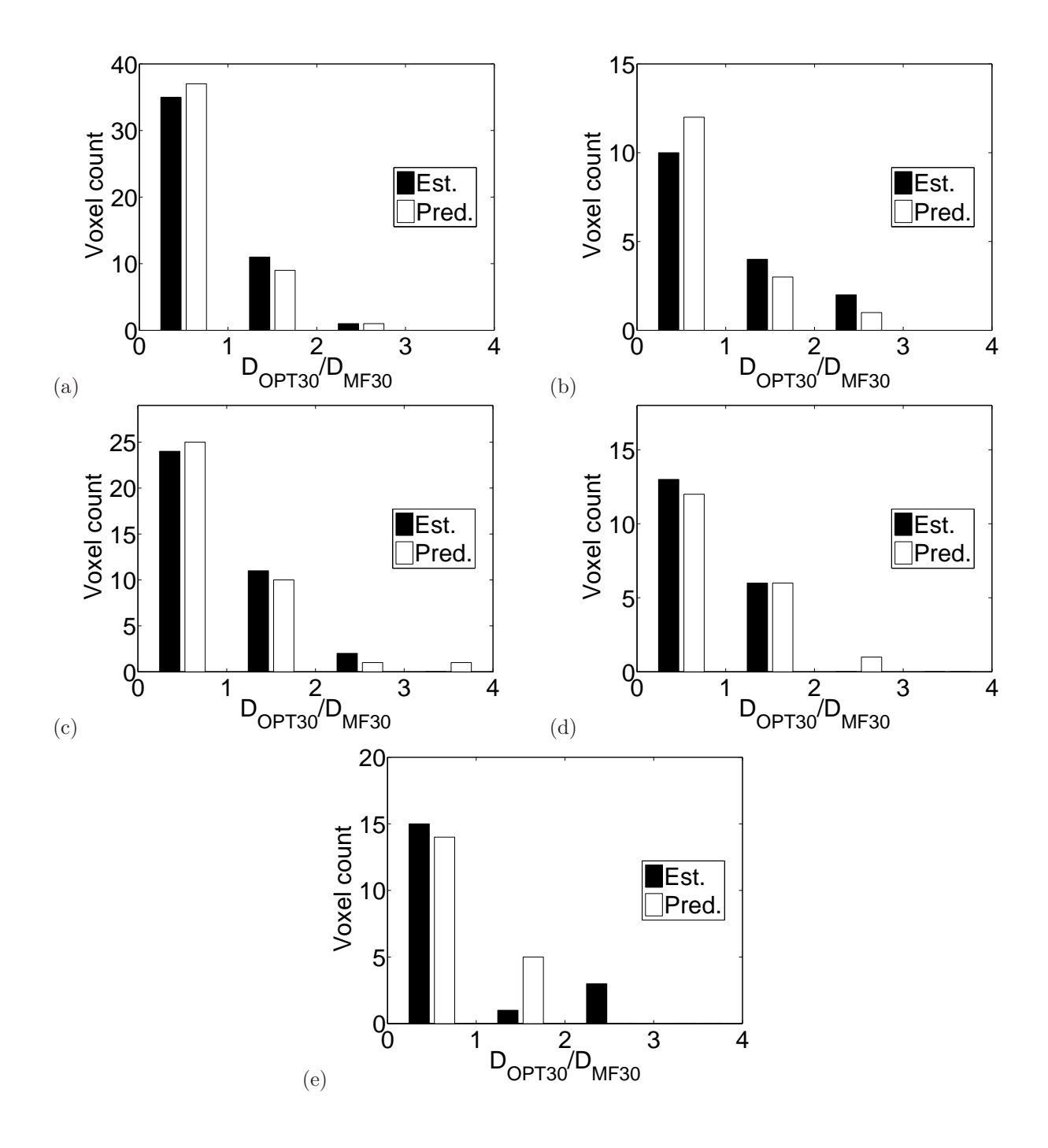


Figure 7.3. Region of interest (ROI) voxel distributions with respect to hypervolume ratio (D_{OPT30}/D_{MF30}) for different subjects. D_{OPT30} and D_{MF30} are square roots of the determinants of covariance matrix of parameter estimation ($\sqrt{\det \Sigma}$ for estimation (Est.) and $\sqrt{\det \Sigma}_{CR}$ for prediction (Pred.)) for OPT30 and MF30 schemes respectively. Figs. (a) to (e) correspond to subject number 1 to 5. Majority of the ROI voxels for each subject are in the less than unity range indicating an overall uncertainty reduction in the parameter estimation.

 D_{\perp}) and angular deviation (α) averaged over ROI voxels for the optimized and MF-based protocol are similar (Table 7.7). The mean % relative differences between these

two protocols (absolute difference divided by the mean) for all five cases in Table 7.7 are 3.52 % for D_{\parallel} , 8.29 % for D_{\perp} and 7.47 % for the mean α . The effect of optimization on the accuracies of the estimated diffusivities and angular deviation is less than 10% with respect to the MF30 protocol and can be considered as not affecting the estimation accuracy (or bias) sufficiently.

4) Signal-to-noise ratio: The optimized protocol has consistently higher eSNR as compared to the MF-based protocol as shown in Table 7.2, suggesting that the optimized gradient scheme samples the gradient space better than the MF30 case with respect to the eSNR.

Table 7.2. Performance comparison of the optimized scheme (OPT30) and MF30 from subject data

Subjects	Total voxels	P_S	P_S (%)		μ_{r1}		$D = \sqrt{\det \Sigma} \times 10^{-11}$			
		Est.	Pred.	Est.	Pred.	MF30	OPT30	<i>p</i> -value		
1	47	74.5	78.7	0.521	0.541	5.550	3.267	0.002		
2	16	62.5	75.0	0.457	0.536	7.273	4.785	0.021		
3	37	64.9	67.6	0.539	0.563	4.688	3.482	0.088		
4	19	68.4	63.2	0.544	0.608	6.982	3.627	0.108		
5	19	78.9	73.7	0.453	0.551	13.969	6.779	0.029		

 \overline{D} = hypervolume of uncertainty; $P_S = 100 \times \text{Voxels} \left(D_{OPT30} / D_{MF30} < 1 \right) / \text{Total voxels}; \mu_{r1} = \text{Mean } \left(D_{OPT30} / D_{MF30} \right)$ in successful voxels; eSNR = effective SNR

Table 7.3. eSNR comparison of the optimized scheme (OPT30) and MF30 from DTI subject data

Subjects	eSNR					
	MF30	OPT30				
1	3.780	4.286				
2	3.709	3.934				
3	4.106	4.363				
4	3.945	4.340				
5	3.401	3.828				

7.1.4 Results for optimization without a priori knowledge of cone of fibers

Healthy spinal cord tract fibers tend to be oriented within a narrow angular range. However, pathological spinal cord might have more uncertain fiber orientations. The uncertain

Table 7.4. Comparison of standard deviations (SD) of angular parameters at ROI voxels from subject data using optimized gradient scheme (OPT30) and MF30

Subjects		SD of θ	$O_F(^\circ)$	SD of $\phi_F(^{\circ})$			
	MF30	OPT30	<i>p</i> -value	MF30	OPT30	<i>p</i> -value	
			$(SD_{OPT30} <$			$(SD_{OPT30} <$	
			SD_{MF30}			SD_{MF30}	
1	3.234	2.774	0.0006	3.262	2.758	0.0001	
2	3.800	3.360	0.0274	3.864	3.289	0.0089	
3	3.333	2.976	0.0027	3.334	3.115	0.0430	
4	3.320	2.961	0.0998	3.360	2.965	0.0628	
5	4.341	3.746	0.0387	4.281	3.851	0.1153	

Table 7.5. Comparison of standard deviations (SD) of diffusivities at ROI voxels from subject data using optimized gradient scheme (OPT30) and MF30

Subjects	3	SD of D_{\parallel}	$\times 10^{-3}$	SD of $D_{\perp} \times 10^{-3}$			
	$(\text{mm}^{2'} \text{s}^{-1})$			$(\mathrm{mm}^2~\mathrm{s}^{-1})$			
	MF30	OPT30	<i>p</i> -value	MF30	OPT30	<i>p</i> -value	
			$(SD_{OPT30} <$			$(SD_{OPT30} <$	
			SD_{MF30})			SD_{MF30}	
1	0.315	0.291	0.0836	0.064	0.058	0.0047	
2	0.318	0.278	0.1035	0.066	0.066	0.6012	
3	0.269	0.239	0.0809	0.060	0.059	0.3832	
4	0.330	0.278 0.1796		0.064	0.055	0.0757	
5	0.387	0.295	0.0449	0.071	0.058	0.0067	

Table 7.6. Comparison of standard deviations (SD) of FA at ROI voxels from subject data using optimized gradient scheme (OPT30) and MF30

Subjects	SD of FA							
	MF30	OPT30	<i>p</i> -value					
			$(SD_{OPT30} <$					
			SD_{MF30}					
1	0.046	0.039	0.0003					
2	0.054	0.051	0.2514					
3	0.045	0.046	0.6365					
4	0.046	0.045	0.4522					
5	0.057	0.047	0.0154					

fiber orientation scenario was experimentally simulated by first generating the optimized gradient scheme with $\Lambda = 90^{\circ}$ (OPT30-90) for a healthy subject (subject 1). Next, the ADTI experiment was conducted using the OPT30-90 and MF30 schemes and the ROI voxels (62 voxels) were selected in the brain stem region (beyond the spinal cord region,

Table 7.7. Comparison of mean values of diffusivities and angular deviation at ROI voxels from subject data using optimized gradient scheme (OPT30) and MF30

Subjects	$D_{\parallel} \times 10^{-3} \text{ mm}^2 \text{ s}^{-1}$		$D_{\perp} \times 1$	$10^{-3} \text{ mm}^2 \text{ s}^{-1}$	α (°)		
	MF30	OPT30	MF30	OPT30	MF30	OPT30	
1	2.334	2.354	0.269	0.259	4.90 ± 1.00	4.50 ± 1.30	
2	1.989	2.103	0.224	0.256	6.70 ± 1.30	7.20 ± 1.30	
3	2.017	2.009	0.217	0.250	5.00 ± 1.00	5.80 ± 1.70	
4	2.282	2.127	0.283	0.304	6.90 ± 1.60	7.30 ± 3.40	
5	2.059	1.983	0.223	0.230	8.10 ± 1.10	8.20 ± 1.90	

see Fig. 7.1) where the mean angular deviation of fibers are higher than the upper spinal cord tracts ($\alpha \sim 19 \pm 9^{\circ}$ (using MF30)). From the data analysis, it is found that the P_S (61.3% (estimated) and 62.9% (predicted)) is less than for the previous human studies (for $\Lambda < 90^{\circ}$ cases), but the eSNR of OPT30-90 (4.180) is still better than MF30 (3.808). The standard deviations of the estimated ADTI model parameters and FA are shown in Table 7.8. From the analysis results, it is observed that the use of OPT30-90 reduced the uncertainty of the diffusivity parameters and FA significantly while not changing the uncertainties in the fiber orientation angles sufficiently. This is expected for the fiber orientation estimation since the fiber orientation is completely uncertain from a priori knowledge. The mean diffusivities of OPT30-90 and MF30 are approximately equal to each other. $D_{\parallel} = 1.575 \times 10^{-3} \text{ mm}^2 \text{ s}^{-1} (\text{for MF30})$ and $1.570 \times 10^{-3} \text{ mm}^2 \text{ s}^{-1} (\text{for OPT30-90})$, $D_{\perp} = 0.540 \times 10^{-3} \text{ mm}^2 \text{ s}^{-1} (\text{for MF30})$ and $0.514 \times 10^{-3} \text{ mm}^2 \text{ s}^{-1} (\text{for OPT30-90})$. Thus, an overall reduction of the estimation uncertainty via the optimization is achieved. This procedure suggests that the optimization process can be applied to pathological cases with a higher uncertainty in fiber orientation.

7.2 Fiber tracking analysis

In this section, a quantitative analysis of the effect of the diffusion gradient optimization on the tracking metrics is studied. Firstly, a simulation experiment is performed where fiber tracking is conducted based on data from OPT30 and MF30 gradient schemes on a simulated fiber bundle and is used to compare fiber tracking metrics (TF, AF and AL)

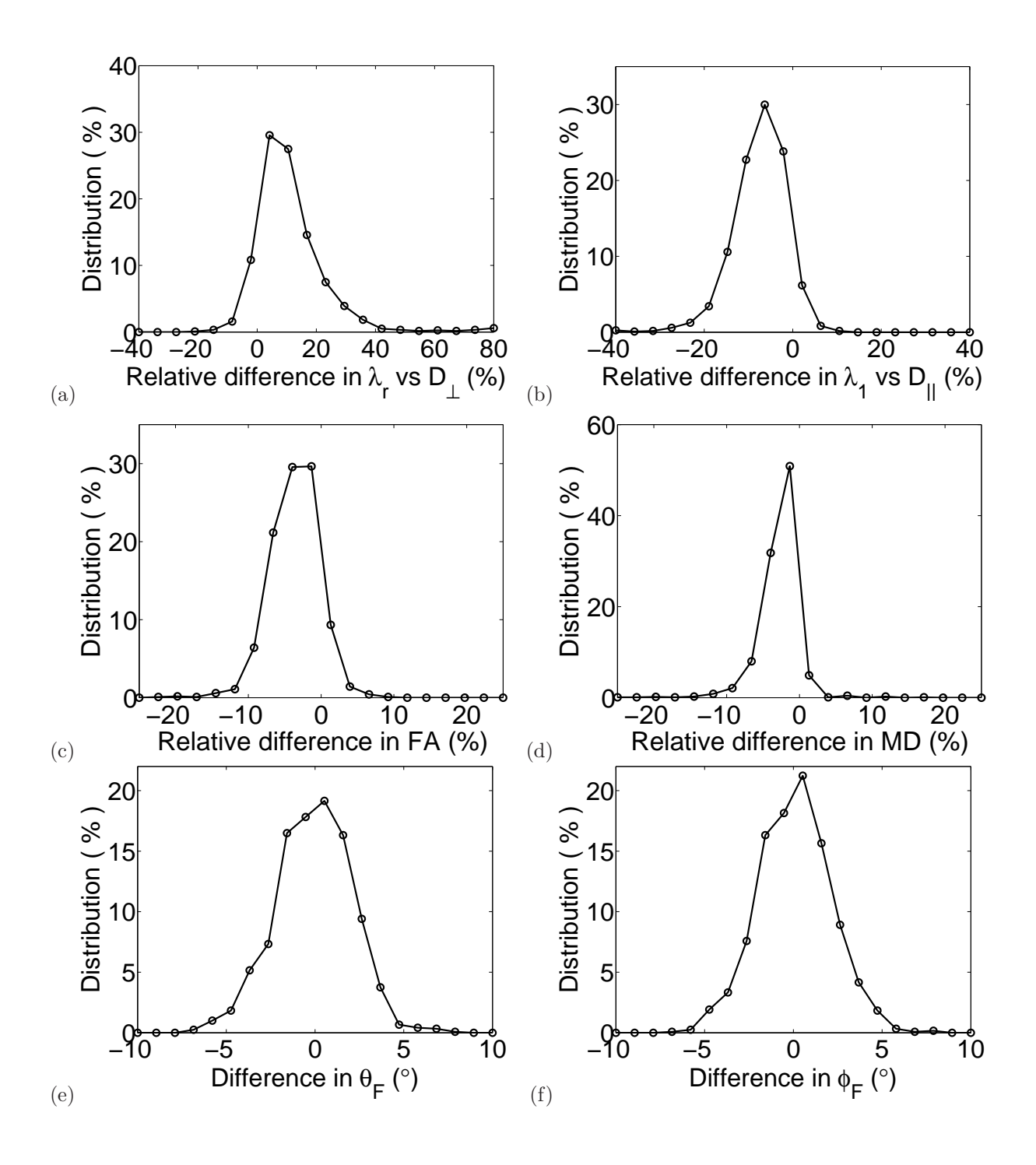


Figure 7.4. Distributions of relative differences for various estimated quantities under the DTI and ADTI model. Differences of (a) $\lambda_r = (\lambda_2 + \lambda_3)/2$ and D_{\perp} , (b) λ_1 and D_{\parallel} , (c) FA (d) MD, (e) θ_F and (f) ϕ_F are shown. These results are based on the voxels in the cervical spinal cord white matter tracts (C1-C2 region) from five subject data collected using the MF30 gradient scheme.

Table 7.8. Comparison of standard deviations (SD) of estimated ADTI model parameters and FA at the ROI voxels for subject 1 with gradients optimized for a completely uncertain fiber orientation (OPT30-90) and MF30.

Model parameters	MF30	OPT30-90	$ \begin{array}{c} p\text{-value} \\ (SD_{OPT30-90} < SD_{MF30}) \end{array} $
$D_{\parallel} \times 10^{-3} (\mathrm{mm}^2\mathrm{s}^{-1})$	0.236	0.187	0.047
$D_{\perp} \times 10^{-3} (\text{ mm}^2 \text{s}^{-1})$	0.068	0.062	0.028
$\theta_F(^\circ)$	6.551	6.745	0.306
$\phi_F(^\circ)$	7.852	9.239	0.246
FA	0.086	0.080	0.024

under the two schemes. Secondly, ADTI experimental data on healthy subjects collected in the previous section are used for fiber tracking and comparing tracking metrics. The results from both the simulations and experimental data indicate that by optimization of the diffusion encoding gradients, fiber tracking in general can be improved.

7.2.1 Method

A simulation experiment is performed where a synthetic fiber bundle of radius 6 mm and length 46 mm oriented along the +Z direction and surrounded by a 12 mm radius cylinder of isotropic medium is simulated. 10 sets of ADTI data are generated using both MF30 and OPT30 schemes. For the fibers, the following diffusion model parameters were used: $D_{\parallel} = 1.6204 \times 10^{-3} \text{ mm}^2 \text{ s}^{-1}, D_{\perp} = 0.148 \times 10^{-3} \text{ mm}^2 \text{ s}^{-1}, \theta_F = 0^{\circ}, \phi_F = 0^{\circ} \text{ (FA} = 0.9, MD = 0.639 \times 10^{-3} \text{ mm}^2 \text{ s}^{-1}). \text{ For the surrounding medium, isotropic diffusion was assumed with MD = <math>2.6 \times 10^{-3}$, FA = 0. Rician noise is added to the data at $\sigma = 0.1$. $b = 1000 \text{ s mm}^{-2}$ and N = 30 gradient directions. ADTI data is processed using diffusion tensor calculations and fiber tracking modules in DTIStudio (version 3.0.2) (Copyright Mori, Jiang, Radiology department, Johns Hopkins University, Baltimore, MD, USA) [103]. Fiber tracking settings were: starting FA = 0.6, stopping FA = 0.6 and curvature limit = 40° . TF, AF and AL metrics were calculated for each dataset. Fig. 7.5 shows the fiber tracking done on one of the MF30-based simulated data.

For the fiber tracking analysis of experimental data, the five subject ADTI data was used which was collected using the MF30 and OPT30 protocols (described in the section

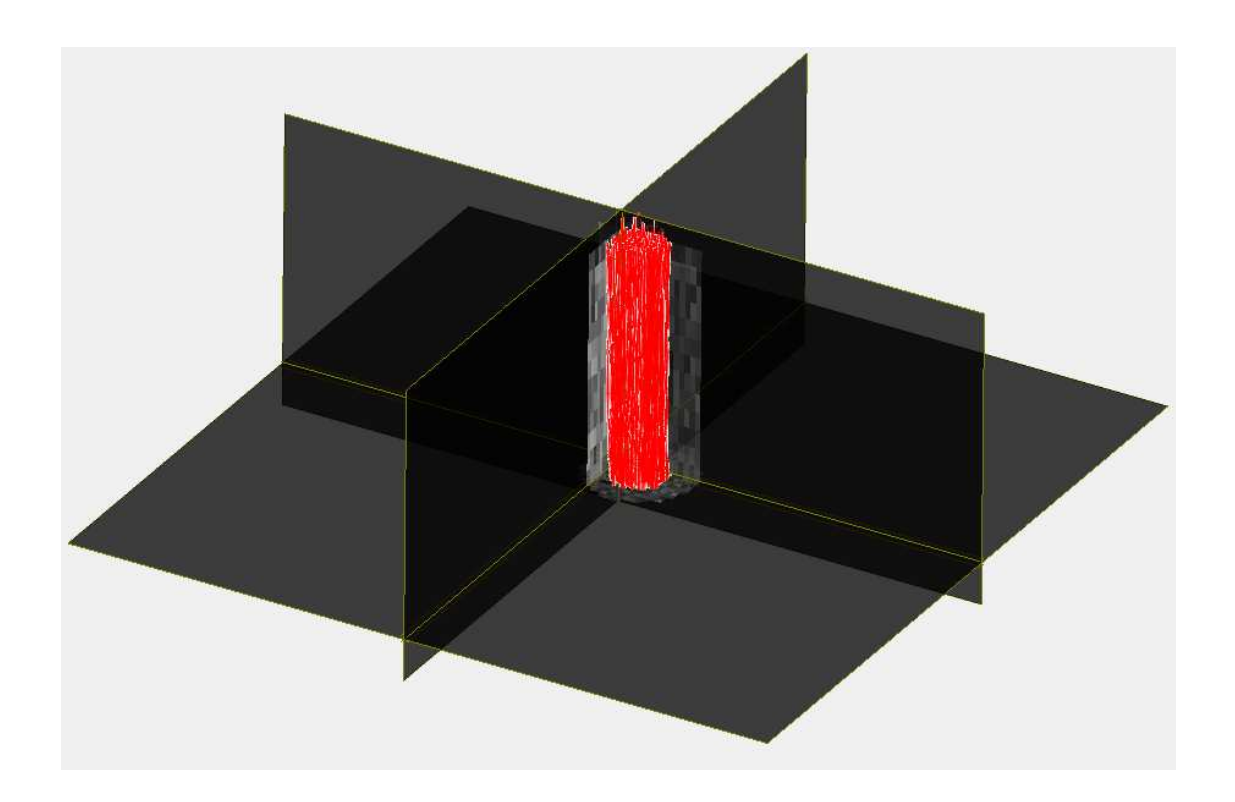


Figure 7.5. Fiber tracking based on simulated fiber bundle surrounded by isotropic medium.

7.1). The 12 volume data collected for each subject are co-registered using FLIRT in FSL package [126]. The seed ROI is drawn manually for each subject case in the inferior end of the cervical spinal cord below the C2 vertebral level (shown for one subject case in Fig. 7.6) and used for fiber tracking in all the 12 co-registered volume data. The following FACT settings were used: starting FA = 0.6, stopping FA = 0.6 and angle of curvature limit = 40°. FA value of 0.6 has been reported for the cervical spinal cord region previously [28,69]. The FACT curvature limit equal to or similar to 40° has been used previously [67,103]. Fibers tracked using the seed ROI for one subject are shown in Fig. 7.7. After the tracks were reconstructed, the metrics TF, AF and AL were calculated.

7.2.2 Fiber tracking results

Table 7.9 shows the fiber tracking results for the simulation experiment. It is observed that both the TF and AF metrics are significantly higher for OPT30 than MF30. The AL is almost equal for both the cases.

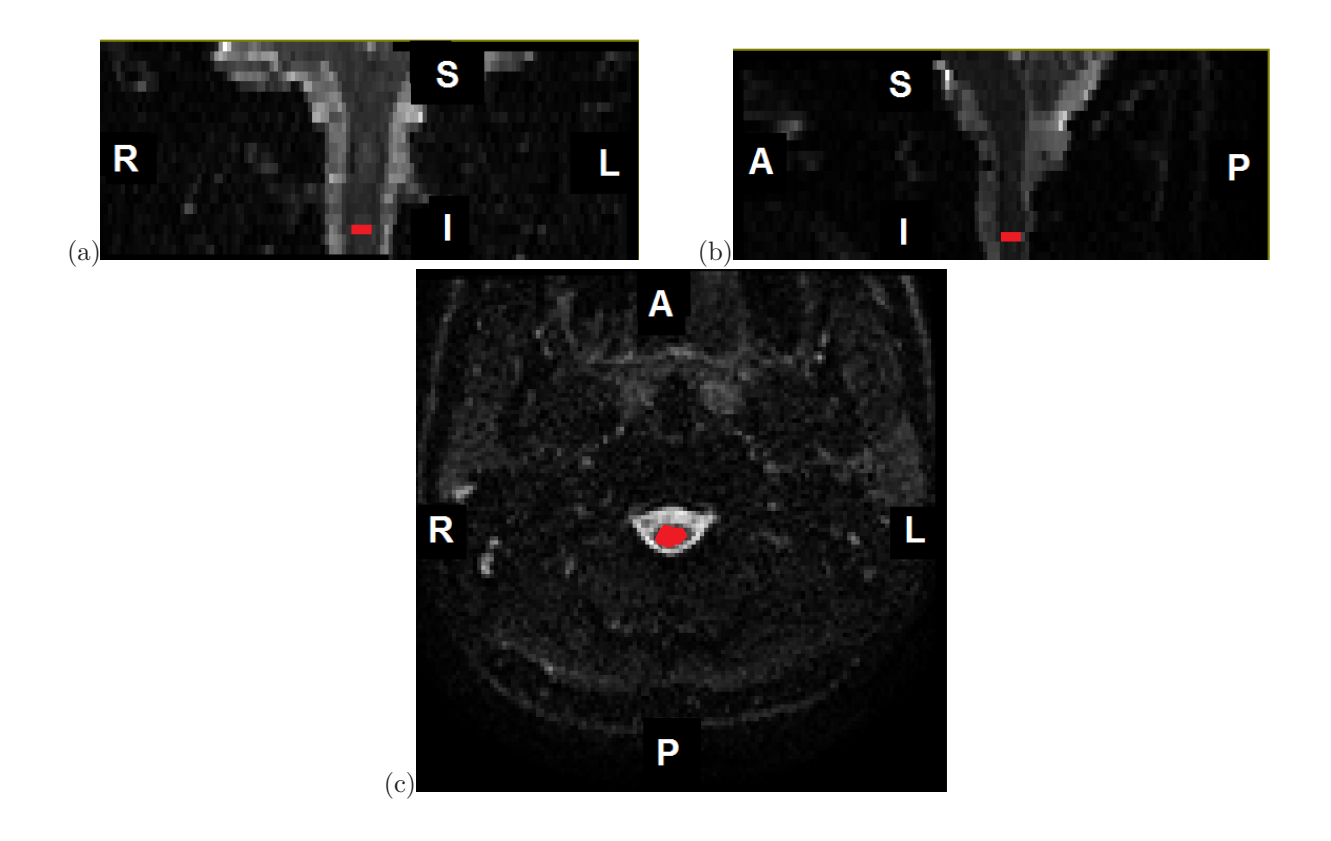


Figure 7.6. (a) Coronal view, (b) sagittal view and (c) axial view of T2-weighted image of the cervical spinal cord with the seed ROI shown in red.

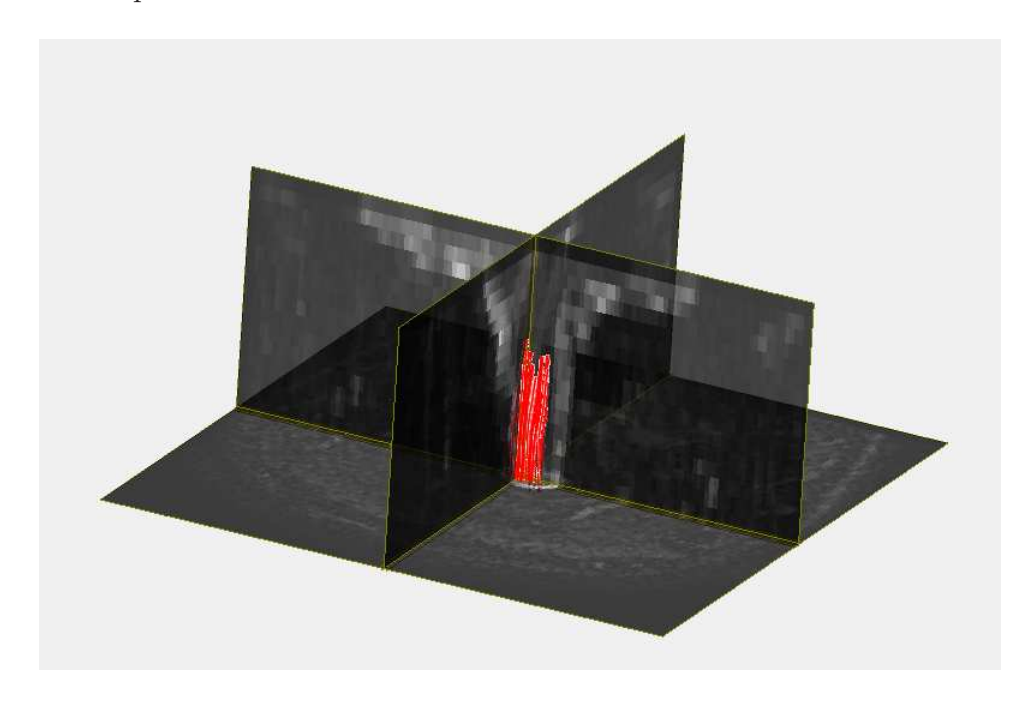


Figure 7.7. 3D fiber tracking shown in the cervical spinal cord region using the DTIStudio software.

Table 7.9. Comparison of fiber tracking results for OPT30 and MF30 protocols using simulated fibers.

Metric	MF30	OPT30	<i>p</i> -value
TF (number of fibers)	1025 ± 30	1066 ± 28	0.003
AF (fibers per voxel)	15.1 ± 0.4	15.5 ± 0.4	0.014
AL (mm)	45.4 ± 0.05	45.4 ± 0.04	0.335

Table 7.10 shows the estimated TF metric from the same seed ROI for each subject in the 12 datasets under the two gradient schemes (OPT30 and MF30). It is observed that the total number of fibers is higher on an average for the OPT30 protocol as compared to the MF30 protocol. Table 7.11 shows the AF metric for all the subjects. This quantity is also higher on an average for the 5 subjects for OPT30 protocol compared to MF30 protocol. Finally, Table 7.12 shows the estimated AL metric for all the subject data. The average length of fibers tracked is moderately higher for the OPT30 protocol than that of the MF30 protocol.

The OPT30 scheme is designed to improve the overall precision of the estimated diffusion model parameters which is expected to improve any secondary processing done based on these parameters. In the previous section, the fiber orientation estimation showed better precision (less standard deviation) when using the OPT30 scheme. Also, FA = 0.6 was used in the design of the OPT30 scheme (for the extraction of white matter voxels). In the FACT algorithm, FA = 0.6 was also used and all other FACT parameters, seed ROI as well as the imaging parameters (except for the gradient scheme) were same for both the OPT30 and MF30 cases. Thus, an unbiased comparison of the fiber tracking was performed for the two cases. Since the FACT algorithm traces streamlines in the image space based on the estimates of the local fiber orientation and FA, number of streamlines traced reduces if these estimates are less precise. Thus, improvement in the precision of diffusion parameter estimation shows up as an increase in the number of fibers tracked (TF). The increase in TF also increases the AF metric. The AL metric was only moderately high for the OPT30 case indicating less effect of the gradient optimization on the length of the fibers tracked.

Table 7.10. Comparison of fiber tracking results for OPT30 and MF30 protocol for the total number of reconstructed fibers (TF) through the ROI using 5 ADTI subject data

Subjects	Grad. Sch.		Γ	atase	ts 1 –	6		Mean \pm SD
1	OPT30	227	166	224	219	168	189	199 ± 28
1	MF30	158	133	175	124	128	137	143 ± 20
2	OPT30	140	186	115	134	132	134	140 ± 24
	MF30	70	88	134	135	111	93	105 ± 26
3	OPT30	202	176	167	161	164	203	179 ± 19
J	MF30	110	123	142	120	149	133	130 ± 15
4	OPT30	203	176	178	190	184	179	185 ± 10
4	MF30	164	146	132	125	160	146	146 ± 15
5	OPT30	140	157	173	172	186	156	164 ± 16
	MF30	167	105	127	139	106	110	126 ± 24

Table 7.11. Comparison of fiber tracking results for OPT30 and MF30 protocol for the average fibers per voxel (AF) using 5 ADTI subject data

Subjects	Grad. Sch.		D	atase	ts 1 –	6		Mean \pm SD
1	OPT30	7.6	6.4	7.4	7.1	6.4	6.6	6.9 ± 0.5
1	MF30	6.6	5.5	7.2	5.8	6.1	5.9	6.2 ± 0.6
2	OPT30	5.7	6.5	5.1	5.4	5.8	5.0	5.6 ± 0.5
<u> </u>	MF30	4.1	3.8	5.0	5.4	4.2	4.6	4.5 ± 0.6
3	OPT30	6.1	5.5	5.8	5.4	5.4	5.9	5.7 ± 0.3
J	MF30	5.4	5.2	5.7	4.7	6.2	6.1	5.5 ± 0.6
4	OPT30	7.1	6.0	5.7	6.1	5.5	5.2	5.9 ± 0.6
4	MF30	4.7	5.3	4.6	4.4	5.4	4.8	4.9 ± 0.4
5	OPT30	4.9	5.1	6.3	5.6	5.9	5.7	5.6 ± 0.5
0	MF30	5.4	4.6	4.6	5.0	4.4	4.8	4.8 ± 0.4

Table 7.12. Comparison of fiber tracking results for OPT30 and MF30 protocol for the average length (in mm) of fibers (AL) tracked using 5 ADTI subject data

Subjects	Grad. Sch.		I	Datase •	ts 1 –	6		Mean \pm SD
1	OPT30	30.7	25.7	27.6	26.6	26.0	29.2	27.6 ± 1.9
1	MF30	27.9	25.1	32.1	27.8	28.4	25.5	27.8 ± 2.5
2	OPT30	24.1	26.6	23.8	21.6	23.0	21.4	23.4 ± 1.9
	MF30	17.8	18.1	21.4	20.7	19.7	20.7	19.7 ± 1.5
3	OPT30	27.1	24.9	24.9	23.8	23.1	24.7	24.8 ± 1.4
0	MF30	25.2	22.8	24.6	22.2	26.0	26.0	24.4 ± 1.6
4	OPT30	28.6	27.8	24.4	26.4	24.4	24.5	26.0 ± 1.9
4	MF30	21.1	20.8	19.5	19.2	20.2	21.3	20.3 ± 0.9
5	OPT30	20.6	24.4	26.9	23.5	26.4	25.9	24.6 ± 2.3
J	MF30	22.4	21.6	22.4	24.3	20.8	24.0	22.6 ± 1.3

7.3 A partitioned CRLB based optimization of b-factor and diffusion gradient scheme

Optimization of DTI experimental parameters depends on the selection of the cost function that is minimized during the optimization process. Hasan *et al.* [17] discuss a number of cost functions which have been previously reported, such as the total variance of estimates of the diffusion tensor matrix elements [18], the Coulomb's force or energy assuming the gradient directions are point charges on a unit sphere [22], the product of the inverse of the squares of singular values of the encoding matrix, condition number of the encoding matrix, variance of secondary metrics such as FA [21] or ADC (apparent diffusion coefficient) [24].

The CRLB provides a theoretical lower bound of the variance of the estimated diffusion model parameters in terms of the signal noise and the DTI experimental parameters provided the noise pdf is known and follows regularity condition [109]. Previous use of CRLB can be seen in the work by Brihuega-Moreno et al. [24] for optimizing the b-factor for improved precision of ADC estimation and Alexander [23] for optimizing the diffusion gradient strength, the pulse interval between the diffusion gradient pulses and the diffusion pulse duration for reducing the overall uncertainty of the simplified CHARMED model parameters [9]. For a multi-parameter diffusion model, such as DTI or ADTI, the CRLB matrix can be partitioned to select the uncertainty bounds of only a subset of the diffusion model parameters (as shown in Chapter 5, section 3). The determinant of the sub-matrix corresponding to the subset of the model parameters can be minimized with respect to experimental parameters to obtain D-optimal experimental parameters (gradient scheme or b-factor or both).

For the spinal cord tracts, the axon bundles are oriented in the superior-inferior orientation within a narrow range of fiber directions. Thus, the range of fiber angles is fairly known a priori which can be used to improve the precision of the diffusion parameter estimation. As described in Chapter 5, the subsets of the set of diffusion model parameters can be in general grouped into diffusivities (such as D_{\parallel} and D_{\perp} for the ADTI model)

and angular parameters for the fiber orientation (θ_F and ϕ_F). In this section, a combined b-factor and gradient scheme optimization technique is developed for the cervical spinal cord tracts where the precision in the estimation of only diffusivities is improved by using a partitioned CRLB as the cost function and the a priori fiber orientation range information.

7.3.1 Method

Definition of the partitioned CRLB

The cost function for the partitioned CRLB matrix for the ADTI model for diffusivities only case has been defined previously in Chapter 5, section 5.3.1. The determinant of the sub-matrix B_1 can be minimized with respect to both the b-factor and the gradient directions such that the overall uncertainty of the diffusivities is reduced.

Optimization procedure

For the optimization of the b-factor and gradient scheme, the prior information used were as follows: $D_{\parallel} = 1.6 \times 10^{-3} \text{ mm}^2 \text{ s}^{-1}$, $D_{\perp} = 0.148 \times 10^{-3} \text{ mm}^2 \text{ s}^{-1}$, $(\theta_F, \phi_F) = (0^{\circ}, 0^{\circ})$ (+Z-axis). This corresponds to an FA = 0.9 and MD = $0.639 \times 10^{-3} \text{ mm}^2 \text{ s}^{-1}$. The range of fiber orientation (cone angle), $\Lambda = 25^{\circ}$. The cone angle value is smaller than the values used previously since this corresponds to voxels with a high mean FA = 0.9. The number of gradient directions is fixed to 30 directions. The optimization was performed by minimizing the cost function (det(B_1)) within the cone angle of fiber orientation using simulated annealing technique [73] (flowchart for this step is described in Appendix I). The optimized b-factor was found to be 2062 s mm^{-2} and the gradient scheme is shown in Fig. 7.8.

Experiment

This study was approved by the Institutional Review Board (IRB) for conducting research on human subjects. One healthy subject (male, age 29 years) participated in this study and provided his signed IRB-approved informed consent. The experiment was conducted

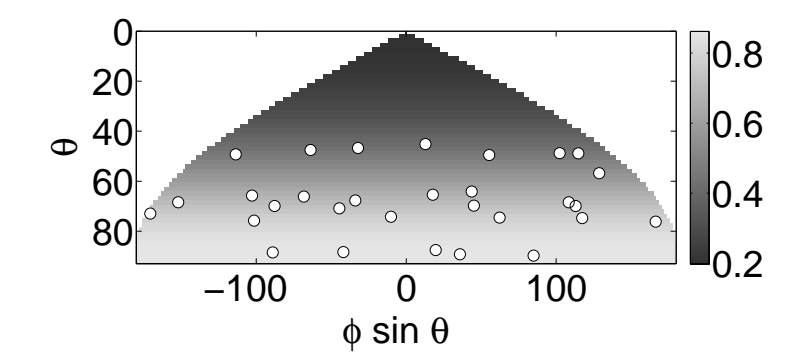


Figure 7.8. Distribution of 30 gradient directions (white circles) on a opened unit hemisphere shown with an underlay image of the normalized MR signal at $b = 2062 \text{ s mm}^{-2}$ and FA = 0.9.

using OPT30 and MF30 schemes at the C1-C2 vertebral location of the cervical spinal cord with the following settings: T2 and diffusion-weighted images were obtained using a dual spin-echo EPI sequence on a 3T GE Signa HDx scanner (GE Healthcare, Waukesha, WI), equipped with an 8-channel head coil with the following parameters, 12 contiguous 3-mm axial interleaved slices, $T_R = 4500$ ms, $T_E = 90.3$ ms, matrix size =128 x 128, FOV = 16 cm x 16 cm, number of excitations = 4, parallel imaging acceleration factor = 2, b = 2062 s mm⁻², 30 diffusion gradient directions and scan time per dataset = 9 min 23 sec. Maximum likelihood estimator was used for the ADTI model parameter estimation assuming Rician noise model. The post-processing technique is same as described in section 7.1.1.

7.3.2 Results

Fig. 7.9 shows the ROI voxel distribution with respect to the hypervolume ratio and it is observed that majority of the voxels ($P_S = 72.2\%$ of 36 ROI voxels) have reduced overall uncertainty in the diffusivities estimation ($\mu_{r1} = 0.742$). The prediction based on the partitioned Rician CRLB matrix shows similar results with $P_S = 69.4\%$ and $\mu_{r1} = 0.786$. The eSNR is 2.736 for the MF30 and 2.881 for the OPT30 case, thus indicating improvement in the overall SNR. These eSNR values are less than the previously reported values in section 7.1 (which were around 5) due to the use of a higher b-factor ($b = 2062 \text{ s mm}^{-2}$) in this experiment than the previous case ($b = 1000 \text{ s mm}^{-2}$). Simulations

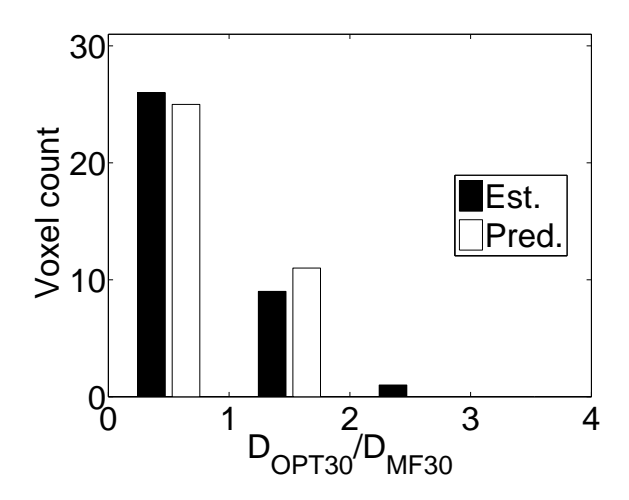


Figure 7.9. ROI voxel distribution with respect to hypervolume ratio (D_{OPT30}/D_{MF30}) based on the ADTI datasets from MF30 and OPT30 gradient scheme for one healthy subject. Estimated $P_S = 72.2\%$ and $\mu_{r1} = 0.742$ for 36 ROI voxels. Estimation is based on the covariance of estimates and prediction is based on the Rician CRLB formulation.

in Chapter 6 section 6.4.3 also demonstrate the decreasing trend of eSNR with increasing b-factor.

Table 7.13. Comparison of ADTI parameter standard deviations (RMS) in the ROI voxels for data based on MF30 and OPT30 gradient schemes and one healthy subject

Model parameters	MF30	OPT30 (<i>b</i> opt.)	<i>p</i> -value
			$SD_{OPT30} < SD_{MF30}$
$D_{\parallel} \times 10^{-3} \; \text{mm}^2 \text{s}^{-1}$	0.562	0.527	0.122
$D_{\perp} \times 10^{-3} \mathrm{mm}^2 \mathrm{s}^{-1}$	0.046	0.043	0.045
$MD \times 10^{-3} \text{ mm}^2 \text{ s}^{-1}$	0.169	0.159	0.141
FA	0.0543	0.0536	0.495
$\theta_F(^\circ)$	2.992	2.945	0.355
$\phi_F(^\circ)$	3.082	2.962	0.238

Table 7.13 shows the RMS standard deviations (SD) of the ADTI parameters for the ROI voxels when using MF30 and OPT30 schemes on a single healthy subject. In general, the SD values for all the parameters are less for the OPT30 case than the MF30 case indicating reduction in the parameter estimation uncertainty due to optimization. However, for the diffusivities estimation, the reduction is more statistically significant (especially for D_{\perp}) than the angular parameters estimation which is expected since the optimization cost function specifically optimized for the partitioned Rician CRLB for the

Table 7.14. Comparison of ADTI parameter mean values in the ROI voxels for data based on MF30 and OPT30 gradient schemes and one healthy subject

Model parameters	MF30	OPT30 (<i>b</i> opt.)
$D_{\parallel} \times 10^{-3} \mathrm{mm}^2 \mathrm{s}^{-1}$	2.311	2.246
$D_{\perp} \times 10^{-3} \mathrm{mm}^2 \mathrm{s}^{-1}$	0.212	0.233
$MD \times 10^{-3} \text{ mm}^2 \text{ s}^{-1}$	0.912	0.904
FA	0.886	0.873
$\theta_F(^{\circ})$	88.413	88.545
$\phi_F(^\circ)$	0.294	0.868

diffusivities. Table 7.14 shows the mean values of the estimated ADTI parameters and FA and MD obtained by averaging over the ROI voxels for the MF30 and OPT30 schemes. The parameters values are similar under the two protocols indicating no significant bias due to the gradient scheme and b-factor optimization. Note that the coordinate axis is rotated towards the X-axis so that the mean fiber angles are close to $(\theta_F, \phi_F) = (90^\circ, 0^\circ)$. This is done to avoid the discontinuity in ϕ_F at $(0^\circ, 0^\circ)$ which affects the calculation of mean and SD.

7.4 Discussion

7.4.1 Justification for the use of axisymmetric diffusion model for cervical spinal cord

In this section, the pertinence of the choice of the ADTI model is examined instead of the use of the general DTI model by comparing the estimated values of the diffusion model parameters, FA and MD. To estimate these quantities, the five subject data collected using the MF30 scheme only and the same ROI voxels from the C1-C2 region of the cervical spinal cord as described in the procedure in the "Experimental Protocol" section were used.

For transverse diffusivities, the following group statistics (mean and standard deviation (SD)) were obtained: $D_{\perp} = (0.345 \pm 0.131) \times 10^{-3} \text{ mm}^2 \text{ s}^{-1}, \lambda_2 = (0.468 \pm 0.147) \times 10^{-3} \text{ mm}^2 \text{ s}^{-1}$ and $\lambda_3 = (0.288 \pm 0.133) \times 10^{-3} \text{ mm}^2 \text{ s}^{-1}$. The radial diffusivity (λ_r)

is defined as the mean of the secondary and tertiary eigenvalues of the diffusion tensor $(\lambda_r = (\lambda_2 + \lambda_3)/2)$ and find that $\lambda_r = (0.378 \pm 0.13) \times 10^{-3} \text{ mm}^2 \text{ s}^{-1}$. Fig. 7.4(a) shows the distribution of the relative difference between λ_r and D_{\perp} , defined as $100 \times (\lambda_r - D_{\perp})/((\lambda_r + D_{\perp})/2)$, for which the mean and SD are (11.1 ± 12.6) %. Also, it is observed that about 70% of the voxels have less than 10% difference between D_{\perp} and λ_r (90% voxels less than 21% difference). These results indicate that D_{\perp} is approximately equal to the λ_r with a relatively small bias. With regard to longitudinal diffusivities, $D_{\parallel} = (1.84 \pm 0.34) \times 10^{-3} \text{ mm}^2 \text{ s}^{-1}$ and $\lambda_1 = (1.70 \pm 0.29) \times 10^{-3} \text{ mm}^2 \text{ s}^{-1}$. In Fig. 7.4(b), the group mean and SD for the relative difference between λ_1 and D_{\parallel} , defined as $100 \times (\lambda_1 - D_{\parallel})/((\lambda_1 + D_{\parallel})/2)$, is (-7.4 - 5.9)% and about 80% of the voxels have the relative difference less than 10% between D_{\parallel} and λ_1 , thereby revealing that D_{\parallel} obtained with ADTI is equivalent to the primary eigenvalue λ_1 obtained with DTI.

Figs. 7.4(c)–(f) show the distributions of the relative differences in FA, MD and difference in angular parameters (θ_F , ϕ_F) between the ADTI and the DTI models. The group means and SDs for the relative difference for FA (defined as $100 \times (\text{FA}_{\text{DTI}} - \text{FA}_{\text{ADTI}})$) is (-3.6 ± 3.3) % and for MD (defined as $100 \times (\text{MD}_{\text{DTI}} - \text{MD}_{\text{ADTI}})/\text{MD}_{\text{DTI}}$) is (-2.57 2.58) %. Similarly, for the angular parameters, the group mean and SDs for the difference is (-0.08 2.13)° for θ_F and $(0.09 \pm 2.04)^\circ$ for ϕ_F . Thus, both models lead to similar estimations of FA, MD and the angular parameters (θ_F , ϕ_F). Hence, any diagnosis based on FA, MD or fiber tractography should not be affected by the ADTI assumption. Moreover, the ADTI model reduces the number of diffusion model parameters from six to four, and thus allows a shorter computation time for the optimization framework. This is advantageous for routine clinical studies.

Thus, in terms of diffusivities, the ADTI and DTI models result in analogous distributions in the cervical spinal cord white matter tracts (C1-C2 region). Hence, this framework based on the ADTI model can be used in applications where only the transverse diffusivity is used to characterize the tissue properties. To deal with the inherent limitation of the ADTI model in cases where the secondary and tertiary eigenvalues of the diffusion tensor need to be characterized, a future study based on the non-axisymmetric

DTI model will be performed.

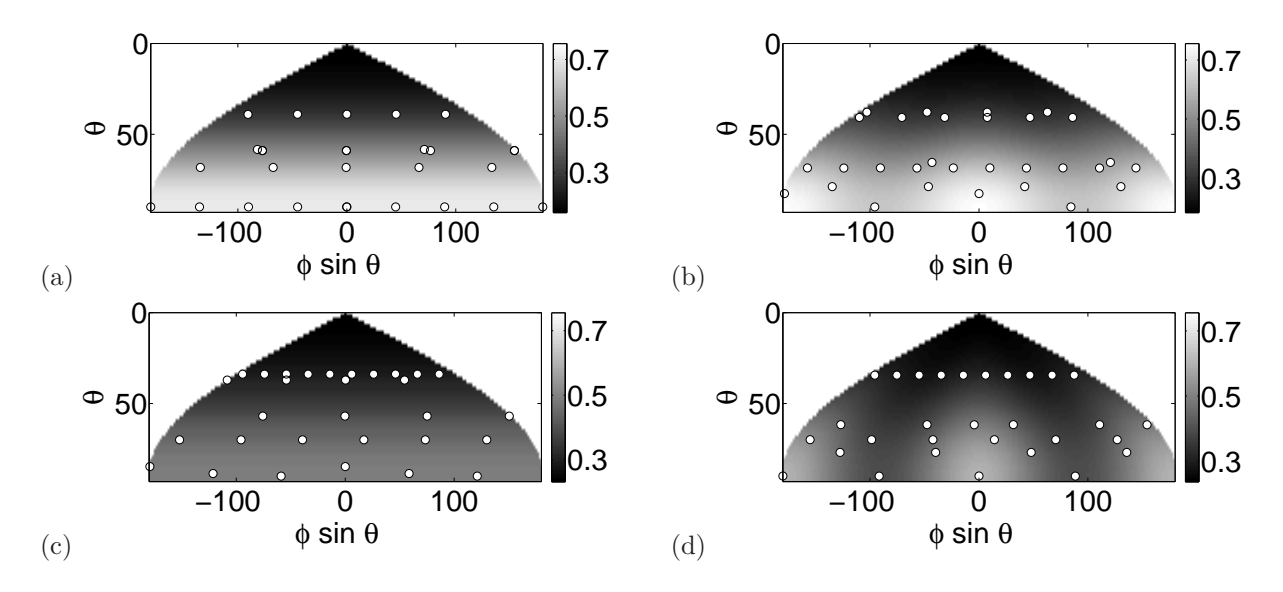


Figure 7.10. Distributions of optimized diffusion gradient directions (indicated by white circles) on an opened unit hemisphere. Underlying grayscale image shows the normalized MR signal levels over the hemisphere changing with respect to the diffusion gradient direction (θ_F, ϕ_F) . Optimized gradients are shown for the ADTI model in (a) and the non-axisymmetric DTI model in (b) for healthy white matter tracts with FA = 0.745, MD = 0.818 × 10⁻³ mm² s⁻¹. For the pathological case (cervical spinal cord in ALS patients), optimized gradients are shown for the ADTI model in (c) and the non-axisymmetric DTI model in (d) with FA = 0.45, MD = 0.96 × 10⁻³ mm² s⁻¹. For all cases, the fiber orientation angle is $(\theta_F, \phi_F) = (0^{\circ}, 0^{\circ})$.

7.4.2 Optimized distribution of gradient directions

The optimized gradient schemes computed based on the ADTI and DTI models lead to different characteristics in the spatial distribution of gradient directions. Figs. 7.10(a) and 7.10(b) represent the optimized gradient distributions from these two model assuming FA = 0.745 and MD = 0.818 × 10⁻³ mm² s⁻¹ obtained from the group averages of the healthy subjects. Let us then consider a pathological condition (amyotrophic lateral sclerosis (ALS) case reported by Nair *et al.* [128]), for which the DTI diffusivities were calculated directly from the definition of FA, MD and λ_r : $\lambda_1 = 1.44 \times 10^{-3}$ mm² s⁻¹, $\lambda_2 = 0.927 \times 10^{-3}$ mm² s⁻¹ and $\lambda_3 = 0.513 \times 10^{-3}$ mm² s⁻¹, resulting in $\lambda_r = 0.72 \times 10^{-3}$ mm² s⁻¹. The ADTI diffusivities are calculated by fitting the ADTI model to 30 diffusion-weighted normalized MR signals, which are simulated based on the eigenvalues of the diffusion

tensor values above, b-factor = 1000 s mm⁻², MF30 gradient scheme and fiber oriented along +Z direction. The estimated ADTI parameters are: $D_{\parallel} = 1.46 \times 10^{-3} \text{ mm}^2 \text{ s}^{-1}$ and $D_{\perp} = 0.712 \times 10^{-3} \text{ mm}^2 \text{ s}^{-1}$. Figs. 7.10(c) and 7.10(d) show the corresponding optimized gradient distributions using DTI and ADTI, respectively, with FA = 0.45, MD = $0.96 \times 10^{-3} \text{ mm}^2 \text{ s}^{-1}$ for the pathological condition defined above. It is observed that the optimized gradients are distributed more uniformly in the transverse orientation in the ADTI case than in the DTI case for both the healthy and the pathological case. This is expected given the axisymmetry assumption in the ADTI model, which results in the axisymmetry of the MR signal with respect to the fiber orientation as shown in the underlay images in Figs. 7.10(a) and 7.10(c).

The optimized distribution of the gradient direction on the unit sphere largely depends on the symmetry in the transverse diffusivity, the overall diffusion anisotropy (the difference in the longitudinal and transverse diffusivity) and the cone angle within which the optimal performance is designed. The higher the overall diffusion anisotropy, the greater the MR signal is in the transverse direction to the fiber orientation in comparison to the MR signal in the longitudinal direction (as seen in the underlay images in Fig. 7.10). Since D-optimality based framework uses the square of sensitivity matrices (which are also a function of normalized MR signal), regions of higher sensitivities are along the transverse direction rather than along the direction of the fiber orientation when diffusion anisotropy is high. The axisymmetry assumption of the diffusion tensor results in the normalized MR signal and diffusivity sensitivities also being axisymmetric about the fiber orientation (see Figs. 7.10(a) and 7.10(c)). Thus, for the ADTI model, the optimized gradient directions tend to be uniformly distributed about the fiber orientation (also see Fig. 5.12). This is an important effect of the gradient optimization framework on the gradient distribution.

If the general DTI model is used, and if the secondary and tertiary eigenvalues of the diffusion tensor are significantly different from each other, the optimized gradients will no longer tend to be distributed uniformly about the axis along the fiber orientation (also see Fig. 5.13). The gradients will sample more of the region corresponding to the direction

of the tertiary eigenvector than the region corresponding to the secondary eigenvector of the diffusion tensor (shown in Fig. 7.10(d)). In this case, the diffusion tensor model without the axisymmetric assumption has to be employed in the signal formulation since the use of the axisymmetric DTI formulation would result in additional uncertainty in the estimation of diffusion model parameters. The case when the overall diffusion anisotropy is low (low FA cases), the signal level difference between the longitudinal and transverse directions will also become low. Under such circumstance, the optimization framework would distribute the gradients more evenly on the unit sphere as compared to more transversely in case of high anisotropy (as seen in Fig. 7.10(c)).

7.4.3 Clinical relevance

FA threshold of 0.6 has been used to extract white matter tracts specifically and minimize the selection of voxels with gray matter of CSF contamination. Since the validation study was only on healthy subjects, this high FA thresholding worked well. Also, use of FA threshold for ROI voxel extraction has been previously reported by Wheeler-Kingshott et al. [129]. For low FA cases (pathology), the choice of the FA threshold will depend on the application. If only the pathological voxels need to be extracted, a specific range of FA values (corresponding to the pathology) can be used instead of a high FA cutoff. A manual segmentation based on the anatomical structure would be more appropriate (for example, using T1-weighted or T2*-weighted anatomical images). But the assistance from the FA image has been quite valuable based on my experience in identifying the white matter regions without gray matter or CSF contamination.

Cardiac and respiratory motions were not factored in this protocol optimization. The parameter estimation will likely be improved if the effect of the cardiac and respiratory motion is reduced through the use of gated sequences. However, these procedures require more acquisition time and were not suitable in the present study. Both the bulk motions mentioned above have been minimized by applying image co-registration techniques in the pre-processing steps. In addition, physiological motion would affect both the optimized schemes and MF30 equally, without changing the outcome of the comparisons.

A limitation in the proposed work is that the optimization procedure needs a preliminary scan (2 min for the OPT30 protocol). An extra 20 min is required to generate the optimized gradient scheme with four 3.3 GHz CPUs. The computation time can be shortened by parallelizing more CPUs which will allow the data acquisition with the optimized gradient scheme in the same scan session as the preliminary scan. Most clinical spinal cord MR protocols consist of routine anatomical scans. These scans can be conducted while the computation of the optimized gradient scheme is being performed.

The use of the determinant of the CRLB matrix results in a global optimal state with respect to the uncertainty in the estimation of the diffusion model parameters. But the precisions of all the individual diffusion model parameters might not be improved simultaneously. If one aims to optimize the estimation of only a subset of the diffusion model parameters (for example, only the diffusivity parameters and not the angular parameters), then the diffusion gradients can be optimized by minimizing the determinant of a partition of the CRLB matrix for D-optimality [120].

Finally, it is noted that the use of the gradient optimization can be extended to regions outside the central nervous system wherever the white matter tracts are directed in a particular orientation and over a range of distance, such as the median nerves in human wrists. Work done by Meek et al. [29] who demonstrated the feasibility of in vivo three-dimensional reconstruction of the median nerves in human wrists by DTI-based fiber tracking can be further improved by this gradient optimization. The ADTI can also be applied to non-nervous tissues that exhibit organized and orientated structure, such as the skeletal muscle tissues. DTI has been reported to track muscle fibers in skeletal muscles and to create biomechanical models of the muscles based on the estimate of local orientation of the fibers (pennation angle), fiber length and cross-section of the fiber bundles in humans [32]. An optimized gradient scheme will improve the estimation of such metrics.

7.4.4 Fiber tracking in cervical spinal cord

The effect of the gradient scheme optimization on fiber tracking metrics (TF, AF and AL) can be shown by a simple demonstration of the FACT algorithm given in Fig. 7.11. In this case, a 2D FACT algorithm is implemented using brute-force method [103] for an image of size 5×3 . The boxes represent the image pixels, the arrows indicate the fiber orientations within the pixels and the orange lines are the fiber tracks. The true fiber orientation is along the vertical direction.

Going from left to right column, the number of pixels with uncertain fiber orientation increases. It is observed that the left column with the least uncertain fiber orientations has the most number of tracks reaching the seed voxels. Also, the number of tracks per voxel is higher for this column of fibers and the fibers track the length of the column. For the middle column, there is a pixel in the middle with higher uncertain fiber orientation which results in reduced track density although the number of fibers reaching the seed voxels is same as in the left column. Finally, at the right column, there are more pixels with uncertain fiber orientations and this affects both the number of fibers reaching the seed voxels as well as the track density.

This simple demonstration clearly explains the fiber tracking results from the simulation experiment as well as ADTI experiment based on the 5 subject ADTI data where the tracking using the OPT30 protocol gave higher TF and AF metrics on an average for each subject than the MF30 protocol. The average length of the fiber tracks were only moderately higher for the OPT30 protocol indicating that MF30 could also track similar distances as OPT30 but only with fewer tracks. The larger the number of tracks generated, the better is the confidence in the estimated tract bundle which indicates reduced uncertainty in the overall fiber tracking. This shows that gradient scheme optimization to reduce the uncertainty of the diffusion model parameters also reduces the uncertainty in the results of a secondary post-processing such as fiber tracking.

Fiber tracking results can be sensitive to the choice of FACT thresholds (FA and track curvature) and could result in the omission of certain tracks by minor change in the threshold values as shown by Brecheisen *et al.* in the brain [106]. However, FA ~ 0.6 has

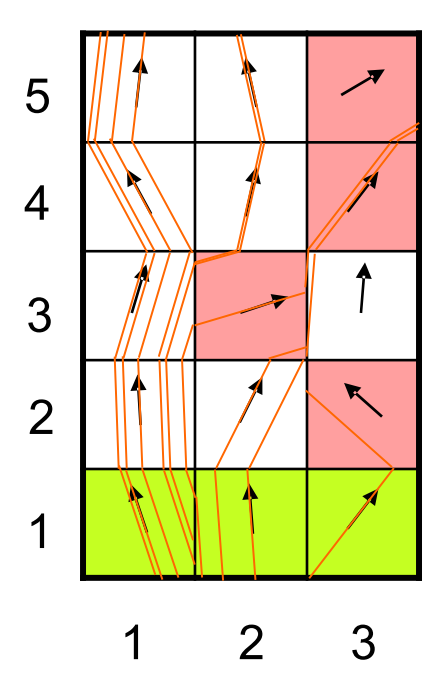


Figure 7.11. An illustration of the FACT algorithm applied to a 2D distribution of fiber orientations. Tracks are shown in orange. Each box represents a pixel with the fiber orientation shown by the arrow. True fiber orientation is along the vertical. Light red pixels are ones with more uncertain fiber orientation. The green pixels are the seed (ROI) pixels. Only tracks penetrating the seed pixels are retained.

been widely reported for the healthy cervical spinal cord white matter in other studies [28,69,129] and its selection as a threshold should reduce spurious fiber tracks passing through gray matter and CSF. The curvature threshold is to prevent sharp turns in the fiber track within the locality of the voxels and use of a 40° threshold is also commonly used [67,103] and is not a restrictive value. Moreover, by generating more tracks because of the gradient scheme optimization, the sensitivity of these thresholds to fiber tracking could potentially reduce.

7.4.5 Partitioned CRLB-based b-factor and gradient scheme optimization

This validation experiment aimed to verify two aspects of the CRLB-based optimization, namely, the use of the partitioned CRLB to selectively improve the precision of a subset of the diffusion model parameters and the use of a combined b-factor and gradient scheme

optimization. The study can be considered to be a more general case of the study for only gradients directions described in section 7.1.

Simultaneous optimization of b-factor and gradient scheme optimization has been recently reported by Gao et al. [39] where they demonstrated a unified optimization approach for the selection of the b-factor, the diffusion gradient directions and the timing parameters (such as Δ , δ , TE and readout time, R) using a stochastic optimization framework based on the simulated annealing algorithm [122]. They also used a cone of fiber angle information as a prior knowledge for the optimization. Their work aimed to minimize the trace of the covariance of the estimated parameters assuming an additive white Gaussian noise model. While their work is similar to the work presented in this section, there are certain limitations of their work that have also been considered here. They did not use a Rician noise model which is relevant for magnitude MR signals at low SNR, such as in DTI of the cervical spinal cord. Also, the selective improvement in precision of subset of diffusion parameters was not used by them.

In this work, the b-factor has been considered as a single lumped experimental parameter. However, this assumes that TE and the readout time for the b = 0 and $b \neq 0$ images are kept equal and are not optimized. The b-factor and the gradient directions are independent of each other and can be simultaneously optimized (as done in this work) since the b-factor can be decoupled from the **b** matrix definition as shown by Basser et al. [12] (for trapezoidal diffusion gradient pulses in traditional spin-echo sequence) and Finsterbusch [94] (for square gradient pulses in dual-spin echo sequence).

This work presents a generalized framework for the selective improvement in the precision of a subset of diffusion parameters based on CRLB. For the validation, the precision of the diffusivities are minimized. A somewhat similar work has been reported by Brihuega-Moreno *et al.* [24] where *b*-factor was optimized for reducing the Gaussian CRLB of the estimated ADC values either for a single ADC measurement or a range of ADC measurements. The full CRLB matrix consisted of the S_0 (non-diffusion weighted MR signal) as well as ADC as the model parameter and the *b*-factor optimization focused on the element of the CRLB matrix corresponding to ADC only. However, their framework was much simplified due to the use of scalar ADC instead of the diffusion tensor and also the use of Gaussian noise model. This work and work on Chapter 5 section 5.3 provides a more generalized framework for DTI/ADTI model and for both Rician and Gaussian noise model.

Increase in the b-factor affects the SNR of the DWIs adversely (as shown by the simulations in Chapter 6, section 6.4) since higher b-factors are achieved by higher gradient strength and/or longer TE and timing parameters all of which result in lower MR signal. In this section, the optimized b-factor at an FA = 0.9 was 2062 s mm⁻² which is higher than the generally used b = 1000 s mm⁻². The eSNR was correspondingly lower (~ 3) for this study as compared to section 7.1 (~ 5). This variation in the SNR necessitates the use of the Rician noise model especially when b-factor is optimized in a DTI experiment.

7.4.6 Justification for the use of prior information

Use of prior information in the optimization of gradient scheme can have potential drawbacks and is debatable. Firstly, using prior knowledge results in improved parameter estimation only towards estimating certain specific model parameter values. Secondly, if prior knowledge is available with certainty, there is no need for imaging. The optimization framework developed in this work intends to address these issues and thereby justify the use of such optimized scheme as compared to un-optimized schemes.

In the developed optimization technique, preliminary short DTI scans are performed on each subject to collect subject-specific information, such as the cone angle (A) and mean diffusivities $(D_{\parallel}, D_{\perp})$. The cone angle used as an input for solving the robust optimization problem not only results in improved overall precision of estimates within the cone but also beyond it, upto certain safety margin, as shown in the performance curves in Section 5.5.2. Similarly, for diffusivities, ranges of FA and MD can also be used to constrain the robust optimization problem along with the use of cone angle, as described in Section 5.4.5. Use of subject-specific information and presence of safety margin indicates that the optimization framework improves the parameter estimation for subject-specific parameter values, which is relevant, and allows for a range or margin beyond the subject-

specific parameter values, making it less biased. Even for pathological cases, the proper subject-specific information would help improve the precision of parameter estimation since pathological condition does not necessarily mean completely uncertain scenario. For example, DTI of pathological cases (e.g., multiple sclerosis [130]) report pathological ranges of FA or MD values and degeneration of nerve fibers can result in larger cone angle values. This subject-specific information can be used to develop optimized scheme for pathological cases also. Also, the prior knowledge is only approximate and not known with certainty since it is based on a short DTI scan (with fewer diffusion gradient directions), thus there is a need for a full scan with the optimized gradient scheme and the prescribed number of gradient directions.

A practical scenario for the use of the optimization framework can be outlined as follows: a preliminary scan on the subject provides subject-specific information on the diffusion model parameter values. While the program for computing the optimized gradient scheme is running, the subject goes through routine scans, such as T_1 -weighted volumetric and T_2 -weighted. These routine scans take about 20 minutes in total which is similar to the computation time to obtain the optimized gradients. Finally, data is acquired using the optimized gradient scheme. By using multi-core computers, the optimized gradients can be computed faster than 20 minutes. And thus the total procedure can be "online" without having the patient exit the scanner.

CHAPTER 8

Conclusions

8.1 Summary

Diffusion-weighted imaging provides a non-invasive technique to delineate the nerve fiber tracts at a macroscopic level and to perform in vivo fiber tracking. Compared to other neuroanatomical imaging methods which are generally microscopy-based methods (for example, scanning electron microscope [52], MR microscopy [49]) which require special hardware and high field gradients (MR microscopy [49]) and cannot image in vivo or are invasive (tract tracing using fluorescent dyes [4]), DWI-based methods can be easily implemented on a conventional MRI scanner and does not require special hardware requirements for the scanner. This technique is applicable to humans in vivo and a considerable coverage of the imaged target is achievable (for example, full brain DTI). While neurophysiology-based methods, such as EEG and fMRI can provide effective and functional connectivity information in neural networks respectively, the neuroanatomical information can be used to validate and augment such connectivity information, thus providing a complete picture of the neuronal connectivity. Owing to these advantages, DWI-based methods (especially, diffusion tensor imaging, DTI [7]) is being used extensively to explore nerve fiber tracks.

The focus of this research work was to develop a diffusion gradient optimization framework for DTI to improve the precision or reduce the uncertainty in the diffusion model parameter estimation. A detailed evaluation of the effect of experimental settings (such as the b-factor, number of diffusion gradients (N)), effects of selection of noise models and effects of selection of parameter estimators on the overall estimation uncertainty has been demonstrated. Finally, the estimation performance of the gradient optimization is validated by computer simulations and a five-subject human study for cervical spinal cord DTI.

8.1.1 Gradient scheme optimization

The diffusion gradient optimization framework is developed for the DTI and the ADTI diffusion models. These are investigated under both Rician and Gaussian noise. The diffusion gradient optimization framework is based on D-optimality ([33, 34]) which minimizes the CRLB on the estimation variances of the diffusion model parameters. The framework utilizes the prior structural knowledge of the imaged organ. For the spinal cord, the prior structural information of the nerve fibers can be represented by a cone model with known mean fiber orientation and the spread of the fibers from the mean as defined by the cone angle (Λ) . The gradients are optimized to perform within the cone angle and thus for a range of fiber orientations. The gradient optimization can be performed for improved estimation of either all the diffusion model parameters or for selected model parameters, such as only for diffusivities or angular parameters for fiber orientation. Depending on the user's choice of the model parameters to have improved estimation, appropriate optimization cost function can be selected.

The optimization framework was extended to include b-factor optimization along with the optimization of the diffusion gradient directions. Due to limitation of scanner hardware, b-factor cannot be set any value and hence its optimization requires more constraints (such as limits on the gradient strength and the timing parameters) than that of the diffusion gradient directions. In this work, the gradient scheme optimization was performed at an assumed fixed value of the diffusion model parameters (i.e., diffusivities and the mean fiber direction are fixed) which are obtained from preliminary DTI experiments. While the cone angle (Λ) incorporates a range of fiber orientation for which the diffusion

gradients are optimized by the optimization framework, a range of diffusivity values can also be used as prior information in the optimization problem, thus, generalizing the prior knowledge to both diffusivity and fiber direction information.

8.1.2 Simulation experiments

An evaluation of the noise models used for the normalized MR signal is performed by simulations. The normalized MR signal being a ratio of two magnitude MR signals is a ratio of two Rician distributed random variables. However, in this work, the ratio pdf has been approximated by a Rician pdf assuming that the normalizing signal has a negligible variance as compared to its magnitude (hence high SNR). This approximation allows using a fixed value of σ in the Rician CRLB definition. The simulations indicated that when the Rician approximation is not used, σ of the Rician fit of the ratio pdf shows dependence on the normalized MR signal. However, this dependence can be minimized by increasing the number of MR signal acquisitions (NEX). The DTI experiments are conducted at NEX = 2 for which I assume the approximation of fixed σ holds good.

Next, a comparison of the estimation performance of three estimators, namely, LS, LSC and ML estimators, is done. While LS estimator is applicable when noise model is not known, LSC is more applicable when systematic error (bias) is needed to be removed from the measurements. ML estimator is used when noise model is known a priori. From the performance comparison of the estimators for both the optimized gradient and MF30 gradient scheme, it was shown that while LS estimator obtained marginally lower hypervolume values than ML estimator, ML provided the most unbiased estimates of the ADTI model parameters while having comparatively low hypervolume values. Thus, ML estimator was used for the data analysis in the spinal cord ADTI experiment. Also, the performance curves which shows the variation of the normalized hypervolume with respect to angular deviation from the mean fiber orientation was validated by Monte Carlo simulations with all the three estimators (for the Rician noise) and LS estimator (for the Gaussian noise). The simulations indicated that MLE was the most appropriate estimator in the case of Rician noise model and ADTI diffusion model.

For the study on the effect of b-factor, it was shown that for both the optimized and MF30 schemes, the performance (based on performance indices μ_{r1} and P_S) only improves within a certain range of b-factor. However, for the optimized case, the range of high performance is broader than the MF30 case. Thus, when a cone angle of fiber distribution is used for optimizing the diffusion gradient, the b-factor range increased as compared to an un-optimized (MF-based) scheme. Increase in b-factor reduces the eSNR. This shows that a limit on allowable eSNR can also be applied while doing the b-factor optimization. For the effect of the number of gradient directions, it was seen that increasing the number of gradients reduced the estimation uncertainty which was expected since more measurements result in more extracted information from the data. For the effect of cone angle, smaller the cone angle, better is the estimation performance (i.e., more reduced is the uncertainty). Smaller cone angle indicates less uncertainty in the fiber orientations.

Monte Carlo simulations for the ADTI and DTI experiments were conducted to assess the estimation performance of the optimized gradient scheme compared with the MF30 scheme when either all model parameters or diffusivities only or the angular parameters for fiber orientation only were selected. While the hypervolumes of uncertainty were reduced in all the cases as indicated by the performance indices $(P_S \text{ and } \mu_{r1})$, the effect on individual parameter estimation varied. For example, for ADTI, when all parameters are selected, most of the improvement in precision was visible in the angular parameters. But, when the diffusivity only parameters are selected, uncertainties of both the diffusivities $(D_{\parallel}, D_{\perp})$ as well as uncertainty in FA was reduced. Also, for the angular parameters case, uncertainty of both the angle parameters (θ_F and ϕ_F) and angular deviation (α) was reduced. Results for the DTI model indicated that while overall improvement in the hypervolumes was achieved, individual parameters not always improved in precision, especially D_{\parallel} which showed no improvement for the all parameters and the diffusivities only cases. This was since the majority of the high square sensitivity regions for the diffusion model parameters were transverse to the fiber direction, which was not the case with D_{\parallel} . Improving the precision of D_{\parallel} would require the framework to exclusively optimize for D_{\parallel} and not for other diffusivities.

Selecting all parameters during optimization of diffusion gradients results in a global optimal state and an overall improvement in precision. However, this does not mean improvement in the precision of all the model parameter estimates simultaneously. Selection of model parameters for diffusion gradient optimization finally depends on the application. For diagnosis based on diffusivity-related metrics, such as FA or MD, it would be desirable to improve the precision of diffusivities only. While for fiber tractography applications which rely on the precise estimation of fiber direction angles, the angular parameters should be selected during gradient optimization.

8.1.3 Spinal cord ADTI experiments

This work included a five-subject human study on the cervical spinal cord DTI for the validation of the diffusion gradient optimization for reduced uncertainty in the diffusion model parameter estimation. Step-by-step procedure including the ADTI protocol has been described for conducting the study and analyzing the data.

Based on the spinal cord and brain stem imaging results, it is conclusively demonstrated that the diffusion-encoding gradient optimization has performed significantly well in the region of interest (spinal cord/brain stem white matter tracts). These regions contain fibers oriented within certain range (or cone) of directions and the gradient optimization takes into account this prior knowledge and has performed better in this cone of fiber directions. The new gradient optimization scheme does not bias the estimation as differently as the standard gradient scheme (MF30). This is crucial since a bias in the estimates will affect the secondary metrics, such as FA, MD and would cause erroneous diagnosis of the imaged tissue. Another aspect of the CRLB-based gradient optimization is that performance improvements can be predicted prior to conducting the DTI experiment. This is because the CRLB provides an analytical lower bound on the expected variance. The expected performance can be predicted from the analytical formulation of the CRLB. Such a prediction capability is convenient and essential for the evaluation of the new gradient scheme before human subject scanning is performed.

This work assumes axisymmetry in the diffusion tensor model, i.e., the secondary and the tertiary eigenvalues of the diffusion tensor are assumed equal. The comparison of the estimates of the ADTI and the DTI parameters indicated that D_{\parallel} and D_{\perp} of the ADTI model are equivalent to λ_1 (primary eigenvalue of diffusion tensor) and λ_r (radial diffusivity defined as the mean of secondary and tertiary eigenvalues of diffusion tensor) of the DTI model, respectively. Also, FA, MD and the fiber angles (θ_F, ϕ_F) estimated for both the ADTI and DTI models were approximately equal indicating that the use of the ADTI model will not affect any diagnosis based on these metrics. Also, the transverse diffusivity (D_{\perp}) estimated from the ADTI model could be potentially used for diagnosing spinal cord pathology.

By reducing the uncertainty in parameter estimation, more confidence is ensured in the estimates of diffusivities and fiber orientation. This implies that any secondary processing, such as fiber tracking, performed based on these estimates would also have lower uncertainty. In the fiber tractography analysis, FACT-based [16] fiber tracking was performed on the ADTI datasets in the cervical spinal cord region. For all the five subjects, the average of number of fibers tracked and the average fiber density were higher for the optimized ADTI protocol than MF30 protocol. This shows that the quality of fibers tracked in the spinal cord region improved upon the optimization of the gradient scheme.

Since the optimization has so far used a narrow cone angle representing higher certainty in the fiber direction, a case where the cone angle of 90° indicating completely uncertain fiber orientation was used for gradient optimization and its performance was validated by a one-subject ADTI experiment. The estimation results indicate that the optimized gradient scheme still outperformed the MF-based technique, albeit marginally.

In this work, a combined b-factor and gradient scheme optimization method was also developed and a preliminary experimental validation was presented by a one-subject ADTI experiment. The technique is applied in the cervical spinal cord/brain stem region near C1-C2 vertebral levels and aimed at reducing uncertainty of only the diffusivities while using prior knowledge of the fiber orientation. The optimization was performed at a high FA value (FA = 0.9). From the validation experiment, the model parameter estimation

results indicate that the uncertainty of the diffusivities was reduced as expected from the CRLB formulation. Also, the estimates were not biased. It was observed that at high b-factor, the SNR of the DW image was low and only at higher NEX (= 4) could a discernible diffusion-weighted image be scanned. Also, the T_R and T_E of the sequence was changed to accommodate the high b-factor. This indicates that changes in the b-factor requires additional consideration and these could be formulated as constraints in the optimization problem.

Use of prior information can be justified since by using subject-specific information based on a preliminary scan, each optimized gradient scheme is made specifically optimized for the subject. Also, safety margin on the performance extends the range of expected performance. Finally, development of an "online" method where the subject does not exit the scanner, will make the optimization more practical.

8.2 Contributions

The research work done in this thesis contributes to different aspects in optimal design of DTI/ADTI experiments. The following are some of the contributions of this research work:

- 1. The diffusion gradient scheme for DTI/ADTI was improved so as to achieve more precise estimates of tissues properties (diffusivities and fiber orientation). Practical application to spinal cord ADTI experiments was demonstrated. Improvements in the fiber tracking of white matter tracts was also verified from the experiments.
- 2. A five-subject human study on the spinal cord as well as detailed simulations to validate the optimization procedure was presented. There are no stringent requirements on the MRI scanner in terms of the RF pulse strength and timing, gradient strengths or use of custom-built pulse-sequence. Hence, this technique is readily usable by other research groups in further studies and the results can be cross-validated easily.

- 3. Application of advanced techniques in the design of optimal experiments were proposed, such as the use of CRLB, injection of prior knowledge into the optimization problem, use of various signal and noise models, partitioned-CRLB methods and use of various estimators. The theoretical framework for the optimization can be used for the design of any experiment that fits similar requirements of the DTI experiment. This shows an immense possibility of the use of techniques developed in this research for other fields, either within MRI or beyond.
- 4. The equivalence of the 4-parameter ADTI model and general 6-parameter DTI model is demonstrated in terms of the estimates of longitudinal and transverse diffusivities. Also, the FA, MD and fiber angle orientations are similar in these two models. Since only four diffusion-weighted MR images are sufficient to estimate the ADTI diffusion parameters, ADTI experiments can be shorter in scan time than a general DTI experiment which indicates potential clinical application.
- 5. ADTI diffusion gradients can be optimized to precisely estimate the transverse diffusivity, which has recently shown high sensitivity to the detection of spinal cord diseases, such as ALS or MS. ADTI optimized gradient schemes can be used in place of current protocols to detect such pathologies.

8.3 Future Work

In this research, a comprehensive diffusion-encoding gradient optimization framework has been developed and analyzed for the ADTI/DTI model with Rician or Gaussian noise. The framework uses subject-specific information and performs within the prescribed range of diffusion parameter values including certain safety margin, thus making this technique less biased and more applicable to clinical DTI studies. An important future work would be the development of an online optimization technique where the subject does not exit the scanner and the total examination time is within an acceptable time limit.

Although the work has mainly focussed on ADTI/DTI, the framework can be extended to any diffusion model, such as the CHARMED model ([9, 131]) and any cost function

can also be used (for example, determinant of CRLB matrix can be replaced by variance of FA). In methods such as HARDI or q-ball imaging [86,88], the post-processing does not use any assumption of the diffusion model although the data acquisition is done using the similar DWI pulse sequences as DTI, such as Stejskal-Tanner PGSE sequence. These non-parametric techniques estimate the orientation distribution function directly from the diffusion-weighted MRI data, but require a large amount of data due to their non-parametric nature. In the study of the effect of number of gradient directions on the estimation performance, it was seen that equivalent estimation performance (in terms of performance indices) was predicted with the use of fewer diffusion gradient directions when optimization of the gradient directions was performed based on prior structural knowledge. This observation can be exploited in the case of non-parametric DWI (such as q-ball imaging) to reduce the number of gradient directions used in the DWI experiment. This could potentially reduce the overall acquisition time and make these non-parametric techniques more clinically usable.

Instead of using a cone angle of the fiber orientation, information of the range of diffusivities (or FA and MD) can also be used for the optimization of the gradient scheme. One application that seems relevant in this regard is the tract-based spatial statistics (TBSS) [14]. TBSS is a voxel-based multiple subject analysis of diffusion-weighted data where FA maps from a group of subjects are co-registered using non-linear techniques and from the group mean of the aligned FA maps a "group mean FA skeleton" is created. The FA skeleton is obtained by thinning the FA maps and applying thresholding to remove low mean FA and/or high inter-subject variability. Essentially, the mean FA skeleton corresponds to the centers of all fiber bundles that are common to the subjects and generally the range of FA in the mean skeleton is narrow. If a priori knowledge of the FA range in the mean skeleton FA is available about a subject group, this optimization framework could potentially be used to estimate the FA values in the range more precisely and hence extract the FA skeleton more precisely as well.

Going beyond neuroimaging, DTI has also been applied to track muscle fibers in skeletal muscles to study the three-dimensional (3D) architecture of skeletal muscles in mice ([63])

and in humans [64]. DTI has also been reported to be used to create biomechanical models of the quadriceps mechanism in humans [32]. These studies show feasibility of fiber tracking using DTI of skeletal muscles. The fiber tracking provides information on the local orientation of the fibers (pennation angle), fiber length and cross-section of the fiber bundles which correlate with muscles physiological cross sectional area, an indicator of force that the muscle can exert [32]. Muscle fibers are fairly organized and oriented in a particular direction. This prior knowledge of the fiber orientation can be incorporated in the DTI gradient scheme optimization framework to more precisely estimate the pennation angle.

By the above instances, the potential future uses of the gradient scheme optimization framework are demonstrated for applications in neuroimaging and imaging of non-nervous tissues, such as skeletal muscles.

APPENDICES

APPENDIX A

Flowcharts and instructions for the overall optimization procedure

In this section, a detailed step-by-step description along with flowcharts of the overall procedure is given. The steps should provide necessary information for any third party to optimize the gradients, conduct the optimized DTI experiment and perform the post-processing necessary. Although the described steps are specifically for spinal cord ADTI experiment, the gradient optimization algorithm can be extended to other regions, such as the brain or muscles. I begin with some information on the selection of subjects and other formalities, such as Institutional Review Board (IRB) approval.

- 1. Obtain IRB approval to conduct human research: A proper certificate of approval from the Institution's review board (for Michigan State University, this is the Biomedical and Health IRB under the Human Research Protection Program) must be obtained if DTI experiments are to be carried out on human subjects. For animal subjects, certificate of approval needs to be obtained from appropriate authority (for Michigan State University, this is the Institutional Animal Care and Use Committee).
- 2. Subject recruitment: For the optimization study, no specific subject recruitment criterion was used. Only criterion was that subject should be normal with no history of spinal cord disease or injury. Age matching is not necessary, but was

used for the experiments.

- 3. Preliminary DTI scan: This step is to collect subject-specific structural information of the spinal cord region. A standard MF15 based DTI protocol is used. Typical protocol is given by: T₂ and diffusion-weighted images acquired using a dual spin-echo EPI sequence on a 3T GE Signa HDx scanner (GE Healthcare, Waukesha, WI), equipped with an 8-channel head coil with the following parameters: 22 contiguous 3-mm axial interleaved slices, T_R = 7000 ms, T_E = 77.4 ms, matrix size =128 x 128, FOV = 16 cm x 16 cm, number of excitations = 1, parallel imaging acceleration factor = 2, b = 1000 s mm⁻², 15 diffusion gradient directions (MF15) and scan time = 1 min 52 sec.
- 4. Preliminary DTI data processing: The flowchart of the preliminary data processing is shown in Fig. A.1. DTI images from the scanner are stored in DICOM (Digital Imaging and Communications in Medicine) format which are converted to NIfTI (Neuroimaging Informatics Technology Initiative) 4D volume data format. The data ordering in the NifTI file is converted from neurological (RAS) to radiological (LAS) order so as to use this data in FSL software package. Eddy current correction is performed to reduce the image distortion (contraction, shift and shear) caused due to eddy currents. This is performed using FSL's FDT toolbox "eddy_correct" routine. Here the diffusion-weighted images are registered with the T₂-weighted image (i.e., the image with no diffusion weighting) using affine transformation (12) degrees of freedom). After the preprocessing, spinal cord region is identified visually and DTI/ADTI fit is performed to estimate the model parameters. Also, FA, MD are calculated. Spinal cord is extracted from the region by applying FA > 0.35 and $\rm MD < 2.5 \times 10^{-3} mm^2 s^{-1}$ thresholds. Now, distribution of fiber angular deviation (α) is computed and the cone angle is determined by selecting the α at 80% cumulative distribution. Next, spinal cord tracts voxels are extracted in the spinal cord region by putting $\alpha < \Lambda$ and FA > 0.6 thresholds. Finally, the mean diffusivities and the fiber angle in the spinal cord tract voxels are calculated and along with the cone angle information are saved for the gradient scheme optimization.

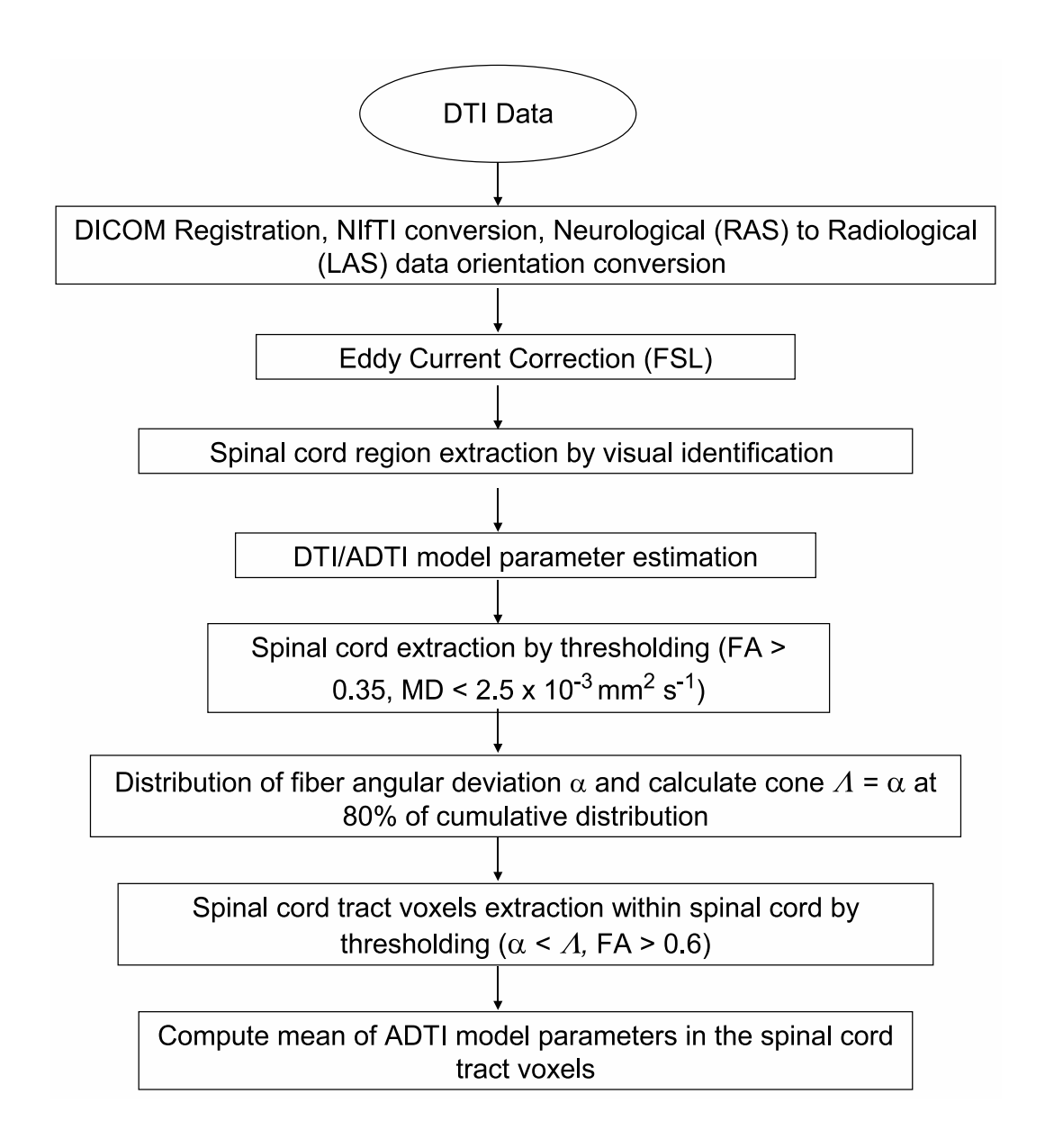


Figure A.1. Flowchart for the processing of the preliminary DTI data to compute the cone angle (Λ) and the mean of ADTI model parameters in the spinal cord tract region.

5. Gradient scheme optimization: The optimization is performed off-line and the subject does not need to be in the scanner during the calculation of the optimized gradient scheme. The flowcharts for the optimization scheme including b-factor optimization are shown the following figures (Fig. A.2 to Fig. A.6). At the beginning, the optimization problem is initialized by selecting the signal model (ADTI/DTI) parameters, noise model(Rician/Gaussian), cost function (full CRLB or partial CRLB), prior knowledge (cone angle and mean values of diffusion model parameters) and finally to include b-factor optimization or not. Depending on

whether b-factor optimization is used or not, there are two options for the optimization. One is for only gradient direction optimization which uses a user input b-factor and the other is the optimization of both b-factor and gradient directions. For the optimization of the gradient directions only, the procedure asks the user for a b-factor and then proceeds in a two-stage gradient directions optimization. In the first stage, a sub-optimal solution of the optimization problem (i.e., a set of gradient directions Ω) is obtained by simulated annealing method (see Fig. A 3). At this

first stage, a sub-optimal solution of the optimization problem (i.e., a set of gradient directions, Ω) is obtained by simulated annealing method (see Fig. A.3). At this stage of the optimization, the cost function is minimized without using the cone angle (Λ) (uses only the mean values of the model parameters). Basic flowchart of the simulated annealing method is shown in Fig. A.3 and the stopping criteria is expanded in Fig. A.4. Simulated annealing (SA) is a stochastic method [73] used here for the minimization of the cost function. The method is inspired from the annealing technique in material science which involves heating the material to a temperature and then cooling is slowly in a controlled fashion so that the crystals in the material are formed without defects. In SA, at each iteration, the algorithm allows for an additional case where the intermediate solution is accepted even if the cost function is not reduced. The criteria is based on a probabilistic thresholding method shown in the flowchart (Fig. A.3). This helps to prevent local minima problems which are particularly rampant in gradient-based methods.

The next step in the optimization is the robust optimization of the gradient directions which uses the cone angle information (see Fig. A.5). The algorithm starts by using the sub-optimal solution. Then, it discretizes the cone of angles into a set of angular locations (grid) and looks for the worst case of cost function (maximum) within the discretized cone of angles. After the worst case location is identified, gradient of the cost function is calculated by finite difference method at the worst case location and the solution is updated along the negative gradient direction (for minimization of cost function). The process is iterated till generally the relative difference in the cost function is within tolerance levels or number of iterations have exceeded or if the solution starts to oscillate. The oscillation issue arises due to

fixed step size issues. At each iteration, the algorithm finds a different worst case location within the cone of angles and minimizes the cost function at that location. Thus, this algorithm literally flattens the cost function curve within the cone of angles and thus brings a uniform cost performance for a range of angles in the cone, making the gradient scheme robust within the cone. Another important aspect of this algorithm is the reformulation of the gradient scheme into a ring-based distribution of gradient directions. This greatly reduces the number of optimization parameters (from the original set of gradient directions angles to a few parameters such as number of rings, number of points on the rings and there zenith angle and azimuthal offset angles). Algorithm uses a predefined set of number of rings and number of points on the rings and tries a number of such configurations to choose the best case.

For the b-factor optimization step, a simulated annealing method is preferred since both the b-factor as well as the gradient directions are varied simultaneously and local minima problems are significant. Gradient-based methods are bound to be stuck at the local minima instead of the global minimum. The algorithm merges the SA methods with the robust optimization methods described previously except for the reformulation of the gradient scheme part. The flowchart is shown in Fig. A.6.

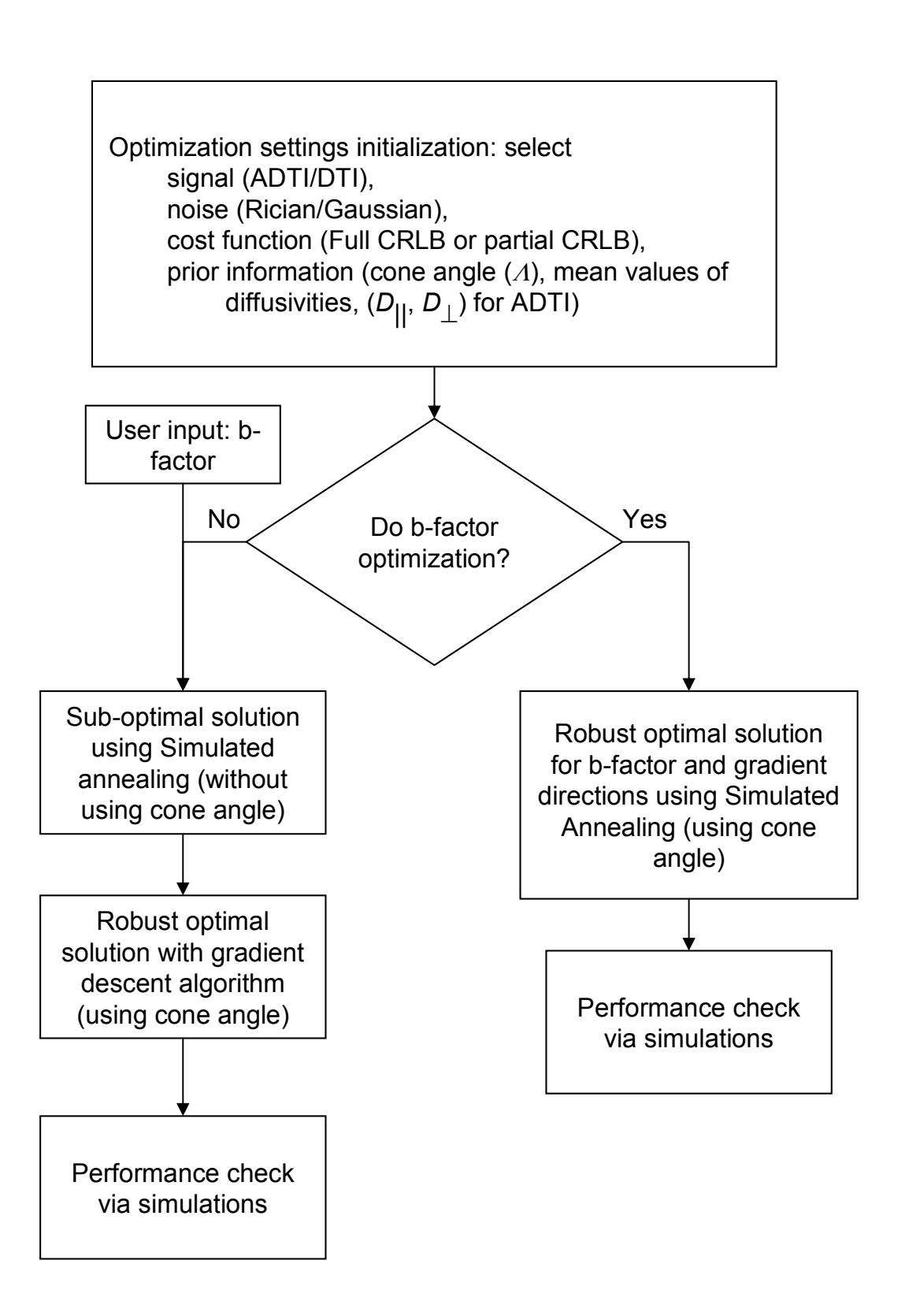


Figure A.2. General overview of the overall gradient and b-factor optimization scheme. Flowcharts for simulated annealing, robust optimization and b-factor optimization are shown in Figs. A.3–A.6.

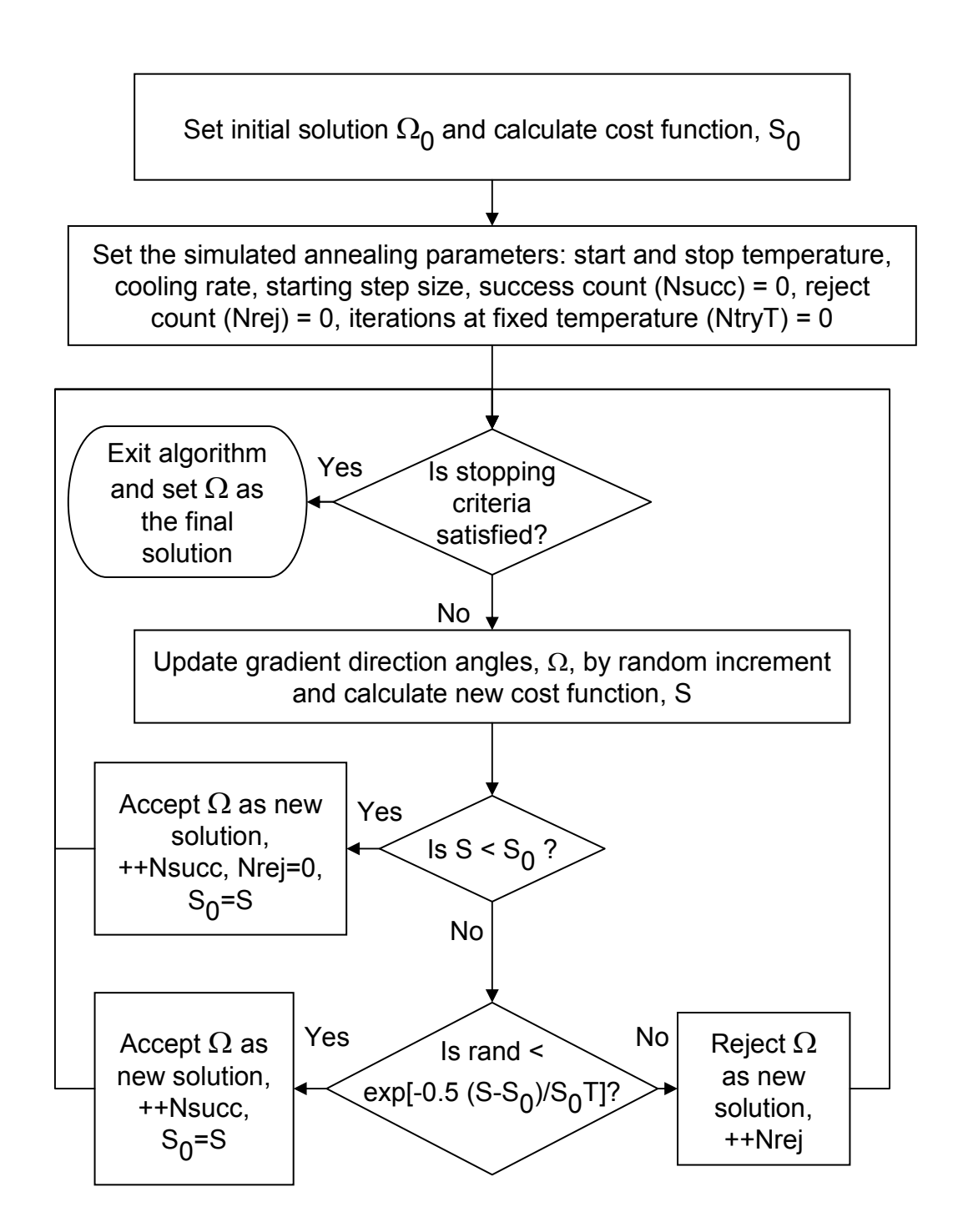


Figure A.3. Flowchart describing the simulated annealing algorithm to find the suboptimal solution (not using the cone angle information). $\Omega = \{g_i; i \in [1, N]\}$, N is
the number of gradient directions (N = 30). g_i is the ith gradient direction vector: $g_i \equiv [g_{xi}, g_{yi}, g_{zi}] \equiv [\theta_i, \phi_i]$. Cost function, $S = \det \Sigma_{CR}$, f_{ull} or $\det \Sigma_{CR}$, p_{artial} . S is a
function of Ω . S_0 is the initial value of cost function for gradient scheme Ω_0 and it is later
updated in every iteration. 'rand' is a function that generates random numbers between
0 and 1 with uniform probability. The flowchart for the decision box for stopping criteria
is shown in Fig. A.4.

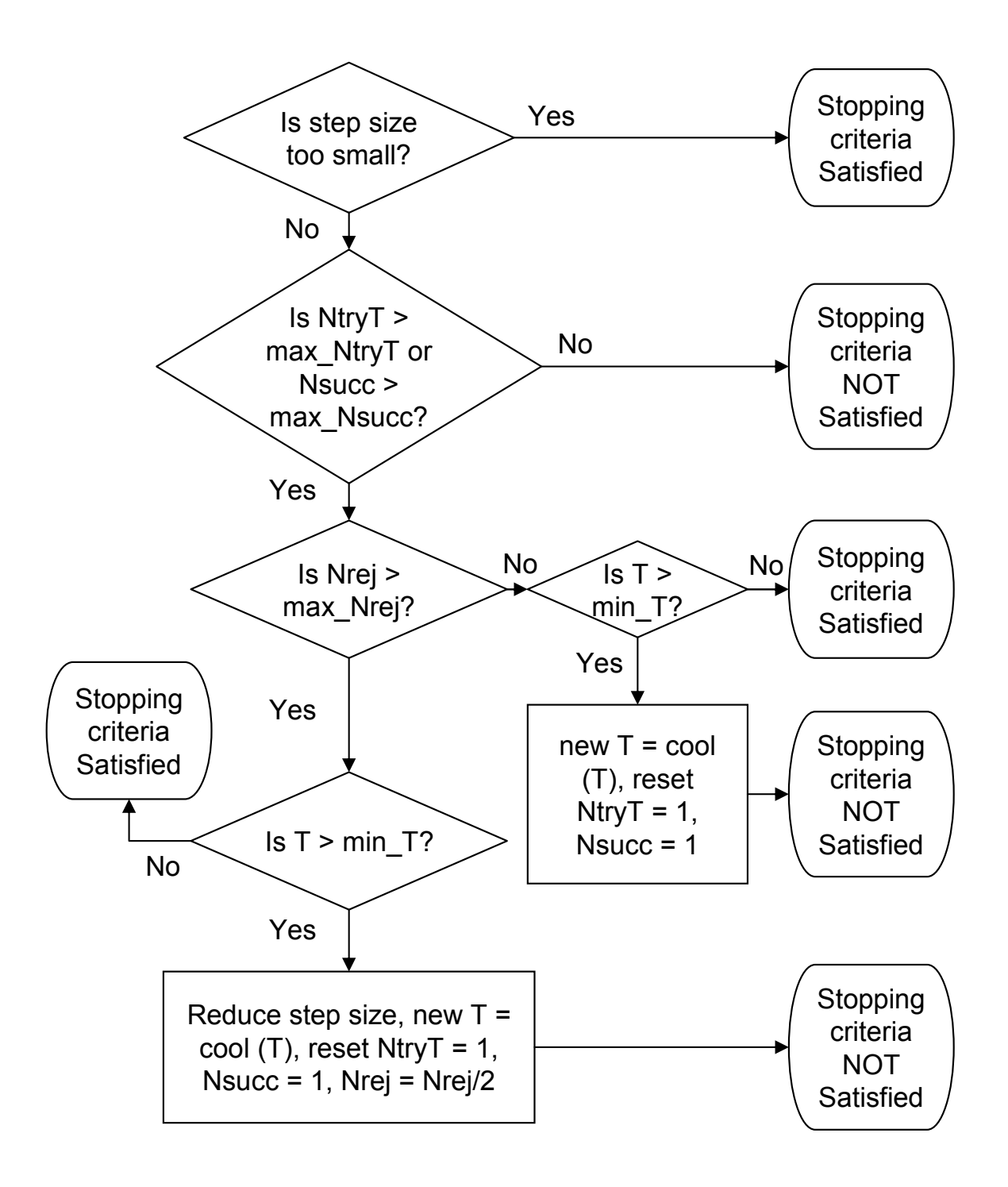


Figure A.4. Flowchart for the stopping criteria in the simulated annealing algorithm. Here, NtryT = number of trials at a fixed temperature T, $max_NtryT = maximum$ limit of NtryT, Nsucc = success count, $max_Nsucc = maximum$ limit of Nsucc, Nrej = consecutive rejection count, $max_Nrej = maximum$ limit of Nrej, T = temperature(simulated), $min_T = minimum$ limit of T, cool(T) = cooling method for T.

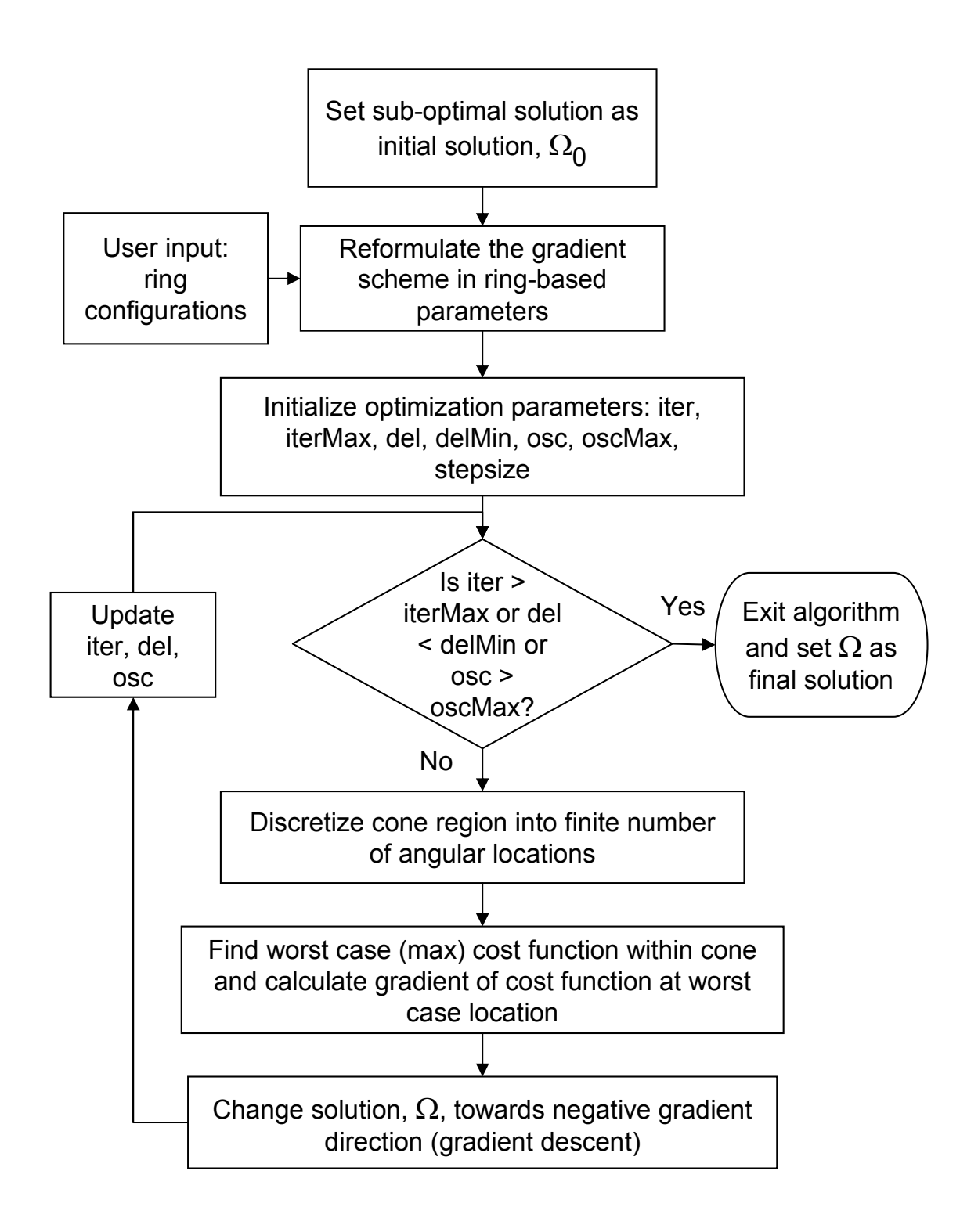


Figure A.5. Flowchart for the robust optimization procedure for the gradient directions utilizing the cone angle information of fiber orientations. $\Omega = \{g_i; i \in [1, N]\}$, N is the number of gradient directions (N = 30). g_i is the ith gradient direction vector. Cost function, $S = \det \Sigma_{CR, full}$ or $\det \Sigma_{CR, partial}$. iter = number of iterations, iterMax = maximum limit of iter, del = absolute relative change in the cost function (abs $(S - S_0/S_0)$), delMin = minimum limit of del, osc = number of oscillations in the cost function, oscMax = maximum limit of osc.

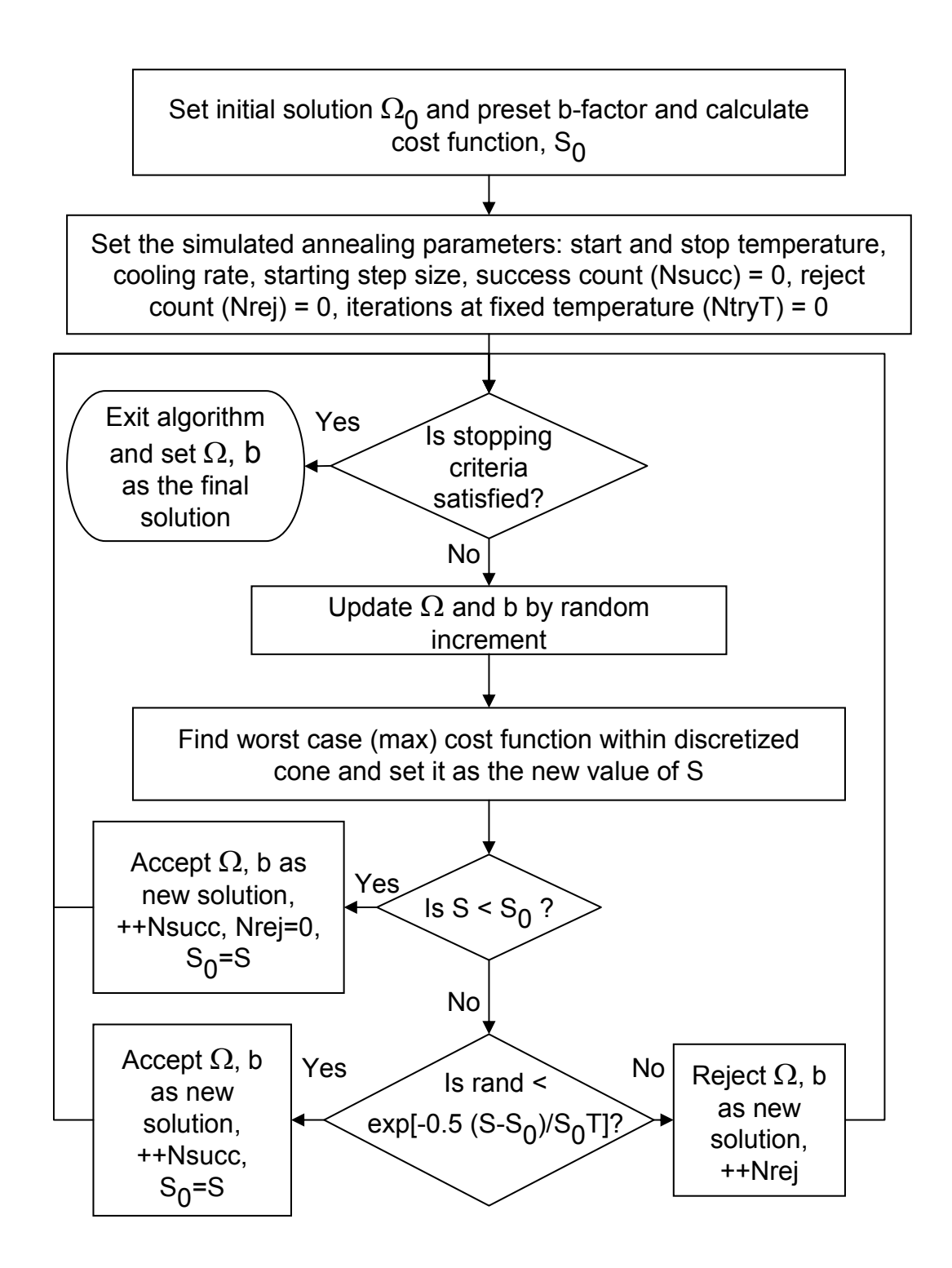


Figure A.6. Flowchart for the robust optimization of gradient directions and b-factor using simulated annealing algorithm utilizing the cone angle information of fiber orientations. Here, $\Omega = \{g_i; i \in [1, N]\}$, N is the number of gradient directions (N = 30). g_i is the *i*th gradient direction vector: $g_i \equiv [g_{xi}, g_{yi}, g_{zi}] \equiv [\theta_i, \phi_i]$. Cost function, $S = \det \Sigma_{CR, full}$ or $\det \Sigma_{CR, partial}$. S is a function of Ω . S_0 is the initial value of cost function for gradient scheme Ω_0 and it is later updated in every iteration. The flowchart for the decision box for stopping criteria is shown in Fig. A.4.

- 6. The performance check consists of calculating the 1D plot the cost function w.r.t. angular deviation, α , or 2D plot of cost function w.r.t. (θ_F, ϕ_F) . Next, the cost functions are calculated using the CRLB formulation for a range of diffusivity as well as fiber directions. Finally, performance indices, such as mean ratio of cost functions of OPT30 versus MF30 under successful voxels (μ_{r1}) and the percentage success (P_S) is calculated from simulations.
- 7. Performing the DTI/ADTI experiment with optimized gradient and/or b-factor: Multiple sets of data are collected using the optimized protocol and a standard MF30 protocol. Typical protocol remains the same as the preliminary DTI scan except that number of excitations = 2 (for additional SNR improvement). The scan time per dataset was typically 7 min 21 sec. For b-factor optimization, the optimized b-factor is used and number of excitations = 4. Since a different b-factor is used, this results in different T_E .
- 8. Processing of the data from the optimized ADTI/DTI scan: The flowchart for the processing is shown in Fig. A.7. The flowchart is similar to the preliminary DTI data processing except that since multiple datasets are involved, a 4D volume registration technique is incorporated in the work flow. After the spinal cord tract voxels are extracted in each of the 4D volume, a common set of voxels are identified amongst all the datasets. This common voxels data is then extrapolated using repetition bootstrapping method to obtain 6000 data samples. The extrapolated dataset is then used for model parameter estimations and calculation of covariance matrix and the variances of various quantities.

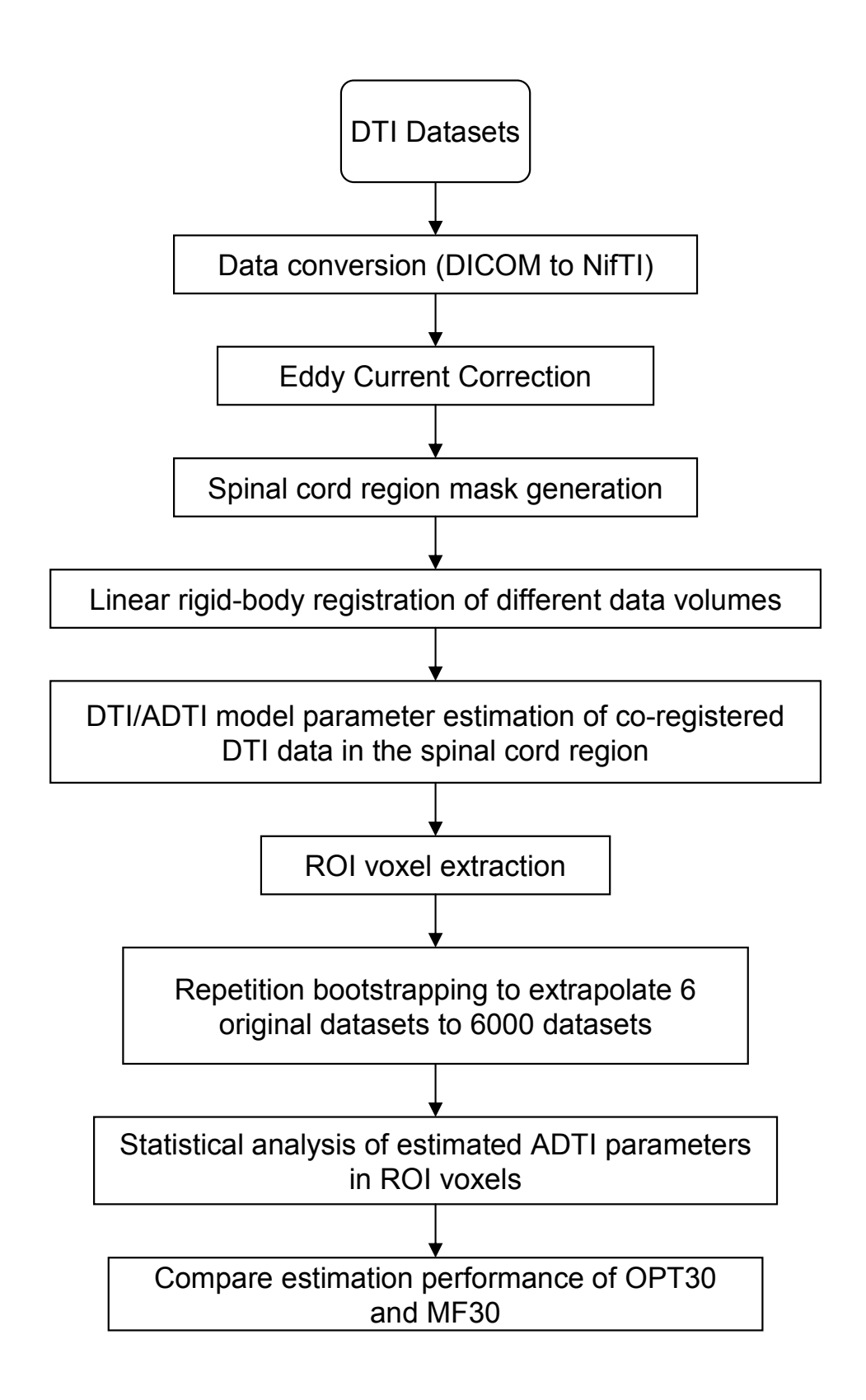


Figure A.7. Flowchart for the processing of the multiple DTI 4D volume datasets obtained by using the optimized protocol and compared to the MF30 protocol.

APPENDIX B

Gradient tables for the spinal cord imaging study

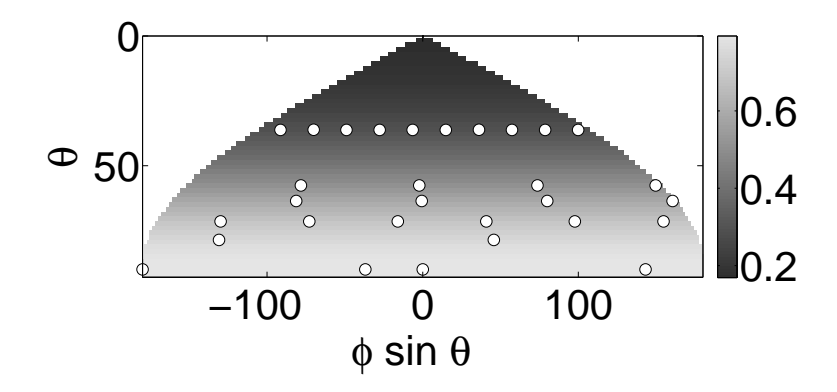


Figure B.1. Diffusion gradient directions (white circles) for Subject 1 optimized using prior structural information. The underlay shows the normalized MR signal w.r.t. gradient direction angles (θ, ϕ) .

Table B.1. DTI Gradient Table for Subject 1 $\,$

g_x	g_y	g_z	g_x	g_y	g_z
1.000	-0.000	0.001	0.215	-0.923	0.318
-1.000	-0.000	0.001	-0.692	-0.648	0.318
0.800	-0.600	0.001	-0.907	0.275	0.318
-0.800	0.600	0.001	-0.215	0.923	0.318
0.674	0.712	0.198	0.692	0.648	0.318
-0.674	-0.712	0.198	0.580	-0.111	0.807
0.896	-0.011	0.445	0.404	-0.430	0.807
-0.011	-0.896	0.445	0.074	-0.586	0.807
-0.896	0.011	0.445	-0.284	-0.517	0.807
0.011	0.896	0.445	-0.534	-0.251	0.807
0.843	-0.039	0.536	-0.580	0.111	0.807
-0.039	-0.843	0.536	-0.404	0.430	0.807
-0.843	0.039	0.536	-0.074	0.586	0.807
0.039	0.843	0.536	0.284	0.517	0.807
0.907	-0.275	0.318	0.534	0.251	0.807

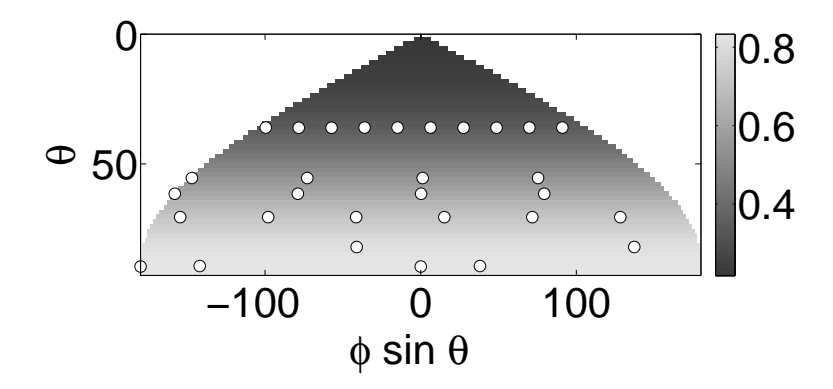


Figure B.2. Diffusion gradient directions (white circles) for Subject 2 optimized using prior structural information. The underlay shows the normalized MR signal w.r.t. gradient direction angles (θ, ϕ) .

Table B.2. DTI Gradient Table for Subject 2

g_x	g_y	g_z	g_x	g_y	g_z
-1.000	-0.000	0.008	-0.227	-0.915	0.334
1.000	-0.000	0.008	0.679	-0.654	0.334
-0.787	-0.617	0.011	0.906	0.261	0.334
0.787	0.617	0.011	0.227	0.915	0.334
-0.742	0.656	0.139	-0.679	0.654	0.334
0.742	-0.656	0.139	-0.578	-0.110	0.809
-0.879	-0.004	0.477	-0.403	-0.429	0.809
0.004	-0.879	0.477	-0.074	-0.584	0.809
0.879	0.004	0.477	0.283	-0.516	0.809
-0.004	0.879	0.477	0.532	-0.251	0.809
-0.823	-0.023	0.567	0.578	0.110	0.809
0.023	-0.823	0.567	0.403	0.429	0.809
0.823	0.023	0.567	0.074	0.584	0.809
-0.023	0.823	0.567	-0.283	0.516	0.809
-0.906	-0.261	0.334	-0.532	0.251	0.809

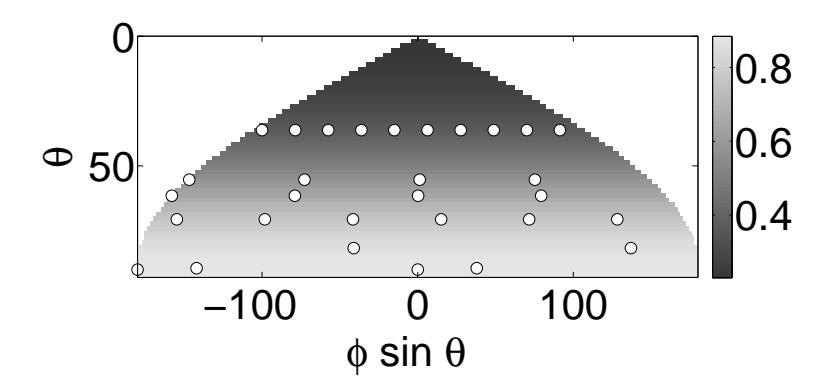


Figure B.3. Diffusion gradient directions (white circles) for Subject 3 optimized using prior structural information. The underlay shows the normalized MR signal w.r.t. gradient direction angles (θ, ϕ) .

Table B.3. DTI Gradient Table for Subject 3

g_x	g_y	g_z	g_x	g_y	g_z
-1.000	-0.000	-0.000	-0.229	-0.915	0.332
1.000	-0.000	-0.000	0.678	-0.656	0.332
-0.789	-0.615	0.010	0.907	0.259	0.332
0.789	0.615	0.010	0.229	0.915	0.332
-0.740	0.656	0.144	-0.678	0.656	0.332
0.740	-0.656	0.144	-0.580	-0.110	0.807
-0.879	-0.004	0.477	-0.404	-0.430	0.807
0.004	-0.879	0.477	-0.075	-0.586	0.807
0.879	0.004	0.477	0.284	-0.518	0.807
-0.004	0.879	0.477	0.534	-0.252	0.807
-0.822	-0.022	0.569	0.580	0.110	0.807
0.022	-0.822	0.569	0.404	0.430	0.807
0.822	0.022	0.569	0.075	0.586	0.807
-0.022	0.822	0.569	-0.284	0.518	0.807
-0.907	-0.259	0.332	-0.534	0.252	0.807

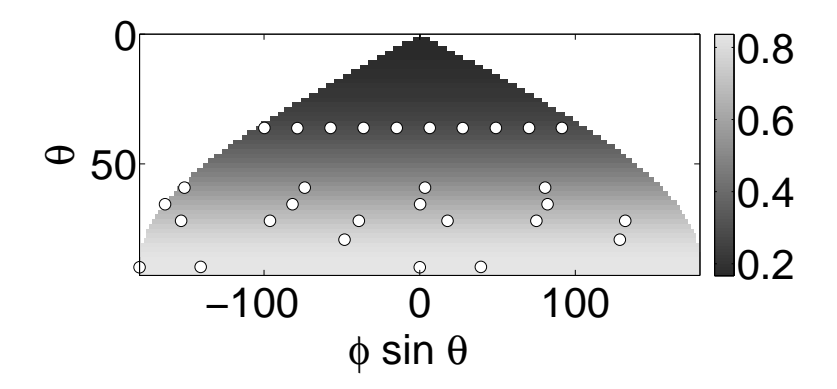


Figure B.4. Diffusion gradient directions (white circles) for Subject 4 optimized using prior structural information. The underlay shows the normalized MR signal w.r.t. gradient direction angles (θ, ϕ) .

Table B.4. DTI Gradient Table for Subject 4

g_x	g_y	g_z	g_x	g_y	g_z
-1.000	-0.000	0.003	-0.184	-0.933	0.310
1.000	0.000	0.003	0.716	-0.626	0.310
-0.774	-0.634	0.005	0.900	0.307	0.310
0.774	0.634	0.005	0.184	0.933	0.310
-0.643	0.743	0.187	-0.716	0.626	0.310
0.643	-0.743	0.187	-0.579	-0.112	0.807
-0.910	-0.004	0.414	-0.403	-0.431	0.807
0.004	-0.910	0.414	-0.072	-0.585	0.807
0.910	0.004	0.414	0.286	-0.516	0.807
-0.004	0.910	0.414	0.534	-0.250	0.807
-0.856	-0.059	0.513	0.579	0.112	0.807
0.059	-0.856	0.513	0.403	0.431	0.807
0.856	0.059	0.513	0.072	0.585	0.807
-0.059	0.856	0.513	-0.286	0.516	0.807
-0.900	-0.307	0.310	-0.534	0.250	0.807

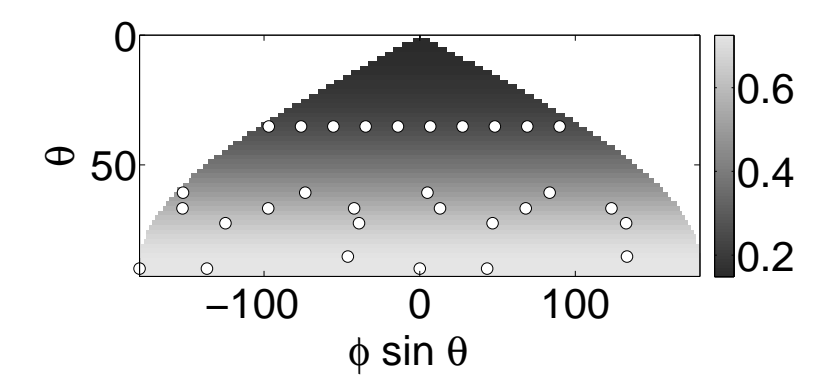


Figure B.5. Diffusion gradient directions (white circles) for Subject 5 optimized using prior structural information. The underlay shows the normalized MR signal w.r.t. gradient direction angles (θ, ϕ) .

Table B.5. DTI Gradient Table for Subject 5

g_x	g_y	g_z	g_x	g_y	g_z
-1.000	-0.000	0.000	-0.251	-0.884	0.395
1.000	0.000	0.000	0.640	-0.659	0.395
-0.728	-0.686	0.001	0.891	0.225	0.395
0.728	0.686	0.001	0.251	0.884	0.395
-0.688	0.721	0.082	-0.640	0.659	0.395
0.688	-0.721	0.082	-0.564	-0.118	0.817
-0.721	0.624	0.301	-0.387	-0.427	0.817
-0.624	-0.721	0.301	-0.062	-0.573	0.817
0.721	-0.624	0.301	0.287	-0.500	0.817
0.624	0.721	0.301	0.526	-0.236	0.817
-0.868	-0.087	0.489	0.564	0.118	0.817
0.087	-0.868	0.489	0.387	0.427	0.817
0.868	0.087	0.489	0.062	0.573	0.817
-0.087	0.868	0.489	-0.287	0.500	0.817
-0.891	-0.225	0.395	-0.526	0.236	0.817

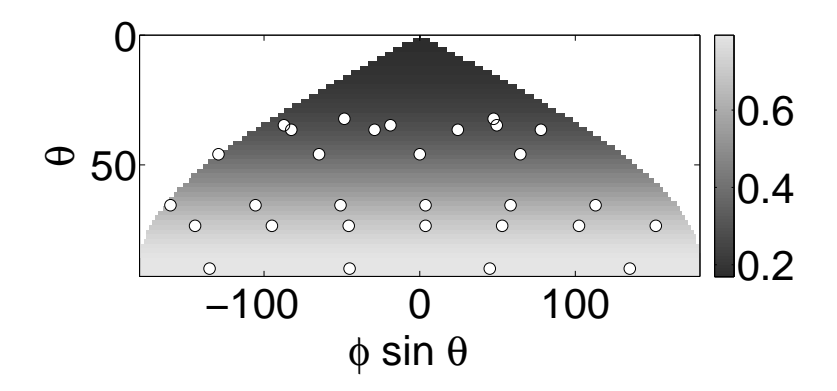


Figure B.6. Diffusion gradient directions (white circles) for Subject 1 optimized using completely uncertain fiber orientation. The underlay shows the normalized MR signal w.r.t. gradient direction angles (θ, ϕ) .

Table B.6. DTI Gradient Table for Subject 1 with $\Lambda=90^{\circ}$

g_x	g_y	g_z	g_x	g_y	g_z
-0.718	-0.000	0.696	0.908	0.065	0.414
0.000	-0.718	0.696	0.398	0.819	0.414
0.718	0.000	0.696	-0.510	0.754	0.414
0.000	0.718	0.696	-0.508	-0.258	0.822
-0.707	-0.707	0.000	0.478	-0.311	0.822
0.707	-0.707	0.000	0.030	0.569	0.822
0.707	0.707	0.000	-0.008	-0.533	0.846
-0.707	0.707	0.000	0.008	0.533	0.846
-0.447	-0.391	0.804	-0.834	-0.473	0.284
0.391	-0.447	0.804	-0.150	-0.947	0.284
0.447	0.391	0.804	0.647	-0.708	0.284
-0.391	0.447	0.804	0.957	0.065	0.284
-0.908	-0.065	0.414	0.546	0.788	0.284
-0.398	-0.819	0.414	-0.276	0.918	0.284
0.510	-0.754	0.414	-0.890	0.357	0.284

BIBLIOGRAPHY

BIBLIOGRAPHY

- [1] B. Horwitz. The elusive concept of brain connectivity. *NeuroImage*, 19:466–470, 2003.
- [2] L. Lee, L. M. Harrison, and A. Mechelli. A report of the functional connectivity workshop, Dusseldorf 2002. *NeuroImage*, 19:457–465, 2003.
- [3] S. A. Huettel, A. W. Song, and G. McCarthy. Functional Magnetic Resonance Imaging. Sinauer Associates, Sunderland, MA, USA, 2004.
- [4] D. L. Sparks, L.-F. Lue, T. A. Martin, and J. Rogers. Neural tract tracing using Di-I: a review and a new method to make fast Di-I faster in human brain. *J. Neuroscience Methods*, 103:3–10, 2000.
- [5] E. O. Stejskal and J. E. Tanner. Spin diffusion measurements: Spin Echoes in the Presence of Time-Dependent Field Gradients. J. Chem. Phys., 42:288–292, 1965.
- [6] E. O. Stejskal. Use of spin echoes in a pulsed magnetic-field gradient to study anisotropic, restricted diffusion and flow. *J. Chem. Phys.*, 43:3597–3603, 1965.
- [7] P. J. Basser, J. Matiello, and D. Le Bihan. MR diffusion tensor spectroscopy and imaging. *Biophys. J.*, 66(1):259–267, 1994.
- [8] L. G. Raguin, D. Hernando, D. C. Karampinos, L. Ciobanu, B. P. Sutton, Z.-P. Liang, and J. G. Georgiadis. Quantitative Analysis of q-Space MRI Data. In IFMBE Proc. 3rd European Medical and Biological Engineering Conference, vol. 11, 2005.
- [9] Y. Assaf, R. Z. Freidlin, G. K. Rohde, and P. J. Basser. New modeling and experimental framework to characterize hindered and restricted water diffusion in brain white matter. *Magn. Reson. Med.*, 52(5):965–978, 2004.
- [10] V. J. Wedeen, T. J. Reese, D. S. Tuch, and et al. Mapping fiber orientation spectra in cerebral white matter with Fourier-transform diffusion MRI. In Proc. Int. Soc. Magn. Reson. Med. 7th Scientific meeting ISMRM99, page 321, 1999.
- [11] D. S. Tuch. Q-Ball Imaging. Magn. Reson. Med., 52:1358–1372, 2004.
- [12] P. J. Basser, J. Matiello, and D. Le Bihan. Estimation of the effective self-diffusion tensor from the NMR spin echo. *J. Magn. Reson. B*, 103:247–254, 1994.
- [13] P. B. Kingsley. Introduction to diffusion tensor imaging mathematics part II: Anisotropy, diffusion weighting factors and gradient encoding schemes. *Concept Magnetic Res. A*, 28:101–122, 2006.

- [14] S. M. Smith, M. Jenkinson, H. Johansen-Berg, D. Rueckert, T. E. Nichols, C. E. Mackay, K. E. Watkins, O. Ciccarelli, M. Z. Cader, P. M. Matthews, and T. E. J. Behrens. Tract-based spatial statistics: Voxelwise analysis of multi-subject diffusion data. *NeuroImage*, 31:1487–1505, 2006.
- [15] P. J. Basser, S. Pajevic, C. Pierpaoli, J. Duda, and A. Aldroubi. In vivo fiber tractography using DT-MRI data. *Magn. Reson. Med.*, 44:625–632, 2000.
- [16] S. Mori, B. J. Crain, V. P. Chacko, and P. C. van Zijl. Three-dimensional tracking of axonal projections in the brain by magnetic resonance imaging. *Ann. Neurol.*, 45:265–269, 1999.
- [17] K. M. Hasan, D. L. Parker, and A. L. Alexander. Comparison of gradient encoding schemes for diffusion-tensor MRI. J. Magn. Reson. Imag., 13:769–780, 2001.
- [18] N. G. Papadakis, D. Xing, C. L.-H. Huang, L. D. Hall, and T. A. Carpenter. A comparative study of acquisition schemes for diffusion tensor imaging using MRI. J. Magn. Reson., 137(1):67–82, 1999.
- [19] S. Skare, M. Hedehus, M. E. Moseley, and T.-Q. Li. Condition number as a measure of noise performance of diffusion tensor data acquisition schemes with MRI. J. Magn. Reson., 147(2):340–352, 2000.
- [20] P. G. Batchelor, D. Atkinson, D. L. G. Hill, F. Calamante, and A. Connelly. Anisotropic noise propagation in diffusion tensor MRI sampling schemes. *Magn. Reson. Med.*, 49(6):1143–1151, 2003.
- [21] H. Peng and K. Arfanakis. Diffusion tensor encoding schemes optimized for white matter fibers with selected orientations. *Magn. Reson. Imaging*, 25:147–153, 2007.
- [22] D. K. Jones, M. A. Horsfield, and A. Simmons. Optimal strategies for measuring diffusion in anisotropic systems by magnetic resonance imaging. *Magn. Reson. Med.*, 42(3):515–525, 1999.
- [23] D. C. Alexander. A general framework for experiment design in diffusion MRI and its application in measuring direct tissue-microstructure features. *Mag. Res. Med.*, 60(2):439–448, 2008.
- [24] O. Brihuega-Moreno, F. P. Heese, and L. D. Hall. Optimization of diffusion measurements using Cramer-Rao lower bound theory and its application to articular cartilage. *Mag. Res. Med.*, 50(5):1069–1076, 2003.
- [25] S. Standring. Gray's Anatomy: The Anatomical Basis of Clinical Practice. Churchill-Livingstone, London, UK, 40th edition, 2008.
- [26] J. C. E. Underwood and S. S. Cross. *General and systematic pathology*. Churchill-Livingstone, London, UK, 5th edition, 2009.

- [27] D. Facon, A. Ozanne, P. Fillard, J. F. Lepeintre, C. Tournoux-Facon, and D. Ducreux. MR diffusion tensor imaging and fiber tracking in spinal cord compression. Am J Neuroradiol., 26(6):1587–1594, 2005.
- [28] K. Shanmuganathan, R. P. Gullapalli, J. Zhuo, and S. E. Mirvis. Diffusion tensor MR imaging in cervical spine trauma. American Journal of Neuroradiology, 29:655–659, 2008.
- [29] M. F. Meek, M. W. Stenekes, H. M. Hoogduin, and J. P. Nicolai. In vivo three-dimensional reconstruction of human median nerves by diffusion tensor imaging. Experimental Neurology, 198:479–482, 2006.
- [30] U. Techavipoo, A. F. Okai, J. Lackey, J. Shi, M. A. Dresner, T. P. Leist, and S. Lai. Toward a practical protocol for human optic nerve DTI with EPI geometric distortion correction. J Magn Reson Imaging, 30:699-707, 2009.
- [31] J. Hiltunen, T. Suortti, S. Arvela, M. Seppa, R. Joensuu, and R. Hari. Diffusion tensor imaging and tractography of distal peripheral nerves at 3 T. *Clin Neuro-physiol*, 116:2315–2323, 2005.
- [32] J. H. Kan, A. M. Heemskerk, Z. Ding, A. Gregory, G. Mencio, K. Spindler, and B. M. Damon. DTI-based muscle fiber tracking of the quadriceps mechanism in lateral patellar dislocation. *Journal of Magnetic Resonance Imaging*, 29:663–670, 2009.
- [33] J. V. Beck and K. J. Arnold. Parameter Estimation in Engineering and Science. John Wiley & Sons, New York, NY, USA, 1977.
- [34] J. V. Beck and K. A Woodbury. Inverse problems and parameter estimation: integration of measurements and analysis . *Meas. Sci. Technol.*, 9:839–847, 1998.
- [35] P. G. Lindberg, A. Feydy, and M. A. Maier. White matter organization in cervical spinal cord relates differently to age and control of grip force in healthy subjects. *J. Neurosci.*, 30:4102–4109, 2010.
- [36] S. Morisaki, Y. Kawai, M. Umeda, M. Nishi, R. Oda, H. Fujiwara, K. Yamada, T. Higuchi, C. Tanaka, M. Kawata, and T. Kubo. In vivo assessment of peripheral nerve regeneration by diffusion tensor imaging. *J Magn Reson Imaging*, 33:535–542, 2011.
- [37] S. M. Hesseltine, M. Law, J. Babb, M. Rad, S. Lopez, Y. Ge, G. Johnson, and R. I. Grossman. Diffusion tensor imaging in multiple sclerosis: assessment of regional differences in the axial plane within normal-appearing cervical spinal cord. AJNR Am J Neuroradiol, 27:1189–1193, 2006.
- [38] J. Renoux, D. Facon, P. Fillard, I. Huynh, P. Lasjaunias, and D. Ducreux. MR diffusion tensor imaging and fiber tracking in inflammatory diseases of the spinal cord. *AJNR Am J Neuroradiol*, 27:1947–1951, 2006.

- [39] W. Gao, H. Zhu, and W. Lin. A unified optimization approach for diffusion tensor imaging technique. *NeuroImage*, 44:729–741, 2009.
- [40] K. J. Friston. Functional and effective connectivity in neuroimaging: A synthesis. Human Brain Mapping, 2:56–78, 1994.
- [41] A. McLntosh and F. Gonzalez-Lima. Structural equation modeling and its application to network analysis in functional brain imaging. *Human Brain Mapping*, 2:2–22, 1994.
- [42] K. Friston, L. Harrison, and W. Penny. Dynamic causal modelling. *NeuroImage*, 19:1273–1302, 2003.
- [43] R. Goebel, A. Roebroeck, D. Kim, and E. Formisano. Investigating directed cortical interactions in time-resolved fMRI data using vector autoregressive modeling and Granger causality mapping. *Magnetic Resonance Imaging*, 21:1251–1261, 2003.
- [44] L. Harrison, W. Penny, and K. Friston. Multivariate autoregressive modeling of fMRI time series. *NeuroImage*, 19:1477–1491, 2003.
- [45] S. Ogawa, R. S. Menon, D. W. Tank, S. G. Kim, H. Merkle, J. M. Ellermann, and K. Ugurbil. Functional brain mapping by blood oxygenation level-dependent contrast magnetic resonance imaging. A comparison of signal characteristics with a biophysical model. *Biophysical journal*, 64:803–812, 1993.
- [46] J. A. Brunberg, K. A. Frey, J. A. Horton, J. P. Deveikis, D. A. Ross, and R. A. Koeppe. H₂O positron emission tomography determination of cerebral blood flow during balloon test occlusion of the internal carotid artery. American Journal of Neuroradiology, 15:725-732, 1994.
- [47] E. Niedermeyer and F. H. L. Silva. Electroencephalography: basic principles, clinical applications, and related fields. Lippincott Williams & Wilkins, Philadelphia, PA, USA, 2005.
- [48] M. Hämäläinen, R. Hari, R. J. Ilmoniemi, J. Knuutila, and O. V. Lounasmaa. Magnetoencephalography—theory, instrumentation, and applications to noninvasive studies of the working human brain. *Rev. Mod. Phys.*, 65(2):413–497, 1993.
- [49] G. A. Johnson, H. Benveniste, R. D. Black, L. W. Hedlund, R. R. Maronpot, and B. R. Smith. Histology by magnetic resonance microscopy. *Magnetic Resonance Quarterly*, 9:1–30, 1993.
- [50] G. M. Fatterpekar, T. P. Naidich, B. N. Delman, J. G. Aguinaldo, S. H. Gultekin, C. C. Sherwood, P. R. Hof, B. P. Drayer, and Z. A. Fayad. Cytoarchitecture of the human cerebral cortex: MR microscopy of excised specimens at 9.4 Tesla. *American Journal of Neuroradiology*, 23:1313–1321, 2002.

- [51] R. Mizutani, A. Takeuchi, K. Uesugi, S. Takekoshi, R. Y. Osamura, and Y. Suzuki. Microtomographic analysis of neuronal circuits of human brain. *Cerebral Cortex*, 20:1739–1748, 2010.
- [52] K. L. Briggman and W. Denk. Towards neural circuit reconstruction with volume electron microscopy techniques. *Current Opinion in Neurobiology*, 16:562–570, 2006.
- [53] M. D. Greicius, K. Supekar, V. Menon, and R. F. Dougherty. Resting-State Functional Connectivity Reflects Structural Connectivity in the Default Mode Network. Cerebral Cortex, 19:72–78, 2009.
- [54] M. Smits, M. W. Vernooij, P. A. Wielopolski, A. J. Vincent, G. C. Houston, and A. van der Lugt. Incorporating functional MR imaging into diffusion tensor tractography in the preoperative assessment of the corticospinal tract in patients with brain tumors. *American Journal of Neuroradiology*, 28:1354–1361, 2007.
- [55] D. Le Bihan, J. F. Mangin, C. Poupon, C. A. Clark, S. Pappata, N. Molko, and H. Chabriat. Diffusion tensor imaging: concepts and applications. J. Magn. Reson. Imaging, 13:534–546, 2001.
- [56] D. J. Werring, C. A. Clark, G. J. Barker, A. J. Thompson, and D. H. Miller. Diffusion tensor imaging of lesions and normal-appearing white matter in multiple sclerosis. *Neurology*, 52(8):1626–1632, 1999.
- [57] P. J. Basser, S. Pajevic, C. Pierpaoli, J. Duda, and A. Aldroubi. In vivo fiber tractography using DT-MRI data. *Magnetic Resonance in Medicine*, 44:625–632, 2000.
- [58] T. E. Conturo, N. F. Lori, T. S. Cull, E. Akbudak, A. Z. Snyder, J. S. Shimony, R. C. McKinstry, H. Burton, and M. E. Raichle. Tracking neuronal fiber pathways in the living human brain. *Proceedings of National Academy of Science*, USA, 96:10422–10427, 1999.
- [59] T. E. Behrens, H. J. Berg, S. Jbabdi, M. F. Rushworth, and M. W. Woolrich. Probabilistic diffusion tractography with multiple fibre orientations: What can we gain? *Neuroimage*, 34(1:144–155, 2007.
- [60] G. J. M. Parker, H. A. Haroon, and C. A. M. Wheeler-Kingshott. A framework for a streamline-based Probabilistic Index of Connectivity (PICo) using a structural interpretation of MRI diffusion measurements. *J. Magn. Reson. Imaging*, 18:242– 254, 2003.
- [61] C. M. Ellis, A. Simmons, D. K. Jones, J. Bland, J. M. Dawson, M. A. Horsfield, S. C. R. Williams, and P. N. Leigh. Diffusion tensor MRI assesses corticospinal tract damage in ALS. *Neurology*, 53(5):1051–1058, 1999.

- [62] H. Mamata, F. A. Jolesz, and S. E. Maier. Apparent diffusion coefficient and fractional anisotropy in spinal cord: age and cervical spondylosis-related changes. J Magn Reson Imaging, 22(1):38–43, 2005.
- [63] A. M. Heemskerk, G. J. Strijkers, A. Vilanova, M. R. Drost, and K. Nicolay. Determination of mouse skeletal muscle architecture using three-dimensional diffusion tensor imaging. *Magnetic Resonance in Medicine*, 53:1333–1340, 2005.
- [64] D. A. Lansdown, Z. Ding, M. Wadington, J. L. Hornberger, and B. M. Damon. Quantitative diffusion tensor MRI-based fiber tracking of human skeletal muscle. *Journal of Applied Physiology*, 103:673–81, 2007.
- [65] M. Ries, R. A. Jones, V. Dousset, and C. T. Moonen. Diffusion tensor MRI of the spinal cord. Magn. Reson. Med., 44:884–892, 2000.
- [66] J. P. Mottershead, K. Schmierer, M. Clemence, J. S. Thornton, F. Scaravilli, G. J. Barker, P. S. Tofts, J. Newcombe, M. L. Cuzner, R. J. Ordidge, W. I. McDonald, and D. H. Miller. High field mri correlates of myelin content and axonal density in multiple sclerosis: A post-mortem study of the spinal cord. *J. Neurol.*, 250:1293–1301, 2003.
- [67] D. Ducreux, J. F. Lepeintre, P. Fillard, C. Loureiro, M. Tadié, and P. Lasjaunias. MR diffusion tensor imaging and fiber tracking in 5 spinal cord astrocytomas. American J. Neuroradiology, 27:214–216, 2006.
- [68] A. W. Anderson. Measurement of fiber orientation distributions using high angular resolution diffusion imaging. *Magnetic Resonance in Medicine*, 54:1194–1206, 2005.
- [69] M. Onu, P. Gervai, J. Cohen-Adad, J. Lawrence, J. Kornelsen, B. Tomanek, and U. N. Sboto-Frankenstein. Human cervical spinal cord funiculi: investigation with magnetic resonance diffusion tensor imaging. *Journal of Magnetic Resonance Imag*ing, 31:829–837, 2010.
- [70] J. Gullapalli, J. Krejza, and E. D. Schwartz. In vivo DTI evaluation of white matter tracts in rat spinal cord. *J. Magn. Reson. Imaging*, 24(1):231–234, 2006.
- [71] V. Gulani, G. A. Iwamoto, H. Jiang, J. S. Shimony, A. G. Webb, and P. C. Lauterbur. A multiple echo pulse sequence for diffusion tensor imaging and its application in excised rat spinal cords. *Mag. Res. Med.*, 38(6):868–873, 1997.
- [72] N. Yanasak, J. D. Allison, Q. Zhao, T. C.-C. Hu, and K. Dhandapani. Non-uniform gradient prescription for precise angular measurements using DTI. Med. Image. Comput. Comput. Assist. Interv., 5241:866–873, 2008.
- [73] N. Metropolis, A. W. Rosenbluth, M. N. Rosenbluth, A. H. Teller, and E. Teller. Equations of State Calculations by Fast Computing Machines. J. Chem. Phys., 21:1087–1092, 1953.

- [74] J. L. R. Andersson. Maximum a posteriori estimation of diffusion tensor parameters using a Rician noise model: Why, how and but. *NeuroImage*, 42(4):1340–1356, 2008.
- [75] E. M. Haacke, R. W. Brown, M. R. Thompson, and R. Venkatesan. Magnetic Resonance Imaging: Physical Principles and Sequence Design. Wiley-LISS, New York, NY, USA, 1999.
- [76] D. G. Nishimura. *Principles of Magnetic Resonance Imaging*. Stanford University, Stanford, CA, USA, 1996.
- [77] P. Woodward. MRI for Technologists. McGraw-Hill, New York, NY, USA, 2nd edition, 2001.
- [78] A. Einstein. Über die von der molekularkinetischen Theorie der Wärme geforderte Bewegung von in ruhenden Flüssigkeiten suspendierten Teilchen. (English: On the movement of small particles suspended in a stationary liquid demanded by the molecular-kinetic theory of heat.). Annalen der Physik, 322:549–560, 1905.
- [79] P. T. Callaghan. How Two Pairs of Gradient Pulses Give Access to New Information about Molecular Dynamics. *The Open-Access Journal for the Basic Principles of Diffusion Theory, Experiment and Application: Diffusion Fundamentals* 2, 64:1–18, 2005.
- [80] H. C. Torrey. Bloch equations with diffusion terms. *Physical Review*, 104:563–565, 1956.
- [81] J. Mattiello, P. J. Basser, and D. Le Bihan. Analytical expressions for the b matrix in nmr diffusion imaging and spectroscopy. *JMRA*, 108:131–141, 1994.
- [82] J. E. Tanner and E. O. Stejskal. Restricted self-diffusion of protons in colloidal systems by the pulsed-gradient, spin-echo method. *J. Chem. Phys.*, 49(4):1768–1777, 1968.
- [83] P. T. Callaghan. Pulsed-gradient spin-echo NMR for planar, cylindrical, and spherical pores under conditions of wall relaxation. J. Magn. Reson. A, 113:53–59, 1995.
- [84] S. Majumdar, S. S. Udpa, and L. G. Raguin. Robust optimization of diffusion-weighted MRI protocols used for fiber reconstruction. *J. Phys: Conf. Series*, 135:012069, 2008.
- [85] S. Majumdar, D. C. Zhu, G. Raguin, and S. S. Udpa. Optimization of diffusion encoding gradients in axisymmetric diffusion tensor imaging using a priori structure information. In Proc. Int. Soc. Magn. Reson. Med. 17th Scientific meeting ISMRM09, 2009.
- [86] D. S. Tuch, T. G. Reese, M. R. Wiegell, and V. J. Wedeen. Diffusion MRI of complex neural architecture. *Neuron*, 40:885–895, 2003.

- [87] D. C. Alexander. Multiple-Fiber Reconstruction Algorithms for Diffusion MRI. Ann. N.Y. Acad. Sci., 1064:113–133, 2005.
- [88] D. S Tuch, T. G. Reese, M.R. Wiegell, N. Makris, J.W. Belliveau, and V. J. Wedeen. High angular resolution diffusion imaging reveals intravoxel white matter fiber heterogeneity. *Mag. Res. Med.*, 48:577–582, 2002.
- [89] C. P. Hess, P. Mukherjee, E. T. Han, D. Xu, and D. B. Vigneron. Q-ball reconstruction of multimodal fiber orientations using the spherical harmonic basis. *Magnetic Resonance in Medicine*, 56:104–17, 2006.
- [90] C. Lenglet, J. S. Campbell, M. Descoteaux, G. Haro, P. Savadjiev, D. Wassermann, A. Anwander, R. Deriche, G. B. Pike, G. Sapiro, K. Siddiqi, and P. M. Thompson. Mathematical methods for diffusion MRI processing. *NeuroImage*, 45:S111–S122, 2009.
- [91] P. Mansfield. Multi-planar image formation by using NMR spin-echoes. *J Phys C*, 10:L55–L58, 1977.
- [92] F. Schick, J. Forster, J. Machann, R. Kuntz, and C. D. Claussen. Improved Clinical Echo-Planar MRI Using Spatial-Spectral Excitation. *JMRI*, 8:960–967, 1998.
- [93] T. G. Reese, O. Heid, R. M. Weisskoff, and V. J. Wedeen. Reduction of Eddy-Current-Induced Distortion in Diffusion MRI Using a Twice-Refocused Spin Echo. Mag. Res. Med., 49:177–182, 2003.
- [94] J. Finsterbusch. Double-spin-echo diffusion weighting with a modified eddy current adjustment. *Mag. Res. Imag.*, 28:434–440, 2010.
- [95] B. J. Mock and C. R. Michelich. B-value calculation and correction using a linear segment gradient waveform model. United States Patent, 2003. Patent no. US 6 670 812 B1.
- [96] P. J. Basser, S. Pajevic, C. Pierpaoli, J. Duda, and A. Aldroubi. In vivo fiber tractography using DT MRI data. *Magn. Reson. Med.*, 44(4):625–632, 2000.
- [97] C. Poupon, C. A. Clark, V. Frouin, J. Regis, I. Bloch, D. Le Bihan, and J. Mangin. Regularization of diffusion-based direction maps for the tracking of brain white matter fascicles. *Neuroimage*, 12:184–195, 2000.
- [98] G. J. Parker and D. C. Alexander. Probabilistic anatomical connectivity derived from the microscopic persistent angular structure of cerebral tissue. *Philos. Trans. R. Soc. Lond.*, *B, Biol. Sci.*, 360:893–902, 2005.
- [99] B. Chen and A. W. Song. Diffusion tensor imaging fiber tracking with local tissue property sensitivity: phantom and in vivo validation. *Magn Reson Imaging*, 26:103–108, 2008.

- [100] M. W. Woolrich, S. Jbabdi, B. Patenaude, M. Chappell, S. Makni, T. Behrens, C. Beckmann, M. Jenkinson, and S. M. Smith. Bayesian analysis of neuroimaging data in FSL. *Neuroimage*, 45:S173–186, 2009.
- [101] T. E. J. Behrens, M. W. Woolrich, M. Jenkinson, H. Johansen-Berg, R. G. Nunes, S. Clare, P. M. Matthews, J. M. Brady, and S. M. Smith. Characterization and propagation of uncertainty in diffusion-weighted MR imaging. *Mag. Res. Med.*, 50(5):1077–1088, 2003.
- [102] S. Mori and P. C. M. van Zijl. Fiber tracking: principles and strategies a technical review. *NMR in Biomedicine*, 15:468–480, 2002.
- [103] H. Jiang, P. C. van Zijl, J. Kim, G. D. Pearlson, and S. Mori. DtiStudio: resource program for diffusion tensor computation and fiber bundle tracking. *Comput Methods Programs Biomed*, 81:106–116, 2006.
- [104] S. Mori, W. E. Kaufmann, C. Davatzikos, B. Stieltjes, L. Amodei, K. Fredericksen, G. D. Pearlson, E. R. Melhem, M. Solaiyappan, G. V. Raymond, H. W. Moser, and P. C. van Zijl. Imaging cortical association tracts in the human brain using diffusion-tensor-based axonal tracking. *Magn Reson Med*, 47:215–223, 2002.
- [105] S. Hofer and J. Frahm. Topography of the human corpus callosum revisited—comprehensive fiber tractography using diffusion tensor magnetic resonance imaging. *Neuroimage*, 32:989–994, 2006.
- [106] R. Brecheisen, B. Platel, A. Vilanova, and B. ter Haar Romeny. Parameter sensitivity visualization for DTI fiber tracking. *IEEE Trans Vis Comput Graph*, 15:1441–1448, 2009.
- [107] S. Correia, S. Y. Lee, T. Voorn, D. F. Tate, R. H. Paul, S. Zhang, S. P. Salloway, P. F. Malloy, and D. H. Laidlaw. Quantitative tractography metrics of white matter integrity in diffusion-tensor MRI. *Neuroimage*, 42:568–581, 2008.
- [108] A. Stadlbauer, E. Salomonowitz, G. Strunk, T. Hammen, and O. Ganslandt. Agerelated degradation in the central nervous system: assessment with diffusion-tensor imaging and quantitative fiber tracking. *Radiology*, 247:179–188, 2008.
- [109] S. M. Kay. Fundamentals of Statistical Signal Processing: Estimation Theory. Prentice Hall, New Jersey, USA, 1 edition, 1993. pp. 47–49.
- [110] R. M. Henkelman. Measurement of signal intensities in the presence of noise in MR images. *Med. Phys.*, 12(2):232–233, 1985.
- [111] S. O. Rice. Mathematical analysis of random noise. *J. Bell System Tech.*, 23:282–332, 1944.
- [112] S. O. Rice. Mathematical Analysis of Random Noise. J. Bell System Tech., 24:46–156, 1945.

- [113] H. Gudbjartsson and S. Patz. The Rician distribution of noisy MRI data. *Magn. Reson. Med.*, 34(6):910–914, 1995.
- [114] C. G. Koay and P. J. Basser. Analytically exact correction scheme for signal extraction from noisy magnitude MR signals. *J. Mag. Res.*, 179(2):317–322, 2006.
- [115] K. Levenberg. A Method for the solution of certain non-linear problems in least squares. The Quarterly of Applied Mathematics, 2:164–168, 1944.
- [116] D. Marquardt. An algorithm for least-squares estimation of nonlinear parameters. SIAM Journal on Applied Mathematics, 11:431–441, 1963.
- [117] J Sijbers, A. J. den Dekker, P. Scheunders, and D. Van Dyck. Maximum-likelihood estimation of Rician distribution parameters. *IEEE Trans. Med. Imag.*, 17(3):357–361, 1998.
- [118] D. C. Alexander. Axon radius measurements in vivo from diffusion MRI: a feasibility study. In *Proc. Eleventh IEEE International Conference on Computer Vision*, Workshop on Mathematical Methods in Biomedical Image Analysis, pages 1–8, 2007.
- [119] L. G. Raguin, S. Majumdar, and S. S. Udpa. Design of optimal experimental parameters for diffusion-weighted MRI fiber-tracking protocols. *Int. J. Appl. Electromagn. Mech.*, 28(1–2):61–67, 2008.
- [120] L. L. Scharf and L. T. McWhorter. Geometry of the Cramer-Rao bound. In *Proc. IEEE Sixth SP Workshop on Statistical Signal and Array Processing*, pages 5–8, 1992.
- [121] M. A. Woodbury. Inverting modified matrices. Memorandum Rept., Statistical Research Group, Princeton University, 42:4, 1950.
- [122] S. Kirkpatrick, C. D. Gelatt, and M. P. Vecchi. Optimization by Simulated Annealing. *Science*, 220(4598):671–680, 1983.
- [123] W. H. Press, S. A. Teukolsky, W. T. Vetterling, and B. P. Flannery. *Numerical recipes in C: the art of scientific computing*. Cambridge University Press, Cambridge, MA, USA, 2 edition, 1992.
- [124] National Electrical Manufacturers Association. Determination of signa-to-noise ratio (SNR) in diagnostic magnetic resonance images. Technical Report No. MS 1, NEMA, 2008.
- [125] A. H. Poonawalla and X. J. Zhou. Analytical error propagation in diffusion anisotropy calculations. *J. Mag. Res. Imag.*, 19:489–498, 2004.
- [126] M. Jenkinson, P. R. Bannister, J. M. Brady, and S. M. Smith. Improved optimization for the robust and accurate linear registration and motion correction of brain images. *NeuroImage*, 17(2):825–841, 2002.

- [127] S. Pajevic and P. J. Basser. Parametric and non-parametric statistical analysis of DT-MRI data. *JMR*, 161:1–14, 2003.
- [128] G. Nair, J. D. Carew, S. Usher, D. Lu, X. P. Hu, and M. Benatar. Diffusion tensor imaging reveals regional differences in the cervical spinal cord in amyotrophic lateral sclerosis. *NeuroImage*, 53:576–583, 2010.
- [129] C. A. Wheeler-Kingshott, S. J. Hickman, G. J. Parker, O. Ciccarelli, M. R. Symms, D. H. Miller, and G. J. Barker. Investigating cervical spinal cord structure using axial diffusion tensor imaging. *Neuroimage*, 16:93–102, 2002.
- [130] M. Filippi, M. Cercignani, M. Inglese, M. A. Horsfield, and G. Comi. Diffusion tensor magnetic resonance imaging in multiple sclerosis. *Neurology*, 56:304–311, 2001.
- [131] Y. Assaf and P. J. Basser. Composite hindered and restricted model of diffusion(charmed) mr imaging of human brain. *J. Neuroimage*, 27:48–58, 2005.